

The conserved role of MafB in macrophage differentiation and functional identity

Domien Vanneste



Promoter	Prof. Dr. Thomas MARICHAL
Thesis committee	Prof. Dr. Bénédicte MACHIELS Prof. Dr. Pierre CLOSE
Examination board	Prof. Dr. Elvira MASS Prof. Dr. Kiavash MOVAHEDI Prof. Dr. Francesca RAPINO Prof. Dr. Franck DEQUIEDT Prof. Dr. Laurent GILLET Prof. Dr. Alain CHARIOT
President of the board	Prof. Dr. Nicolas KORSAK KOULAGENKO



UNIVERSITE DE LIEGE

FACULTE DE MEDECINE VETERINAIRE

DEPARTEMENT DES SCIENCES FONCTIONELLES

LABORATOIRE D'IMMUNOPHYSIOLOGIE

Le rôle conservé de MafB dans la différenciation et l'identité
fonctionnelle des macrophages

The conserved role of MafB in macrophage differentiation
and functional identity

Domien VANNESTE

THESE PRESENTEE EN VUE DE L'OBTENTION DU GRADE DE
DOCTORAT EN SCIENCES VETERINAIRES

ANNEE ACADEMIQUE 2025-2026

Illustration of the cover:

Front: this cover art portrays the heterogeneity and plasticity of macrophages, illustrating how macrophages adopt diverse phenotypes in response to their microenvironment. The composition draws inspiration from Wassily Kandinsky's Squares with Concentric Circles, reimagined through a biological lens to reflect the complexity of innate immune regulation. Artwork by Domien Vanneste.

Back: This cover was inspired by Wassily Kandinsky's Squares with Concentric Circles. Artwork by Moon Veerle Vanneste Ngaji.

Citation:

Vanneste, D. (2026). The conserved role of MafB in macrophage differentiation and functional identity (Doctoral dissertation, Universite de Liege (Belgium)).

ISBN: 978-2-87543-250-6

19 June 2026

Acknowledgements

This thesis would not have been possible without the support, guidance, and encouragement of many people to whom I would like to express my sincere gratitude. First and foremost, I would like to thank my promotor for the continuous guidance, valuable insights, and support provided throughout the course of this research project. Their expertise and constructive feedback have been essential to the development and completion of this thesis. I would also like to extend my gratitude to the members of my thesis committee for their time, thoughtful suggestions, and academic guidance during the different stages of this work. In addition, I sincerely thank the members of the jury for carefully evaluating this thesis and for their valuable comments and observations. I am grateful to everyone who contributed, directly or indirectly, to this achievement and supported me throughout this journey. I would especially like to acknowledge and thank the following people for their important role in the completion of this thesis.

Domien

Table of Contents

SUMMARY	1
RÉSUMÉ	5
ABBREVIATIONS	9
INTRODUCTION	13
A brief history of Macrophages	14
The mononuclear phagocyte system.....	16
Macrophage activation and polarization	17
The role of macrophages in adaptive immunity	18
The macrophage niche	18
Macrophage Origin.....	20
Evolutionary origin.....	20
Cellular origin.....	23
Macrophage heterogeneity: How to study macrophage diversity in practice?	28
Choosing the right model.....	28
Tools and markers to study and untangle macrophage heterogeneity	31
Macrophage state vs subset	42
Functional specialization of macrophages	44
Macrophages are indispensable	44
Macrophages as regulators of tissue homeostasis and physiology	46
Transcription factors and regulation of gene expression	51
Transcriptional regulation of macrophage specification and function	54
Abstract	55
Macrophage lineage-determining transcription factors	59
Macrophage identity-imprinting transcription factors	61

Tissue-specific macrophage identity-imprinting transcription factors	64
Beyond steady-state: macrophage transcriptional dynamics during tissue perturbation	72
Conclusion.....	75
OBJECTIVES	76
EXPERIMENTAL SECTION	80
Part I: MafB-restricted local monocyte proliferation precedes lung interstitial macrophage differentiation	81
Abstract	82
Introduction.....	84
Materials and Methods	86
Results	101
Supplementary Information	124
Part II: MafB is a conserved transcriptional regulator of macrophage development and functional identity across tissues and species.....	138
Abstract	139
Introduction.....	141
Materials and Methods	144
Results	162
Supplementary Information	182
DISCUSSION	198
Part I: Dynamic regulation of monocyte-to-macrophage differentiation <i>in vivo</i>	199
Part II: MafB as a central regulator of macrophage maturation, identity and function.....	214
Conclusion	231
REFERENCES	233
APPENDICES	261
Appendix 1: Supplementary tables	262
CURRICULUM VITAE.....	287

SUMMARY

SUMMARY

Macrophages are a specialized type of immune cells that reside within virtually all organs of vertebrate organisms. Their main function is to remove foreign material, dying cells and debris by engulfment and subsequent digestion, a process called phagocytosis. Hence, they act as the clean-up crew and form the first line of defence against pathogens. Macrophages are indispensable, as their absence results in developmental abnormalities and disease. In many tissues macrophages are resident, hence termed resident tissue macrophages (RTMs). Their residency is maintained through self-renewal or constant refill by circulating monocytes that enter the tissue and differentiate into RTMs. Interestingly, unlike many other tissue-resident immune cells, macrophages express highly tissue-specific gene programs that depend on their organ of residence. This specialized gene signature is largely imprinted by local niche-derived instructive signals and often correlates with specialized functions adapted to each tissue. In addition to this tissue-specific identity, RTMs share a conserved core macrophage gene program that defines their lineage and supports fundamental functions such as phagocytosis.

Transcription factors (TFs) regulate immune cell differentiation by controlling gene expression programs that determine lineage commitment, functional specialization and long-term maintenance. In macrophages, this layered regulation is particularly evident, as their differentiation and function rely on the coordinated action of distinct but interconnected transcriptional networks. Broadly, TFs establish and maintain the global macrophage program required for lineage commitment and core functions, and integrate tissue-derived signals to imprint tissue-specific identity and specialized functions within each organ. In this thesis, we investigated how transcriptional regulation governs macrophage maturation and the establishment of macrophage identity and function.

SUMMARY

In the first part of this thesis, we investigated how circulating monocytes differentiate into RTMs *in vivo* and how successive transitional states are regulated within the tissue niche. To address this, we established a model of inducible lung interstitial macrophage (IM) depletion, allowing synchronized niche refilling and enabling the capture of rare intermediate differentiation stages under controlled conditions. Using time-resolved transcriptomic and phenotypic analyses, we identified a proliferative transitioning monocyte population that arises from classical monocytes during niche repopulation and precedes the acquisition of mature IM identity. Proliferation of these cells was shown to be dependent on signaling through colony-stimulating factor-1 receptor (Csf1r). Concomitantly, we observed that MafB expression was initially low in proliferating intermediates and progressively increased as cells acquired a mature IM phenotype. Furthermore, mice with myeloid-intrinsic deficiencies in the TF MafB exhibited severe impairments in IM development and identity, suggesting that MafB functions as a molecular switch linking cessation of proliferation to terminal macrophage differentiation and stabilization of tissue-resident identity.

Building on this observation and the fact that MafB has been proposed as a macrophage marker, in the second part of this thesis we aimed to determine the global role of MafB in RTM development, identity and function across tissues. We verified that MafB is broadly expressed across RTMs and progressively upregulated during differentiation. Myeloid-specific absence of MafB led to impaired macrophage maturation, altered transcriptional identity and defective functional capacities *in vivo*. Single-cell transcriptomic, phenotypic and epigenetic analyses further revealed that MafB directly controls core macrophage gene programs through *cis*-regulatory elements while also contributing to tissue-specific specialization. Importantly, MafB binding sites

SUMMARY

exhibited strong evolutionary conservation across vertebrates and substantially overlapped between mouse and human macrophages, indicating that the MafB-driven transcriptional network is deeply conserved. Together, these findings identified MafB as a central and evolutionarily conserved transcriptional regulator that integrates differentiation cues and stabilizes macrophage identity and function across diverse tissue environments.

RÉSUMÉ

RÉSUMÉ

Les macrophages sont un type de cellules immunitaires spécialisées qui résident dans pratiquement tous les organes des organismes vertébrés. Leur fonction principale est d'éliminer les corps étrangers, les cellules mourantes et les débris par un processus d'ingestion et de digestion appelé phagocytose. Ils agissent ainsi comme une équipe de nettoyage et constituent la première ligne de défense contre les agents pathogènes. Les macrophages sont indispensables, car leur absence entraîne des anomalies du développement et des maladies. Dans de nombreux tissus, les macrophages sont résidents ; on les appelle alors macrophages résidents tissulaires (MRT). Leur maintien dans les tissus repose soit sur leur auto-renouvellement, soit sur un apport continu de monocytes circulants qui pénètrent dans le tissu et se différencient en MRT. Fait intéressant, contrairement à de nombreuses autres cellules immunitaires résidentes des tissus, les macrophages expriment des programmes géniques hautement spécifiques au tissu, dépendant de leur organe de résidence. Cette signature génique spécialisée est en grande partie façonnée par des signaux instructifs dérivés de la niche locale et est souvent corrélée à des fonctions spécialisées adaptées à chaque tissu. En plus de cette identité spécifique au tissu, les RTM partagent un programme génique central conservé des macrophages, qui définit leur lignée et soutient des fonctions fondamentales telles que la phagocytose.

Les facteurs de transcription (FT) régulent la différenciation des cellules immunitaires en contrôlant les programmes d'expression génique qui déterminent l'engagement de lignée, la spécialisation fonctionnelle et le maintien à long terme. Chez les macrophages, cette régulation à plusieurs niveaux est particulièrement évidente, car leur différenciation et leur fonction reposent sur l'action coordonnée de réseaux transcriptionnels distincts mais interconnectés. De manière générale, les FT établissent et maintiennent le programme macrophagique global requis pour l'engagement de lignée et les

RÉSUMÉ

fonctions fondamentales, tout en intégrant les signaux dérivés des tissus afin d'imprimer une identité spécifique au tissu et des fonctions spécialisées propres à chaque organe. Dans cette thèse, nous avons étudié comment la régulation transcriptionnelle gouverne la maturation des macrophages ainsi que l'établissement de leur identité et de leurs fonctions.

Dans la première partie de cette thèse, nous avons étudié comment les monocytes circulants se différencient en MRT *in vivo* et comment les états transitionnels successifs sont régulés au sein de la niche tissulaire. Pour cela, nous avons établi un modèle de déplétion inductible des macrophages interstitiels pulmonaires (MI), permettant une recolonisation synchronisée de la niche et la capture d'états intermédiaires rares de différenciation dans des conditions contrôlées. Grâce à des analyses transcriptomiques et phénotypiques résolues dans le temps, nous avons identifié une population proliférative de monocytes en transition qui apparaît transitoirement à partir des monocytes classiques lors de la repopulation de la niche et précède l'acquisition d'une identité MI mature. La prolifération de ces cellules s'est révélée dépendante de la signalisation via le récepteur du facteur de stimulation des colonies 1 (Csf1r). Parallèlement, nous avons observé que l'expression de MafB était initialement faible dans les intermédiaires prolifératifs, puis augmentait progressivement à mesure que les cellules acquéraient un phénotype MI mature. De plus, des souris présentant une déficience intrinsèque myéloïde du FT MafB ont montré des altérations sévères du développement et de l'identité des MI, suggérant que MafB agit comme un interrupteur moléculaire reliant l'arrêt de la prolifération à la différenciation terminale des macrophages et à la stabilisation de leur identité résidente tissulaire.

Sur la base de cette observation et du fait que MafB ait été proposé comme marqueur des macrophages, la seconde partie de cette thèse visait à déterminer

RÉSUMÉ

le rôle global de MafB dans le développement, l'identité et la fonction des MRT à travers différents tissus. Nous avons confirmé que MafB était largement exprimé dans les MRT et que son expression augmentait progressivement au cours de leur différenciation. L'absence spécifique de MafB dans la lignée myéloïde a conduit à une altération de la maturation macrophagique, à une modification de l'identité transcriptionnelle et à des défauts fonctionnels *in vivo*. Des analyses transcriptomiques, phénotypiques et épigénétiques ont en outre révélé que MafB contrôle directement les programmes géniques centraux des macrophages via des éléments *cis*-régulateurs, tout en contribuant à la spécialisation spécifique au tissu. Fait important, les sites de liaison de MafB présentent une forte conservation évolutive chez les vertébrés et se chevauchent largement entre les macrophages murins et humains, indiquant que le réseau transcriptionnel dépendant de MafB est profondément conservé. Ensemble, ces résultats identifient MafB comme un régulateur transcriptionnel central et évolutivement conservé qui intègre les signaux de différenciation et stabilise l'identité et la fonction des macrophages dans divers environnements tissulaires.

ABBREVIATIONS

Ab	Antibody
AGM	aorta-gonad-mesonephros
AM	alveolar macrophage
ANOVA	analysis of variance
BAM	border-associated macrophage
BM	bone marrow
BMDM	BM-derived macrophage
BMMo	BM monocyte
BMP	bone morphogenetic protein
C/EBP	CCAAT/enhancer binding protein
cDC	classical DC
CDP	common DC progenitor
CITE-seq	cellular indexing of transcriptomes and epitopes by sequencing
CM	colonic macrophage
cMo	classical monocyte
cMoP	common monocyte progenitor
CMP	common myeloid progenitor
CNS	central nervous system
CLL	clodronate-loaded liposomes
CLP	common lymphoid progenitor
C LPM	colon lamina propria macrophage
CUT&RUN	cleavage under targets and release using nuclease
CUREA	<i>Csf1r</i> upstream regulatory element A
Cr	complement receptor
cRE	<i>cis</i> -regulatory element
Csf1	colony-stimulating factor 1
Csf1r	Csf1 receptor
DAPI	4',6-diamidino-2-phenylindole
DC	dendritic cell
DEG	differentially expressed gene
DM	dermal macrophage
DT	diphtheria toxin
DTR	DT receptor
E	embryonic day
EdU	5-ethynyl-2'-deoxyuridine

EMP	erythro-myeloid progenitor
Eos	eosinophil
FACS	fluorescence activated cell sorting
FDR	false discovery rate
FIRE	fms-intronic regulatory element
GBM	glioblastoma
GMP	granulocyte-monocyte progenitor
GO	gene ontology
GP	granulocyte progenitors
GSEA	gene set enrichment analysis
HSC	hematopoietic stem cell
Id	inhibitor of DNA
IFN- γ	interferon- γ
IGF-1	insulin-like growth factor 1
IM	interstitial macrophage
IGV	Integrative Genomics Viewer
i.p.	intra peritoneal
iPSC	induced pluripotent stem cell
Irf	Interferon regulatory factor
i.v.	intra venous
kb	kilo base
KC	kupffer cell
Klf	krüppel-like factor
KO	knock-out
KRM	kidney resident macrophage
LC	langerhans cell
LCM	liver capsular macrophage
LDTF	lineage-determining transcription factor
LDL	low-density lipoprotein
LPM	large peritoneal macrophage
LSK	Lin ⁻ Sca-1 ⁺ c-Kit ⁺
LXR	liver X receptor
Mac	macrophage
MafB	Maf basic leucine zipper transcription factor B
MDM	monocyte-derived macrophage
MDP	monocyte-DC progenitor
MFI	mean fluorescence intensity
MG	microglia
MHC	major histocompatibility complex
MITF	macrophage identity imprinting transcription factor
MLN	mesenteric lymph node
MM	muscularis macrophage

MMM	marginal metallophilic macrophage
Mo	monocyte
MyP	myeloid lineage-committed progenitors
MZM	marginal zone macrophage
Neu	neutrophil
NES	normalized enrichment score
NGS	next-generation sequencing
ns	not significant
PAP	pulmonary alveolar proteinosis
PCA	pig cell atlas
PCR	polymerase chain reaction
pDC	plasmacytoid DC
pMo	patrolling monocyte
pre-Mac	pre-macrophage
PRR	pattern recognition receptor
PU.1	purine-rich box1
RBC	red blood cell
RA	retinoic acid
RAR β	RA nuclear receptor β
RBC	red blood cell
RbpJ	recombination signal binding protein for immunoglobulin kappa J
RES	reticuloendothelial system
RFTF	RTM function-imprinting transcription factor
RITF	RTM identity-imprinting transcription factor
RNA-seq	RNA-sequencing
RPM	red pulp macrophage
RTM	resident tissue macrophage
RXR	retinoid X receptor
Sall1	Spalt like transcription factor 1
scRNA-seq	single cell RNA-seq
SEACR	sparse enrichment analysis for CUT&RUN
SEM or s.e.m.	standard error of the mean
SI MM	small intestinal muscularis macrophage
SI LPM	small intestine lamina propria macrophage
SLN	skin-draining lymph node
SPM	small peritoneal macrophage
sRBC	senescent RBC
TAM	tumor-associated macrophage
Tgf β	transforming growth factor β
TF	transcription factor
TM	tabula microcebus

TMS	tabula muris senis
TS	tabula sapiens
TTS	transcription termination site
transMac	transitioning macrophage
Tr-Mo	transitioning monocytes
TSS	transcription start site
WGTT	whole gut transit time
WT	wild-type
XCL	xenopus cell landscape
ZCL	zebrafish cell landscape
Zeb	Zinc finger E box binding homeobox

INTRODUCTION

A brief history of Macrophages

In 1882, the zoologist Ilya Ilyich Mechnikov (Élie Metchnikoff) described the process by which cells ingest and destroy foreign particles such as bacteria, a phenomenon he termed phagocytosis (**Figure 1.1**)^{1,2}. This discovery is often considered the birth of innate immunity, and Mechnikov is honoured as its



Figure 1.1: Migration of phagocytes around a splinter in starfish larvae. After Metchnikoff, E. (1892). Lectures on the comparative pathology of inflammation, by Elie Metchnikoff¹.

founding figure. Although Mechnikov was the first to define these cells capable of recognizing, engulfing, and digesting foreign particles and dead host cells, earlier observations had hinted at similar cell types. In 1847, Rudolf Albert von Kölliker described stellate (star-shaped) cells in the connective tissue of the liver and spleen³, and in 1867 Emil Preyer observed splenic cells internalizing erythrocytes and suggested this occurred by an active process⁴. In 1876, Karl Wilhelm von Kupffer reported “Sternzellen” (star cells) cells within the liver sinusoids, initially thought to be endothelial cells⁵. Subsequent work by Wyssokowitch (1886) and Tadeusz Browicz (1898) demonstrated that these Kupffer cells phagocytose bacteria and senescent erythrocytes⁶.

It was, however, Mechnikov who truly established the significance of these cells: he investigated the uptake of foreign materials across a wide range of animals, from starfish to mammals, and highlighted the functional identity of the cells responsible for engulfing such material. Moreover, he distinguished two

types of phagocytic cells based on size: macrophages, large phagocytes with a single, non-lobed nucleus, and microphages, smaller phagocytes with lobed or fragmented nuclei—later recognized as neutrophils⁷.

The conceptual framework surrounding macrophages expanded notably throughout the twentieth century as new technologies emerged. The introduction of electron microscopy in the 1950s–1960s revealed the dense lysosomal networks and phagolysosomes characteristic of macrophages, providing a structural basis for their degradative and phagocytic functions^{8,9}. Early biochemical assays further demonstrated macrophage secretion, metabolism, and enzymatic activity, highlighting that macrophages act as dynamic and metabolically active players in tissue homeostasis rather than passive scavengers^{10,11}.

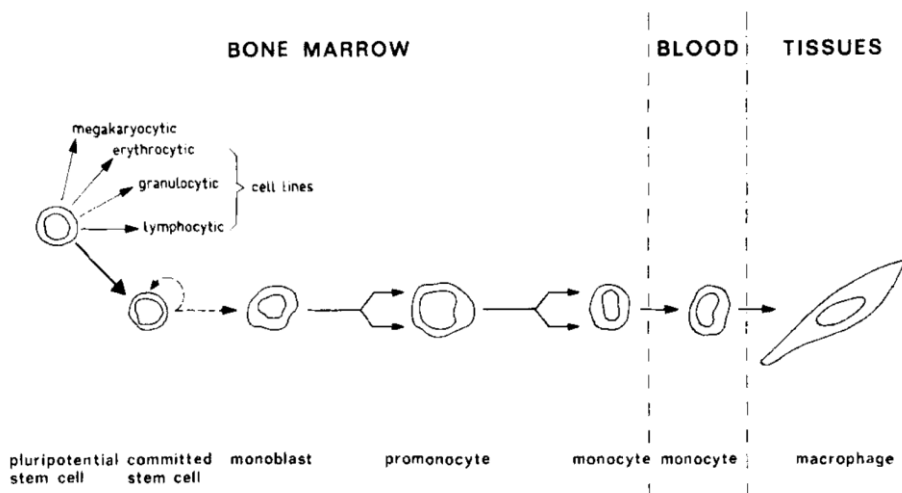


Figure 1.2: Schematic representation of the mononuclear phagocyte system. After van Furth, R. (1976). Origin and kinetic of mononuclear phagocytes. *Annals of the New York Academy of Sciences*, 278: 161-175¹².

The mononuclear phagocyte system

In the early twentieth century, experiments involving the injection of histological dyes such as lithium carmine, trypan blue, neutral red, isamine blue, and other colloids revealed that macrophages capable of ingesting these dyes in large quantities are distributed throughout the entire body. Systematic studies of tissue distribution and dye uptake led Karl Albert Ludwig Aschoff (1924) to introduce the term “reticuloendothelial system” (RES) to describe this group of cells capable of incorporating vital dyes from the circulation¹³. The prefix reticulo- referred to the tendency of these large phagocytic cells to form a network or reticulum through their cytoplasmic extensions, while endothelial reflected their close association with the vascular endothelium. The capture and removal of unwanted particulate material from the blood and lymph were regarded as the principal functions of the RES. The RES comprised a broad array of cells, including reticular cells, endothelial cells, fibroblasts, histiocytes, and monocytes. Aschoff proposed that RES cells were locally derived and that histiocytes and reticular cells shared a common origin. Subsequent studies, however, demonstrated that the RES also included cells of non-macrophage lineage and did not constitute a true system with a shared origin. Consequently, in 1969, Ralph van Furth and colleagues proposed to replace the RES by the mononuclear phagocyte system (MPS), which encompasses tissue macrophages, circulating monocytes, and their precursors in the bone marrow (**Figure 1.2**)¹⁴. van Furth together with Cohn also proposed that tissue macroph-

ages originate from circulating adult blood monocytes¹⁵. This view has dominated for the next 20 years, despite evidence that tissue macrophages populations are sustained even when circulating monocytes are depleted^{16,17}.

From the 1990s to 2010s, scientists realized that most resident tissue macrophages (RTM) are able to self-maintain, at least partly. This was shown by organ transplantation studies which revealed that donor macrophages can self-maintain for years in transplanted tissues¹⁸⁻²². In addition, these studies also showed that circulating host cells can engraft the donor tissue and contribute to the macrophage population. Experiments using parabiotic mice and monocyte lineage-specific tracing mice have demonstrated that circulating monocytes can be recruited to tissues and can differentiate into tissue macrophages²³⁻²⁹. The contribution of circulating monocytes to the macrophage pool at steady state, in mice raised in specific pathogen free conditions, seems to be tissue-intrinsic²⁹. Despite this long-term persistence, RTMs are not intrinsically resistant to cell death but are maintained through continuous exposure to niche-derived survival signals, while retaining the capacity to undergo apoptosis in response to inflammatory or tissue remodeling cues.

Macrophage activation and polarization

Another conceptual development occurred in the 1960s when George Mackaness demonstrated that macrophages could be “activated” following exposure to certain pathogens, acquiring enhanced microbicidal activity³⁰⁻³³. This challenged the long-standing idea that macrophages were static cell types and established them as highly responsive immune effectors. Over the following decades, a broad range of microbial and cytokine stimuli were shown to modulate macrophage behaviour. The identification of interferon- γ (IFN- γ) as a macrophage-activating cytokine in the early 1980s provided a molecular basis for this activation³⁴. Subsequent work highlighted the complexity of macrophage activation induced by different microbial and cytokine stimuli³⁵. In the late 1990s and early 2000s, discoveries showing that IL-4 and IL-13 could drive an *alternative activation* program led to the M1/M2 polarization paradigm^{36,37}. M1

classical activated macrophages were characterized as pro-inflammatory and microbicidal, whereas M2 *alternatively activated* macrophages were associated with anti-inflammatory, tissue-repair, and remodelling functions. Although modern single-cell analysis has revealed that macrophage activation exists along a continuum rather than in discrete categories, the M1/M2 paradigm remains historically important for illustrating that macrophage phenotype is shaped by microenvironmental cues rather than being intrinsically fixed.

The role of macrophages in adaptive immunity

In addition to their phagocytic role, macrophages were later recognized as critical contributors to adaptive immune responses. In the 1970s, macrophages were shown to be essential for antigen presentation to T lymphocytes³⁸. The discovery of MHC-restricted antigen recognition by T cells further illustrated this role³⁹. Subsequent work established macrophages as professional antigen-presenting cells capable of generating immunogenic peptides⁴⁰. They were also shown to secrete cytokines and chemokines that shape T cell activation, differentiation, and recruitment, positioning them as central orchestrators of immune responses⁴¹.

The macrophage niche

RTMs exhibit pronounced differences in their gene expression profiles and exert specific functions inherent to their tissue of residence⁴². Interestingly, postnatal monocyte-derived RTMs exhibit similar characteristics as their embryonic-derived counterparts in terms of self-maintenance, genetic and functional specification, and spatial tissue distribution^{43,44}. This indicates that key identity features of RTMs are not only determined by origin but mostly by specific properties of the tissue in which they reside (i.e. the *macrophage niche*)⁴⁵. The

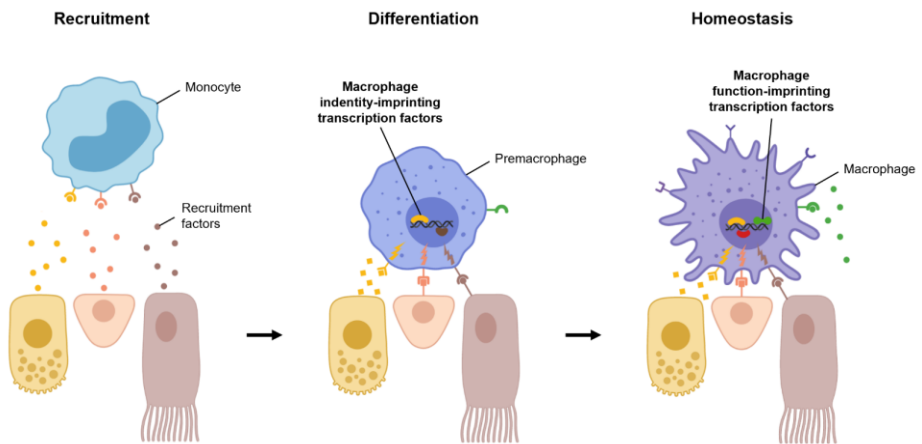


Figure 1.3: The macrophage niche model. Embryonic macrophage precursors or adult blood circulating monocytes are recruited to the niche by tissue-derived recruitment factors. Niche-derived tissue instructive signals initiate the differentiation of macrophage precursors through expression of core transcription factors, which drive key transcriptional programs of differentiation (the core macrophage program), thus imprinting macrophage identity. Additional signals imprint macrophage function during late stages of differentiation through expression of transcription factors which drive key transcriptional programs of macrophage function. Figure was created with BioRender.

macrophage niche model postulates that tissue-specific functions of macrophages are imprinted by niche-derived tissue-instructive signals. These signals trigger the expression of specific transcription factors (TFs), which drive transcriptional modules responsible for RTM differentiation and specification, thus tailoring a particular identity and function.

Macrophage Origin

Evolutionary origin

Phagocytosis can be broadly defined as the cellular process in which a cell surrounds, engulfs, and internalizes solid particles—such as food, microbes, or debris—by forming membrane-bound vesicles called phagosomes⁴⁶. Phagocytosis begins when receptors on the cell surface bind to molecules (ligands) on the target particle. This “tasting” allows the cell to detect what it is interacting with, such as proteins, sugars, nucleic acids, or lipids on a microorganism or debris. Once initial binding occurs, the phagocyte starts to “feel” the particle by extending parts of its plasma membrane around it. When the membrane extensions fully surround the target, they fuse together and pinch off from the cell surface. This creates a new internal compartment called a phagosome. The phagosome then undergoes “digesting”, a maturation process involving a series of fusion and fission events with intracellular compartments. Through this maturation, it becomes a phagolysosome enriched with antimicrobial molecules and degradative enzymes such as proteases, lipases, and nucleases. These enzymes break down the internalized particle, and reactive oxygen species may also be produced to help kill microbes and degrade debris.

Phagocytosis is an ancient eukaryotic trait that predates multicellularity and underpins both nutrient acquisition and innate immunity. In unicellular eukaryote amoeba such as *Dictyostelium* and *Acanthamoeba*, phagocytosis is driven mostly by cytoskeletal machinery, primarily actin polymerization, membrane curvature generation, and dynamic rearrangements of the cortex that permit engulfment of particles⁴⁷. These mechanisms are highly conserved

across eukaryotes and represent the foundational molecular architecture upon which animal immune phagocytes later evolved⁴⁸.

The emergence of multicellular organisms introduced new ecological pressures, including the need for tissue homeostasis, apoptotic cell clearance, and defence against microbial infections. Early metazoans therefore evolved *proto-phagocytes*, cells that retained the cytoskeletal engulfment machinery of single-celled eukaryotes but acquired novel phagocytic receptors, including scavenger receptors, C-type lectins, and integrins⁴⁹. These innovations enabled selective recognition of microbial or apoptotic targets and represent a key evolutionary transition toward immune specialization.

Within protostomes (e.g., arthropods, mollusks), proto-phagocytes diversified into hemocytes, a broad category of circulating immune cells that perform phagocytosis, encapsulation, coagulation, and wound healing. Hemocytes exhibit the first clear integration of pattern-recognition receptors (PRRs), including Toll, peptidoglycan-recognition proteins, and fibrinogen-related proteins, which allows discrimination of microbial motifs^{50,51}. This marks the emergence of innate immune specificity. Among deuterostomes, echinoderms such as sea urchins possess coelomocytes, which include professional phagocytes capable of robust particle uptake, oxidative responses, and clot formation. Coelomocytes express C3 and Factor B homologs, establishing that complement-assisted phagocytosis is an ancestral feature of deuterostome immunity. This indicates that the alternative complement pathway predates the vertebrate lineage by hundreds of millions of years^{52,53}.

The rise of vertebrates introduced a new degree of cellular specialization. Macrophages derived from myeloid progenitors represent the most functionally elaborate phagocytes in animals. Vertebrate macrophages integrate the full suite

of mechanisms observed in earlier phagocytes (cytoskeletal engulfment, phagocytic receptors, PRRs) with additional layers of immune regulation, including complement receptors (Cr3, Cr4) and Fc receptors, enabling high-affinity uptake of antibody- or complement-opsonized targets⁵⁴. This cellular complexity is supported by a conserved transcriptional program, prominently regulated by colony-stimulating factor 1 receptor (Csf1r) signalling, which are essential for macrophage differentiation, survival, and identity. The receptor tyrosine kinase Csf1r originated early in vertebrate evolution and displays deep functional conservation from jawless vertebrates through mammals^{55,56}.

The origin of vertebrate lineage also coincides with the emergence of stable RTM populations. RTM originate predominantly from embryonic progenitors (e.g., yolk sac erythro-myeloid progenitors) and seed tissues before birth. They undergo extensive self-renewal and persist for the lifetime of the organism, maintaining specialized functions tailored to their local microenvironment. Examples include microglia in the central nervous system, Kupffer cells (KCs) in the liver, Langerhans cells (LCs) in the skin, and alveolar macrophages (AMs) in the lung. These populations integrate Csf1r signalling with tissue-specific cues such as transforming growth factor β (Tgf β), bone morphogenetic proteins (BMPs), and local metabolic or structural signals to acquire distinct transcriptional identities and functional specializations⁵⁷⁻⁶⁰. Moreover, Guilliams et al have demonstrated a significant overlap in KC transcriptomes from human, macaque, mouse, hamster, pig, chicken, and zebrafish, suggesting that KC signatures are conserved across species⁶¹.

Cellular origin

RTMs arise from a series of consecutive spatiotemporal developmental waves⁶³. While the number of waves and progenitors that generate RTMs is still an ongoing debate, two clear developmental waves can be defined (**Figure 1.4**). RTMs can arise during embryogenesis, hence embryonically-derived, or be generated postnatally from monocytes of hematopoietic origin, hence monocyte-derived. At embryonic day 7.0 (E7.0), erythro-myeloid progenitors (EMPs) emerge from blood islands and capillary endothelium in the yolk sac⁶⁴. At E8.5, during the first wave, EMPs begin to give rise to Cx3cr1⁺ pre-macrophages (pre-Macs)^{65,66}. pre-Macs proliferate in the yolk sac and migrate to the embryo through newly formed blood vessels⁶⁶. During organogenesis, between E8.5 and

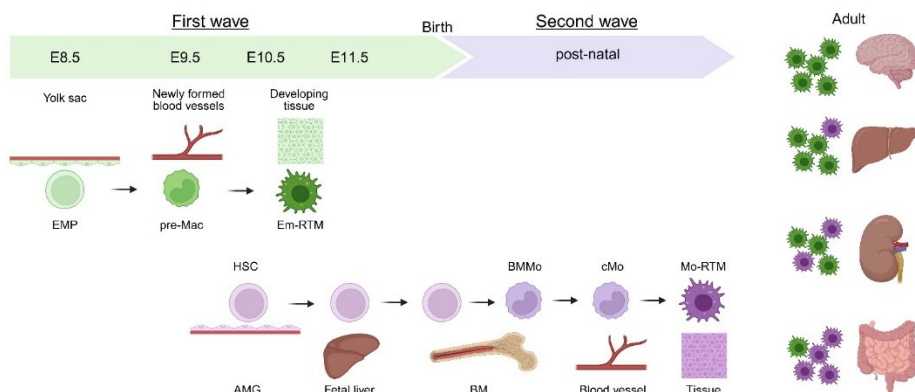


Figure 1.4. Developmental waves generating resident tissue macrophages. RTMs originate from two consecutive developmental waves. During the first wave, yolk sac-derived EMPs generate pre-Macs that seed embryonic tissues and differentiate into RTMs. The second wave arises from HSCs formed in the AGM region, which expand in the fetal liver, establish bone marrow hematopoiesis, and postnatally give rise to circulating monocytes that can contribute to RTM pools. The relative replacement of embryonic-derived RTMs (Em-RTMs) by monocyte-derived RTMs (Mo-RTMs) in adulthood is tissue dependent and influenced by environmental perturbations. Figure was created with BioRender. Inspired by Viola, M. F., Franco Taveras, E., & Mass, E. (2024). Developmental programming of tissue-resident macrophages. *Frontiers in immunology*, 15, 1475369.⁶²

E9.5, pre-Macs seed and colonize the developing organs, where they differentiate into RTMs^{65–67}. Although the second wave does not generate RTMs before birth, its origin lies in embryogenesis. At E10.0–E10.5, hematopoietic stem cells (HSCs) arise from the hemogenic endothelium in the aorta-gonad-mesonephros (AGM) region and subsequently seed the fetal liver at E11.5^{68–70}. Within the fetal liver, HSCs undergo extensive expansion and give rise to multiple leukocyte lineages, but not macrophages. Prior to birth, HSCs migrate to the bone marrow, where they are maintained throughout life and continuously replenish the circulating monocyte pool²⁴. After birth, these circulating monocytes contribute to the RTM compartment. The first wave gives rise to functional RTMs that depending on the colonized tissue can be self-maintained with minimal input of the postnatally second wave-derived monocytes. However, in adults, embryonic RTMs are thought to be replaced by monocyte-derived cells at rates that depend on the tissue of residence, its accessibility from the bloodstream, and the nature and extent of perturbations.

Does origin matter?

“It doesn’t matter where you are coming from. All that matters is where you are going.” – Brian Tracy

With the ongoing debate on macrophage ontogeny, one can ask the question: does origin matter? In other words, do macrophages have discrete functions depending on their origin? Current evidence suggests that it might not be the case at steady-state, during homeostasis. For instance, alveolar macrophages (AMs) are embryonically derived and self-maintained throughout life, with minimal input from BM-derived monocytes. However, depletion of AMs following intranasal administration of clodronate-loaded liposomes results in the recruitment of monocytes that subsequently differentiate into BM-derived AMs.

These BM-derived AMs display a strikingly similar transcriptomic profile to their embryonically derived counterparts⁷¹. Similarly, yolk sac-, fetal liver-, and BM-derived monocytes adoptively transferred into neonatal *Csf2rb*-deficient mice lacking AMs differentiate into a fully functional and stable AM population⁴³. KCs are also embryonically derived, long-lived and self-renewing. Using a model of diphtheria toxin-mediated depletion of KCs (*Clec4f*^{DTR}), Scott et al showed that circulating monocytes engraft the liver and gradually adopt a transcriptomic profile nearly identical to embryonically derived KCs⁴⁴. Comparable findings have been reported across multiple tissues, showing that after lethal irradiation and reconstitution with congenically labeled bone marrow, newly generated macrophages adopt transcriptomic profiles that closely match those of resident macrophages⁷². However, this convergence is not universal. Microglia (MG) represent a notable exception, as monocyte-derived macrophages entering the central nervous system (CNS) fail to fully recapitulate the transcriptional and functional identity of embryonically-derived MG, even after long-term engraftment⁷³. Notably, these cells fail to induce expression of *Sall1*⁷³, a key transcription factor that is critical for establishing and maintaining microglial identity⁷⁴. As a result, monocyte-derived macrophages retain a distinct epigenetic and transcriptional profile, failing to fully acquire core microglial features⁷³. Interestingly, adoptive transfer studies have shown that fetal liver progenitors engrafting the central nervous system can differentiate into MG that more closely resemble endogenously derived microglia, including expression of *Sall1* and other core microglial genes⁷⁵. This may be explained by differences in epigenetic priming, as the *Sall1* locus remains accessible in fetal liver progenitors, as revealed by single cell ATAC-seq, whereas it is largely inaccessible in adult bone marrow-derived progenitors⁷⁵. These findings suggest that the inability of monocyte-derived macrophages to fully acquire MG identity reflects intrinsic epigenetic constraints established during development, rather than an absolute

inability to respond to the tissue environment. This suggests that, in certain tissues, ontogeny can impose lasting constraints on macrophage identity. Taken together, these findings indicate that, while notable exceptions such as MG exist, the tissue microenvironment remains the dominant driver of RTM subset-specific gene expression in most contexts⁷⁶. Accordingly, the “macrophage niche” concept posits that local environmental cues are the primary determinants of macrophage identity and function. However, these experimental systems introduce progenitors into niches that are empty or altered by irradiation, potentially affecting niche accessibility, cell–cell interactions, and competition with endogenous cells. Under physiological conditions, macrophage recruitment is largely governed by niche accessibility and timing, with progenitor identity reflecting availability at specific developmental stages, as illustrated by the yolk sac origin of MG and the perinatal establishment of AMs from fetal monocytes. Nonetheless, intrinsic differences between progenitors exist, as fetal monocytes more efficiently generate AMs, and resident macrophages can outcompete monocyte-derived cells during niche replenishment. Thus, although multiple progenitors can give rise to RTMs, their actual contribution under unperturbed conditions is shaped by competition and niche constraints.

Does origin matter during non-homeostatic conditions?

The combined effects of developmental origin and local microenvironment are especially critical for macrophage identity under non-homeostatic conditions such as infection, injury, and inflammatory or fibrotic disease, where different RTM subsets display highly variable responses⁷⁷. Perturbation of tissue homeostasis commonly triggers monocyte recruitment for effector functions and can reduce resident macrophage numbers⁷⁸. In some contexts, macrophage populations are replenished by the expansion of surviving resident cells⁷⁹,

whereas in others, partial replacement by monocytes reshapes the developmental origins of the resident macrophage compartment^{27,80,81}. Although these monocyte-derived macrophages can become phenotypically indistinguishable from pre-existing residents^{43,44,73}, their imprinting may differ, reflecting differentiation in a perturbed environment. Such cells may therefore retain epigenetic “memories” that influence their responses to subsequent insults. Indeed, mice in which influenza A infection induces monocyte-derived replacement of AMs show improved resistance to subsequent *Streptococcus pneumoniae* infection⁸². Moreover, these infection-experienced monocyte-derived AMs exhibit persistent transcriptional reprogramming and produce elevated levels of IL-6 upon secondary bacterial challenge. In contrast, influenza-experienced embryonically-derived resident AMs remain largely similar to naive AMs. Thus, the substitution of embryonically-derived resident macrophages with trained, monocyte-derived macrophages confers a protective advantage, a process widely referred to as “trained immunity”⁸³. This illustrates how shifts in macrophage ontogeny following tissue perturbation can have enduring functional consequences for tissue immunity.

Macrophage heterogeneity: How to study macrophage diversity in practice?

After: Domien Vanneste & Thomas Marichal (2026). Guidelines for non experts: How to study macrophage diversity in practice? As part of a consensus article on macrophage diversity for the *European journal of immunology*.

“We are all the same, but different. We are all different, but the same.” – Unknown

Macrophages display unexpected degree of diversity across tissues, developmental origins, and physiological states. However, this growing complexity also presents a major challenge, particularly for non-specialists: which experimental systems, markers, and analytical approaches are most appropriate for studying macrophage heterogeneity in a given context? In this section, we provide practical guidance on model selection, methodological strategies, and experimental considerations to help investigators design robust and interpretable studies of macrophage diversity.

Choosing the right model

Understanding and investigating macrophage heterogeneity requires experimental models that preserve tissue context, ontogeny, and environmental cues. The choice of model therefore critically depends on the specific research question, the required level of biological complexity, and the available technical and logistical resources.

Human-based models offer the highest translational relevance. Primary human RTMs directly reflect human macrophage heterogeneity and disease-associated

states, retaining tissue-imprinted transcriptional and functional programs. However, their use is limited by restricted availability, low cell numbers, inter-donor variability, and the difficulty of performing longitudinal or genetic studies. Human assembloid-based systems partially overcome these limitations by enabling controlled manipulation and repeated experimentation while preserving aspects of tissue architecture. Assembloids are self-organizing three-dimensional cellular structures (organoids) co-cultured with macrophages, such as peripheral blood monocyte-derived macrophages (MDMs) or induced pluripotent stem cell (iPSC)-derived macrophages⁸⁴. Notably, when human iPSC-derived primitive macrophages (iMacs) are cultured with brain organoids, they acquire key microglial functions and express microglia-associated genes and regulons, indicating that assembloids can support macrophage differentiation and tissue adaptation⁸⁵. Moreover, the presence of microglia promotes neuronal maturation within organoids, making this a more physiologically relevant model for studying human brain development. Nevertheless, assembloids still incompletely recapitulate full tissue complexity, vascularization, and long-term macrophage maintenance. In the context of cancer, tumor spheroids co-cultured with MDMs provide a tractable system to study tumor-associated macrophages (TAMs)⁸⁶.

Mouse models remain the most experimentally versatile systems for studying macrophage heterogeneity. Analyses of primary RTMs across organs have been fundamental in defining ontogeny- and niche-driven macrophage diversity. Key advantages include extensive genetic tractability, the availability of reporter and fate-mapping systems, and compatibility with single-cell, spatial, and intravital imaging approaches. However, species-specific differences in immune regulation and macrophage differentiation can limit direct translation to human biology. For example, although serous cavity-resident mononuclear phagocytes in

humans and mice share common features, the relative abundance of various macrophage subsets differs markedly between the two species⁸⁷. Humanized mouse models help bridge this translational gap. Non-obese diabetic severe combined immunodeficient *Il2rg*^{-/-} (NSG) mice possess a profoundly compromised immune system that prevents xenogeneic rejection and allows stable engraftment of human cells⁸⁸. However, hematopoietic stem cell (HSC) transfer into NSG mice predominantly results in human B- and T-cell reconstitution, with very limited development of monocytes and macrophages⁸⁹. Additional deletion of Fcγ receptors in NSG mice increases human myeloid cell representation, and human macrophages can be detected in the bone marrow and liver of these animals⁹⁰. Despite these improvements, NSG-based models still poorly support human macrophage development due to inefficient cross-species cytokine signaling (e.g. M-CSF/Csf1 and GM-CSF/Csf2). MISTRG mice represent a major advance for modeling human macrophage heterogeneity *in vivo*. In this model, several key murine cytokine genes (M-CSF, IL-3, GM-CSF, and TPO) are replaced by their human counterparts, and human SIRPα is expressed, enabling efficient development and survival of human myeloid cells⁸⁹. Engrafted MISTRG mice show a markedly increased proportion of myeloid cells, and their peripheral blood composition more closely resembles that of humans. Notably, Willinger and colleagues demonstrated that human CD34⁺ fetal liver cells engrafted into MISTRG mice populate the lung and differentiate into alveolar and interstitial macrophages with human-specific characteristics⁹¹. Despite their advantages, these models remain limited by incomplete immune reconstitution, residual murine niche signals, high cost, and technical complexity.

Other vertebrate models provide additional, context-specific advantages. Rats and pigs, for example, could offer closer anatomical and physiological similarity to humans, making them attractive for translational and preclinical studies^{92,93},

although genetic tools and immunological resources are less developed than in mice. Zebrafish provide exceptional opportunities to study macrophages during development, regeneration, and inflammation due to their optical transparency and suitability for real-time imaging^{94,95}. However, differences in immune system organization and the limited availability of species-specific antibodies constrain deep phenotypic characterization.

Tools and markers to study and untangle macrophage heterogeneity

From the discovery and description of macrophages by Elie Metchnikoff already more than a century ago, the study of macrophage diversity has often been technology-driven. For much of the century after their first description, microscopy remained the primary technique for identifying and classifying macrophages based on spatial localization, morphology, and the uptake of certain colorimetric dyes. The emergence of monoclonal antibodies and flow cytometry in the early 1980s has had a significant impact on macrophage research even to this day.

Macrophage-specific monoclonal antibodies (e.g. CD11b and F4/80), combined with flow cytometry, enable the identification, isolation, and characterization of macrophages from a single cell suspension, as well as the discrimination of macrophage subsets and activation states based on their marker expression. Over time, advances in cytometry instruments and the expanding repertoire of macrophage- and immune-associated antigens, have established flow cytometry workhorse technology in many immunology labs to this day. At the present, the availability of flow cytometers capable of detecting 15 or more parameters can be considered standard for most research institutes. We therefore propose a standardized panel of core markers to delineate macrophages in a robust and reproducible manner across tissues.

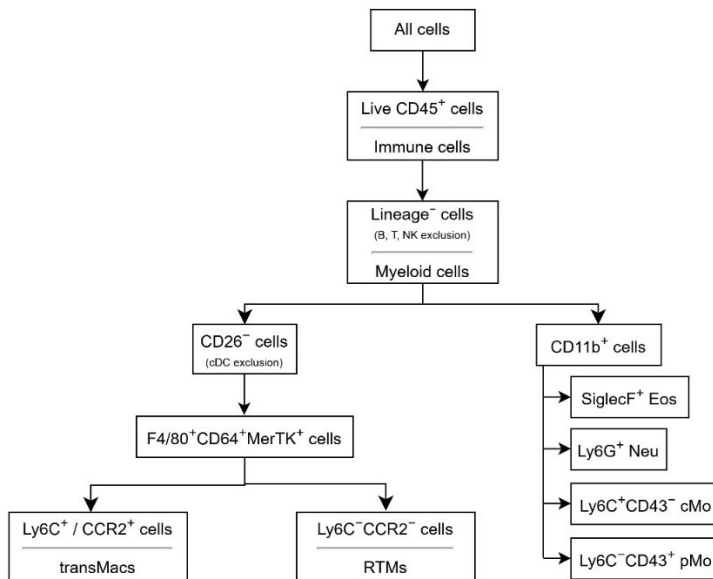


Figure 1.5. Overview of markers and gating strategy to define RTMs. Eos, eosinophils; Neu, neutrophils. Figure was created in Diagrams.net.

To study mouse RTMs, this panel includes several categories of markers with complementary purposes (**Figure 1.5**). The pan-leukocyte marker CD45 is used to discriminate CD45⁺ immune cells from CD45⁻ non-immune cells. A lineage marker is included to exclude other hematopoietic populations such as B cells, T cells, and NK cells. However, caution is required when selecting lineage markers, as certain macrophage subsets can express markers traditionally considered restricted to other lineages. For example, some intestinal macrophages express the T helper cell marker CD4⁹⁶, and alveolar macrophages (AMs) highly express the eosinophil marker SiglecF. Moreover, short-lived monocyte-derived macrophages expressing the prototypical neutrophil marker Ly6G have recently been described during the early recovery phase following viral-triggered lung injury⁹⁷. To avoid misclassification, SiglecF and Ly6G are therefore included as separate markers to specifically gate eosinophils and neutrophils, respectively. The classical dendritic cell (cDC) marker CD26 is used to distinguish cDCs from

macrophages⁹⁸. Monocyte populations are identified using CD11b, Ly6C, and CD43, allowing discrimination between Ly6C⁺CD43⁻ classical monocytes (cMo) and Ly6C⁻CD43⁺ patrolling monocytes (pMo). General macrophage identity is supported by the expression of F4/80, CD64, and MerTK. Transitioning macrophages (transMacs) represent intermediate differentiation states between recruited monocytes and fully mature resident tissue macrophages. These cells have already acquired core macrophage features, including expression of markers such as F4/80 and CD64, but have not yet fully established the tissue-specific transcriptional programs that define terminal RTM identity. As such, transMacs are thought to be differentiating macrophages that still require niche-derived cues to complete their specialization and functional imprinting. transMacs are typically observed in tissues characterized by high monocyte turnover and continuous replenishment, such as the intestine, but can also emerge during inflammatory responses or following niche depletion, when recruited monocytes undergo stepwise differentiation toward resident macrophage states. They can be distinguished from fully differentiated macrophages by the retention of monocyte-associated markers, most notably Ly6C and/or CCR2, which gradually decline as differentiation proceeds^{99,100}. In the gut, these cells form the well-described “monocyte waterfall,” a stepwise maturation continuum in which Ly6C⁺ monocytes enter the tissue, acquire CD64 and F4/80, progressively downregulate Ly6C, and sequentially upregulate markers such as MHC-II, Cx3cr1 and CD11c as they transition into mature resident macrophages¹⁰¹. Optionally additional markers such as MHC-II, CD11c, CD206, Tim4, Cx3cr1, Lyve1 can be incorporated to provide further phenotypic resolution of macrophage subsets^{99,102–104}. For example, Chakarov and colleagues, unbiasedly identified two independent interstitial macrophage (IM) subpopulations that were conserved across tissues and species: CD206⁻ (Lyve1^{lo}MHCII^{hi}) and CD206⁺ (Lyve1^{hi}MHCII^{lo}) IMs, displaying distinct gene

expression profiles, phenotypes, functions, and localizations¹⁰³. The group of Marichal independently confirmed the existence of these two IM subsets¹⁰⁴. Alternatively, Dick *et al.* describe three RTM subsets that can be stratified based on expression of Tim4, Lyve1, Fcrl2, CCR2, and MHC-II into: TLF⁺ macrophages (expressing Tim4 and/or Lyve1 and/or Fcrl2), CCR2⁺ (Tim4⁻Lyve1⁻Fcrl2⁻) macrophages, and MHC-II^{hi} (Tim4⁻Lyve1⁻Fcrl2⁻CCR2⁻) macrophages⁹⁹. These subsets were shown to be conserved across mouse organs and developmental stages, as well as in human tissues. TLF⁺ macrophages largely resemble CD206⁺ IMs, whereas MHC-II^{hi} macrophages resemble CD206⁻ IMs. In contrast, CCR2⁺ macrophages are predominantly monocyte derived and express markers associated with pre-Macs, such as CCR2 and CD52. These CCR2⁺ macrophages represent infiltrating monocytes undergoing differentiation into RTMs, and should therefore be referred to as transMacs. Tissue-specific RTM markers can be used to define distinct macrophage populations, including SiglecF, CD2, and CD22 for AMs¹⁰⁵; Clec4f for Kupffer cells (KC)⁴⁴; CD226 for small peritoneal macrophages (SPM)¹⁰⁶; CD102 (ICAM-2) for large peritoneal macrophages (LPM)¹⁰⁷; CD207 for Langerhans cells (LC)¹⁰⁸; and Tmem119, P2ry12, and Fcrls for microglia (MG)⁵⁷.

While flow cytometry provides high-dimensional phenotypic information at the single-cell level, it often requires enzymatic digestion of tissues to generate single-cell suspensions. This process inevitably leads to the loss of spatial information, preventing the analysis of cellular localization, tissue architecture, and cell–cell interactions. In addition, tissue digestion does not always result in complete or unbiased recovery of all cell types, as certain populations may be more fragile, tightly embedded in the tissue, or differentially sensitive to enzymatic treatment. Microscopy-based techniques therefore provide an essential complementary approach, enabling the study of RTMs within their

native tissue context. Some markers and monoclonal antibodies that are routinely used for flow cytometry can also be applied to immunofluorescence microscopy; however, their performance is not automatically transferable. Antibodies must always be carefully tested and validated for microscopy, as epitope accessibility, fixation sensitivity, signal-to-noise ratio, and background staining can differ substantially from flow cytometry conditions. In practice, macrophages are most commonly identified in situ using markers such as F4/80, CD68, Iba1, and CD64, often in combination with tissue- or subset-specific markers including Tim4, Lyve1, or MHC-II to refine macrophage identity and localization.

Microscopy is however limited by the number of markers that can be analyzed simultaneously. On standard confocal microscopes, multiplexing is typically restricted to approximately 4-5 fluorophores due to spectral overlap and detector limitations. Spectral confocal or spectral unmixing microscopes substantially extend this capacity, allowing the simultaneous detection of up to 12 markers, depending on fluorophore selection, tissue autofluorescence, and unmixing performance. These technical constraints should be carefully considered when designing microscopy panels to complement flow cytometry analyses. To overcome these limitations, recent highly multiplexed imaging technologies such as CODEX, MACSima, and COMET enable the simultaneous detection of dozens of membrane and intracellular markers in intact tissue sections, allowing accurate identification of macrophages, other immune cells and structural cells while preserving spatial organization and tissue architecture.

Genetic reporter mouse models in which fluorescent reporters are expressed under the control of endogenous regulatory elements, enable marker-independent identification, fate mapping, and longitudinal tracking of macrophage and monocyte populations by flow cytometry or fluorescent

imaging. Moreover, these reporter mice are compatible not only with *ex vivo* flow cytometry and fixed-tissue microscopy, but also with intravital imaging, enabling real-time visualization of macrophage localization, migration, and interactions within living tissues.

Cx3cr1^{GFP} mice¹⁰⁹, which label circulating monocytes and many RTMs, are widely used for *ex vivo* and *in vivo* imaging of macrophage populations. *Cx3cr1* expression is maintained in multiple macrophage lineages but can also be used to discriminate macrophage subsets in specific tissues. For example, in the lung, *Cx3cr1* expression is largely restricted to IMs, whereas AMs are *Cx3cr1*^{low/-}, enabling segregation of these populations^{102–104,110}.

Ccr2^{GFP} reporter mice¹¹¹ highlight circulating and recently recruited (inflammatory) monocyte, as well as differentiating transMac. The groups of Guilliams and Scott crossed these mice with *Clec4f*^{Cre}*Rosa26*^{LSL-TdTomato} mice, which specifically label KCs, to study the dynamics of monocyte recruitment and subsequent KC differentiation by intravital imaging. These approaches have been applied both in models of KC depletion⁵⁸ and during liver injury¹¹², providing direct visualization of monocyte-to-macrophage differentiation *in vivo*.

Ms4a3^{Cre}*Rosa26*^{LSL-TdTomato} mice specifically label granulocyte-monocyte progenitor(GMP)-derived cells and have rapidly become a standard tool to distinguish RTMs from monocytic versus embryonic origin in steady state and inflammation²⁹. In tamoxifen-inducible *Ms4a3*^{CreERT2}*Rosa26*^{LSL-tdTomato} mice, tamoxifen administration triggers tdTomato expression in GMP-derived, short-lived circulating monocytes. These labeled cells persist in the circulation for approximately six days before being replaced by newly generated tdTomato⁻ monocytes²⁹. This system enables temporal “time-stamping” of consecutive waves of monocyte recruitment and subsequent macrophage differentiation,

particularly in inflammatory contexts¹⁰⁰. In addition, *Ms4a3*^{FlpO} mice are available, in which the FlpO recombinase is expressed under the control of the *Ms4a3* promoter. These models provide an alternative recombinase system for selectively targeting monocyte-derived cells and can be combined with Flp-dependent reporter or effector alleles, or intersected with Cre-based strategies, for refined genetic labeling and fate-mapping of monocyte-derived macrophages. The group of Mass crossed these mice to create a *Tnfrsf11a*^{Cre}*Rosa26*^{LSL-YFP};*Ms4a3*^{FlpO}*Rosa26*^{FSF-TdTomato} double fate-mapping mouse, which enables the simultaneous tracking of yolk sac-derived and bone marrow-derived macrophages^{113,114}. In this system, embryonically derived yolk sac macrophages are labeled YFP⁺, whereas circulating monocytes, short-lived macrophages, and differentiating macrophages are labeled tdTomato⁺. Monocyte-derived macrophages that acquire long-term tissue residency express both reporters (YFP⁺tdTomato⁺), allowing direct discrimination of macrophage ontogeny and persistence within tissues. *Ms4a3*^{FlpO}*Rosa26*^{FSF-TdTomato} mice can also be combined with Cre-dependent gene deletion strategies to interrogate origin-specific functions of target genes in RTMs, as well as assessment of how genetic perturbations affect RTM self-renewal, monocyte replacement, and long-term maintenance of macrophage populations within tissues¹¹⁵.

The colony-stimulating factor-1 receptor (*Csf1r*) mRNA is highly expressed in monocytes and all RTMs¹¹⁶. Lower levels of *Csf1r* mRNA also have been reported in cDCs, granulocytes and B lymphocytes^{117,118}. In contrast, *Csf1r* protein is exclusively expressed by all committed progenitors, blood monocytes, and RTMs, and is therefore considered as a macrophage lineage-restricted marker¹¹⁹. Anti-CD115 antibody can be used to assess *Csf1r* surface expression on macrophage progenitors in the bone marrow (BM), blood monocytes, and peritoneal macrophages by flow cytometry^{29,110,120}. However, CD115 staining is

reduced or even completely abolished on monocytes and macrophages isolated from solid organs after enzymatic digestion in order to obtain a single cell suspension¹²¹. This loss of detection is likely a consequence of competition with endogenous ligands Csf1 and IL-34 that are released during tissue processing, as well as ligand-induced internalization and degradation of Csf1r¹²². Mechanical disintegration and/or enzyme-based cold digestion at 4°C preserves Csf1r surface expression on tissue monocytes¹²¹. However, such dissociation might not be sufficient to retrieve RTMs that reside deep within the tissue. Challenging Csf1r staining can be overcome by the use of available *Csf1r* reporter mice^{117,123}. Notably, *Csf1r*^{mApple} (MacApple) mice¹²³ were crossed with *Csf1r*^{Gal4VP16;UAS^{ECFP}} (MacBlue) mice¹²⁴, in which a 105-bp deletion in the *Csf1r* promoter prevents reporter expression in most mature tissue macrophages¹²⁵, as well as *Cx3cr1*^{GFP} mice, to generate triple reporter RGB-Mac mice¹²⁶. Imaging and flow cytometry analyses demonstrates that the combined use of these three markers enables discrimination of tissue-associated monocytes, tissue-specific macrophages, and three subsets of connective tissue-associated macrophages¹²⁶. Since *Csf1r* reporter mice reflect transcriptional activity rather than protein expression; and therefore also label other cells that express *Csf1r* mRNA, the group of Hume generated a Csf1r protein reporter mouse by inserting a FusionRed (FRed) cassette in-frame with the C terminus of Csf1r, separated by a T2A-self-cleavable linker¹¹⁹. Csf1r^{FRed} expression is restricted to monocytes and macrophages and absent in granulocytes and lymphocytes, confirming that Csf1r is a bona fide monocyte/macrophage lineage marker.

For models involving other species there, some macrophage-specific antibodies are available, yet resources remain limited^{127,128}. In rats, several reporter strains have been developed, including *Csf1r*^{mApple} rats, enabling direct visualization of macrophages *in vivo*^{129,130}. Due to the limited availability of fish-

specific antibodies and the poor cross-reactivity of mammalian antibodies with fish antigens, most zebrafish studies rely on transgenic lines expressing fluorescent proteins under lineage-specific regulatory elements. These models allow identification and analysis of zebrafish macrophages *in vivo*, on tissue sections, and by flow cytometry. For example, the group of Wittamer described a *mpeg1.1*^{EGFP};*ptprc*^{DsRed} double reporter strain, enabling the isolation of RTMs from different organs based on the combined expression patterns of *mpeg1.1* (macrophage expressed gene 1, tandem duplicate 1) and *ptprc* (cd45)¹³¹.

Finally, even with recent advances in spectral flow cytometry and multiplexed imaging, the resolution of antibody-based approaches remains constrained by instrument capacity, the number of markers that can be measured simultaneously, and the availability of high-quality reagents. Moreover, these techniques are inherently biased by marker selection, highlighting the need for more unbiased approaches such as single-cell and spatial transcriptomics to complement marker-based analyses.

The current understanding on macrophage heterogeneity has been profoundly shaped by advances in transcriptomic technologies. Early large-scale efforts relied on DNA microarrays, which enabled the parallel measurement of thousands of transcripts by hybridization of fluorescently labeled cDNA or RNA to predefined probes. A landmark application of this technology in macrophage biology was the Immunological Genome (ImmGen) Project¹³². Using microarray-based profiling, Gautier et al. compared macrophages isolated from multiple mouse tissues and revealed extensive transcriptional diversity across tissue-resident macrophage populations⁴². Importantly, this work also identified a conserved macrophage core signature, including genes such as *Fcgr1* (coding for the high-affinity Fcγ receptor CD64) and *Mertk* (coding for the tyrosine kinase receptor MerTK), which distinguishes macrophages from other mononuclear

phagocytes. Subsequent microarray studies led to the identification of tissue-specific macrophage markers, such as Clec4F for KC⁴⁴; CD226 for SPM¹⁰⁶; CD4 for colonic macrophages^{96,133}; and Tmem119, Fcrls, and P2ry12 for MG⁵⁷.

The subsequent development of next-generation sequencing (NGS) technologies paved the way for RNA sequencing (RNA-seq). Unlike microarrays, RNA-seq directly sequences RNA molecules, providing digital readouts of transcript abundance and enabling comprehensive transcriptome analysis without prior knowledge of genomic sequences. RNA-seq quickly became the gold standard for transcriptomic studies, offering unprecedented insights into gene regulation, RNA processing, and functional genomics. While bulk RNA-seq can provide valuable information about average gene expression levels within a cell population, it lacks the ability to capture transcriptional heterogeneity between individual cells.

Over the past decade, single cell RNA-seq (scRNA-seq) technologies, emerged and became a powerful technique to dissect cellular diversity, characterize rare cell populations, and unravel complex biological processes at the single-cell level. Recent developments and commercialization of plate-, microfluidics- and droplet-based platforms have made scRNA-seq available to a broader community in academia and industry at a reasonable cost. Indeed, scRNA-seq has been proven a powerful tool to study macrophage heterogeneity and to uncover macrophages subsets^{99,103,104,134}. Since then scRNA-seq datasets of macrophages from different species, organs and contexts have increased considerably^{61,135}. In parallel, the development of lineage-tracing models together with the rapid emergence of spatial and single-cell multiomics technologies has considerably expanded the landscape of macrophage research and beyond. While the breadth of these technological advances is mind-blowing, it may also represent a challenge for researchers, who must decide how to

effectively harness these diverse tools and approaches to unravel the heterogeneity of both homeostatic RTM and of non-homeostatic recruited monocyte-derived macrophage subsets and states in health and disease. One key element to take into consideration in addressing macrophage diversity is the evidence for a distinct temporal and functional specification. While high-dimensional data that can be obtained from the analysis of protein and RNA expression within macrophage subsets can help to infer putative functions, they remain descriptive and are not full conclusive.

More recently, the development of Cellular Indexing of Transcriptomes and Epitopes by sequencing (CITE-seq) has further expanded the toolbox for marker discovery. CITE-seq combines scRNA sequencing with the simultaneous quantification of surface proteins using oligonucleotide-barcoded antibodies, thereby linking transcriptomic states directly to protein expression at the single-cell level. This multimodal approach overcomes the well-known disconnect between mRNA and protein abundance and enables the robust identification of cell type-specific and state-specific markers. In macrophage research, CITE-seq is particularly valuable for validating transcriptionally defined subsets, refining phenotypic definitions, and discovering surface markers that are amenable to flow cytometry and imaging-based applications. For example, protein expression from CITE-seq data can be used to design gating strategies for flow cytometry, as elegantly demonstrated by Guilliams *et al.* who identify and gate KC and non-KC macrophages in the liver macrophage compartment as $V\text{sig}4^+\text{Tim}4^+$ and $V\text{sig}4^-\text{Tim}4^-$ cells, respectively⁶¹. Similarly, CITE-seq identified CD2 and CD22 as markers enabling discrimination of resident AMs by flow cytometry¹⁰⁵.

Spatial transcriptomics technologies have added a new dimension to the study of macrophage heterogeneity by coupling gene expression profiling with spatial context within intact tissues. Unlike dissociation-based scRNA sequencing,

spatial transcriptomics preserves tissue architecture, enabling the localization of transcriptionally distinct macrophage subsets within defined anatomical niches and microenvironments. This is particularly important for macrophages, whose identity and function are tightly shaped by local cues such as stromal interactions, vascular proximity, neuronal signals, and gradients of cytokines and metabolites. Spatial transcriptomics has revealed that transcriptionally similar macrophages can occupy distinct spatial niches and, conversely, that neighboring macrophages can adopt markedly different gene expression programs⁶¹. These approaches have uncovered zonation patterns, identified niche-specific activation states in inflammation and cancer, and clarified how resident macrophages interact with epithelial, endothelial, and immune cells *in situ*^{100,112,136–138}. By integrating spatial transcriptomics with scRNA-seq, multiplexed imaging, and genetic fate-mapping, it is now possible to link macrophage ontogeny, phenotype, and function to precise tissue locations, providing a more comprehensive and physiologically relevant understanding of macrophage heterogeneity.

Together, the integration of scRNA-seq, CITE-seq, spatial transcriptomics, multiplexed imaging, and genetic fate-mapping now enables macrophage heterogeneity to be studied across dimensions of ontogeny, phenotype, function, time, and space. Harnessing these complementary approaches will be essential to move beyond descriptive atlases toward a mechanistic understanding of macrophage specialization in health and disease.

Macrophage state vs subset

High-dimensional approaches such as scRNA-seq have greatly expanded the number of transcriptionally-defined macrophage populations. However, not all clusters represent bona fide subsets. Many transcriptional clusters instead

reflect activation states superimposed on a stable subset identity¹³⁹. Discriminating macrophage subsets from states therefore requires integrating transcriptional data with ontogeny, temporal stability, spatial localization, and functional assays. This distinction is essential to avoid overinterpreting context-dependent macrophage activation programs as novel cell types and to achieve a mechanistic understanding of macrophage heterogeneity in health and disease.

Macrophage subsets are stable populations defined by their ontogeny, long-term tissue residency, and niche-specific transcriptional programs¹⁴⁰. These subsets are typically conserved across individuals under homeostatic conditions. Examples include MG, KCs, AMs, LCs, and LPMs. Such subsets are characterized by persistent expression of core identity genes (e.g. *Csf1r*, *Mafb*, *Mertk*) together with tissue-imprinted markers (e.g. *Tmem119* in MG, *Clec4f* in KCs, *Siglecf* in AMs) and occupy defined niches. Their identity is often reinforced by local environmental cues and self-renewal capacity.

Macrophage states, by contrast, describe transient and context-dependent functional programs adopted by macrophages within a given subset or lineage. These states are driven by environmental signals such as infection, tissue injury, metabolic stress, or tumor-derived factors and are often reversible. Examples include inflammatory, interferon-responsive, tissue-repair, lipid-associated, or proliferative states. Importantly, similar states can be observed across multiple macrophage subsets and tissues, reflecting convergent responses to shared stimuli rather than distinct lineages.

Functional specialization of macrophages

“Macrophages are the Forrest Gump of immunology and are involved in almost everything” – Ido Amit

Macrophages are indispensable

Macrophages are present in virtually all organs, often in large numbers. Globally, they account for ~10% of immune cells yet contribute nearly 50% of total immune cellular mass because of their large size¹⁴¹. They seed and expand within tissues during organogenesis, and their populations are maintained through self-renewal or continuous replenishment from circulating monocytes. When adult macrophages are transiently depleted, vacant niches rapidly recruit monocytes that differentiate locally and acquire transcriptional programs closely resembling resident macrophages^{43,44,58,59,72,73}. In some contexts, a small fraction of surviving resident macrophages can also proliferate and contribute to niche refilling^{44,58,59,142}. Together, these observations indicate that macrophage pools are actively established and dynamically maintained.

As noted above, *Csf1r* protein expression is largely restricted to the macrophage lineage, including progenitors, monocytes, and RTMs¹¹⁹. *Csf1r* signalling is essential for macrophage development, survival, recruitment, and proliferation, as *Csf1r*^{-/-} mice display markedly reduced macrophage numbers across tissues^{129,143,144}. *Csf1r* signals through two ligands, *Csf1* and *IL-34*, whose functions are partially nonredundant: loss of a single ligand selectively affects particular macrophage populations. *IL-34* deficiency primarily reduces LCs and MG^{145,146}, whereas *Csf1* deficiency leaves these populations intact but diminishes most other RTMs¹⁴³. Consistent with this specialization, *IL-34* is not detected in circulation and instead acts locally in tissues where it is produced^{147,148}. In the

skin IL-34 is mainly expressed in the keratinocytes, while in the brain neurons are the main source of IL-34, as demonstrated by Greter *et al.*¹⁴⁵. Recently, the group of Greter also showed that the maintenance of perivascular border-associated macrophages (BAMs) is dependent on local production of IL-34 by mural cells and perivascular fibroblasts¹⁴⁹.

Csf1 is produced as both soluble and membrane-bound isoforms¹⁵⁰. Secreted Csf1 isoforms can enter the bloodstream and contribute to a circulating Csf1 pool, but their functional contributions differ from membrane-bound forms^{151,152}. Transgenic rescue experiments in Csf1-deficient mice show that soluble Csf1 restores most resident macrophage populations, whereas membrane-bound Csf1 only partially rescues certain tissue macrophages, highlighting a key role for the soluble form in specific organs^{151–153}. Overall, these findings indicate that circulating Csf1 regulates macrophage homeostasis in selected tissues, while other macrophages populations primarily rely on locally provided Csf1. Supporting this concept, conditional deletion of Csf1 in WT1⁺ red pulp fibroblasts selectively reduces splenic red pulp macrophages (RPMs)¹⁵⁴, and loss of Csf1 in Dpt⁺ skin fibroblasts leads to a decrease in dermal macrophages¹⁵⁵, highlighting the critical role of local niche-derived Csf1 in maintaining tissue-resident macrophages.

Disruption of Csf1r signalling, either genetically or pharmacologically, results not only in widespread macrophage deficiency but also in major developmental and physiological abnormalities¹⁵⁶. Csf1r-deficient mice exhibit impaired growth, osteoclast defects, osteopetrosis, and reduced macrophage density across multiple organs, and similar phenotypes are observed after blocking anti-Csf1r/CD115 antibody treatment¹⁵⁷. In humans, homozygous Csf1r loss-of-function mutations cause severe developmental defects including microglial absence, skeletal dysplasia, and osteopetrosis^{158–160}, whereas heterozygous

mutations lead to adult-onset leukoencephalopathy^{161,162}. Moreover, therapeutic Csf1r blockade to deplete tumour-associated macrophages can induce systemic effects such as oedema and altered circulating matrix components¹⁶³. Collectively, these findings indicate that macrophages are indispensable for organ development, tissue function, and homeostasis, a conclusion further supported by studies showing that tissue-specific macrophage deletion disrupts local physiological processes^{43,60,154,164–168}.

Macrophages as regulators of tissue homeostasis and physiology

RTMs are integral components of organ physiology, where they perform diverse functions that extend far beyond classical immune defense. In the steady state, these cells act as local regulators of tissue homeostasis by clearing apoptotic cells and debris, remodeling extracellular matrix, buffering inflammatory signals, and supporting the function of neighboring parenchymal and stromal cells. Importantly, these activities are not uniform across organs but instead reflect niche-specific specialization shaped by developmental origin, local environmental cues, and long-term tissue residency. As a result, macrophages acquire transcriptional and functional programs tailored to the physiological demands of each tissue, enabling them to contribute to a wide range of specific processes.

Large serous cavity macrophages, characterized by high expression of F4/80, ICAM-2 (CD102), and the transcription factor Gata6, constitute the dominant resident macrophage population within the peritoneal (e.g. LPMs), pleural, and pericardial cavities. Positioned at fluid-tissue interfaces, these cells maintain serosal homeostasis by clearing apoptotic cells, immune complexes, and particulate debris present in cavity fluids¹⁶⁹. Beyond their scavenging role, Gata6⁺ cavity macrophages are highly motile and form a reservoir of mature

macrophages that can be rapidly mobilized upon tissue injury. Following sterile damage, they migrate from the cavity to accumulate at lesion sites, where they contribute to tissue repair and restoration of barrier integrity¹⁷⁰. Moreover, these macrophages can rapidly aggregate at sites of tissue disruption, forming physical plugs that seal focal lesions and limit leakage of serosal fluids¹⁷¹. In addition to these repair functions, they produce anti-inflammatory mediators and support local immune tolerance, underscoring their role as dynamic guardians that couple immune surveillance with rapid tissue protection in serous cavities.

KCs are the most abundant resident tissue macrophages in the liver. In adults, KCs are strategically positioned within the liver sinusoids to filter blood-borne pathogens, bacteria, immune complexes, and cellular debris¹⁷². They also clear aged erythrocytes through erythrophagocytosis and subsequently process, store, and recycle iron bound to heme in hemoglobin¹⁷³. Free hemoglobin released into the circulation is toxic to multiple organs and must be rapidly cleared. This is achieved through its binding to haptoglobin, after which the complex is internalized by cells expressing the scavenger receptor CD163¹⁷³, which is highly expressed by Kupffer cells^{61,174,175}. KCs also contribute to cholesterol homeostasis by recognizing and removing oxidized low-density lipoprotein (LDL), often referred to as “bad” cholesterol, from the circulation and recycling membrane lipids from dying cells¹⁷². Beyond scavenging functions, KCs play a central role in maintaining hepatic immune tolerance by continuously sensing gut-derived microbial products and producing immunoregulatory mediators that restrain excessive inflammation¹⁷⁶. They also participate in hemostatic surveillance by clearing activated platelets and coagulation components^{177,178}, and support tissue repair after injury by releasing growth factors and coordinating recruitment and differentiation of monocyte-derived

macrophages¹⁷⁹. Interestingly, during development KCs do not reside within sinusoids but instead localize in the parenchyma¹⁸⁰, where they interact with fetal liver hematopoietic stem cells and support erythroblast maturation and granulopoiesis^{181,182}.

AMs, localized by definition in the alveoli, are the main resident macrophage of the lung. AMs preserve pulmonary homeostasis by clearing inhaled particles, dying cells, and excess surfactant. By metabolizing surfactant lipids and proteins, they prevent alveolar dysfunction and maintain gas exchange efficiency. Indeed, *Csf2*^{-/-} or *Csf2rb*^{-/-} mice, as patients carrying mutations that impair CSF2 signalling and lack AMs, develop pulmonary alveolar proteinosis (PAP), a disorder characterized by pathological surfactant accumulation in the alveoli^{43,164,165}. AMs also dampen unnecessary inflammation in response to harmless environmental stimuli while retaining the capacity to mount rapid antimicrobial responses when pathogens are encountered^{183,184}. Lung IMs constitute a smaller population of resident macrophages located within the lung parenchyma, between the alveolar epithelium and vascular endothelium. Work from the groups of Bureau and Marichal has shown that IMs exert immunoregulatory functions, notably through IL-10 production, thereby promoting immune tolerance and limiting allergic inflammation^{185,186}. In contrast to AMs, IMs express high levels of MHC-II^{102,104,186}, consistent with antigen-presenting capacity, and we demonstrated that they can process and present soluble antigens in an MHC-II-restricted manner¹⁸⁷. More recently, we further showed that impaired IM differentiation caused by disruption of TGF- β signaling leads to premature declines in lung function resembling features of accelerated aging, highlighting their essential role in maintaining pulmonary homeostasis⁶⁰.

MG serve as long-lived immune and homeostatic regulators of the central nervous system. During development, they contribute to neurogenesis by

regulating the pool of neuronal progenitor cells through phagocytic clearance¹⁸⁸. MG also interact with endothelial cells and developing neurons, thereby influencing vascular formation and guiding interneuron migration within the neocortex^{188,189}. After birth, MG support neuronal survival in part through the production of trophic factors such as insulin-like growth factor 1 (IGF-1)¹⁹⁰. They further shape neural circuit formation by eliminating excess synapses through complement-dependent synaptic pruning and by modulating synaptic maturation and function^{191–193}. In the adult brain, MG continuously survey neuronal activity¹⁹⁴ and participate in the maintenance and turnover of myelin¹⁹⁵, highlighting their sustained role in preserving neural homeostasis. Moreover, disruption of MG function is associated with several neurological disorders, including Parkinson's disease, Alzheimer's disease, schizophrenia, and amyotrophic lateral sclerosis^{196–199}.

Splenic macrophages are highly specialized according to their anatomical localization. RPMs like KCs are known to scavenge senescent erythrocytes and recycle their hemoglobin iron, thus participating in iron metabolism²⁰⁰. Indeed, depletion of RPMs results in heme-bound iron accumulation localized specifically in the red pulp^{154,166}. Marginal zone macrophages (MZMs) are strategically positioned at the interface between the blood-filled marginal sinus and the white pulp, where they act as specialized sentinels for blood-borne antigens. They efficiently capture and clear pathogens, apoptotic cells, and immune complexes through high expression of scavenger and pattern-recognition receptors, including SIGN-R1 and MARCO^{201,202}. Beyond their scavenging role, MZMs play a key immunological function by transferring captured antigens to B cells and dendritic cells, thereby promoting rapid T-independent antibody responses and facilitating the initiation of adaptive immunity^{203,204}. They also contribute to

immune tolerance by clearing circulating self-antigens and immune complexes, preventing aberrant activation of autoreactive lymphocytes²⁰⁵.

RTM in other organs exhibit similarly specialized functions aligned with local physiology. In the kidney they sample urine content and remove intratubular particles to keep the tubular system unobstructed²⁰⁶; in adipose tissue they regulate lipid metabolism and insulin sensitivity^{207–210}; in bone they contribute to remodeling and osteoblast support^{211,212}; in the intestine they sustain epithelial turnover and tolerance to microbiota^{213–215}; and in the heart they influence electrical conduction and tissue repair. These examples illustrate a unifying principle: macrophages adopt tissue-imprinted programs that enable them to act as local regulators of organ function rather than merely immune effector cells.

Transcription factors and regulation of gene expression

Gene expression is the fundamental process by which genetic information encoded in DNA is converted into functional gene products such as proteins or functional RNA molecules. Although virtually all nucleated cells in a multicellular organism contain the same genome, they exhibit strikingly distinct phenotypes and functions. This diversity arises not from differences in DNA sequence, but from selective gene expression programs that define cellular identity and enable context-specific responses. The regulation of gene expression is therefore central to development, homeostasis, and adaptive responses to environmental cues.

Gene expression can be regulated at multiple levels, including chromatin organization, transcription, RNA processing, mRNA stability, translation, and protein turnover. Among these, transcriptional regulation is a primary determinant of cell-type specificity. At the transcriptional level, regulatory information is embedded within *cis*-regulatory elements such as promoters, enhancers, silencers, and insulators. These DNA elements function as platforms for the binding of transcription factors (TFs), which interpret genomic information and translate it into precise patterns of gene activation or repression. The accessibility of these regulatory regions is itself controlled by chromatin structure, which determines whether TFs can physically engage their target sequences.

TFs are sequence-specific DNA-binding proteins that orchestrate gene expression by integrating intrinsic developmental programs with extrinsic environmental signals. By recognizing defined DNA motifs within regulatory

elements, TFs influence the recruitment and activity of the transcriptional machinery, including RNA polymerase II and associated cofactors. In doing so, they shape both the qualitative and quantitative aspects of gene expression. Importantly, TFs rarely act in isolation; rather, they function within combinatorial and hierarchical networks that confer regulatory specificity.

Functionally, transcription factors can be broadly categorized according to their roles in gene regulation. Lineage-determining transcription factors (LDTFs) establish and maintain cell identity by selecting and priming lineage-specific enhancers²¹⁶. These factors often possess pioneer activity, enabling them to bind nucleosomal DNA and initiate chromatin remodeling²¹⁷. Through cooperative interactions with additional TFs and chromatin modifiers, LDTFs create a permissive regulatory landscape that defines the core transcriptional identity of a cell^{59,218}. This foundational architecture constrains and guides subsequent transcriptional responses.

In contrast, signal-dependent transcription factors (SDTFs) are activated downstream of extracellular stimuli such as cytokines, growth factors, or pathogen-associated signals²¹⁸. Upon activation, SDTFs translocate to the nucleus and bind to regulatory elements that are either pre-established by LDTFs or rendered accessible in response to stimulation⁷⁶. These factors modulate gene expression programs in a context-dependent manner, enabling cells to dynamically respond to environmental changes while preserving lineage identity.

At the mechanistic level, TFs regulate gene expression through multiple, non-mutually exclusive mechanisms. They can directly recruit coactivator complexes and the basal transcriptional machinery to promote transcriptional initiation²¹⁹. They can also shape chromatin accessibility by engaging chromatin remodelers and histone-modifying enzymes, thereby altering nucleosome positioning and

histone modification states²²⁰. Conversely, transcriptional repressors recruit corepressor complexes and promote repressive chromatin modifications, ensuring that inappropriate gene programs remain silenced²²¹.

Collectively, TFs operate within interconnected regulatory networks that integrate developmental history with ongoing environmental signals. Through coordinated control of chromatin accessibility, enhancer activity, and transcriptional initiation, TFs provide the molecular framework that enables stable cellular identity while allowing functional plasticity. In macrophages, this balance between stability and adaptability is particularly critical, as transcriptional networks must simultaneously preserve lineage identity and accommodate diverse tissue- and stimulus-specific programs.

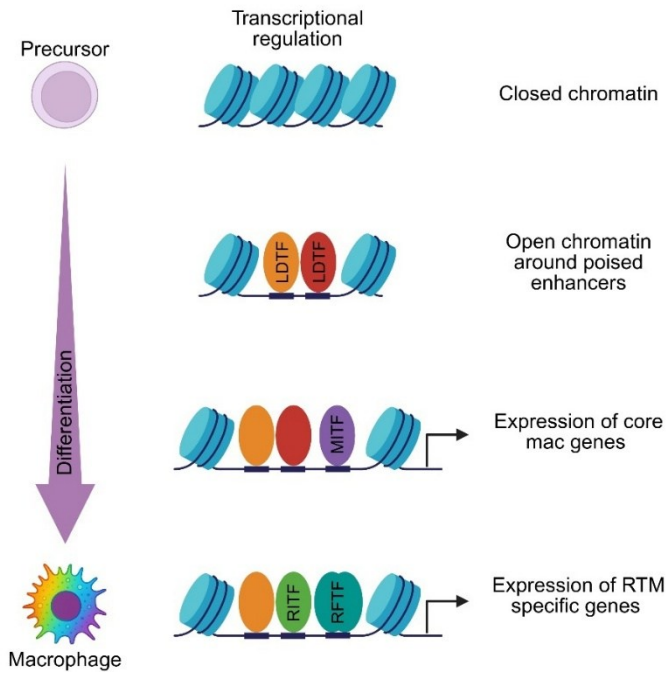
Transcriptional regulation of macrophage specification and function

After: Domien Vanneste & Thomas Marichal (2025). Transcriptional Regulation of Macrophage Specification and Function. *European journal of immunology*, 55(12), e70097. <https://doi.org/10.1002/eji.70097>

Author contributions: D.V. and T.M. research, writing – original draft, writing – review and editing.

Abstract

Tissue-resident and recruited macrophages are integral to organ development, homeostasis, immunity and disease pathogenesis. Their remarkable diversity arises from distinct developmental origins, differentiation trajectories and microenvironmental cues that shape their identity and function. Central to these processes is transcriptional regulation. In this review, we provide a comprehensive overview of the transcription factor (TF) networks that orchestrate resident tissue macrophage (RTM) differentiation from progenitor cells, imprint core macrophage identity, and drive tissue-specific functions. We first delineate the collaborative roles of lineage-determining TFs, such as PU.1 and C/EBPs, which prime macrophage progenitors for commitment. We then examine identity-imprinting TFs that establish and maintain the core macrophage program, and tissue-specific TFs that allow integration of local niche signals to tailor RTM phenotypes across organs. While the focus is on RTMs at steady state, we also highlight how RTMs can undergo transcriptional reprogramming upon tissue perturbation, and how newly recruited macrophages may engage distinct regulatory circuits upon entering diseased tissues, with tumors serving as an example.



Graphical abstract 1. This review highlights the hierarchical transcriptional networks that govern macrophage specification and function. We describe how lineage-determining, identity-imprinting, and tissue-specific transcription factors coordinate macrophage differentiation and specialization across organs, emphasizing the transcriptional regulation underlying macrophage diversity in health and disease. Graphical abstract was created in BioRender.

Introduction

More than a century ago, Ilya Mechnikov described macrophages as phagocytic cells (termed *phagocytes*) able to recognize, ingest and digest foreign particles as well as dead host cells through a process called phagocytosis². Apart from their well-studied role in host defense and clearance of dying cells, it is now clear that resident tissue macrophages (RTMs) are an integral part of the tissues in which they reside, where they play key roles in tissue development, homeostasis, metabolism and repair²²². RTMs derive from the embryo and seed most tissues before birth, where they are thought to exert specific functions inherent to the tissue of residence^{63,223}. After birth, bone marrow (BM)-derived monocytes can also contribute to the RTM pool in proportions that depend on the accessibility of the niche and the level of perturbations they are exposed to. Interestingly, BM-derived RTMs can exhibit similar characteristics as their embryonic-derived counterparts in terms of self-maintenance, genetic profile, functional specification and spatial tissue distribution^{43,44}, supporting that key identity features of RTMs can be determined by specific cues arising from the tissues in which they reside (i.e. the *macrophage niche*)⁴⁵. Besides homeostatic RTMs, non-homeostatic macrophages can differentiate from monocytes and establish in tissues when homeostasis is broken (e.g., following tissue damage, during infection, cancer) and contribute to a wide array of disease-related processes. They can adopt different identities that depend on the diseased tissue microenvironment, the extent and the phase of inflammation, their activation state and the time spent in the tissue^{172,222,224,225}.

A central mechanism by which macrophages acquire and maintain their identity is via transcriptional regulation. Indeed, transcription factors (TFs) can act as molecular switches that integrate external and internal signals, in concert

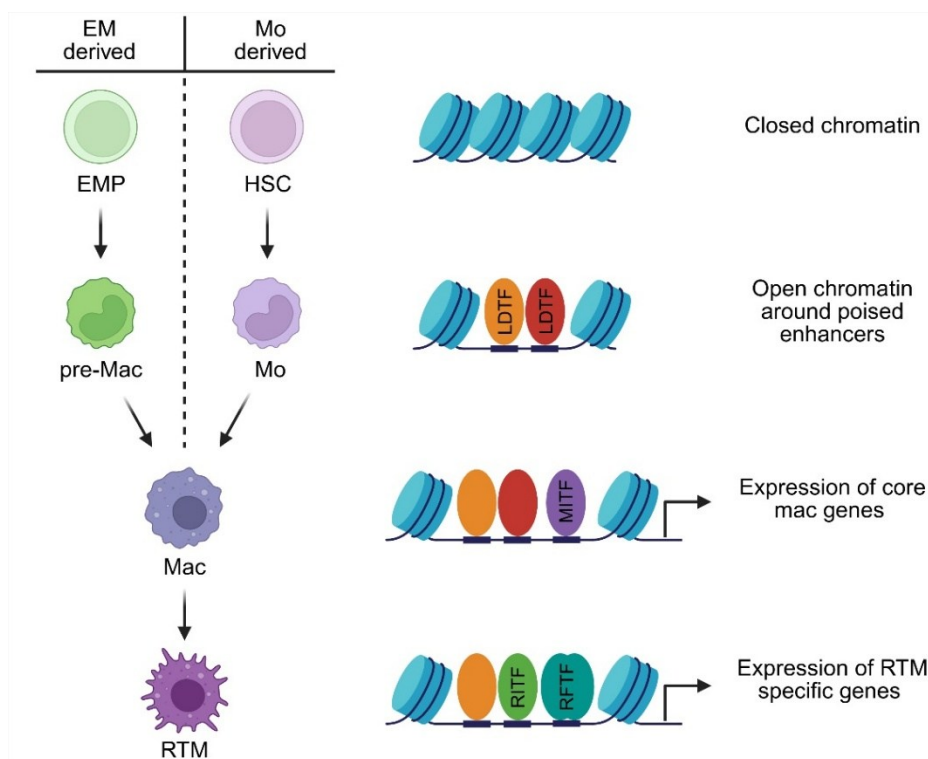


Figure 1.6. Collaborative-hierarchical model of TF binding during macrophage development. In macrophage progenitors, LDTFs bind cooperatively to actively open chromatin and poise/prime enhancers of macrophage specific genes. When macrophage progenitors seed the tissue, MITFs are recruited to poised enhancers to rapidly initiate a core macrophage program common to most macrophages. Local niche-derived factors then activate RITFs and RFTFs to adapt this core macrophage program and to imprint tissue specific RTM identity and function. EMP, erythro-myeloid progenitor; HSC, hematopoietic stem cell; LDTF, lineage-determining transcription factor; Mac, macrophage; MITF, macrophage identity imprinting transcription factor; Mo, monocyte; pre-Mac, pre-macrophage; RTM, resident tissue macrophage; RITF, RTM identity-imprinting transcription factor; RFTF, RTM function-imprinting transcription factor. Figure was created in BioRender.

with epigenetic modifications, to orchestrate cell fate decisions. In the context of macrophage biology, TFs not only dictate macrophage lineage specification during embryogenesis and postnatal hematopoiesis, but also the adaptation of these cells to their local microenvironment and their functional identity.

Understanding how TFs coordinate macrophage differentiation and function is therefore crucial to decipher the mechanisms that govern macrophage diversity across tissues and contexts.

Macrophage development is governed by three sets of distinct TFs: macrophage lineage-determining, macrophage identity-imprinting and tissue specific macrophage identity-imprinting TFs (**Figure 1.6**). These three groups of TFs form a collaborative-hierarchical network that controls RTM differentiation and specialization. First, macrophage lineage-determining TFs collaboratively bind and open chromatin regions in macrophages progenitors (*priming*). Next, macrophage identity-imprinting TFs bind these primed genomic regions to establish a *core macrophage program* in pre-macrophages. Finally, macrophage function-imprinting TFs integrate microenvironmental cues and adapt the core program to perform tissue- or niche-specific functions.

Macrophage lineage-determining transcription factors

RTMs develop in embryo and adults in a series of consecutive waves of differentiation⁶³. At embryonic developmental day 7.0 (E7.0), erythro-myeloid progenitors (EMPs) are formed from blood islands and capillary endothelia in the yolk sac. EMPs give rise to pre-macrophages (pre-Macs), that from E8.5-9.5 seed developing organs and differentiate into RTMs^{65,67}. At E10.0-10.5, hematopoietic stem cells (HSC) arise from the hemogenic endothelium in the aorta-gonad-mesonephros from where they seed the fetal liver at E11.5⁶⁸⁻⁷⁰. Within the fetal liver, HSCs undergo significant expansion and give rise to different leucocyte lineages. Before birth, HSCs migrate to the BM where they are maintained during life and constantly give rise to the pool of circulating monocytes²⁴. After birth, circulating monocytes also contribute to the RTM compartment at rates depending on the tissue of residence and the nature and level of perturbations²⁹.

During the different stages of development, the fate of macrophage progenitors is committed by macrophage lineage-determining TFs.

The Ets-domain transcription factor Purine-rich box1 (PU.1; encoded by *Spi1*) is considered a master regulator of macrophage development and hematopoiesis in general. EMPs, yolk sac-derived and fetal monocyte-derived RTMs are absent in embryos of *Spi1*-deficient mice. In addition, *Spi1*^{-/-} mice also lack T and B cells and die at E18.5, suggesting that PU.1 plays a major role in the commitment to both myeloid and lymphoid progenitors²²⁶. DeKoter and Singh found that PU.1 could control myeloid or lymphoid progenitor fate in a concentration-dependent manner²²⁷. Low levels of PU.1 protein drives B cell development, while a high concentration promotes macrophage differentiation and inhibits B cell formation. In macrophage progenitors, PU.1 binds to the low-affinity binding sites only when its concentration surpasses a specific threshold. PU.1 binding initiates nucleosome remodeling resulting in open and active chromatin regions²¹⁸. Macrophage lineage fate is also determined by the collaborative binding of PU.1, the CCAAT/enhancer binding proteins (C/EBPs; C/EBP α and C/EBP β), and activator protein 1 (AP1) to open and activate macrophage-specific enhancers²¹⁸. c-Myb is a master regulator of hematopoiesis. While late yolk sac-derived EMPs express c-Myb²²⁸, genetic studies indicate that this expression reflects their contribution to erythroid and other non-macrophage lineages. Indeed, *Myb*^{-/-} embryos lack late EMP-derived lineages but still generate normal tissue-resident macrophages^{67,229}. Consistently, *Myb*-deficient iPSC lines can differentiate into macrophages, whereas *Spi1*-deficient lines cannot, supporting that PU.1 but not c-Myb as a non-redundant regulator of macrophage development²³⁰. Thus, although c-Myb expression is detected in EMPs, current evidence does not support a functional requirement for macrophage differentiation. The TF Zeb2 is highly expressed in

the hemogenic endothelium of the aorta-gonad-mesonephros where embryonic HSC are formed and its expression is maintained in adult HSCs²³¹. The lack of *Zeb2* does not affect the migration of HSCs to the fetal liver, however, *Zeb2*-deficient HSCs are unable to further differentiate into fetal monocytes. In addition, inducible deletion of *Zeb2* in adult mice with an *Mx1^{Cre}* system results in a reduction of B cell, dendritic cells and monocytes^{232–234}. Mice lacking an enhancer located 165 kilobases (kb) upstream of the *Zeb2* transcriptional start site (*Zeb2^{Δ-165}*), have reduced numbers of monocytes while RTM counts remained unaffected²³⁵. However, RTMs in *Zeb2^{Δ-165}* mice are entirely from embryonic origin, suggesting that embryonic expression of *Zeb2* depends on the alternative +164-kb *Zeb2* enhancer.

In conclusion, each differentiation wave giving rise to RTMs at different stages of development are controlled by distinct TF that establish macrophage fate. However, in all developmental stages, PU.1 plays a central role by acting as a pioneer that actively opens up the chromatin at promoters and enhancers (poising), allowing the binding of additional TFs that initiate and control the expression of genes involved in macrophage differentiation.

Macrophage identity-imprinting transcription factors

RTMs are a heterogenous population with specific characteristics and functions inherent to their tissue of residence. However, independent of their origin and tissue location, RTMs are characterized by a *core macrophage program* that distinguishes them from other mononuclear phagocytes^{42,236}. Such *core macrophage program* maintains macrophage survival, notably through the expression of *Csf1r* (encoding the *Csf1* receptor), and establishes core functions, including efferocytosis (*Timd4*, *Mertk* and *Sirpa*, involved in apoptotic cell clearance), non-opsonic phagocytosis (*Cd14*, *Cd36*, *Clec7a* and *Mrc1*, necessary

for the direct recognition of foreign particles), opsonic receptor-dependent phagocytosis (*Fcgr1* [coding for CD64]), *Fcgr3*, *Fcgr4* and *Itgam* [coding for CD11b], essential for the ingestion of opsonized pathogens) and complement-dependent tissue immunity (*C1qb*, *C1qc* and *C3ar1*, encoding key components of the complement pathway)^{54,65}. Of note, the establishment of this *core macrophage program* is initiated early in macrophage progenitors upon tissue seeding and is driven by a shared set of macrophage identity-imprinting TF^{58,59,65,110}.

Discovered in 1994²³⁷, Maf basic leucine zipper transcription factor B (MafB) is highly expressed in myelomonocytic cells, including macrophages, and can contribute to monocytic differentiation^{238–240}. Moreover, overexpression of MafB in transformed chicken myeloblasts results in the formation of macrophages, suggesting that MafB is specific and essential for macrophage development⁸⁹. Different studies using reporter mice, lineage-tracing and transcriptome analyses found that MafB was highly expressed in RTMs, distinguishing them from other mononuclear phagocytes, including dendritic cells (DCs) and monocytes^{42,238,241–243}. Yet, surprisingly, alveolar macrophages do not express MafB. In RTMs, MafB can regulate F4/80 expression²⁴¹ and is involved in actin remodeling²⁴⁴. In addition, MafB is thought to play a key role in efferocytosis by directly regulating the expression C1q complement genes (*C1qa*, *C1qb*, *C1qc*)²⁴⁵. MafB, in concert with c-Maf, can also negatively control proliferation of differentiated macrophages by repressing the expression of self-renewal genes such as *Myc*, *Klf2* and *Klf4*^{243,246}. MafB can indeed directly inhibit active enhancers that drive the self-renewal program in RTM. In self-maintaining RTM, such as AM that do not express MafB, it has been suggested that the absence of MafB would stop the inhibition of self-renewal genes and allowing RTM to re-enter cell cycle²⁴³. However, other RTM known to self-maintain

through proliferation, including Kupffer cells (KCs) and MG, express high levels of MafB. In the lung, monocytes seeding an empty interstitial macrophage (IM) niche can undergo a proliferation stage before differentiating in IM, a transition that is regulated by MafB¹¹⁰. Of note, expression of the core macrophage genes CD64 and MerTK is substantially reduced in Mafb-deficient IM. In humans, Goudot *et al* have shown that *MAFB* is highly expressed in monocyte-derived macrophages compared to monocyte-derived DCs, while knockdown of *MAFB* favors mo-DC differentiation²⁴⁷. Even though it has been established that most RTM highly express MafB, the precise role of MafB in imprinting macrophage identity remains unclear and would require more investigations.

While other macrophage identity-imprinting TFs have been proposed, including Zeb2, Batf3 and Irf8, their precise roles in macrophage differentiation and core functions are less clear⁶⁵. For instance, Zeb2 expression, which is conserved in many RTMs, is required to imprint tissue-specific identities and functions rather than a general macrophage identity²³⁶. Noteworthy, this was demonstrated by Cre-mediated deletion of *Zeb2* using Cre lines that are more specific for terminally differentiated macrophages such as *Clec4f^{Cre}* and *Itgax^{Cre}* for KCs and AMs, respectively. Targeting Zeb2 during macrophage differentiation by using mice that express Cre in macrophage progenitors (e.g. *Lyz2^{Cre}* or *Ms4a3^{Cre}*) could provide more insight on the role of Zeb2 as macrophage identity-imprinting TF.

Arguably, much remains to be explored regarding the transcriptional regulation of macrophage core functions, particularly in defining the precise role of various TFs.

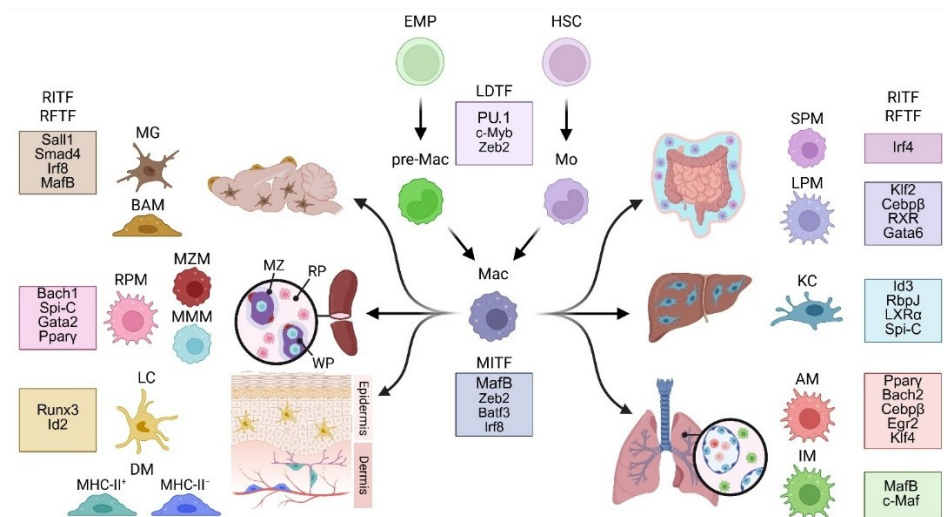


Figure 1.7. Transcriptional regulation of tissue specific macrophage identity and function. AM, alveolar macrophage; BAM, border associated macrophage; DM, dermal macrophage; IM, interstitial macrophage; KC, Kupffer cell; LC, Langerhans cell; LDTF, lineage-determining transcription factor; LPM, large peritoneal macrophage; Mac, macrophage; MG, microglia; MITF, macrophage identity imprinting transcription factor; MMM, marginal metallophilic macrophage; Mo, monocyte; MZM, marginal zone macrophage; pre-Mac, pre-macrophage; RTM, resident tissue macrophage; RITF, RTM identity-imprinting transcription factor; RFTF, RTM function-imprinting transcription factor; RPM, red pulp macrophage; SPM, small peritoneal macrophage. Figure was created in BioRender

Tissue-specific macrophage identity-imprinting transcription factors

The tissue microenvironment is considered as a major determinant of RTM remarkable functional diversity, which is thought to be controlled by dedicated TFs driving transcriptional modules responsible for RTM specification^{72,76,248} (**Figure 1.7**). In this section, we detail key TFs involved in shaping the identity and function of RTMs across different organs, including the peritoneum, liver, lung,

brain, spleen, and skin, illustrating how niche-derived signals converge on unique transcriptional programs to guide RTM specification.

Serous cavity macrophages

Two distinct RTM subsets have been identified in the peritoneal cavity: small peritoneal macrophages (SPM) and large peritoneal macrophages (LPM). LPM are primarily embryonically derived and express prototypical macrophage markers including F4/80 and MerTK, while the monocyte-derived SPMs are characterized by the expression of MHC-II, CD11c and CD226^{87,106,249}. Both subsets express high levels of the TF Cebp β . Notably, *Cebpb*^{-/-} mice exhibit increased numbers of SPMs but lack LPMs, while other RTM subsets in the spleen, kidney, mesenteric lymph nodes, and liver are unaffected²⁵⁰. Interestingly, wild-type SPMs transferred into *Cebpb*-deficient mice can differentiate into LPMs, highlighting an intrinsic role for Cebp β in LPM identity²⁵⁰. SPMs selectively express high levels of the TF Interferon regulatory factor 4 (Irf4) in comparison with LPMs and RTMs from the spleen, lung and brain¹⁰⁶. In the absence of *Irf4*, SPM numbers are reduced, and the expression of the SPM identity gene *Cd226* is lost¹⁰⁶. Compared to other RTMs, LPMs are characterized by the expression of the TF Gata6^{42,107,251,252} and Gata6 reporter mice have been used to study LPM function¹⁷¹. LPMs numbers are reduced in myeloid specific Gata6-deficient mice and Gata6 plays a key role in LPM localization, proliferation, survival and functional maturation^{107,251,252}. Gata6 directly regulates the expression of a number of LPM identity genes including *Tgfb1*, *Cd62p*, *Cd49f*, and *Cd73*²⁵¹. Interestingly, *ex vivo* cultured LPM rapidly lose the expression of Gata6, which can be partially rescued by the addition of peritoneal lavage fluid or retinoic acid (RA)^{251,252}. RA, produced from vitamin A by peritoneal adipose tissue²⁵¹, can be taken up by LPMs and induces Gata6 via binding to the RA nuclear receptor β (RAR β), resulting in the formation of a heterodimer complex

with the retinoid X receptor (RXR) binding to RA response element⁷⁶. Another key TF, Krüppel-like factor 2 (Klf2), is highly expressed in LPM. Mice lacking Klf2 lack LPM, and Klf2-deficient bone marrow-derived macrophages (BMDMs) fail to acquire the expression of LPM identity genes, including *Icam2*, *Timd4*, *Cebpb*, *Mertk*, and *Gata6*, when transferred into the peritoneal cavity²⁵³. Interestingly, in LPM, Klf2 binds to promoters and enhancers of *Cebpb*, *Gata6* and genes encoding the retinoic acid receptors (*Rara*, *Rarg*, and *Rxra*), and its overexpression in BMDMs induces LPM identity *in vitro*. In humans, transcriptional profiling has revealed that peritoneal macrophages also comprise distinct subsets, although they differ from their murine counterparts. GATA6⁺ macrophages, abundant in mice, are far less prominent in adult humans and virtually absent in children⁸⁷. Instead, Irf4-dependent mouse SPM transcriptionally correspond with human CD1c⁺CD14⁺CD64⁺ peritoneal cells that express features of both macrophages and DCs.

Liver macrophages

The liver hosts the largest population of RTM in the body, consisting mostly of KCs, alongside smaller populations of lipid-associated macrophages and capsule macrophages⁶¹. KCs reside in centrilobular and periportal regions, in close contact with sinusoidal endothelial cells. KCs are involved in the clearance of foreign particles, pathogens and apoptotic cells, as well as the metabolism of iron, bilirubin and cholesterol. During KC differentiation, pre-Mac/monocytes start expressing the transcriptional regulators *Id1* and *Id3*, and the TFs *Irf7*, *Nr1h3* and *Spic* upon entering the fetal liver, suggesting their role in imprinting of KC-specific identity⁶⁵. Genetic deletion of inhibitor of DNA 3 (*Id3*) results in reduced numbers of KC, while MG and kidney resident macrophages remain unaffected⁶⁵. Compared to other RTM subsets, the motif of liver X receptor- α (LXR α , encoded by *Nr1h3*) is enriched in KCs⁷² and even though the number of KCs is not affected

in *Nr1h3*-deficient mice, the expression of many KC identity genes including *Clec4f*, *Tim4*, *Cdh5* and *Folr2* are significantly reduced in *Nr1h3*^{-/-} KCs²³⁶. The groups of Glass and Guillems independently showed that KC identity is induced and maintained by Notch ligand Dll4 and Bmp9 produced by sinusoidal endothelial cells and hepatic stellate cells, respectively, and endogenous derived LXR ligands^{58,59,61}. Interaction of Dll4 with the Notch receptor on results in the activation of PU.1 and recombination signal binding protein for immunoglobulin kappa J (RbpJ) poised enhancers, allowing the expression of KC identity specific TFs including *Nr1h3* and *Spic*⁵⁹. These TFs reprogram the KC enhancer landscape so that other signal-dependent TF such as Bmp9 induced Smads can drive the expression of KC-specific genes. Of note, interactions of differentiating KC with hepatocytes induces *Id3* expression⁵⁸. Human KCs also specifically express high levels of NR1H3 and SPIC, consistent with findings in mice²⁵⁴.

Lung macrophages

Two main RTM populations have been identified in the lung: AM and IM²²⁴. By definition, IM are located in the lung interstitium, while AM reside in the airway lumen. The main function of AMs is the phagocytosis of pathogens and dust particles entering the lungs through inhalation, and clearing lipoprotein-containing alveolar surfactant. *Pparg* is expressed in fetal liver pre-Mac/monocytes that seed the alveoli and its expression is maintained in differentiated Ams^{65,255}. *Pparg*-deficient mice have reduced numbers of AM, and develop pulmonary alveolar proteinosis (PAP)—a condition characterized by surfactant accumulation due to the lack of AM^{255–257}. In contrast, *Pparγ* is not implicated in the development of RTMs in the peritoneum, liver, brain, heart, kidneys, intestine and fat²⁵⁷. In humans, it has been shown that PAP is caused by mutations in the CSF2 receptor subunit α or β ¹⁶⁴. Moreover, *Csf2*^{-/-} or *Csf2rb*^{-/-} mice lack AM and develop PAP^{43,164,165}. *Csf2* is mainly produced by alveolar type

II epithelial cells¹⁶⁵, while AMs themselves produce Tgf β in an autocrine manner²⁵⁸. Mice deficient for the Tgf β receptor II (Tgfbr2) have decreased numbers of AMs and have an increased levels of surfactant protein in the bronchioalveolar lavage²⁵⁸. Interestingly, stimulation of BM-derived monocytes⁶⁰ or fetal monocytes^{257,258} with Csf2 or Tgf β induces the expression of Ppar γ . Additional TFs shown to be involved in AM identity are Bach2, Cebp β , Egr2 and Klf4. Mice with a genetic deletion for Bach2 develop PAP-like accumulation of surfactant proteins, independently of the Csf2–Ppar γ signaling axis²⁵⁹. Apart from the previously mentioned reduction in LPMs, *Cebpb*^{-/-} mice also have significantly lower AMs numbers²⁵⁰. Compared to other RTM, Egr2 is highly expressed in AM and conditional deletion of Egr2 results in the loss of AM-specific identity²⁶⁰. In addition, EGR2 expression in AMs is induced by Tgf β and Csf2 in a Ppar γ –dependent manner. Like Ppar γ , compared to other RTM, Klf4 is also exclusively expressed in differentiating AMs⁶⁵. A recent publication found a reduction in both frequency and number of AMs in Klf4-deficient mice, while other myeloid cells remained unaffected²⁵³. Moreover, AMs lacking Klf4 express lower levels of AM markers CD11c, SiglecF, CD169, CD206 and PD-L1, and AM identity genes *Car4*, *Epcam* and *Mrc1*. In humans, AMs display a transcriptional profile broadly conserved with their murine counterparts, including high expression of PPARG and KLF4^{261,262}.

IM are slowly replaced by monocytes in adults^{103,104,110,186} and encompass two main subsets, namely CD206⁻ (Lyve1^{lo}MHCII^{hi}) IM and CD206⁺ (Lyve1^{hi}MHCII^{lo}) IM, which exhibit gene expression profiles and phenotypes, and occupy distinct niches^{103,104,263,264}. IM are thought to exert immunoregulatory functions during allergic asthma^{185–187,265}, to modulate inflammatory responses upon exposure to bleomycin¹⁰³, influenza virus²⁶⁴ or bacteria¹⁸⁶, to coordinate the organization of tertiary lymphoid structures²⁶³ and, more recently, to prevent premature aging

of the lung⁶⁰. Compared to other lung mononuclear phagocytes, IMs show high expression and activity of the TF MafB^{110,224}. IM numbers and the expression IM identity genes (*Pf4*, *Tmem119*, *ApoE*, *C1q*, *Cd63*) were significantly lower in *Mafb*-deficient mice, although it remains unclear whether this reflects general or IM-specific effects. We recently found that *Tgfb1*, released from blood vessel endothelial cells, could act in concert with *Csf-1* to trigger MafB, the IM identity markers *Tmem119*, *Cx3cr1* and *C1qs*, as well as IM development from monocytes⁶⁰. We have generated a transcriptomic atlas of IM subset differentiation and found that c-Maf was specifically expressed in the lineage giving rise to CD206⁺ IM¹¹⁰, and *Maf*-deficient IMs exhibited decreased expression of the CD206⁺ IM identity genes *Folr2* and *Pf4*. A recent study proposed the existence of 10 distinct IM subsets, each defined by chemokine expression and potentially governed by distinct TF networks, although this would require further formal validation²⁶³.

Brain macrophages

MG, the predominant population of RTM of the central nervous system (CNS), are embryonically derived and are involved in maintaining CNS homeostasis by continuously surveying neuronal synapses and contributing to the development of neural circuits via synaptic pruning²⁶⁶. In addition to MG, the CNS harbors other long-lived resident macrophages, collectively referred to as border-associated macrophages (BAMs). BAMs are located at the interfaces of the CNS, including the meninges, perivascular spaces, and choroid plexus, where they act as sentinels regulating barrier integrity, cerebrospinal fluid dynamics, and immune cell trafficking. The Spalt like transcription factor 1 (*Sall1*) is specifically expressed in MG^{65,72} and *Sall1*-deficient MG have a lower expression of MG signature genes, while the expression of other RTM specific identity genes was higher in *Sall1*-deficient MG⁷⁴. These observations suggest a key role for *Sall1* in

MG identity imprinting. Recently, the group of Glass identified a super enhancer located 300 kb upstream of the *Sall1* transcription start site which regulates the expression of *Sall1* in MG²⁶⁷. This study also showed that *Sall1* actively primes enhancers of MG specific genes to allow binding of Smad4, which in turn drives the expression of these genes. In addition, Smad4 also regulates the expression of *Sall1* by binding to the *Sall1* super enhancer. Tgf β signaling is thought to play a critical role in MG identity^{57,74}, possibly by directly activating Smad4 and inducing *Sall1*²⁶⁷. In parallel, *Irf8* is indispensable for MG development and maintenance. *Irf8*^{-/-} mice exhibit markedly reduced microglial numbers and impaired maturation²⁶⁸. Mechanistically, *Irf8* cooperates with PU.1 to shape the microglial enhancer landscape and promote the expression of MG-specific genes such as *Cx3cr1*, *Sall1*, *Trem2*, and *P2ry12*²⁶⁹⁻²⁷¹. Furthermore, compared MG during embryogenesis and in neonates MafB is highly expressed in adult MG. Deletion of MafB in MG revealed a reduced expression of genes associated with the late adult stage of MG development, such as *Ctsh* and *Pmepa1*, highlighting its role in maintaining MG homeostasis²⁷². Similar to their murine counterparts, human microglia exhibit a gene regulatory network dominated by SALL1 and IRF8²⁵⁴.

Splenic macrophages

The spleen consists of white pulp and the red pulp, separated by the marginal zone. The red pulp harbors RPMs, which can degrade senescent red blood cells (RBCs) and recycle Heme-associated iron, while marginal zone macrophages (MZMs) and marginal metallophilic macrophages (MMMs) are located in the marginal zone²⁷³. RPM exclusively express the TF Spi-C^{72,166,274}, and *Spic*^{-/-} mice lack RPM, while monocytes and other RTM counts remain unaffected^{166,274}. Of note, senescent RBCs are normally captured in spleens of *Spic*^{-/-} mice, but fail to be cleared by RPMs resulting in Heme-bound iron accumulation localized

specifically in the red pulp¹⁶⁶. In monocytes, Spi-C expression is inhibited by the transcriptional repressor Bach1²⁷⁴, but upon erythrophagocytosis, heme release results in heme-dependent Bach1 proteasomal degradation, enabling Spi-C expression²⁷⁴. Mechanistically, heme directly binds to Bach1, inducing a conformational change that promotes its nuclear export and ubiquitin-mediated degradation via the proteasome²⁷⁵. Il33 together with heme induce the expression of Spi-C in BMDMs²⁷⁶. Moreover, mice lacking Il33 or its receptor *Il1rl1* have reduced numbers of RPM, and exhibit impaired iron recycling and elevated iron accumulation in the spleen. The TF Gata6 is downregulated in *Il1rl1*-deficient RPMs, suggesting that Gata6 is involved in the differentiation of monocytes to RPMs. Noteworthy, RBCs serve as a main source of Il33. RPM also express *Pparγ* and *Pparg*-deficient mice have reduced numbers of RPMs²⁵⁵. The nuclear receptor LXR α is essential for the differentiation of macrophages in the marginal zone of the spleen as LXR-deficient mice lack MZM and MMM²⁷⁷.

Skin macrophages

The skin consists of three layers: the epidermis, an outermost layer of stratified epithelium; the dermis, the middle connective tissue-rich layer; and the hypodermis, a bottom layer composed mainly of adipose tissue. Langerhans cells (LCs), which are embryonically derived and reside in the epidermis, act as antigen-presenting cells and were long considered a subset of dendritic cells. In contrast, the dermis harbors several macrophage populations. Early studies identified two main subsets of dermal macrophages (DMs), MHC-II⁻ and MHC-II⁺ DMs²³. Recent single-cell and fate-mapping studies have refined our understanding of DMs^{103,278,279}. DMs can be segregated into distinct transcriptionally defined subsets based on anatomical localization and functional specialization. Lyve1^{hi}MHC-II^{lo}Cx3cr1^{lo} DMs (MHC-II⁻ DMs) reside in close association with blood vessels and are therefore termed perivascular

macrophages¹⁰³. In contrast, Lyve1^{lo}MHC-II^{hi}Cx3cr1^{hi} DMs (MHC-II⁺ DMs) sit near sensory nerve fibers²⁷⁸, and sensory neurons can shape the identity of these MHC-II⁺ DMs through Tgf β signaling²⁷⁹. In turn, MHC-II⁺ DMs contribute to nerve regeneration after injury, highlighting the reciprocal communication between the nervous system and DMs²⁷⁸. During LC differentiation, macrophage progenitors that seed the skin in both humans and mice highly express *RUNX3/Runx3*^{65,254}, and *Runx3*^{-/-} mice are deficient for LCs²⁸⁰. Tgf β induces the expression of *Runx3* and, *Tgfb*^{-/-} mice also lack LCs^{280,281}. Furthermore, Tgf β signaling regulates the expression of *Id2*, and LCs are absent in *Id2*^{-/-} mice, suggesting that Tgf β plays a key role in LC differentiation and maintenance.

Beyond steady-state: macrophage transcriptional dynamics during tissue perturbation

In disease contexts such as infection, injury or cancer, RTMs can undergo transcriptional reprogramming in response to altered environmental cues, leading to functional adaptations that may support either recovery or pathology. In parallel, circulating monocytes can be recruited into the affected tissue, where they differentiate into macrophages. Such recruited cells exhibit high plasticity, enabling them to integrate a wide array of local signals, including inflammatory mediators, stress responses, oxygen and nutrient availability, as well as niche-derived factors^{222,282–285}. Accordingly, the transcriptional regulation of monocyte-to-macrophage differentiation is thought to be finely tuned in a spatially and temporally dynamic manner, tailored to the nature and evolution of the perturbation. While this review does not aim to provide an exhaustive overview of macrophage dynamics in disease, we discuss a few examples of resident and recruited tumor-associated macrophage (TAM) transcriptional (re)programming

to illustrate how transcriptional regulators can shape macrophage identity and function in tumors^{100,225}.

TAMs are the most abundant cell type in glioblastoma (GBM), the most aggressive tumor in the central nervous system, and they encompass a heterogeneous mixture of recruited macrophages and transcriptionally reprogrammed MG^{286,287}. In both *in vitro* and *in vivo* mouse models of GBM, GBM-initiating cells can specifically activate mTOR signaling in MG, but not in BMDMs. Such mTOR activation enhances the activity of Stat3 and NF- κ B, driving MG toward an immunosuppressive state. As a result, MG can limit the infiltration, proliferation, and activity of effector T cells within the tumor, helping the tumor escape immune surveillance and supporting its growth²⁸⁸. Inhibiting the mTOR pathway or Stat3 and NF- κ B in MG may thus recondition them toward a more pro-inflammatory, anti-tumor state. In addition, MG that engulf glioblastoma-derived extracellular vesicles undergo profound transcriptional changes, notably marked by the downregulation of homeostatic signaling pathways such as Tgf β and Smad3²⁸⁹. In human mesenchymal GBM, TAMs that promote tumor progression are suggested to be regulated by TFs including Ppar γ , Spi1, and Batf²⁹⁰. Similarly, in melanoma brain metastasis, MG undergo RELA/NF- κ B–dependent transcriptional reprogramming that supports metastatic progression, and targeting this pathway has been shown to enhance antitumor immunity and improve responses to immunotherapy²⁹¹. These findings highlight the extensive transcriptional reprogramming of MG in tumors and the potential of targeting specific TFs to redirect their function in the tumor microenvironment.

In the liver, specific targeting of KCs resulted in higher tumor engraftment in the liver and metastasis, and the expression of KC-intrinsic Id3 was shown to control tumor cell phagocytosis by KCs and a KC peritumoral niche orchestrating

anti-tumor immunity²⁹². Analyses of human liver metastases supported high ID3 expression and engulfment of tumor material by peritumoral liver KCs, supporting the translational relevance of these findings²⁹². In a model of liver metastasis, loss of resident KCs within tumors impaired cancer control²⁹², and bacterial-mediated *in situ* gene editing to simultaneously disrupt c-Maf and MafB in KCs promoted their expansion and reprogramming, leading to improved control of metastatic liver cancer²⁹³.

Several TFs have also emerged as regulators of recruited TAMs. Among these, c-Maf has been shown to drive an immunosuppressive phenotype in BMDMs and is highly expressed in TAMs sorted from subcutaneous Lewis Lung Carcinoma tumors and in tumor-infiltrating monocytes and macrophages from non-small cell lung cancer patients²⁹⁴. Knockdown of c-Maf reduced the tumor-promoting activities of TAMs, and c-Maf conditional deletion in lung myeloid cells using the *Lyz2-Cre* driver line triggered delayed tumor growth and enhanced antitumor immunity in the same model²⁹⁴. Notably, pharmacological inhibition of c-Maf using a small molecule inhibitor showed some therapeutic benefit for overcoming resistance to anti-PD1 treatment. In a pancreatic ductal adenocarcinoma model, monocytes were shown to differentiate into a transient TAM population that could generate transcriptionally, phenotypically and spatially distinct TAM subsets¹⁰⁰. One of these subsets, enriched in hypoxic tumor regions, was regulated by c-Maf and associated with poor patient prognosis, although c-Maf deletion did not affect tumor growth in mice¹⁰⁰. Similarly, in lung adenocarcinoma, a high density of c-Maf-positive macrophages correlated with poor prognosis²⁹⁵.

The transcription factors *Irf8* and *Ets2* were also predicted to be active in c-Maf-dependent monocyte-derived TAMs in pancreatic cancer¹⁰⁰. *Irf8* has been shown to drive an antigen-presenting cell program in TAMs recruited to a mouse

mammary tumor virus–polyoma middle tumor-antigen breast cancer model, thereby promoting cytotoxic T cell exhaustion and tumor progression. Deletion of *Irf8* in TAMs prevented cytotoxic T lymphocyte exhaustion and led to reduced tumor growth²⁹⁶. In the same spontaneous model, as well as in additional orthotopic models, myeloid-specific deletion of *Ets2* resulted in decreased lung metastasis. Mechanistically, *Ets2* was found to repress a transcriptional program that includes several well-characterized inhibitors of angiogenesis²⁹⁶. Together, these findings illustrate how transcriptional regulators such as *c-Maf*, *Irf8*, and *Ets2* cooperate to shape the pro-tumoral functions of recruited TAMs through distinct but complementary mechanisms.

Conclusion

Macrophages exhibit extraordinary diversity in origin, phenotype, and function. Central to this diversity is a dynamic and hierarchical network of TFs that orchestrates macrophage development, core macrophage programs and macrophage subset functional specification. From homeostasis to responses in disease contexts, TFs act as critical molecular integrators of environmental signals, directing context-specific gene expression programs. Future efforts to unravel how individual and combinatorial TF activities regulate macrophage states will deepen our understanding of macrophage biology but also inform innovative strategies to modulate macrophage functions in health and disease.

OBJECTIVES

OBJECTIVES

Resident tissue macrophages (RTMs) form the first line of defense against invading pathogens. In addition to their immunological roles, RTMs are essential for maintaining tissue homeostasis and perform specialized, tissue-specific functions. Despite their diverse developmental origins and anatomical locations, RTMs share a conserved core macrophage transcriptional program that distinguishes them from other mononuclear phagocytes. This core program sustains macrophage development, survival, identity and function, and is established by a set of transcription factors (TFs), referred to as macrophage identity-imprinting TFs¹⁴⁰. These TFs are considered indispensable for macrophage differentiation, such that their loss results in impaired macrophage identity and function. Although several candidate macrophage identity-imprinting TFs have been proposed, their precise roles as transcriptional regulators of macrophage development have not been formally validated *in vivo*.

Therefore, the overarching objective of this thesis is the in-depth identification, functional testing, and validation of bona fide macrophage identity-imprinting transcription factors.

In the first part of this thesis, we aimed to explore the distinct stages of monocyte-to-RTM differentiation and to determine how the transitioning between these states is regulated. Although RTMs can arise either from circulating monocytes or through local self-renewal^{297,298}, the relative contribution of these pathways and the nature of intermediate transitional states remain poorly defined *in vivo*. This limitation is largely due to the slow steady-state turnover of RTMs and the rarity of monocyte-to-RTM differentiation events. Lung interstitial macrophages (IMs) constitute a long-lived RTM population that is gradually replenished in adult animals by circulating Ly6C⁺ classical monocytes and comprises phenotypically distinct subsets, including perivascular CD206⁺ IMs and nerve-associated CD206⁻ IMs^{102–104,186,299}.

OBJECTIVES

These characteristics make lung IMs an ideal model to investigate monocyte-to-RTM differentiation trajectories. First, we aimed to generate a transgenic mouse model enabling diphtheria toxin (DT)-inducible depletion of the IM niche, thereby creating a vacant environment that accelerates and synchronizes IM repopulation. Next, we used this model to perform time-resolved single-cell transcriptomic analyses, combined with multiparameter flow cytometry and chimeric approaches, to characterize transitional cell states in real time during IM niche refilling. We then applied *in silico* regulatory network inference to identify TFs that potentially govern transitions between successive differentiation states. Finally, we used myeloid-specific genetic deletion strategies to validate the functional roles of these transcriptional regulators during distinct stages of monocyte-to-IM differentiation and to determine how they imprint both core macrophage identity and IM-specific specialization.

In the second part of this thesis, we aim to investigate TFs that imprint global macrophage identity and function across tissues and species. Although RTMs display marked developmental and functional heterogeneity shaped by tissue-specific niche signals and transcriptional programs, macrophages nonetheless constitute a distinct and conserved cell lineage^{110,172,224,297,298,300,301}. This lineage is defined by shared characteristics, including the expression of core receptors such as the colony-stimulating factor 1 receptor (Csf1r)^{302,303} and the high-affinity immunoglobulin gamma Fc receptor 1 (Fcgr1)^{42,304}, as well as lineage-defining and identity-imprinting TFs such as PU.1^{226,305} and Zeb2²³⁶, respectively. These observations suggest that additional conserved transcriptional regulators contribute to macrophage identity by coordinating both shared and tissue-specific transcriptional programs across RTM populations. First, we compared the transcriptomic profiles of RTMs with those of other mononuclear phagocytes to identify transcription factors that are selectively expressed and

OBJECTIVES

transcriptionally active across RTMs. Next, we employed *in vivo* conditional gene targeting, *ex vivo* macrophage differentiation systems, and bone marrow chimeric models, combined with multiparameter flow cytometry, microscopy, transcriptomic analyses, and functional assays, to validate the roles of these transcriptional regulators in macrophage development and functional identity. We then applied epigenetic profiling approaches in mouse and human macrophages to gain mechanistic insight into how these TFs directly regulate macrophage differentiation and identity at the level of *cis*-regulatory elements. Finally, we used *in silico* comparative analyses to assess the evolutionary conservation of macrophage identity-imprinting pathways across species.

EXPERIMENTAL SECTION

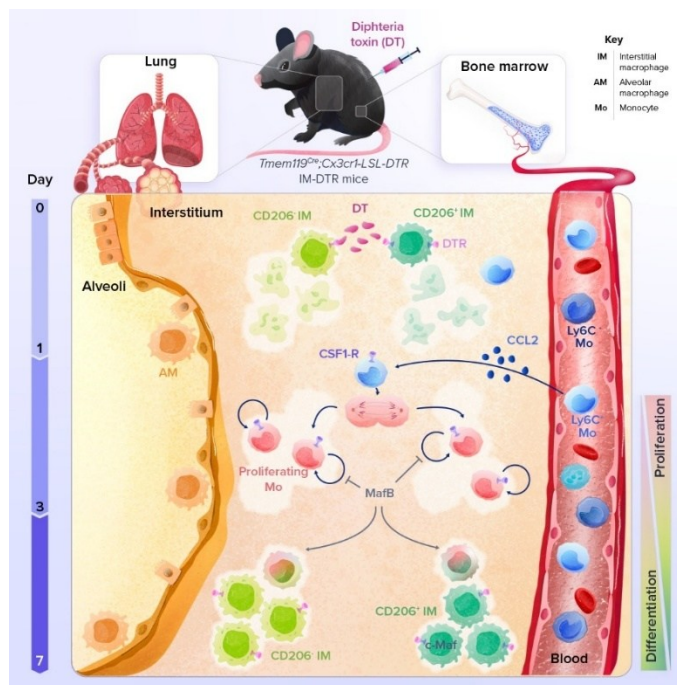
Part I: MafB-restricted local monocyte proliferation precedes lung interstitial macrophage differentiation

After: Domien Vanneste*, Qiang Bai*, Shakir Hasan*, Wen Peng, Dimitri Pirottin, Joey Schyns, Pauline Maréchal, Cecilia Ruscitti, Margot Meunier, Zhaoyuan Liu, Céline Legrand, Laurence Fievez, Florent Ginhoux, Coraline Radermecker, Fabrice Bureau & Thomas Marichal (2023). MafB-restricted local monocyte proliferation precedes lung interstitial macrophage differentiation. *Nature immunology*, 24(5), 827–840. <https://doi.org/10.1038/s41590-023-01468-3> *These authors contributed equally: Domien Vanneste, Qiang Bai, Shakir Hasan.

Author contributions: T.M. conceived, supervised and secured funding for the project; D.V., Q.B., S.H., W.P. and T.M. designed the experiments; D.V., Q.B. and S.H. did most of the experiments, compiled the data and prepared the figures. W.P., J.S., C.L., L.F., S.L., F.G. and C. Radermecker were implicated in experiments related to the analysis of myeloid-restricted *Maf* and *Mafb*-deficient mice; Q.B. performed all the bioinformatic analyses with the help of D.V.; D.P. and F.B. generated *Mafb* floxed mice; P.M. helped with all *in vivo*-related experiments; C. Ruscitti and M.M. performed confocal microscopy experiments. T.M. wrote the manuscript with the help of D.V., Q.B. and S.H. All authors provided feedback on the manuscript.

Abstract

Resident tissue macrophages (RTMs) are differentiated immune cells that populate distinct niches and exert important tissue-supportive functions. RTM maintenance is thought to rely either on differentiation from monocytes or on RTM self-renewal. Here, we used a mouse model of inducible lung interstitial macrophage (IM) niche depletion and refilling to investigate the development of IMs *in vivo*. Using time-course single-cell RNA-sequencing analyses, bone marrow chimeras and gene targeting, we found that engrafted Ly6C⁺ classical monocytes proliferated locally in a *Csf1* receptor-dependent manner before differentiating into IMs. The transition from monocyte proliferation toward IM subset specification was controlled by the transcription factor *MafB*, while *c-Maf* specifically regulated the identity of the CD206⁺ IM subset. Our data provide evidence that, in the mononuclear phagocyte system, the ability to proliferate is not merely restricted to myeloid progenitor cells and mature RTMs but is also a tightly regulated capability of monocytes developing into RTMs *in vivo*.



Graphical abstract 2. Using a DT-induced IM depletion model in *Tmem119^{Cre};Cx3cr1^{LSL-DTR}* mice, called IM^{DTR} mice, we found that the monocyte-to-IM trajectory encompasses a MafB-restricted, Csf1r-dependent local proliferation of transitioning monocytes (Tr-Mo) that precedes the differentiation into CD206⁻ IM or c-Maf-dependent CD206⁺ IM. Graphical abstract was created by Adeline Deward – IllumineScience.

Introduction

RTMs are self-maintaining immune cells that are integral parts of mammalian tissues and exert important tissue-supportive functions. The original understanding that RTMs arise from bone marrow (BM)-derived circulating monocytes, as proposed by van Furth and Cohn¹⁵, has been challenged by multiple reports showing that several RTM populations can arise from embryonic yolk sac macrophages and fetal monocytes that seed the tissues before the establishment of definitive hematopoiesis, and can self-maintain with minimal contribution of monocytes^{24,67,306,307}. Nevertheless, throughout adult life, monocytes can give rise to RTMs in proportions that depend on the tissue accessibility and on the nature and extent of perturbations leading to RTM depletion^{29,282,300,297,308}.

Besides origin, the differentiation trajectories and the tissue cues are thought to be essential determinants of RTM identity and function^{222,298,300}. In a given niche, RTMs can respond to local trophic factors, such as Csf1 for their maintenance, and are instructed by niche-derived signals that trigger the expression of specific transcription factors and differentiation programs, thereby tailoring a specific identity that fulfills the functional needs of a given tissue^{42,72,300,309}.

While currently the repopulation and maintenance of RTM niches is thought to be achieved either through monocyte engraftment and differentiation or through the self-renewal of mature RTMs^{297,298}, the slow turnover of RTMs at steady state and the lack of models that allow the capture of rare events, such as monocyte-to-RTM transitioning cells, have hampered investigations of RTM dynamics *in vivo*. The lung IMs, which are long-lived RTMs that are slowly replenished in adults by Ly6C⁺ classical monocytes (cMo) and encompass

perivascular CD206⁺ IMs and nerve-associated CD206⁻ IMs^{102–104,186,299}, can be used as a model to study monocyte-to-RTM trajectories. Here, we developed a transgenic mouse model of diphtheria toxin (DT)-inducible IM niche depletion that allowed us to capture and explore at the single-cell resolution the dynamics of events that occur during monocyte-to-IM differentiation. In this model, we found that repopulated IMs arose from BM-derived Ly6C⁺ cMo dependent on the monocyte chemoattractant receptor Ccr2 that could undergo a transient Csf1 receptor (Csf1r)-dependent proliferation in vacant tissue niches before their differentiation into CD206⁺ IMs or CD206⁻ IMs, a process that was regulated by MafB. Our data support the idea that tissue monocyte proliferation might represent an underappreciated process involved in monocyte-to-RTM trajectories *in vivo*.

Materials and Methods

Mice

The following mice on the C57BL/6 background were used in this study: CD45.2 wild-type C57BL/6 (The Jackson Laboratory), CD45.1 wild-type C57BL/6J (The Jackson Laboratory, 002014), *Cx3cr1^{GFP/+}* (ref.¹⁰⁹; The Jackson Laboratory, 005582), *Tmem119^{Cre}* (see below), *Rosa26^{LSL-EYFP}* (ref.³¹⁰; The Jackson Laboratory, 006148), *Cx3cr1^{LSL-DTR/+}* (ref.³¹¹; The Jackson Laboratory, 025629), *Ccr2^{-/-}* (ref.³¹²; The Jackson Laboratory, 004999), *Nr4a1^{-/-}* (ref.³¹³; The Jackson Laboratory, 006187), *Maf^{fl/fl}* (ref.³¹⁴; kindly provided by F. Andris), *Mafb^{fl/fl}* (generated by D.P. and the GIGA Mouse facility and Transgenics Platform, Liège University, Belgium, see below), *Lyz2^{Cre}* (ref.³¹⁵; The Jackson Laboratory, 004781) and *Ms4a3^{Cre}* (ref.²⁹). Myeloid-restricted *Maf* or *Mafb* depletion was achieved by crossing *Maf^{fl/fl}* or *Mafb^{fl/fl}* mice with *Lyz2^{Cre}* or *Ms4a3^{Cre}* mice.

C57BL/6 *Tmem119^{Cre}* knock-in mice were generated using CRISPR/Cas-mediated genome engineering by Cyagen Bioscience. In brief, the *Tmem119* targeting vector was designed by cloning a genomic fragment encompassing exon 2 of the *Tmem119* gene from BAC clones RP23-187D5 and RP23-126P3. A *Cre-polyA* cassette was introduced in the *Tmem119* targeting vector upstream of the ATG start codon between a 2.1-kb 5' homology arm and a 2.1-kb 3' homology arm. *Tmem119*-gRNA (protospacer, CAGGGGACCATGTTGAGCTATGG), *Cas9* mRNA and *Tmem119* targeting vector were co-injected into pronuclei of C57BL/6J one-cell-stage zygotes, followed by implantation of the zygotes into surrogate mothers to obtain targeted knock-in offspring. F0 knock-in founder animals were identified by PCR followed by sequence analysis. *Tmem119^{Cre/+}* mice were then back-crossed to CD45.2 or CD45.1 C57BL/6J mice for at least four generations. *Tmem119^{Cre}* mice were genotyped by PCR using the following

primers: PCR primers 1 for mutant allele (annealing temperature, 60.0 °C): forward primer: 5'- TCCGTAACCTGGATAGTGAACAG-3'; reverse primer: 5'- ATATGTCCTTCCGAGTGAGAGAC-3'; product size: 270 bp (mutant). PCR primers 2 for wild-type allele (annealing temperature, 60.0 °C): forward primer: 5'- ACCGAGGACAGAAATGAATAAGATG-3'; reverse primer: 5'- AGGGAACGAGGATGGGTAGTAG-3'; product size: 643 bp (wild type).

C57BL/6 *Mafb^{fl/fl}* mice were generated using recombination-mediated genetic engineering. Briefly, the genomic segment covering the *Mafb* single exon was retrieved to PL253 vector using BAC recombineering. The loxP-EM7-Neo-loxP cassette was cloned by PCR from PL452 plasmid and ligated to the *Mafb* 5' segment (PL253/*Mafb*/Neo 5') and the cassette was 'popped out' by electroporating to SW106 cells expressing *Cre* and 5' loxP left in the construct. The FRT-Neo-FRT-loxP cassette was cloned from PL451 plasmid and ligated to the *Mafb* 3' segment. The purified plasmid was electroporated into mouse embryonic stem cells and the cells were selected under G418 treatment for 1 week. The bona fide clones with successful homologous recombination were screened by Southern blot. Successfully recombined clones were injected into blastocysts to make *Mafb^{fl}-Neo* mice. These mice were crossed to an *FLP*-expressing line to remove the P_{gk}-Neo cassette and generate *Mafb^{fl}* mice. *Mafb^{fl}* mice were genotyped by PCR using the following primers: forward primer: 5'- TCCATCCATCTTGGGAAAAG-3'; reverse primer: 5'-TCAGGACTGGGCTGCTAGTT-3'; product size: 320 bp (Mutant), 220 bp (wild type).

Tmem119^{Cre} and *Rosa26^{LSL-EYFP}* mice were crossed to create *Tmem119^{Cre}Rosa26^{LSL-EYFP}* mice. *Tmem119^{Cre}* and *Cx3cr1^{LSL-DTR/+}* mice were crossed to create *Tmem119^{Cre}Cx3cr1^{LSL-DTR/+}* mice, referred to as 'IM^{DTR}' mice. Since we observed some YFP labeling in CD45⁻ cells in the testis and ovaries of *Tmem119^{Cre}Rosa26^{LSL-EYFP}* mice, we did not use *Tmem119^{Cre}Rosa26^{LSL-EYFP}* or

Tmem119^{Cre}Cx3cr1^{LSL-DTR} mice as breeders to avoid any issues arising from germline recombination. CD45.1/CD45.2 IM^{DTR} mice were generated by crossing CD45.1 *Tmem119^{Cre}* with CD45.2 *Cx3cr1^{LSL-DTR}* mice.

No sex-specific differences were observed in pilot experiments. A mix of male and female mice between 6 and 10 weeks of age were used for each experiment, except for chimera experiments where mice between 11 and 15 weeks of age were used. The mice were bred and housed under specific-pathogen-free conditions at the GIGA Institute (Liège University, Belgium), maintained in a 12-h light-dark cycle, and had access to normal diet chow and water ad libitum. Mice were identified according to genotype and all experiments were performed with age-matched and sex-matched littermates. For *Csf1r*-blocking experiments, mice were randomly assigned to vehicle or isotype antibodies and anti-*Csf1r* treatments. For experiments using IM^{DTR} mice that were treated or not with DT, mice were randomly allocated to DT treatment or not. Investigators were not blinded during the collection and analysis of the data, except for the quantification of microscopy lung sections, where investigators were blinded.

All animal experiments described in this study were reviewed and approved by the Institutional Animal Care and Use Committee of the University of Liège (ethical approval no. DE1956). The 'Guide for the Care and Use of Laboratory Animals,' prepared by the Institute of Laboratory Animal Resources, National Research Council, and published by the National Academy Press, as well as European and local legislations, was followed carefully. Accordingly, the temperature and relative humidity were 21 °C and 45–60%, respectively.

Reagents and antibodies

A complete list of the reagents, antibodies and commercial assays used in this paper can be found in **Supplementary table 2.1**.

In vivo treatments with chemicals and antibodies

For DT-induced depletion of IM, IM^{DTR} mice were injected i.p. with a single dose of 50 ng DT (List Biological Labs, 150), unless otherwise stated. Control mice were either untreated IM^{DTR} mice, or *Tmem119*^{Cre/+} littermate control mice injected with DT. For EdU incorporation experiments, IM^{DTR} mice were injected i.p. with 1 mg EdU (Santa Cruz Biotechnology, sc-284628) in 200 µl PBS 4 h before killing, unless otherwise stated. For all experiments involving EdU incorporation, 1 µg of PerCP-Cy5.5-conjugated anti-mouse CD45 (clone 104, BD Biosciences, 552950) was i.v. injected 10 min before killing to distinguish blood circulating (CD45-PerCP-Cy5.5⁺) and tissue leukocytes (CD45-PerCP-Cy5.5⁻). For Csf1r-blocking experiments, 250 µg of anti-mouse Csf1r-blocking antibody (clone AFS98, Bio X Cell, BE0213) or isotype control (clone 2A3, Bio X Cell, BE0089) was injected i.v. 6 and 28 h after DT injection. For experiments with Csf1r inhibitors, 100 mg per kg body weight of pexidartinib (PLX3397; MedChemExpress, HY-16749) was injected i.p. 24 and 48 h after DT injection.

Bone marrow, blood and tissue leukocyte isolation

Blood was collected by retro-orbital plexus bleeding of terminally anesthetized mice. Mice were then euthanized by cervical dislocation. Peritoneal lavage was obtained by injecting 10 ml HBSS (Lonza, BE10-508F) into the peritoneal cavity and collecting the washout. Mice were then perfused with 10 ml PBS via the left ventricle, and lungs, brain, liver, spleen, intestine and colon were dissected.

For BM cells, femurs and tibiae were dissected and cleaned of soft adhering tissue. Distal and proximal ends were opened, and BM cells were flushed out. After centrifugation, cell pellets were resuspended in ice-cold PBS (Thermo Fisher, 14190094) containing 10 mM EDTA (Merck Millipore, 1084181000) and cell suspensions were filtered using a cell strainer (70 μ m, Corning, 352350) to obtain a single-cell suspension.

Lungs, brains, liver and spleen were cut into small pieces with razor blades, and digested for 1 h at 37 °C in HBSS containing 5% vol/vol FBS (Thermo Fisher, 10270098), 1 mg/ml collagenase A (Sigma, 14190094) and 0.05 mg/ml DNase I (Sigma, 11284932001). After 45 min of digestion, the suspension was flushed using a 18-gauge needle to dissociate aggregates. Ice-cold PBS (Thermo Fisher, 14190094) containing 10 mM EDTA (Merck Millipore, 1084181000) was added to stop the digestion process and cell suspensions were filtered using a cell strainer (70 μ m, Corning, 352350). Mononuclear leukocytes from lungs and livers were enriched using a Percoll density gradient (GE Healthcare, 17089101) and by harvesting cells from the 1.080:1.038 g/ml interface.

For the isolation of leukocytes from the small intestines and colons, small intestines and colons were dissected from the pylorus and the rectum, were separated from the mesenteric tissue from Peyer's patches and from fat and were placed in ice-cold HBSS with 2% FBS. Intestinal content was removed with PBS, and the small intestines and colons were opened by a longitudinal cut and washed three times in ice-cold HBSS with 2% FBS. To remove mucus and epithelial cells, small intestines and colons were incubated with HBSS with 2% FBS and 1 mM 1,4 dithiothreitol (Sigma, 10197777001) for 20 min with constant shaking followed by an incubation with HBSS containing 2% FBS and 1.3 mM EDTA for 40 min. Tissue pieces were then cut into small pieces and incubated for 1 h at 37 °C with RPMI containing 2% FBS, 2 mg/ml collagenase IV (Thermo

Fisher, 17104019) and 40 U/ml DNase I. At the end of incubation, the suspension was homogenized with a 19-gauge syringe and filtered through a 70- μ m strainer.

Generation of bone marrow (competitive) chimeras

Eighteen-week-old CD45.2 or CD45.1/CD45.2 IM^{DTR} mice were anesthetized by i.p. injection of 200 μ l PBS containing ketamine (75 mg per kg body weight; Dechra, 804132) and xylazine (10 mg per kg body weight; Bayer, 0076901). The thoracic cavity was protected with a 0.6-cm-thick lead cover and mice were lethally irradiated with two doses of 6 Gy 15 min apart. Once recovered from the anesthesia, mice were reconstituted by i.v. administration of 10^7 BM cells from congenic CD45.1 wild-type mice. For mixed BM chimeras, mice were injected i.v. with 10^7 BM cells consisting of a 1:1 mix of cells obtained from CD45.1 wild-type and CD45.2 *Ccr2*^{-/-}, *Nr4a1*^{-/-} or *Ms4a3*^{Cre}*Mafb*^{fl/fl} mice. From the day of irradiation, mice were treated for 4 weeks with 0.05 mg/ml of enrofloxacin (Baytril, Bayer) in drinking water. Chimerism was assessed by flow cytometry in the blood 4 weeks after irradiation.

Adoptive transfer of bone marrow monocytes

BM Ly6C⁺ monocytes were isolated from congenic CD45.1 wild-type mice using the Monocyte Isolation Kit (Miltenyi Biotec, 130-100-629). Around 2×10^6 BM Ly6C⁺ monocytes were administered i.v. into CD45.1/CD45.2 IM^{DTR} mice that were injected i.p. with 50 ng DT 24 h before monocyte transfer to deplete endogenous IMs.

Flow cytometry

Cells ($0.5\text{--}5 \times 10^6$) were pre-incubated with Mouse BD Fc Block (BD Biosciences, 553142) to avoid unspecific binding to Fc receptors and stained with appropriate

antibodies at 4 °C in the dark for 30 min. For EdU staining, extracellular-stained cells were permeabilized and stained using Click-iT EdU Alexa Fluor 488 Flow Cytometry Assay Kit (Thermo Fisher, 10632), according to the manufacturer's instructions. For DAPI cell cycle analyses, extracellular-stained cells were permeabilized and stained with 1 µg/ml DAPI (BioLegend, 422801) in the dark for 30 min at room temperature (RT). For Ki67 staining, extracellular-stained cells were permeabilized and stained using either FITC Mouse Anti-Ki67 Set (BD Biosciences, 556026) or PerCP-eFluor710 Mouse Anti-Ki67 (Thermo Fisher, 46-5698-80). Cell viability was assessed using LIVE/DEAD Fixable Near-IR (775) stain (Thermo Fisher, L34976) and the cell suspensions were analyzed with an LSRFortessa (BD Biosciences). Results were analyzed using FlowJo software (Tree Star). For scRNA-seq and bulk RNA-seq, lung myeloid cells were sorted using a FACSAria III (BD Biosciences). The full list of antibodies used can be found in the **Supplementary table 1**.

MCP-1/Ccl2 quantification

IM^{DTR} and littermate control mice were euthanized at indicated time points after DT administration. Blood was collected and lungs were perfused through the right ventricle with 10 ml PBS and isolated. Blood samples were left undisturbed for 30–45 min at RT to allow clot formation. The serum was separated from the blood clot by centrifugation for 10 min at 2,000g at 4 °C. Serum was stored at –80 °C. Dissected lungs were snap frozen and homogenized in 360 µl ice-cold lysis buffer (40 mM Tris-HCl (pH 7.4), 150 mM NaCl, 10% glycerol and cComplete Protease Inhibitor Cocktail (Sigma, 11697498001) using a tissue homogenizer (IKA) with the addition of 1% NP-40 (Sigma, 74385) after homogenization. Samples were then rotated for 20 min at 4 °C, followed by a centrifugation to pellet debris. Protein concentration of cleared lysates was determined using Pierce BCA Protein Assay Kit (Thermo Fisher), according to the manufacturer's

instructions. Cleared lysates were stored at -80°C . Ccl2 levels in serum and lung homogenates were determined using MCP-1/Ccl2 Mouse Uncoated ELISA Kit (Thermo Fisher), according to the manufacturer's instructions.

Bulk RNA-seq: sample preparation and analysis

Native IM subsets, cMo and AMs were isolated from uninjected IM^{DTR} mice, while repopulated IM subsets were isolated from IM^{DTR} mice that had been treated i.p. with 50 ng DT 14 days earlier. Cell populations were FACS sorted using the gating strategy shown in Fig. 1c into TRIzol reagent (Thermo Fisher, 10296010). Total RNA was extracted with the standard TRIzol RNA extraction protocol. RNA quality and quantity were evaluated using a 2100 bioanalyzer (Agilent) and the Quant-iT RiboGreen RNA Assay Kit (Thermo Fisher, R11490). One hundred nanograms of RNA was used to generate the libraries using the TruSeq Stranded mRNA kit (Illumina, 20020594). These libraries were sequenced on an Illumina NovaSeq sequencer on an SP flow cell. Sequence alignment with the mouse genome (GRCm38), sequence counting and quality control were performed using the nf-core/rnaseq pipeline. RNA-seq data were analyzed using R Bioconductor (3.5.1) and DESeq2 package (version 1.26.0)³¹⁶.

scRNA-seq

To compare lung monocytes and IMs from untreated IM^{DTR} mice (group 'no treatment') with those from IM^{DTR} mice treated with 50 ng DT i.p. 96 h before (group 'DT96h'), five mice from each group were killed and lung single-cell suspensions were obtained after enzymatic digestion. CD11b⁺ cells were enriched by MACS using CD11b MicroBeads (Miltenyi Biotec, 130-049-601). Lung monocytes and IMs were then FACS sorted separately as CD45⁺SSC^{lo}CD11b⁺F4/80⁺CD64⁻ and CD64⁺ cells, respectively (**Figure 1C**), and the

10x Genomics platform (Single Cell 3' Solution) was used for scRNA-seq. The IM pool was then enriched in the final single-cell suspension to reach a monocyte/IM ratio of 1:1. For each sample, an aliquot of Trypan blue-treated cells was examined under the microscope for counting, viability and aggregate assessment following FACS sorting. Viability was above 90% for all samples and no aggregates were observed. Cell preparations were resuspended in calcium-free and magnesium-free PBS containing 0.4 mg/ml of UltraPure BSA (Thermo Fisher Scientific, AM2616).

To analyze lung monocytes ($CD45^+SSC^{lo}CD11b^+F4/80^+CD64^-$) and IMs ($CD45^+SSC^{lo}CD11b^+F4/80^+CD64^+$) from IM^{DTR} mice treated 12 h (group 'DT12h'), 24 h (group 'DT24') and 48 h (group 'DT48h') before with 50 ng DT i.p., and to analyze lung monocytes ($CD45^+SSC^{lo}CD11b^+F4/80^+CD64^-$) and CD64⁺ cells ($CD45^+SSC^{lo}CD11b^+F4/80^+CD64^+$) from *Lyz2^{Cre}Mafb^{fl/fl}* (group 'Mafb-KO'), *Lyz2^{Cre}Maf^{fl/fl}* (group 'cMAF-KO') and littermate control (group 'control') mice, a similar protocol was applied, but cells from each group were barcoded with different anti-mouse Hashtag antibodies (BioLegend) before being pooled for encapsulation and library construction. To obtain a higher resolution in analyzing lung myeloid cells in myeloid-restricted Mafb-deficient and Maf-deficient mice, the pooled Mafb-KO/cMAF-KO/control samples were composed of a ratio of monocytes:CD64⁺ cells of 3:7 instead of 1:1.

For library preparation, approximately 3,000 cells per sample (for 'DT96h' and 'no treatment'), or 20,000 cells for pooled hashtag-labeled samples, were loaded into the Chromium Controller, in which they were partitioned, and their polyA RNAs captured and barcoded using Chromium Single Cell 3' GEM, Library & Gel Bead Kit v3 (10x Genomics). The cDNAs were amplified and libraries compatible with Illumina sequencers were generated using Chromium Single Cell 3' GEM, Library & Gel Bead Kit v3 (10x Genomics). For Hash Tag Oligonucleotide (HTO)

library, 1 μ l HTO additive primer v2 (0.2 μ M stock) were added to the mix at the cDNA amplification step. The libraries were sequenced on an Illumina NovaSeq sequencer on an SP100 cell flow (read 1, 28 cy; read 2, 76 cy; index 1, 10 cy; index 2, 10 cy) at a depth of 50,000 reads per cell.

The Cell Ranger (v3.0.2) application (10x Genomics) was then used to demultiplex the BCL files into FASTQ files (cellranger mkfastq), to perform alignment (to Cell Ranger mouse genome references 3.0.2 GRCm38/build 97), filtering and unique molecular identifier counting and to produce gene-barcode matrices (cellranger count).

Filtered matrix files were used for further scRNA-seq analyses with R Bioconductor (3.12) and Seurat (3.2.1)³¹⁷. The cells from pooled hashtag-labeled samples were demultiplexed with the barcode detected in each cell.

Filtered matrices containing cell IDs and feature names in each sample were used to build a Seurat object. We performed quality control by filtering out the cells with less than 200 detected genes, the genes detected in less than three cells and the cells exhibiting more than 10% of mitochondrial genes. Gene counts in each sample were normalized separately by default method *LogNormalize* with a scale factor of 10,000 and log transformation. Two thousand highly variable features were identified with the *vst* method.

After merging cells from all samples, cell contaminants were removed based on the expression of specific genes. Four clusters were identified in the remaining cells using the *FindClusters* function and the DEGs were calculated using the *FindAllMarkers* function (Seurat package).

Single-cell RNA velocity estimation

The counts for unspliced and ambiguous transcripts were calculated from Cell Ranger output using the `velocyto` command-line tool (<http://velocyto.org/>)³¹⁸ and saved in loom files. The single-cell RNA velocities were estimated using `scVelo` toolkit (<https://scvelo.readthedocs.io/>)³¹⁹. Briefly, the loom files were used as input for `scVelo` analysis. Genes with a minimum of 20 of both unspliced and spliced counts and on the top list of 2,000 genes were filtered, normalized and log transformed (`scv.pp.filter_and_normalize` with default parameters). Thirty principal components and 30 neighbors obtained from Euclidean distances in principal-component analysis space were used for computing first-order and second-order moments for each cell. We used generalized dynamical modeling to recover the full splicing kinetics of spliced genes, and the single-cell RNA velocities were plotted with the same cluster labels and embedding as in **Figure 2.4A**.

Gene Ontology enrichment analysis with differentially expressed gene signatures

The DEG lists for enrichment analyses were calculated using `Seurat` function `FindMarkers` with `only.pos = TRUE` to output only positively regulated genes. Thresholds `logfc.threshold` of 0.2 and adjusted *P* value of 0.01 were applied to filter the gene lists. Gene Ontology (GO) enrichment analyses were made using `enrichGO` functions from `clusterProfiler` package (ref.³²⁰) with default arguments. Only biology process terms of ontology were shown in the final results.

Immunofluorescence

For lung immunofluorescence staining, lungs were perfused with 10 ml PBS via the left ventricle and lungs were collected. Lungs were fixed for 4 h in 4%

paraformaldehyde (Thermo Fisher, F/1501/PB15) at 4 °C. Fixed lungs were then cryoprotected in 30% sucrose (VWR, Avantor, 57-50-1) in PBS for 4 h at 4 °C, followed by embedding in optimal cutting temperature compound (OCT; Tissue-Tek, 4583) at -80 °C overnight, and lung OCT sections were cut (7- μ m-thick sections) and blocked in methanol 100% (Merck, 67-56-1) at -20 °C for 20 min. Samples were stained in blocking buffer (PBS with 0.3% Triton X-100 (Merck, 648466) and 2% donkey serum (Sigma Aldrich, D9663)) with rat anti-mouse antibodies directed against MHC class II (I-A/I-E; 1:100 dilution in blocking buffer; clone M5/114.15.2, eBioscience, 14-5321-82) overnight at 4 °C. After washing samples with PBS, secondary donkey anti-rat IgG antibodies conjugated with Alexa Fluor 594 (1:1,000 dilution in blocking buffer; Thermo Fisher, A21209) were added in blocking buffer and incubated for 1 h in the dark at RT. Samples were washed with PBS and incubated with Alexa Fluor 488-conjugated rat anti-mouse antibodies directed against CD206 (clone C068C2, BioLegend, 141710; 1:50 dilution in blocking buffer), eFluor 570-conjugated rat anti-mouse antibodies directed against Ki67 (1:200 dilution in blocking buffer; clone SolA15, eBioscience, 41-5698-82), APC-conjugated rat anti-mouse antibodies directed against CD11b (1:50 dilution in blocking buffer; clone M1/70, eBioscience, 17-0112-83) in blocking buffer for 6 h at 4 °C. Finally, samples were washed one last time with PBS and were mounted with 10 μ l ProLong Antifade reagent (Invitrogen, P36961) containing 0.1% Sytox blue nucleic acid stain (Invitrogen, S11348) on glass slides and stored at RT in the dark overnight.

All samples were analyzed by spectral fluorescence microscopy. Images of full lung sections were acquired on an LSM 980 with Airyscan 2 inverted confocal microscope (Zeiss) using a LD C-Apochromat \times 40/1.1 W objective and Zen Black software. All fluorophores were excited simultaneously, and the emission spectra were collected with a spectral detector 32-channel GaAsP

photomultiplier tube in lambda mode at 8.8-nm bins from 411 to 694 nm. A spectral unmixing was performed based on the monospectral spectra. Images were processed with the Zen Blue software. For quantification, the numbers of CD11b⁺CD206^{lo}MHC-II^{hi} IMs (CD206⁻ IMs), CD11b⁺CD206^{hi}MHC-II^{lo/int} IMs (CD206⁺ IM) and CD11b⁺CD206⁻MHC-II^{lo}Ki67^{hi} cells were counted blindly and manually on a total surface of 12–16 mm² per mouse section. The results were expressed in cell number per mm² of lung section.

Single-cell regulatory network inference and clustering analysis

To predict the potential active transcription factors, Ly6C⁺ cMo, Tr-Mo, CD206⁻ IMs and CD206⁺ IMs were subjected to SCENIC analysis using the SCENIC package³²¹. The normalized counts, nFeature_RNA and nCount_RNA in merged Seurat object were used for the initial SCENIC analysis. The genes expressed with a value of 3 in 0.5% of the cells and detected in 1% of the cells were kept for following SCENIC analysis. Coexpression network analysis was made with GENIE3 in the SCENIC package. To represent the SCENIC results, the results of the '3.4_regulonAUC' output were added to the metadata of Seurat object so that regulon AUC scores could be plotted using the *FeaturePlot* function. The top 50 regulons with highest variance are shown with their z-scores in the heat map.

Monocle, tradeSeq and pseudotime analysis during interstitial macrophage development

To evaluate trajectory-based differential expression analysis during IM development in IM^{DTR} mice, Ly6C⁺ cMo, Tr-Mo, CD206⁻ IMs and CD206⁺ IMs were subjected to Monocle analysis³²². The Monocle CDS object was built with counts and metadata from Seurat object and converted using SeuratWrappers package. Cells were clustered with the *cluster_cells* function using calculated UMAP

coordinates and a resolution of 0.51×10^{-3} . The trajectories along pseudotime were built using *learn_graph* and *order_cells* functions. The DEGs across trajectories were calculated using Moran's I test (*graph_test* function) and only the genes with a q value of 0 and Morans's I value over 0.25 were kept as significant DEGs and subjected to further analyses.

To compare the expression patterns of DEGs across pseudotime, the counts matrix, pseudotime and cell weights calculated above were then used as input in *fitGAM* function (tradeSeq package)³²³. The association of average expression of each gene with pseudotime was tested using *associationTest* and the DEGs between CD206⁻ IM and CD206⁺ IM trajectories were calculated with the *diffEndTest* function. The value of the estimated smoother on a grid of pseudotimes was estimated for each DEG using *predictSmooth*. The DEG with $waldStat > 70$ and $|\log \text{ fold change}| > 2$ were annotated as 'changed genes', meaning that their expression patterns were different in CD206⁻ and CD206⁺ IM trajectories, while the rest of the DEGs were considered as 'unchanged genes', meaning that the expression patterns were similar in both trajectories. Finally, the scaled estimated smoothers calculated by *predictSmooth* were used to build heat maps with the ComplexHeatmap package³²⁴.

Interstitial macrophage and monocyte signature scoring

The IM-specific, cMo-specific and CD16.2⁺ Mo-specific gene signatures were calculated using previously published scRNA-seq data (ref.¹⁰⁴) by comparing IM, cMo or CD16.2⁺ Mo populations to all other cell types in the dataset using the *FindMarker* function (Seurat). The genes with $|\log \text{ fold change}| > 1$ and only positively regulated ones were considered as the IM, cMo or CD16.2⁺ Mo signature. The signatures were then used to calculate the scores for each cell using the VISION package³²⁵ (**Figure 2.8I**) or with *AddModuleScore* function

(Seurat; **Supplementary figure 2.4E**). The scores were stored in Seurat object and plotted with Seurat package.

Statistical analysis

Graphs were prepared with Prism 9 (GraphPad) or R Bioconductor (3.5.1), and ggplot2 for data in **Figure 2.3B**. No statistical methods were used to predetermine sample sizes, but our sample sizes are similar to those reported in previous publications^{104,186,326}. Data distribution was assumed to be normal when parametric tests were performed, but this was not formally tested. Data from independent experiments were pooled for analysis in each data panel, unless otherwise indicated. No data were excluded from the analyses. Statistical analyses were performed with Prism 9 (GraphPad), and with R Bioconductor (3.5.1)³²⁷ and DESeq2³¹⁶ or Seurat (3.2.1.)³¹⁷ for bulk and scRNA-seq data, respectively. The statistical analyses performed for each experiment are indicated in the respective figure legends. We considered a *P* value lower than 0.05 to be significant (*, *P* < 0.05; **, *P* < 0.01; ***, *P* < 0.001; ****, *P* < 0.0001).

Data availability

Single-cell RNA-seq and bulk RNA-seq data have been deposited at the Gene Expression Omnibus and are publicly available under accession GSE194021. A complete list of the data generated and used in this paper can be found in **Supplementary table 2.2**.

Code availability

All original codes have been deposited at GitHub and are available at: https://github.com/BlanQwall/Lung_IM_differentiation.

Results

Lung interstitial macrophages express high levels of *Tmem119* and *Cx3cr1*

We uploaded microarray data from the ImmGen database¹³² and published datasets¹⁸⁶ into the Gene Expression Commons platform³²⁸ and found that IMs, as well as microglia, had high expression of the genes encoding the fractalkine receptor (*Cx3cr1*) and the transmembrane protein 119 (*Tmem119*; **Figure 2.1A** and **2.1B**). Flow cytometry of myeloid cells isolated from the lungs of *Cx3cr1*^{GFP/+} mice indicated that lung CD45⁺SSC^{lo}CD11b⁺F4/80⁺CD64⁺ IMs (called IMs hereafter) expressed high levels of GFP (**Figure 2.1C–E** and **Supplementary figure 2.1A**). Next, we used CRISPR/Cas9-mediated engineering to generate C57BL/6 mice expressing Cre recombinase under the control of endogenous *Tmem119* (hereafter *Tmem119*^{Cre} mice). Quantification of intracellular expression of Cre protein by flow cytometry indicated elevated *Cre* expression in the CD206⁻ IM and CD206⁺ IM subsets, but no detectable Cre in other lung myeloid cells (**Figure 2.1F** and **2.1G**), BM progenitors, blood leukocytes and RTMs in the peritoneum, liver, spleen and gut, with the exception of microglia (**Supplementary figure 2.1B–I** and **Supplementary figure 2.2**) in *Tmem119*^{Cre} mice. We crossed *Tmem119*^{Cre} mice with the *Rosa26*^{LSL-EYFP} reporter strain³¹⁰, resulting in *Tmem119*^{Cre}*Rosa26*^{LSL-EYFP} mice in which persistent enhanced YFP protein expression is induced in *Tmem119*-expressing cells and their progeny. Less than 25% of multipotent, myeloid lineage-committed and common lymphoid progenitors in the BM of *Tmem119*^{Cre}*Rosa26*^{LSL-EYFP} mice were YFP⁺ (**Supplementary figure 2.3A–C**). B cells, T cells, neutrophils and eosinophils in the blood exhibited almost no YFP labeling, while 10–30% of cMo and Ly6C⁻ patrolling monocytes (pMo) were YFP⁺ (**Supplementary figure 2.3D** and **2.3E**).

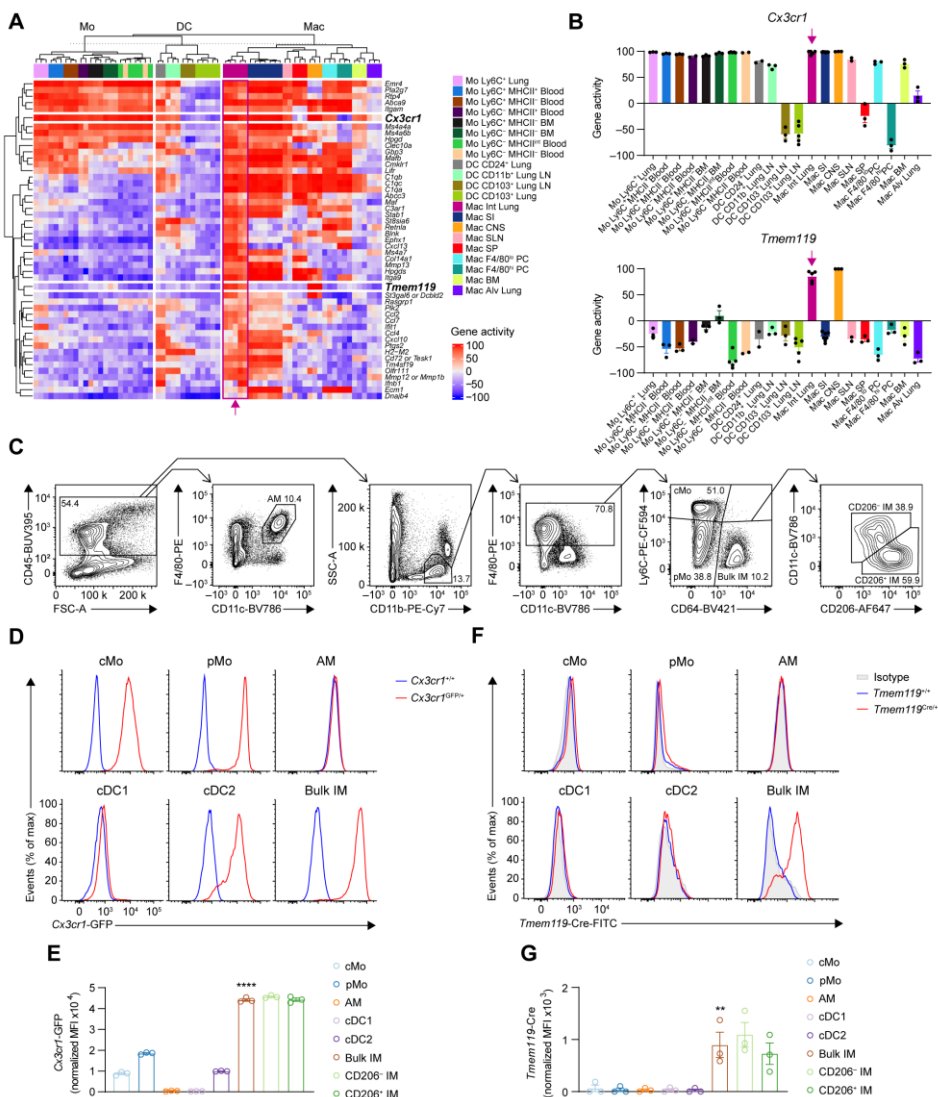


Figure 2.1. Lung interstitial macrophage subsets can be defined as *Cx3cr1*^{hi}*Tmem119*^{hi} cells. (A) Heat map showing gene activity in the indicated myeloid cell populations, inferred from microarray data uploaded on the Gene Expression Commons platform. Alv, alveolar; CNS, central nervous system; Int, interstitial; LN, lymph node; Mo, monocyte; Mac, macrophage; PC, peritoneal cavity; SI, small intestine; SLNs, skin-draining lymph nodes; SP, spleen. (B) Gene activities of *Cx3cr1* and *Tmem119* in the indicated myeloid cell populations, as in A. The arrow indicates lung IMs. (C) Representative flow cytometry gating strategy showing CD45⁺F4/80⁺CD11c⁺ AMs, AM-excluded CD45⁺SSC^{lo}CD11b⁺F4/80⁺Ly6C⁺CD64⁻ cMo, AM-excluded CD45⁺SSC^{lo}CD11b⁺

F4/80⁺Ly6C⁻CD64⁻ pMo, AM-excluded CD45⁺SSC^{lo}CD11b⁺F4/80⁺CD64⁺ bulk IMs further divided into CD206⁺ IMs and CD206⁻ IMs in lungs of wild-type mice at steady state. (D and E) Representative flow cytometry histograms (D) and normalized MFI (E) of GFP expression in lung cMo, pMo, AMs and IMs, as in C, and in CD45⁺CD11c⁺MHC-II⁺CD26⁺CD64⁻CD172a⁻XCR1⁺ type 1 conventional DCs (cDC1) and CD45⁺CD11c⁺MHC-II⁺CD26⁺CD64⁻CD172a⁺MAR1⁻ (cDC2) from *Cx3cr1*^{GFP/+} and *Cx3cr1*^{+/+} mice. (F and G) Representative histograms (F) and normalized MFI (G) of intracellular Cre protein in lung myeloid cells, as in D and E, from *Tmem119*^{Cre/+} and *Tmem119*^{+/+} mice. Data show the mean \pm s.e.m. and individual values (B, E and G: n = 3 replicates, 3 mice and 3 mice, respectively). *P* values were calculated using a one-way analysis of variance (ANOVA) with Tukey's post hoc test and compared bulk IMs with cMo, pMo, AMs, cDC1 and cDC2 (E and G). ***P* < 0.01; *****P* < 0.0001. MFI, mean fluorescence intensity.

While lung CD45⁻ structural cells exhibited very low YFP expression, ~50% of lung cMo, pMo, alveolar macrophages (AMs) and dendritic cells (DCs) were YFP⁺ (**Supplementary figure 2.3F** and **2.3G**). IMs had the highest YFP labeling (92%) among all lung myeloid cell populations tested (**Supplementary figure 2.3F** and **2.3G**). RTMs in other tissues exhibited variable expression of YFP, with microglia (89%) and small (80%) and large (84%) peritoneal macrophages displaying a similar pattern as lung IMs (**Supplementary figure 2.3H** and **2.3I**). Combined with the Cre staining, these results indicated that IMs actively expressed Cre, while YFP labeling observed in lung monocytes, DCs and other RTMs, except microglia, reflected a history of transient *Tmem119* expression in progenitor cells.

Classical monocytes give rise to interstitial macrophage subsets upon niche depletion

Like for most RTM populations, monocyte engraftment and differentiation into IMs are rare events at steady state^{104,186}. Hence, to investigate the dynamics of IM development *in vivo*, we sought to accelerate this process by creating a vacant niche that would presumably be rapidly refilled, as shown for other RTMs^{44,298}. To this end, we generated a transgenic model of DT-induced lung IM depletion

by crossing *Tmem119^{Cre}* and *Cx3cr1^{LSL-DTR}* mice³¹¹. In *Tmem119^{Cre}Cx3cr1^{LSL-DTR}* mice, referred to as IM^{DTR} mice hereafter, cells that express both *Cx3cr1* and *Tmem119* should express the diphtheria toxin receptor (DTR) and be sensitive to DT-induced death. Intraperitoneal (i.p.) injection of IM^{DTR} mice with 50 ng DT led to the efficient depletion of both CD206⁺ IM and CD206⁻ IM subsets 24 h after injection compared with untreated IM^{DTR} mice, while lung AMs, cMo and DC subsets were not affected (**Figure 2.2A–E**). Injections (i.p.) with DT in doses ranging from 0.1 to 500 ng showed a dose-dependent depletion of IMs in IM^{DTR} mice 24 h after injection, but also a partial depletion of lung cMo and pMo at the highest dose (**Figure 2.2D**). Of note, 50 ng DT i.p. did not trigger the recruitment of lung eosinophils or neutrophils at 24 h after injection (**Figure 2.2F**), indicating that the DT-mediated death of IMs did not trigger overt inflammation. We found no significant effect of 50 ng DT on the numbers of BM progenitors, blood monocytes, microglia and RTMs in the peritoneum, spleen and gut, except for an increase in numbers of Kupffer cells in the liver 24 h after injection in IM^{DTR} mice compared to untreated counterparts (**Figure 2.2G and 2.2H**). Of note, 500 ng DT triggered a significant depletion of microglia 72 h after DT in IM^{DTR} mice as compared to controls (**Supplementary figure 2.3J**). As such, both IM subsets were specifically depleted by 50 ng DT i.p. in IM^{DTR} mice.

To assess whether the empty IM niche was repopulated by newly differentiated IMs, we performed flow cytometry time-course studies of lung myeloid cells after DT treatment in IM^{DTR} and control littermates. IM depletion occurred as early as 12 h after DT (**Figure 2.3A and 2.3B**). IM numbers were still low in IM^{DTR} mice at day 2 and day 3 after DT compared to controls and this was associated with a significant increase in the numbers of lung cMo (**Figure 2.3A and 2.3B**). From day 3 onwards, the numbers of IMs increased gradually to reach levels similar to the ones in control littermates at day 7 after DT (**Figure 2.3A and 2.3B**).

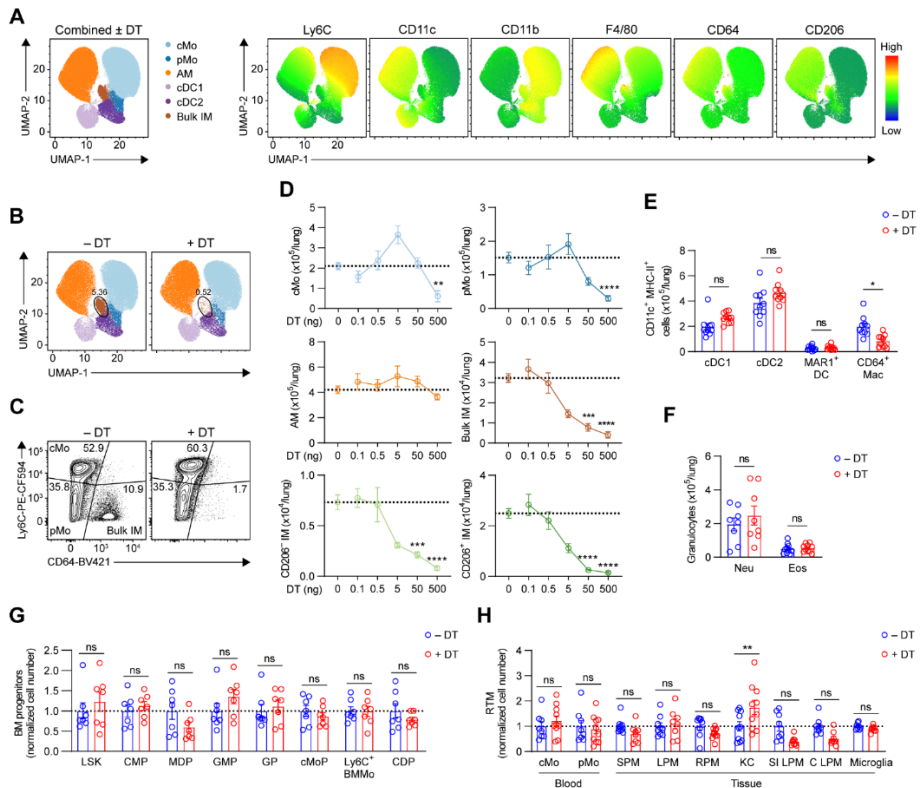


Figure 2.2. Efficiency and specificity of diphtheria toxin-induced interstitial macrophage depletion in IM^{DTR} mice. (A) Representative merged UMAP plots of lung single live CD45⁺CD11b⁺ or CD11c⁺ mononuclear cells analyzed by flow cytometry 24 h after 50 ng DT i.p. injection or no treatment in IM^{DTR} mice (merged data from four mice per group). Cell clusters (left) and heat map plots depicting the expression of Ly6C, CD11c, CD11b, F4/80, CD64 and CD206 (right). (B) Representative UMAP plot, as in a, showing cells from either untreated IM^{DTR} mice or DT-treated IM^{DTR} mice. (C) Representative contour plot of Ly6C and CD64 expression within lung single live AM-excluded CD45⁺SSC^{lo}CD11b⁺F4/80⁺ cells from untreated and DT-treated IM^{DTR} mice, as in A. (D) Absolute numbers of the indicated lung myeloid cell populations quantified by flow cytometry in IM^{DTR} mice, at 24 h after i.p. injection with DT in doses ranging from 0.1 to 500 ng. Horizontal dotted lines represent the average number of cells in untreated IM^{DTR} mice. (E and F) Absolute numbers of lung CD45⁺CD11c⁺MHC-II⁺CD26⁺CD64⁻CD172a⁻XCR1⁺ cDC1, CD45⁺CD11c⁺MHC-II⁺CD26⁺CD64⁻CD172a⁺MAR1⁻ cDC2, CD45⁺CD11c⁺MHC-II⁺CD26⁺CD64⁻CD172a⁺MAR1⁺ DCs (MAR1⁺ DC) and CD45⁺CD11c⁺MHC-II⁺CD26⁻CD64⁺CD172a⁺ macrophages (CD64⁺ Mac) (E) and lung CD45⁺CD11b⁺Ly6G⁺ neutrophils (Neu) and CD45⁺CD11b⁺SiglecF⁺ eosinophils (Eos) (F) quantified by flow cytometry 24 h after 50 ng DT i.p. injection or no treatment in IM^{DTR}

mice. (G and H) Numbers of BM Lin⁻Ly6A/E⁺CD117⁺ LSK, Lin⁻CD16/32⁻CD117⁺CD135⁺CD34⁺CD115⁻ common myeloid progenitors (CMP), Lin⁻CD16/32⁻CD117⁺CD135⁺CD34⁺CD115⁺ monocyte-DC progenitors (MDP), Lin⁻CD16/32⁺CD117⁺CD135⁻CD34⁺CD115⁻Ly6C⁻ granulocyte-monocyte progenitors (GMP), Lin⁻CD16/32⁺CD117⁺CD135⁻CD34⁺CD115⁻Ly6C⁺ granulocyte progenitors (GP), Lin⁻CD16/32⁺CD117⁺CD135⁻CD34⁺CD115⁺Ly6C⁺ monocyte progenitors (cMoP), Lin⁻CD16/32⁺CD117⁻CD115⁺Ly6C⁺ monocytes (Ly6C⁺ BMMo), Lin⁻CD16/32⁻CD117⁻CD135⁺CD115⁺CD34⁻Ly6C⁻ common DC progenitors (CDP) (G), blood CD45⁺CD3⁻CD19⁻Ly6G⁻SiglecF⁻CD115⁺ Ly6C⁺ cMo or Ly6C⁻ pMo, CD45⁺Ly6G⁻SiglecF⁻Ly6C⁻CD115⁺CD11b⁺ F4/80^{hi} large (LPM) or F4/80^{lo} small peritoneal macrophages (SPM), liver CD45⁺CD31⁻F4/80⁺CD11b^{int}CD64⁺ Kupffer cells (KC), spleen Lin⁻F4/80⁺CD11b⁻ red pulp macrophages (RPM), small intestinal (SI) and colon (C) CD45⁺Ly6C⁻CD11b⁺F4/80⁺CD64⁺ lamina propria macrophages (LPM) and FSC^{lo}CD45^{int}F4/80⁺CD11b⁺CD64⁺Ly6C⁻ microglia (H), as in E. Data show the mean \pm s.e.m. and are pooled from 2–4 independent experiments (D–H: n = 6–15, 10, 8–10, 7, 8–10 mice per group, respectively). *P* values were calculated using a two-way ANOVA with Tukey's post hoc test. **P* < 0.05; ***P* < 0.01; ****P* < 0.001; *****P* < 0.0001; ns, not significant.

The influx of cMo into the lungs of DT-treated IM^{DTR} mice at day 2 after DT was preceded by a significant increase in the amount of the monocyte chemoattractant Ccl2 in the lung and serum 12 and 24 h after DT in IM^{DTR} mice compared to controls (**Figure 2.3C**), suggesting that cMo were attracted to the lung in a Ccr2-dependent manner.

To investigate whether cMo contributed to IM replenishment, we performed three sets of experiments. First, we generated chimeric mice in which lethally irradiated, thorax-protected CD45.2 IM^{DTR} mice were reconstituted with CD45.1 wild-type BM cells. At week 4 after transfer, the donor chimerism of blood cMo was 87%, while the donor chimerism of AMs and IMs was very low (**Figure 2.3D** and **2.3E**), indicating efficient BM donor reconstitution and thorax protection, respectively. When the chimeric IM^{DTR} mice were injected or not with DT at week 4 after transfer, the donor chimerism of IMs was significantly increased in the DT-treated chimeric IM^{DTR} mice (92%) compared to untreated counterparts at

day 7 after DT, and reached levels similar to those observed in blood cMo (**Figure 2.3D** and **2.3E**), consistent with a major contribution of BM cells to the replenishment of the IM niche. Second, we generated BM competitive chimeras in thorax-protected CD45.1/CD45.2 IM^{DTR} mice engrafted with a 1:1 mix of CD45.1 *Ccr2*^{+/+} and CD45.2 *Ccr2*^{-/-} BM cells. At week 4 after reconstitution, only a few blood cMo were of donor *Ccr2*^{-/-} origin, as expected³²⁹ (**Figure 2.3F** and **2.3G**). When such competitive chimeras were injected or not with DT at week 4 after transfer, the majority of IMs (70%) were of donor *Ccr2*^{+/+} origin at day 7 after DT, comparable to the blood cMo (59%; **Figure 2.3F** and **2.3G**), indicating their dependency on *Ccr2*. Previous single-cell RNA-sequencing (scRNA-seq) analyses of lung CD64⁺ cells indicated, based on trajectory RNA velocity analyses, that *Nr4a1*-dependent CD16.2⁺ monocytes might represent precursors of CD206⁻ IMs¹⁰⁴. BM competitive chimeras in thorax-protected CD45.1/CD45.2 IM^{DTR} mice engrafted with a 1:1 mix of CD45.1 *Nr4a1*^{+/+} and CD45.2 *Nr4a1*^{-/-} BM cells showed that donor *Nr4a1*^{-/-} chimerism of IMs (43%) was similar to donor *Nr4a1*^{+/+} chimerism of IMs (44%) at day 7 after DT (**Supplementary figure 2.4A**), indicating that IM replenishment was independent of *Nr4a1* (ref.¹⁰⁴) and suggesting that CD16.2⁺ monocytes contributed minimally to IM repopulation as compared to *Ccr2*-dependent cMo. Third, we transferred CD45.1 wild-type BM Ly6C⁺ cMo intravenously (i.v.) into CD45.1/CD45.2 IM^{DTR} mice 1 d after DT. CD45.1⁺CD45.2⁻ cMo were mainly detected as Ly6C⁺CD64⁻ cells at day 2 after DT in the lung, while some CD45.1⁺CD45.2⁻ cells were detected as Ly6C⁻CD64⁺ cells at day 14 after DT in the lung (**Figure 2.3H**), indicating that Ly6C⁺ cMo could differentiate into IM.

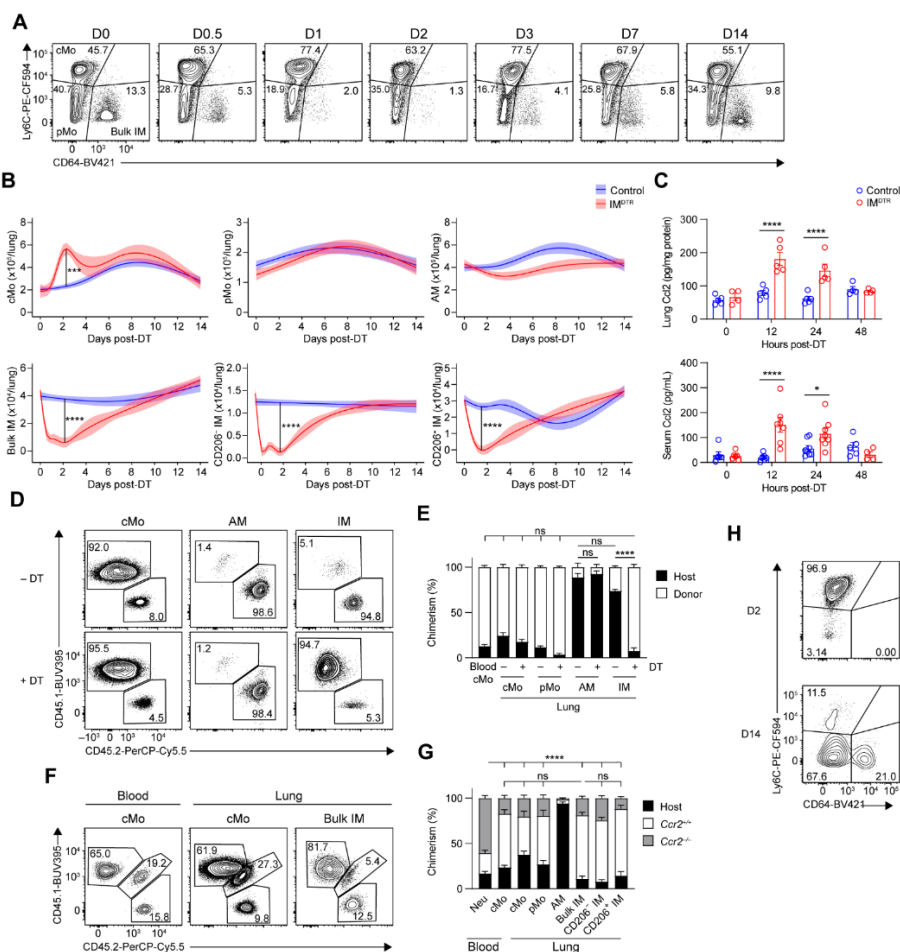


Figure 2.3. A vacant interstitial macrophage niche is repopulated by Ccr2-dependent classical monocyte differentiating into interstitial macrophages. (A) Representative plots of Ly6C and CD64 expression within lung AM-excluded CD45⁺F4/80⁺SSC^{lo}CD11b⁺ cells at days 0, 0.5, 1, 2, 3, 7 and 14 after 50 ng DT i.p. in IM^{DTR} mice. (B) Time course of absolute numbers of cMo, pMo, AMs, bulk IMs, CD206⁻ IMs and CD206⁺ IMs quantified by flow cytometry in IM^{DTR} and littermate controls, as in A. Data show the mean (centerline) ± s.e.m. (colored area) and are pooled from ≥2 independent experiments (n = 8–10 mice per time point). (C) Amount of Ccl2 in the lung and serum of IM^{DTR} and littermate controls at 0, 12, 24 and 48 h after DT i.p. injection. (D and E) Representative CD45.1 and CD45.2 contour plots (D) and bar graphs showing the percentage of CD45.1 donor and CD45.2 host chimerism (E) in the indicated cell populations from lethally irradiated thorax-protected CD45.2 IM^{DTR} mice reconstituted with CD45.1 wild-type BM donor cells, injected or not with 50 ng DT i.p. 4 weeks later and evaluated at day 7 after

DT. (F and G) Representative CD45.1 and CD45.2 contour plots (F) and bar graphs showing the percentage of *Ccr2*^{+/+} donor, *Ccr2*^{-/-} donor and host chimerism (G) in the indicated cell populations from lethally irradiated, thorax-protected CD45.1/CD45.2 IM^{DTR} mice transplanted with a 1:1 mix of CD45.2 *Ccr2*^{-/-} and CD45.1 *Ccr2*^{+/+} BM cells, injected with 50 ng DT i.p. 4 weeks later and evaluated at day 7 after DT. (H) Representative contour plot of Ly6C and CD64 expression within lung single live AM-excluded CD45⁺F4/80⁺SSC^{lo}CD11b⁺ cells in CD45.1/CD45.2 IM^{DTR} mice treated with 50 ng DT i.p., transferred with CD45.1 BM wild-type cMo i.v. 24 h after DT and evaluated at days 2 and 14 after DT. Plots are representative of 5 mice, each of them giving similar results. Data show the mean \pm s.e.m. and are pooled from two independent experiments (C, E and G: n = 4–8, 4–8 and 6 mice per group, respectively). *P* values were calculated by likelihood ratio tests (B), two-way ANOVA with Tukey's post hoc tests (C and E) or one-way ANOVA with Sidak's post hoc tests (G). **P* < 0.05; ***P* < 0.01; ****P* < 0.001; *****P* < 0.0001.

Finally, we analyzed lung cMo, AMs, CD206⁺ IMs and CD206⁻ IMs from untreated IM^{DTR} mice and repopulated lung CD206⁺ IMs and CD206⁻ IMs from DT-treated IM^{DTR} mice at day 14 after DT by bulk RNA-seq. Repopulated CD206⁺ IM and CD206⁻ IM subsets were largely similar to native IMs, with only 30 and 28 differentially expressed genes (DEGs) between native and repopulated CD206⁺ IMs and CD206⁻ IMs, respectively (log₂ fold change \pm 1, adjusted *P* value < 0.05; **Supplementary figure 2.4B** and **2.4C**). Although *Tmem119* mRNA expression was lower in repopulated CD206⁺ IM and CD206⁻ IM subsets as compared to native CD206⁺ IM and CD206⁻ IM subsets, respectively (**Supplementary figure 2.4C**), they could still be efficiently re-depleted by DT at day 14 after first DT treatment (**Supplementary figure 2.4D**). Thus, similar to the steady-state situation^{103,104,186}, *Ccr2*-dependent cMo could give rise to differentiated CD206⁺ IM and CD206⁻ IM subsets in DT-treated IM^{DTR} mice.

scRNA-seq captures interstitial macrophage development from classical monocytes

Lung monocytes and IMs were sorted from five IM^{DTR} mice at 0, 12, 24, 48 and 96 h after DT and were subjected to single-cell droplet encapsulation with the 10x Genomics platform³³⁰, scRNA-seq and quality-control filtering. A total of 15,941 myeloid cells were analyzed and projected to global and time-specific uniform manifold approximation and projection (UMAP) plots (**Figure 2.4A** and **2.4B**), which led to the identification of seven distinct cell clusters (**Figure 2.4A–C**). Based on differential expression analysis, we identified clusters corresponding to cMo (*Ccr2*, *Ly6c2*; cluster (C) 1), pMo (*Ace*, *Nr4a1*; C2), CD206⁻ IM (*H2-Ab1*, *Cd74*; C3) and CD206⁺ IM (*Lyve1*, *Mrc1*; C4; **Figure 2.4D** and **2.4E**). C3 not only encompassed CD206⁻ IM but also contained nonclassical CD16.2⁺ monocytes (*Fcgr4*, *Ace*)¹⁰⁴ (**Supplementary figure 2.5**). C5 upregulated apoptosis-related genes (*Bax*, *Trp53*, *Tnf*), was almost uniquely present 12 h after DT and disappeared afterwards (**Figure 2.4B–E**), likely representing DT-targeted native IM undergoing cell death, while C7 encompassed few contaminating DCs (*Zbtb46*, *Ccr7*; **Figure 2.4D** and **2.4E**). C6 encompassed cells expressing *Ccr2* and *Ly6c2* that were rare at steady state but enriched between 24 and 96 h after DT and made a transient bridge between cMo and a branching point leading to CD206⁺ IM and CD206⁻ IM subsets (**Figure 2.4B–E**), which we named transitioning monocytes (Tr-Mo). RNA velocity analysis indicated that Tr-Mo moved from cMo toward IM subsets (**Figure 2.4F**). These experiments thus captured the full pattern of monocyte-to-IM trajectory at the single-cell transcriptomic level.

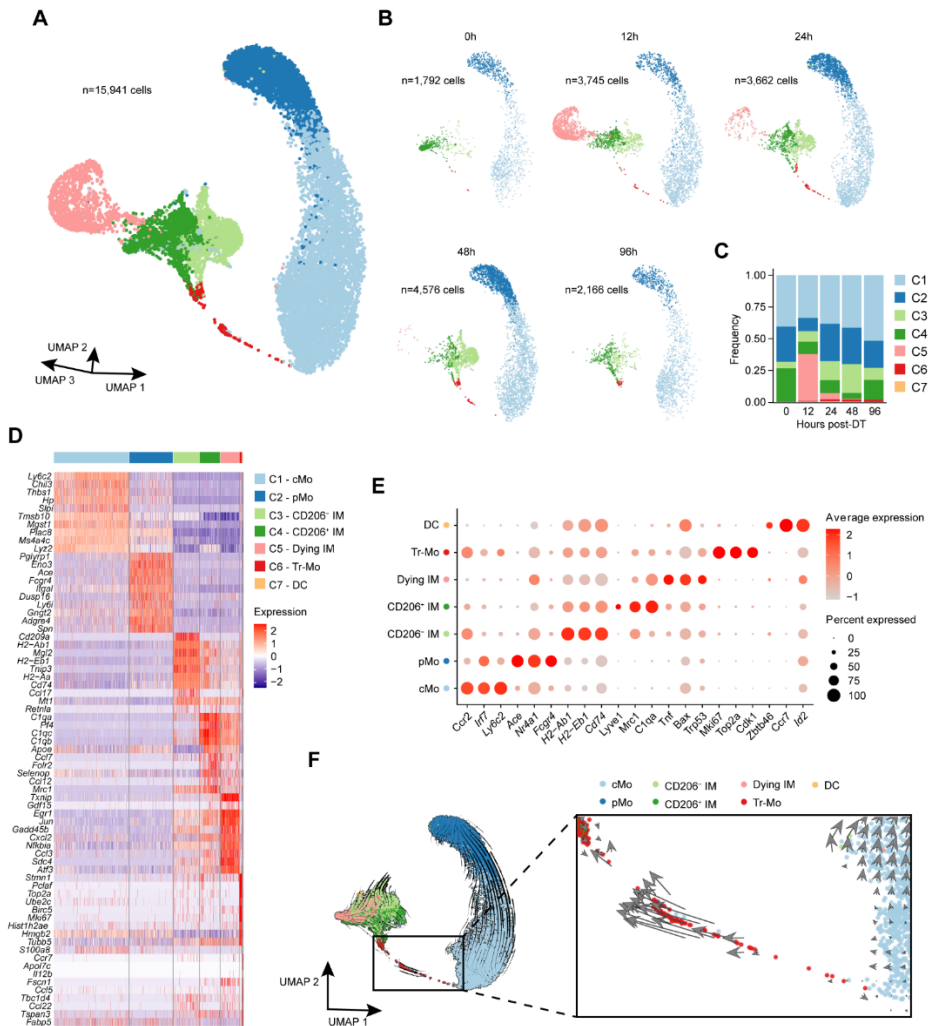


Figure 2.4. Time-course scRNA-seq analyses of interstitial macrophage niche refilling reveal discrete transitioning cells. (A) Three-dimensional UMAP plot depicting the transcriptional identity of sorted lung CD45⁺SSC^{lo}CD11b⁺F4/80⁺CD64⁻ monocytes and CD45⁺SSC^{lo}CD11b⁺F4/80⁺CD64⁺ IMs merged from IM^{DTR} mice injected with DT i.p. at 0, 12, 24, 48 and 96 h before the analysis (n = 5 pooled mice per time point). (B) UMAP plots from the five separate time points after DT, as in a. Inset indicates the number of cells analyzed (A and B). (C) Histogram showing the frequency of each cluster at each time point after DT. (D) Heat map depicting the single-cell expression of the ten most upregulated genes within each cluster. (E) Dot plots show average expression of the indicated genes and the percentage of cells expressing the genes within each cluster. (F) Prevalent pattern of RNA velocities substantiated by arrows and visualized on the same

UMAP plot as shown in A. The square on the right shows a higher magnification of the area in the left square.

Transitioning monocytes transiently express cell cycling genes

Next, we applied Monocle single-cell trajectory analysis³²² to the scRNA-seq data encompassing cMo, Tr-Mo, CD206⁺ IMs and CD206⁻ IMs, and identified two main trajectories, both starting from cMo, moving across Tr-Mo until a branching point, and then bifurcating toward either CD206⁻ IMs or CD206⁺ IMs, in line with the real-time analysis (**Figure 2.5A** and **2.5B**). Genes that exhibited the same pattern of regulation along pseudotime in both CD206⁺ IM and CD206⁻ IM trajectories, as analyzed using tradeSeq³²³, encompassed three main classes of genes. First, cMo expressed genes enriched in cellular extravasation, leukocyte migration and chemotaxis (**Figure 2.5C** and **2.5D**), in line with tissue recruitment. Second, we observed a time-restricted upregulation of genes associated with cell proliferation (*Ube2c, Aurkb, Racgap1, Cdk1, Ccnb2, Mki67*; **Figure 2.5C** and **2.5D**) that peaked between 5 and 10 pseudotime units and corresponded to Tr-Mo, as attested by their elevated S and G2/M cell cycle score (**Figure 2.5E**), indicative of DNA replication and mitosis, respectively. Such a state was then followed by increased expression of genes enriched in cell adhesion (**Figure 2.5C** and **2.5D**), supporting the idea of cell engraftment into their niche^{103,104}. By mapping cMo signature, S and G2/M phases, as well as IM signature scores along pseudotime, we could sequentially observe the downregulation of cMo signature accompanied by an upregulation of cell division-related genes, which then decreased concomitantly to the acquisition of an IM signature that became predominant at the end of the trajectory (**Figure 2.5F**). These data suggested that cMo, once in a vacant niche, became Tr-Mo that could re-enter the cell cycle and expand before differentiating into CD206⁺ IM or CD206⁻ IM subsets.

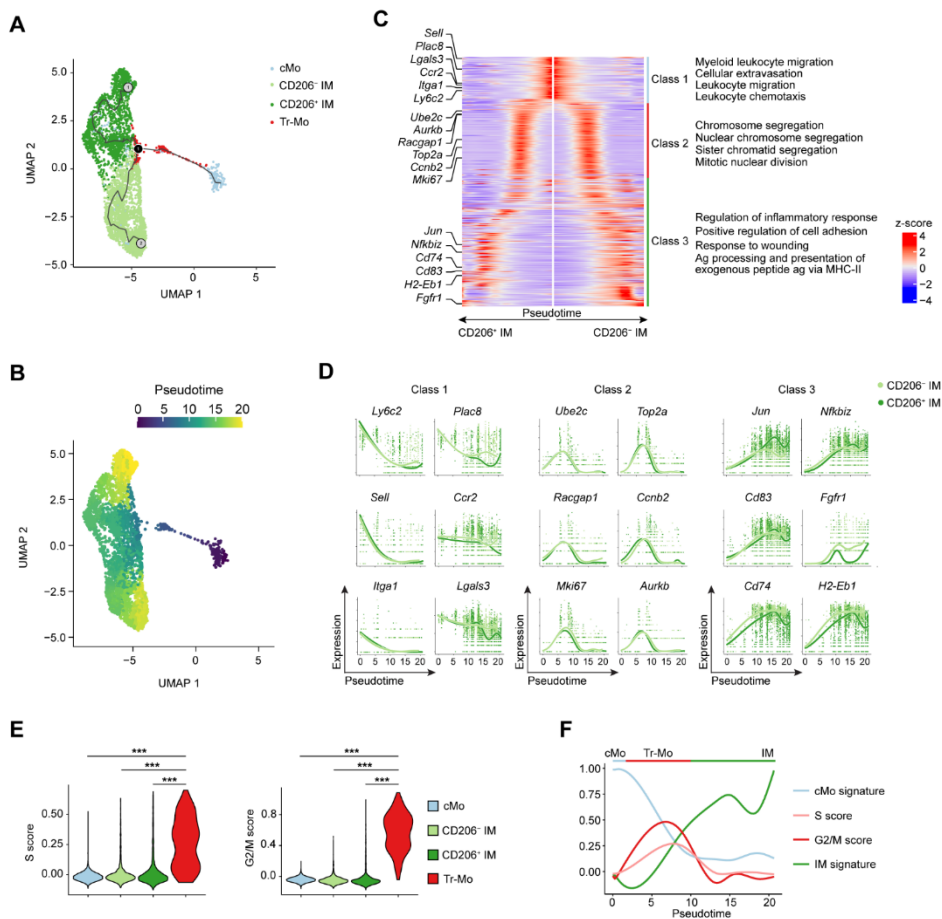


Figure 2.5. Trajectory analyses of interstitial macrophage development identify transient proliferating monocytes. (A) Two-dimensional UMAP plot depicting the transcriptional identity and cell trajectories of lung cMo, Tr-Mo, CD206⁻IMs and CD206⁺IMs, as in **Figure 2.4A**, evaluated by Monocle analysis. (B) Two-dimensional UMAP plot depicting the pseudotime trajectory values of lung cMo, Tr-Mo, CD206⁻IMs and CD206⁺IMs, as in A. (C) Heat map plot depicting the DEGs along pseudotime evaluated by tradeSeq in the common trajectory starting from cMo (middle) and ending in CD206⁻IM and CD206⁺IM subsets. DEGs are divided into three classes, and examples of genes and the main biological responses enriched in each class are represented on the left and right, respectively. (D) Gene expression of the indicated genes along pseudotime evaluated by tradeSeq in both trajectories leading either to CD206⁻IM or CD206⁺IM subsets. (E) S and G2/M cell cycle scores of single cells within cMo, Tr-Mo, CD206⁻IMs and CD206⁺IMs, as depicted by violin plots (height: score; width: abundance of cells).

(F) cMo and IM signatures, and S and G2/M scores depicted along pseudotime, as in B. *P* values were calculated by one-way ANOVA with Tukey's post hoc tests (E). ****P* < 0.001.

Transitioning monocytes proliferate locally in a *Csf1r*-dependent way

Next, we aimed to detect the Tr-Mo in vivo during the time of IM niche refilling. IM^{DTR} mice i.p. injected or not with DT were i.p. injected with 5-ethynyl-2'-deoxyuridine (EdU) 4 h before the analysis, at day 2 after DT, a time point when the IM niche was depleted and Tr-Mo were detected by scRNA-seq. Mice were treated with CD45 antibodies i.v. 10 min before killing to discriminate blood from tissue cells by flow cytometry. Under these experimental conditions, virtually no EdU⁺ cells were detected in the intravascular and extravascular cMo (**Figure 2.6A–C**), indicating that the EdU signal did not reflect a history of proliferation in the BM. Notably, we detected a significant increase in the percentage of EdU⁺ cells in the lung extravascular CD45⁺SSC^{lo}CD11b⁺F4/80⁺CD64^{int/hi} cells (CD64⁺ cells hereafter; **Figure 2.6A**), at day 2 after DT in IM^{DTR} mice as compared to non-treated IM^{DTR} mice (**Figure 2.6C** and **2.6D**). Moreover, staining with 4',6-diamidino-2-phenylindole (DAPI) showed an increase in the percentage of CD64⁺ cells in the S phase at day 2 after DT in IM^{DTR} mice as compared to non-treated IM^{DTR} mice (**Figure 2.6E** and **2.6F**).

Because RTMs can self-renew through proliferation, we tested whether the EdU⁺CD64⁺ cells corresponded to Tr-Mo or to differentiated IMs that were not depleted by DT treatment and underwent local proliferation. The expression of IM-associated markers such as MerTK, class II major histocompatibility complex (MHC-II), CD206 and C1qa¹⁰⁴ on EdU⁺CD64⁺ cells was intermediate between that detected in cMo, which was significantly lower, and that detected in EdU⁻CD64⁺ cells, which was significantly higher than on EdU⁺CD64⁺ cells (**Figure 2.6G** and **Supplementary figure 2.6A**), suggesting that EdU⁺CD64⁺ cells corresponded to

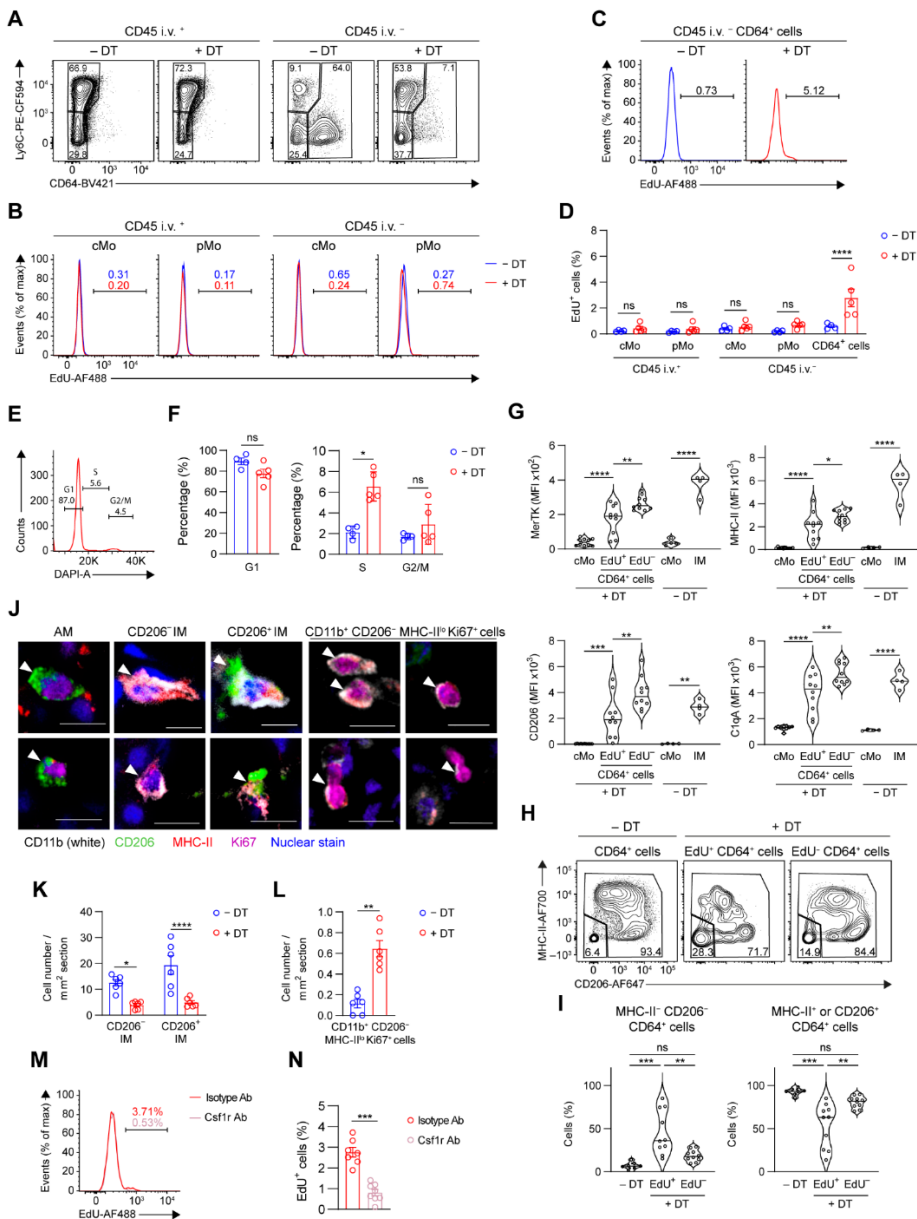


Figure 2.6. Transitioning monocytes can proliferate via Csf1r-dependent mechanisms. (A) Representative plots of Ly6C and CD64 expression within lung CD45 i.v.⁺ and CD45 i.v.⁻ AM-excluded CD45⁺F4/80⁺SSC^{lo}CD11b⁺ cells from EdU-pulsed IM^{DTR} mice treated or not with 50 ng DT i.p. 2 d before. (B) Representative histograms of EdU levels in lung cMo and pMo, as in A. (C) Representative histograms of EdU levels in lung CD64⁺ cells, as in A. (D) Bar graphs showing the percentage of EdU⁺ cells in lung cMo and pMo, and

in lung CD64⁺ cells, as in A. (E) Representative histograms of DAPI signal in lung CD64⁺ cells, as in A. (F) Bar graph showing the percentage of lung extravascular CD64⁺ cells in G1, S and G2/M phases, as in E. (G) Expression of the indicated markers in lung cMo, EdU⁺CD64⁺ cells and EdU⁻CD64⁺ cells from EdU-pulsed IM^{DTR} mice at day 2 after DT and in lung cMo and IMs from untreated IM^{DTR} mice, as depicted by violin plots (height: MFI; width: abundance of cells). (H) Representative plots of MHC-II and CD206 expression within lung CD64⁺ cells from untreated IM^{DTR} mice and EdU⁻/EdU⁺CD64⁺ cells from DT-treated EdU-pulsed IM^{DTR} mice, as in G. (I) Percentage of MHC-II⁻CD206⁻ cells and MHC-II⁺ or CD206⁺ cells within lung CD64⁺ cells from untreated IM^{DTR} mice and EdU⁻/EdU⁺CD64⁺ cells from DT-treated EdU-pulsed IM^{DTR} mice, as in H, as depicted by violin plots (height: percentage; width: abundance of cells). (J) Representative images of AMs, CD206⁻ IMs, CD206⁺ IMs and CD11b⁺CD206⁻MHC-II^{lo}Ki67^{hi} cells, identified by confocal microscopy on lung sections from untreated and DT-treated IM^{DTR} mice, at day 2 after DT. (K and L) Number of CD206⁻ IMs and CD206⁺ IMs (K) and CD11b⁺CD206⁻MHC-II^{lo}Ki67^{hi} cells (L) per mm², as in J. (M) Representative histograms of EdU levels in lung CD64⁺ cells from DT-treated IM^{DTR} mice, as in A, and treated i.v. with Csf1r antibodies (Ab) or isotype control 6 and 28 h after DT. (N) Bar graph showing the percentage of EdU⁺ cells in lung CD64⁺ cells, as in M. Data show the mean \pm s.e.m. and are pooled from two independent experiments (D, F, G, I, K, L and N: n = 4–5, 4–5, 4–10, 7–10, 6, 6 and 7–8 mice per group, respectively). *P* values were calculated using a two-way ANOVA with Sidak's post hoc tests (B and K), a two-tailed Mann–Whitney test (E, L and N) or one-way ANOVA with Tukey's post hoc tests (G and I). **P* < 0.05; ***P* < 0.01; ****P* < 0.001; *****P* < 0.0001. Scale bar, 10 μ m.

the Tr-Mo transcriptional subset. While CD64⁺ cells from DT-untreated IM^{DTR} mice contained more than 90% of IMs (either as MHC-II^{hi}CD206^{int/lo} IM or MHC-II^{lo}CD206⁺ IM subsets^{103,104}), the EdU⁺CD64⁺ cells from IM^{DTR} mice at day 2 after DT were significantly enriched in MHC-II⁻CD206⁻ monocytes (**Figure 2.6H** and **2.6I**). Conversely, like in DT-untreated IM^{DTR} mice, EdU⁻CD64⁺ cells from IM^{DTR} mice at day 2 after DT were mainly composed of MHC-II^{hi}CD206^{int/lo} IM or MHC-II^{lo}CD206⁺ IM subsets (**Figure 2.6H** and **2.6I**).

Next, we generated chimeric mice in which lethally irradiated, thorax-protected CD45.2 IM^{DTR} mice were reconstituted with CD45.1 wild-type BM donor cells. At day 2 after DT and 4 h after EdU i.p. injections, EdU⁺CD64⁺ cells were almost uniquely detected among donor cells, and not among host cells

(**Supplementary figure 2.6B**). Confocal microscopy of lung sections from IM^{DTR} mice at day 2 after DT indicated efficient depletion of CD206⁺ IMs and CD206⁻ IMs and a significant increase in CD11b⁺CD206⁻MHC-II^{lo}Ki67^{hi} monocytic proliferating cells compared to untreated IM^{DTR} mice (**Figure 2.6J–L** and **Supplementary figure 2.6C**). Altogether, these data suggested that EdU⁺CD64⁺ cells represented BM-derived monocytes that proliferated locally and were in transition between cMo and differentiated IMs.

Csf1 receptor (Csf1r) signaling has an important role in the regulation of cell proliferation in the mononuclear phagocyte system^{264,297,298,331,332}. To assess the contribution of Csf1r to the proliferation of EdU⁺CD64⁺ cells in our model, IM^{DTR} mice were injected with DT i.p. and treated i.v. with 250 µg mouse Csf1r antibodies or isotype control 6 and 28 h after DT. The percentage of EdU⁺ cells within CD64⁺ cells was significantly decreased in Csf1r antibody-treated mice as compared to isotype-treated DT-injected IM^{DTR} mice (**Figure 2.6M** and **2.6N**). We also treated DT-injected IM^{DTR} mice with the Csf1r small-molecule inhibitor pexidartinib (PLX3397) or vehicle i.p. at days 1 and 2 after DT and found that EdU incorporation was almost completely abrogated at day 3 after DT in CD64⁺ cells from PLX3397-treated mice compared to vehicle-treated counterparts (**Supplementary figure 2.6D** and **2.6E**). In conclusion, EdU⁺CD64⁺ cells proliferated in the tissue through Csf1r-dependent mechanisms before differentiating into IMs.

MafB restricts the proliferation and mediates interstitial macrophage development

To gain insights into the transcriptional control of the balance between Tr-Mo proliferation and IM differentiation, we applied the single-cell regulatory network inference and clustering (SCENIC) algorithm³²¹ to our scRNA-seq data to

map gene regulatory networks and predict transcription factor activities at the single-cell level. MafB was one of the high activity score transcription factors in CD206⁺ IMs (**Figure 2.7A**). MafB restricts Csf1-dependent proliferation of myeloid progenitor cells *in vivo*³³³, as well as the self-renewal ability of macrophages^{243,246}. TradeSeq trajectories showed that the transient upregulation of the cycling gene Mki67 was followed by an increase in the expression of *Mafb* between 10 and 15 pseudotime units in both CD206⁻ and CD206⁺ IM trajectories (**Figure 2.7B**), suggesting that MafB activation might restrict Tr-Mo proliferation and facilitate IM development from Tr-Mo. MafB intracellular staining of lung myeloid cells from wild-type C57BL/6 mice indicated an elevated expression of MafB in lung IMs, especially in CD206⁺ IMs, as compared to lung cMo, pMo, AMs and DCs (**Figure 2.7C** and **2.7D**). We also assessed the expression of MafB in lung CD64⁺ cells in EdU-pulsed IM^{DTR} mice at day 2 after DT. MafB expression was significantly lower in EdU⁻Ki67⁺ and EdU⁺Ki67⁺ CD64⁺ cells as compared to cMo (**Figure 2.7E**), supporting that the proliferation of CD64⁺ cells required low expression of MafB.

Next, we generated C57BL/6 *Mafb*^{fl/fl} mice and crossed them with mice constitutively expressing Cre recombinase under the control of the lysozyme M promoter (*Lyz2*^{Cre}) or the Ms4a3 promoter (*Ms4a3*^{Cre}) to generate mice with myeloid-restricted *Mafb* deficiency. To assess whether MafB mediated IM development from cMo *in vivo*, we generated BM competitive chimeras in thorax-protected CD45.1/CD45.2 IM^{DTR} mice engrafted with a 1:1 BM cell mix from CD45.1 wild-type and CD45.2 *Ms4a3*^{Cre}*Mafb*^{fl/fl} mice. At day 7 after DT, evaluation of myeloid cell chimerism in the lung indicated that myeloid-restricted *Mafb* deficiency strongly impaired the ability of cMo to repopulate the niches of both IM subsets (**Figure 2.7F** and **2.7G**). MafB protein was absent in CD64⁺ cells from *Lyz2*^{Cre}*Mafb*^{fl/fl} mice (**Figure 2.7H**) and the numbers of CD64⁺

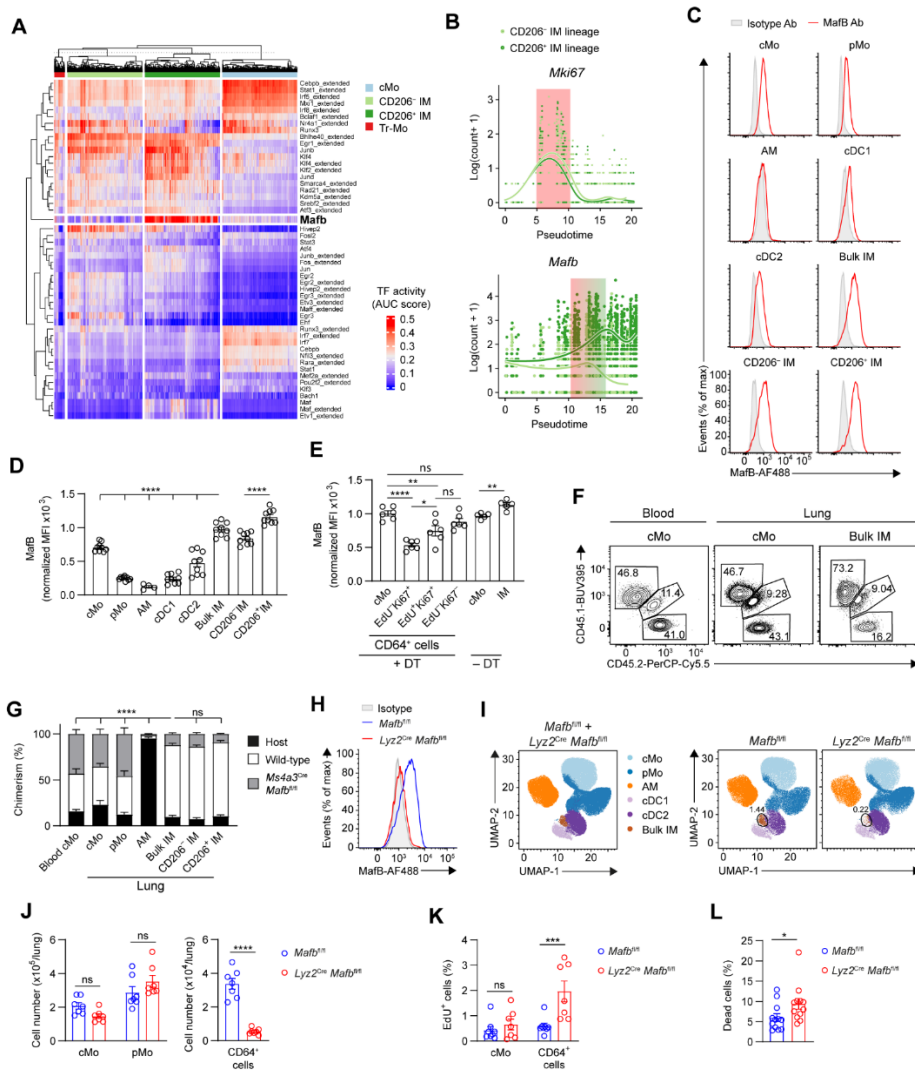


Figure 2.7. MafB restricts proliferation and mediates interstitial macrophage development. (A) Heat map depicting predicted transcription factor (TF) activities across lung myeloid cells analyzed by scRNA-seq, as in **Figure 2.4A**, as assessed by SCENIC. (B) Expression of *Mki67* and *Mafb* along pseudotime evaluated by tradeSeq in both CD206⁻ IM or CD206⁺ IM trajectories, as in **Figure 2.5D**. (C and D) Representative histograms (C) and bar graphs showing normalized MFI (D) of MafB expression in the indicated lung myeloid cell populations from wild-type mice. (E) Bar graphs showing expression of MafB in lung cMo and IMs from untreated IM^{DTR} mice, and in lung cMo, EdU⁺Ki67⁺, EdU⁺Ki67⁻ or EdU⁻Ki67⁻ CD64⁺ cells from EdU-pulsed IM^{DTR} mice at day 2 after DT. (F and G)

Representative CD45.1 and CD45.2 plots (F) and bar graphs showing the percentage of wild-type donor, *Ms4a3^{Cre}Mafb^{fl/fl}* donor and host chimerism (G) in the indicated cell populations from lethally irradiated, thorax-protected CD45.1/CD45.2 IM^{DTR} mice transplanted with a 1:1 mix of CD45.2 *Ms4a3^{Cre}Mafb^{fl/fl}* and CD45.1 wild-type BM cells, injected with 50 ng DT i.p. 4 weeks later and evaluated at day 7 after DT. (H) Efficiency of *Mafb* depletion within lung CD64⁺ cells from *Lyz2^{Cre}Mafb^{fl/fl}* mice evaluated by MafB intracellular staining. Data are representative of five mice, each of them giving similar results. (I) Representative UMAP plots of lung CD45⁺CD11b⁺ or CD11c⁺ mononuclear cells analyzed by flow cytometry in *Lyz2^{Cre}Mafb^{fl/fl}* and *Mafb^{fl/fl}* littermate controls (merged data from four mice per group). (J–L) Absolute numbers of lung cMo, pMo and CD64⁺ cells (J), bar graphs showing the percentage of EdU⁺ cells within cMo and CD64⁺ cells (K) and bar graph showing the percentage of dead cells within CD64⁺ cells (L) from *Lyz2^{Cre}Mafb^{fl/fl}* and *Mafb^{fl/fl}* mice. Data show the mean ± s.e.m. and are pooled from 2–3 independent experiments (D, E, G, J, K and M: n = 9, 5–6, 4–7, 7, 7–8 and 12 mice per group, respectively). *P* values were calculated using a one-way ANOVA with Tukey's post hoc tests (d, e and g), a two-way ANOVA with Sidak's post hoc tests (j and k) or a two-tailed Mann–Whitney test (M). In D, *P* values compare bulk IM versus every other population, or CD206⁺ IM versus CD206⁻ IM. In G, *P* values compare the percentage of donor CD45.1 wild-type chimerism. **P* < 0.05; ***P* < 0.01; ****P* < 0.001; *****P* < 0.0001. AUC, area under the curve.

cells were significantly decreased in *Lyz2^{Cre}Mafb^{fl/fl}* mice compared to *Mafb^{fl/fl}* mice, while the numbers of cMo and pMo were identical (**Figure 2.7I** and **2.7J**). Ki67 staining indicated an increased proliferative ability of the few CD64⁺ cells present in *Lyz2^{Cre}Mafb^{fl/fl}* mice compared to *Mafb^{fl/fl}* mice (**Supplementary figure 2.7**). Similarly, i.p. EdU treatment 4 h before killing indicated a significant increase in the percentage of EdU⁺ cells within CD64⁺ cells from *Lyz2^{Cre}Mafb^{fl/fl}* mice compared to littermate controls (**Figure 2.7K**). Finally, we found that the percentage of dead cells was significantly higher in CD64⁺ cells from *Lyz2^{Cre}Mafb^{fl/fl}* mice compared to littermate controls (**Figure 2.7L**), suggesting that the higher proliferative rate observed in MafB-deficient CD64⁺ cells did not lead to an increase in the number of CD64⁺ cells because of the increased cell death. Altogether, these data suggested that MafB could restrict the proliferation of lung CD64⁺ cells and mediate IM development.

MafB and c-Maf differentially control lung interstitial macrophage identity

Next, we investigated to what extent the identity of CD64⁺ cells was impacted by myeloid-restricted MafB deficiency, as well as the contribution of myeloid-restricted c-Maf to IM maintenance and identity. MafB and c-Maf are b-ZIP transcription factors that belong to the same family of large Maf proteins³³⁴ and can cooperate together in some contexts, such as in the regulation of macrophage self-renewal²⁴⁶. Maf activity (**Figure 2.7A**), *Maf* gene expression (**Supplementary figure 2.8A and 2.8B**) and Maf protein expression (**Supplementary figure 2.8C and 2.8D**) were elevated in CD206⁺ IMs compared to CD206⁻ IMs. Nevertheless, unlike in *Lyz2^{Cre}Mafb^{fl/fl}* mice, IM numbers were normal in *Lyz2^{Cre}Maf^{fl/fl}* mice (**Supplementary figure 2.8E and 2.8F**).

Hence, we performed scRNA-seq analysis of lung cMo, pMo and CD64⁺ cells from *Lyz2^{Cre}Mafb^{fl/fl}*, *Lyz2^{Cre}Maf^{fl/fl}* and control littermates. Compared to the lungs of *Mafb^{fl/fl}* or *Maf^{fl/fl}* control mice, which contained cMo (C1), pMo (C2) and CD206⁺ IMs and CD206⁻ IMs (C3), *Lyz2^{Cre}Mafb^{fl/fl}* mice lacked all IMs in the lung (C3), while a transcriptionally distinct cluster of cells (*Clec4b1*, *Mgl2*, *Tnip3*; C4) was enriched instead (**Figure 2.8A–D**), suggesting that the few CD64⁺ cells present in *Lyz2^{Cre}Mafb^{fl/fl}* mice had a completely different transcriptional profile than wild-type IMs. Of note, we found 216 DEGs (\log_2 fold change ± 0.5 , adjusted *P* value $< 5 \times 10^{-2}$) between the wild-type IM cluster (C3) and the cluster enriched in *Lyz2^{Cre}Mafb^{fl/fl}* mice (C4; **Figure 2.8E**). The expression of prototypical IM identity genes (*Mrc1*, *Adgre1*, *Pf4*, *Tmem176a*, *Tmem176b*, *Tmem119*, *ApoE*, *C1q*, *Mafb*, *Cd63*)¹⁰⁴ was significantly decreased in C4 as compared to wild-type IMs (C3; **Figure 2.8F**). Flow cytometry of CD64⁺ cells from *Lyz2^{Cre}Mafb^{fl/fl}* mice indicated that they exhibited decreased expression of CD64 and MerTK protein

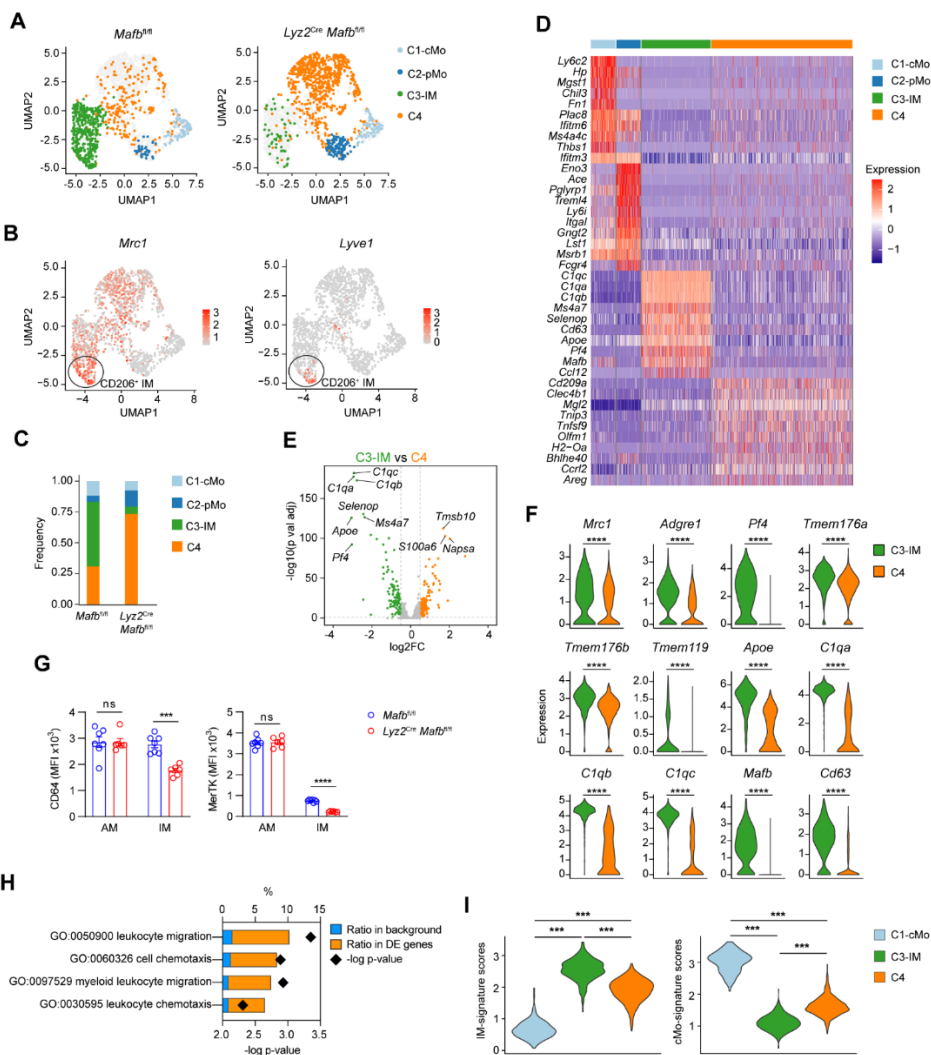


Figure 2.8. Interstitial macrophage identity is severely impaired in myeloid-restricted *Mafb*-deficient mice. (A) UMAP plots depicting the transcriptional identity of lung CD45⁺SSC^{lo}CD11b⁺F4/80⁺ CD64⁻ monocytes and CD64⁺ cells from *Lyz2^{Cre}Mafb^{fl/fl}* mice and littermate controls (n=5 pooled mice per group). (B) UMAP feature plots representing single-cell expression of *Mrc1* and *Lyve1* in lung myeloid cells merged from *Lyz2^{Cre}Mafb^{fl/fl}* mice and littermate controls, as in A. (C) Histogram showing frequency of each cluster in *Lyz2^{Cre}Mafb^{fl/fl}* mice and littermate controls. (D) Heat map depicting the single-cell expression of the ten most upregulated genes within each cluster. (E) Volcano plot depicting DEGs between C3 and C4 clusters. Transcripts significantly upregulated in C3 and C4 are colored in green and orange, respectively (log₂ fold change ± 0.5 and adjusted P value < 0.05). (F) Expression of the indicated genes within C3 and C4 clusters, **** p < 0.0001. (G) Bar graphs showing MFI of CD64 and MerTK in AM and IM cells. Legend: *Mafb^{fl/fl}* (blue), *Lyz2^{Cre}Mafb^{fl/fl}* (red). Significance levels: ns (not significant), *** p < 0.001, **** p < 0.0001. (H) GO enrichment plot showing enrichment of leukocyte migration and chemotaxis terms. Legend: Ratio in background (blue), Ratio in DE genes (orange), -log p-value (black diamond). (I) Violin plots showing IM-signature scores and cMo-signature scores. Legend: C1-cMo (blue), C3-IM (green), C4 (orange). Significance levels: *** p < 0.001.

as depicted by violin plots (height: expression; width: abundance of cells). (G) Surface expression of CD64 and MerTK in lung AMs and CD64⁺ cells, evaluated by flow cytometry in *Lyz2^{Cre}Mafb^{fl/fl}* and littermate controls. (H) GO enrichment analysis performed on the upregulated genes in C4 as compared to C3. (I) IM and cMo signature scores within C1, C3 and C4 clusters, as depicted by violin plots (height: scores; width: abundance of cells). Data show the mean \pm s.e.m. and are pooled from two independent experiments (G; n = 6–7 mice per group). *P* values were calculated using a Wilcoxon rank sum test (E and F), a two-way ANOVA with Sidak's post hoc test (G), a two-tailed Mann–Whitney U test with Benjamini–Hochberg false discovery rate correction (H), or a one-way ANOVA with Tukey's post hoc test (I). ****P* < 0.001; *****P* < 0.0001.

compared to those from *Mafb^{fl/fl}* control littermates (**Figure 2.8G**). In addition, the profile of C4 in *Lyz2^{Cre}Mafb^{fl/fl}* mice was enriched in biological responses similar to those found at the beginning of the cMo-to-IM trajectory, such as leukocyte migration and chemotaxis (**Figure 2.8H**) and was intermediate between cMo and IMs (**Figure 2.8I**). Conversely, we found only a few DEGs between IMs from *Mafb^{fl/fl}* and *Lyz2^{Cre}Mafb^{fl/fl}* mice (**Supplementary figure 2.8G–I**). *Folr2* was among the genes significantly downregulated in c-Maf-deficient IMs compared to wild-type IMs (**Supplementary figure 2.8I**), suggesting that the identity of the CD206⁺ IM subset was regulated by c-Maf¹⁰⁴. In line with this, CD206 protein expression was significantly decreased in IMs from *Lyz2^{Cre}Mafb^{fl/fl}* mice compared to those from *Mafb^{fl/fl}* controls (**Supplementary figure 2.8J**), suggesting that c-Maf had a specific role in the CD206⁺ IM subset. Altogether, these data showed that CD64⁺ cells from *Lyz2^{Cre}Mafb^{fl/fl}* mice shared similarities with Tr-Mo, and indicated a severe impairment of IM development and identity in the absence of MafB.

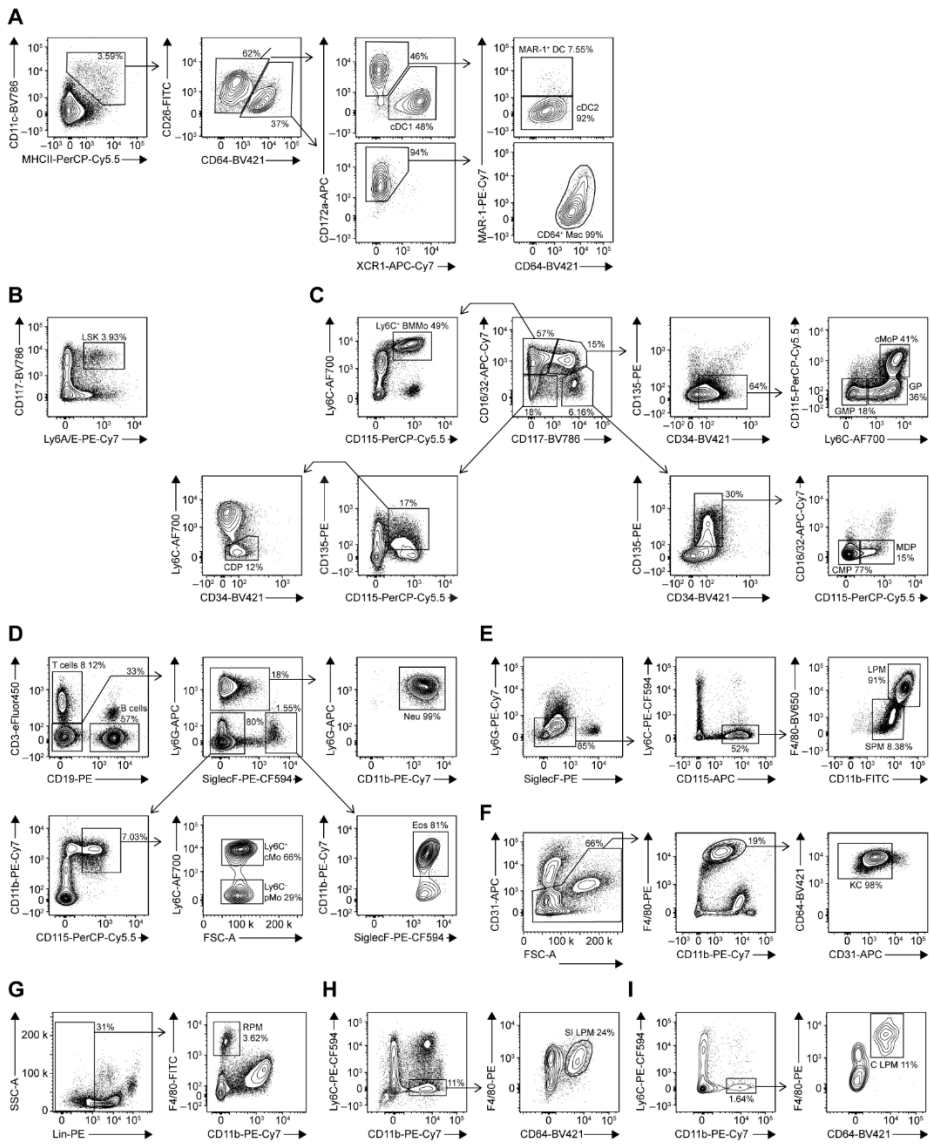
Supplementary Information

Supplementary tables

Supplementary table 2.1. List of reagents, antibodies and commercial assays used in this study. (*Appendix 1*)

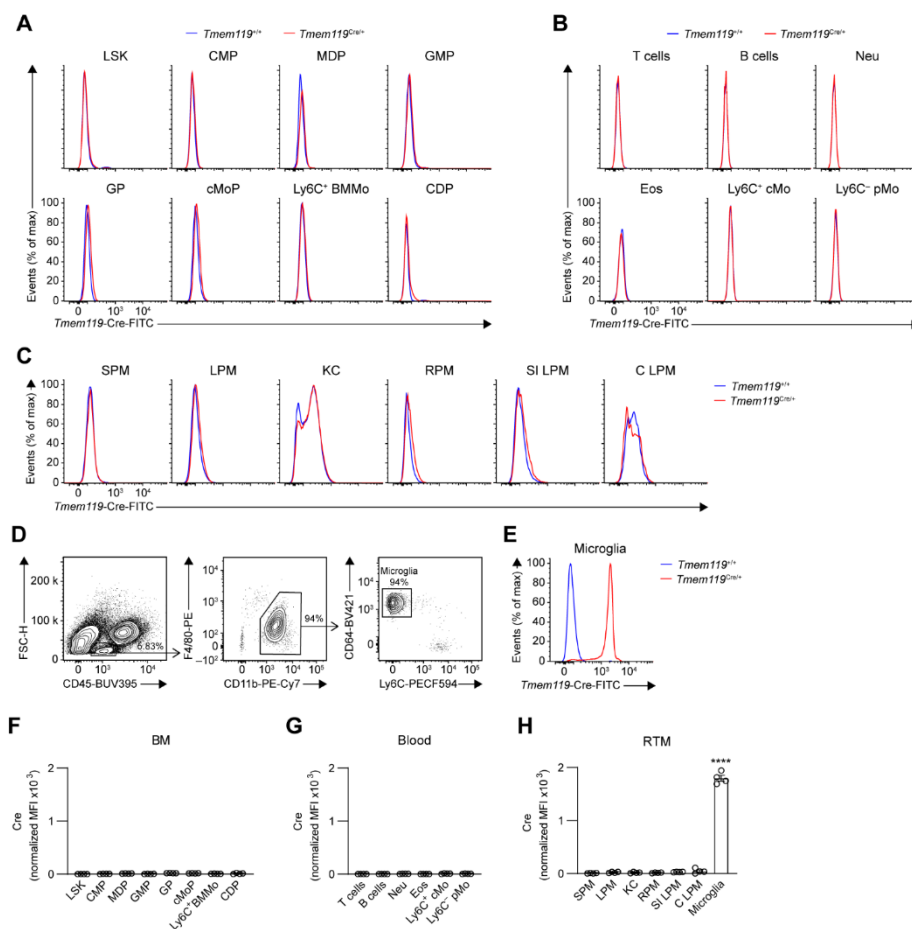
Supplementary table 2.2. List of the deposited data generated and used in this study. (*Appendix 1*)

Supplementary figures



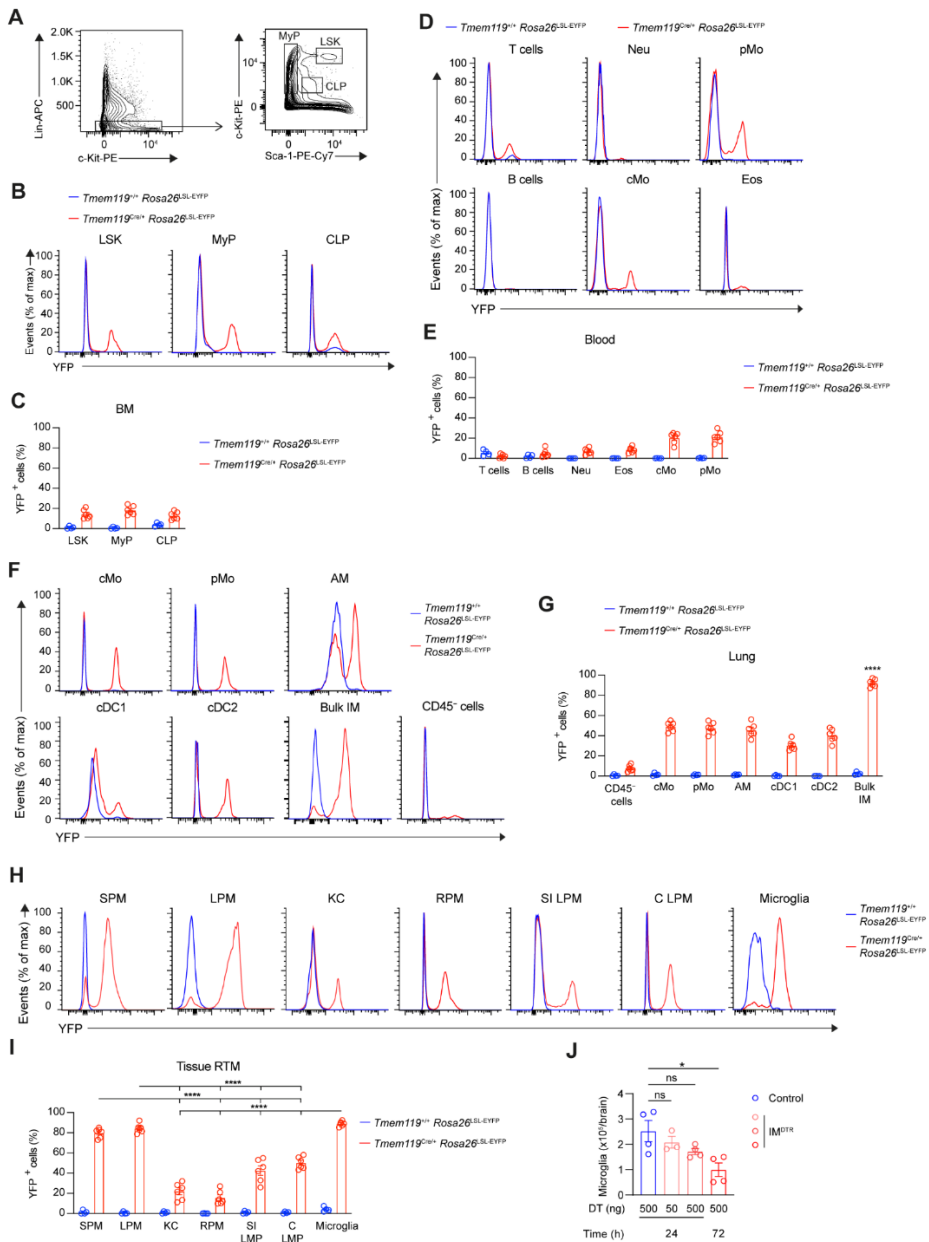
Supplementary figure 2.1. Flow cytometry gating strategies to delineate lung DCs, BM progenitors, blood immune cells and RTM. Flow cytometry gating strategy used to delineate lung CD45⁺CD11c⁺MHC-II⁺CD26⁺CD64⁻CD172a⁻XCR1⁺ type 1 conventional DC (cDC1), CD45⁺CD11c⁺MHC-II⁺CD26⁺CD64⁻CD172a⁺MAR1⁻ type 2 conventional DC (cDC2),

CD45⁺CD11c⁺MHC-II⁺CD26⁺CD64⁻CD172a⁺MAR1⁺ DCs (MAR1⁺ DC) and CD45⁺CD11c⁺MHC-II⁺CD26⁻CD64⁺CD172a⁺ macrophages (CD64⁺ Mac) (A), BM Lin⁻Ly6A/E⁺CD117⁺ LSK (B), Lin⁻CD16/32⁻CD117⁺CD135⁺CD34⁺CD115⁻ common myeloid progenitors (CMP), Lin⁻CD16/32⁻CD117⁺CD135⁺CD34⁺CD115⁺ monocyte-DC progenitors (MDP), Lin⁻CD16/32⁺CD117⁺CD135⁻CD34⁺CD115⁻Ly6C⁻ granulocyte-monocyte progenitors (GMP), Lin⁻CD16/32⁺CD117⁺CD135⁻CD34⁺CD115⁻Ly6C⁺ granulocyte progenitors (GP), Lin⁻CD16/32⁺CD117⁺CD135⁻CD34⁺CD115⁺Ly6C⁺ monocyte progenitors (cMoP), Lin⁻CD16/32⁺CD117⁻CD115⁺Ly6C⁺ monocytes (Ly6C⁺ BMMo), Lin⁻CD16/32⁻CD117⁻CD135⁺CD115⁺CD34⁻Ly6C⁻ common DC progenitors (CDP) (C), blood CD45⁺CD3⁺CD19⁻ T cells, CD45⁺CD3⁻CD19⁺ B cells, CD45⁺CD3⁻CD19⁻Ly6G⁻SiglecF⁻CD115⁺ Ly6C⁺ cMo or Ly6C⁻ pMo, CD45⁺CD3⁻CD19⁻Ly6G⁺CD11b⁺ neutrophils (Neu), CD45⁺CD3⁻CD19⁻CD11b⁺SiglecF⁺ eosinophils (Eos) (D), CD45⁺Ly6G⁻SiglecF⁻Ly6C⁻CD115⁺CD11b⁺ F4/80^{hi} large (LPM) or F4/80^{lo} small peritoneal macrophages (SPM) (E), liver CD45⁺CD31⁻F4/80⁺CD11b^{int}CD64⁺ Kupffer cells (KC) (F), spleen Lin⁻F4/80⁺CD11b⁻ red pulp macrophages (RPM) (G), small intestinal CD45⁺Ly6C⁻CD11b⁺F4/80⁺CD64⁺ lamina propria macrophages (SI LPM) (H) and colon CD45⁺Ly6C⁻CD11b⁺F4/80⁺CD64⁺ lamina propria macrophages (C LPM) (I). Mac, macrophage.



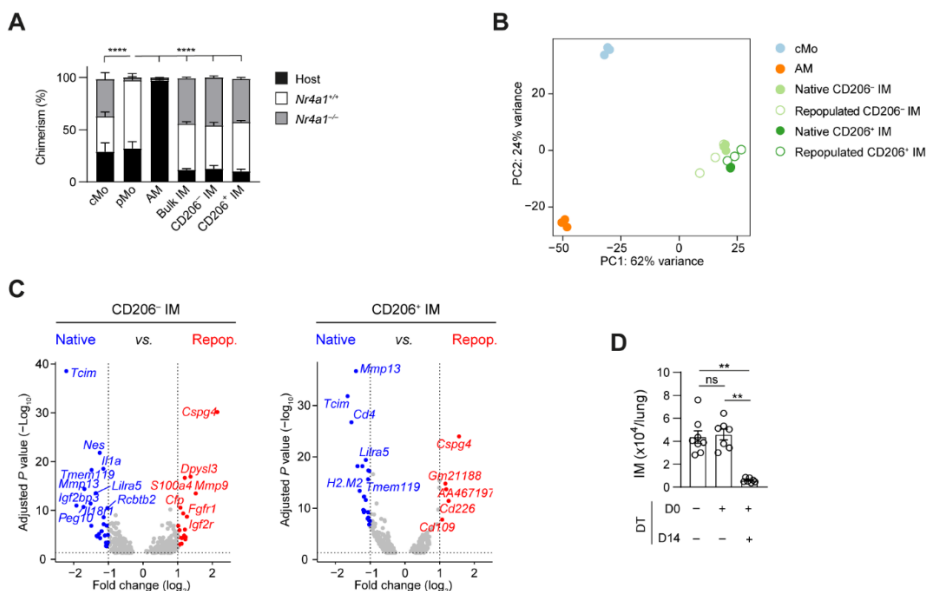
Supplementary figure 2.2. Assessment of intracellular Cre protein expression in BM progenitors, blood leukocytes and RTM. (A–C) Representative histograms of Cre intracellular expression in BM progenitors (A), in blood leukocytes (B), and in small and large peritoneal macrophages (SPM and LPM, respectively), Kupffer cells (KC), red pulp splenic macrophages (RPM), small intestinal (SI) and colon (C) lamina propria macrophages (LPM) (C) from *Tmem119*^{+/+} (blue) and *Tmem119*^{Cre/+} (red) mice. (D) Flow cytometry gating strategy to show brain FSC^{lo}CD45^{int}F4/80⁺CD11b⁺CD64⁺Ly6C⁻ microglia. (E) Representative histograms of Cre intracellular protein expression in microglia from *Tmem119*^{+/+} (blue) and *Tmem119*^{Cre/+} (red) mice. (F–H) Bar graphs showing normalized Cre expression in the indicated cell populations from the BM (F) and the blood (G), and in tissue RTM (H). Data show mean \pm SEM (*n* = 4 mice per group). In H, *P* values compare microglia vs. every other population and were calculated using a one-way analysis of variance (ANOVA) with Tukey's post hoc tests. Raw data and *P* values are provided as a source data file. ****, *P* < 0.0001. CDP,

common plasmacytoid and dendritic cell progenitor; cMoP, common monocyte progenitor; CMP, common myeloid progenitor; GMP, granulocyte-monocyte progenitor; GP, granulocyte progenitor; LSK, lineage(Lin)⁻Sca-1⁺cKit⁺ multipotent progenitor; MDP, monocyte-dendritic cell progenitor.

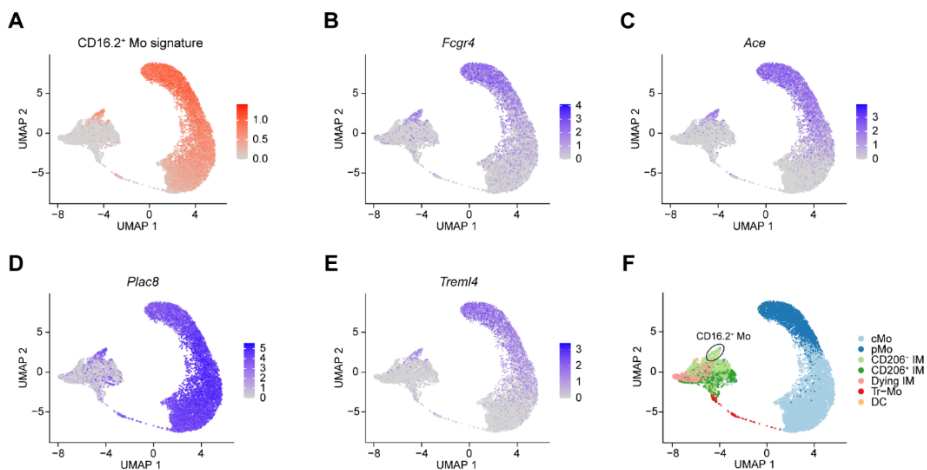


Supplementary figure 2.3. Assessment of YFP labeling in *Tmem119^{Cre}Rosa26^{LSL-EYFP}* mice and of microglia depletion in IM^{DTR} mice. (A) Flow cytometry gating strategy to show Lin⁻Sca-1⁺c-Kit⁺ (LSK) multipotent progenitors, Lin⁻Sca-1⁻c-Kit^{int/hi} myeloid lineage-committed progenitors (MyP) and Lin⁻Sca-1^{int}c-Kit^{int} common lymphoid progenitors (CLP). (B and C) Representative histograms of YFP expression (B) and bar

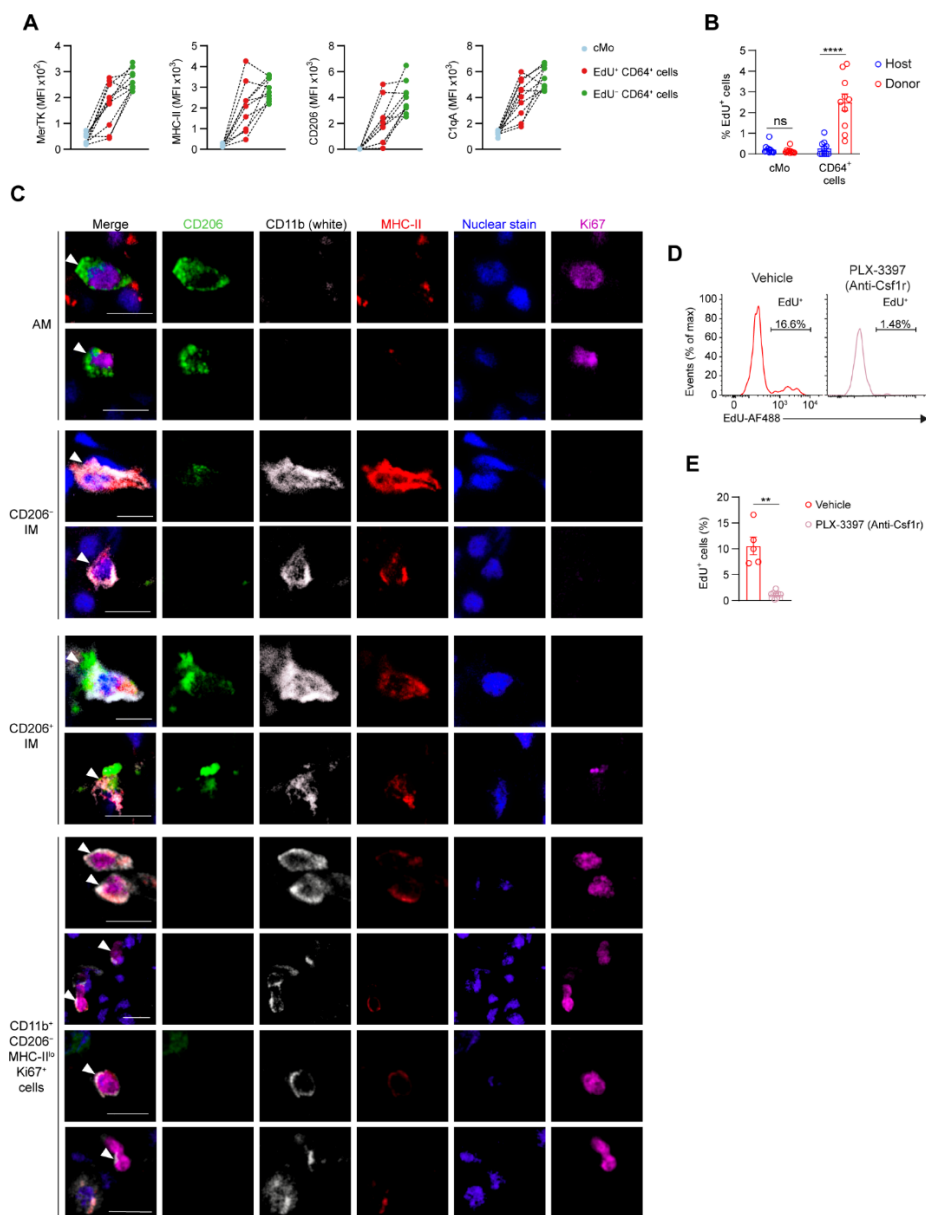
graphs showing % of YFP⁺ cells (C) in BM LSK, MyP and CLP from *Tmem119^{+/+}Rosa26^{LSL-EYFP}* (blue) and *Tmem119^{Cre/+}Rosa26^{LSL-EYFP}* (red) mice. (D and E) Representative histograms of YFP expression (D) and bar graphs showing % of YFP⁺ cells (E) in blood CD45⁺CD3⁺CD19⁻ T cells, CD45⁺CD3⁻CD19⁺ B cells, CD45⁺CD3⁻CD19⁻Ly6G⁻SiglecF⁻CD115⁺ Ly6C⁺ cMo or Ly6C⁻ pMo, CD45⁺CD3⁻CD19⁻Ly6G⁺CD11b⁺ neutrophils (Neu), CD45⁺CD3⁻CD19⁻CD11b⁺SiglecF⁺ eosinophils (Eos) from *Tmem119^{+/+}Rosa26^{LSL-EYFP}* (blue) and *Tmem119^{Cre/+}Rosa26^{LSL-EYFP}* (red) mice. (F and G) Representative histograms of YFP expression (F) and bar graphs showing % of YFP⁺ cells (G) in lung cMo, pMo, cDC1, cDC2, AMs, IMs and CD45⁻ structural cells from *Tmem119^{+/+}Rosa26^{LSL-EYFP}* (blue) and *Tmem119^{Cre/+}Rosa26^{LSL-EYFP}* (red) mice. (H and I) Representative histograms of YFP expression (H) and bar graphs showing % of YFP⁺ cells (I) in small and large peritoneal macrophages (SPM and LPM, respectively), Kupffer cells (KC), red pulp splenic macrophages (RPM), small intestinal (SI) and colon (C) lamina propria macrophages (LPM) and microglia from *Tmem119^{+/+}Rosa26^{LSL-EYFP}* (blue) and *Tmem119^{Cre/+}Rosa26^{LSL-EYFP}* (red) mice. (J) Numbers of microglia quantified by flow cytometry in IM^{DTR} and littermate control mice injected i.p. with 50 or 500 ng DT and evaluated 24 or 72 h post-DT injection. Data show mean ± SEM and are pooled from 2 independent experiments (C, E, G, I, J) (C, E, G, I: *Tmem119^{+/+}Rosa26^{LSL-EYFP}*; *Tmem119^{Cre/+}Rosa26^{LSL-EYFP}*: n = 4; 6 mice per group, respectively; J: n = 3-4 mice per group). *P* values were calculated using a two-way (C, E, G, I) or a one-way (J) analysis of variance (ANOVA) with Tukey's post hoc test. In G, *P* values compare IMs vs. every other population. Raw data and *P* values are provided as a source data file. *, *P* < 0.05; ****, *P* < 0.0001. ns, not significant.



Supplementary figure 2.4. IM niche refilling is independent of *Nr4a1* and repopulated IMs are largely similar to native IMs 14 days post-DT in IM^{DTR} mice. (A) Bar graphs showing % of *Nr4a1*^{+/+} donor, *Nr4a1*^{-/-} donor and host chimerism in the indicated cell populations from lethally-irradiated, thorax-protected CD45.1/CD45.2 IM^{DTR} mice transplanted with a 1:1 mix of CD45.2 *Nr4a1*^{-/-} and CD45.1 *Nr4a1*^{+/+} BM cells, injected with 50 ng DT i.p. 4 weeks later and evaluated at day 7 post-DT. (B) Principal Component (PC) analysis plot with % indicating the variability explained by each PC component, obtained by bulk RNA-seq analysis of lung cMo, AMs, CD206⁻ IMs and CD206⁺ IMs from untreated IM^{DTR} mice, and of lung CD206⁻ IMs and CD206⁺ IMs from DT-treated IM^{DTR} mice at day 14 post-DT (n = 3 pooled mice per replicate, 3 replicates per condition). (C) Volcano plots depicting the DEG between native and repopulated CD206⁻ IMs (left) and native and repopulated CD206⁺ IMs (right). Transcripts significantly upregulated in native and repopulated IM subsets are colored in blue and red, respectively (log₂ fold-change ± 1 and adjusted *P* value < 10⁻²). (D) Bar graph showing lung IM numbers assessed by flow cytometry in IM^{DTR} mice treated or not with DT i.p. at day 0 and 14, and analyzed 24 h after the last DT treatment (day 15). Data show mean ± SEM and are pooled from 2 independent experiments (A, D) (A, D: n = 4, 7-8 mice per group, respectively). *P* values were calculated using a one-way ANOVA with Tukey's post-hoc tests, and compare donor CD45.1 *Nr4a1*^{+/+} chimerism between cell populations in a. Raw data and *P* values are provided as a source data file. **, *P* < 0.01; ****, *P* < 0.0001. ns, not significant.

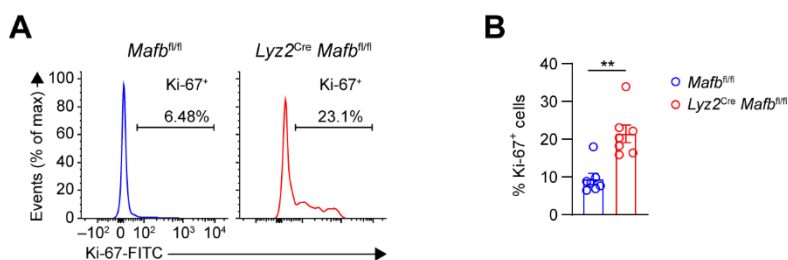


Supplementary figure 2.5. Identification of non-classical CD16.2⁺ monocytes in scRNA-seq data of monocyte-to-IM trajectory. UMAP feature plot depicting the transcriptional identity of sorted lung CD45⁺SSC^{lo}CD11b⁺F4/80⁺CD64⁻ monocytes and CD45⁺SSC^{lo}CD11b⁺F4/80⁺CD64⁺ IMs merged from IM^{DTR} mice injected with DT i.p. at 0, 12, 24, 48 and 96 hours before the analysis (n = 5 pooled mice per time point), according to their CD16.2⁺ monocyte (Mo) signature score (A) and to the expression of the indicated genes (B–E). (F) Two-dimensional UMAP plot, as in A, identifying CD16.2⁺ monocytes.

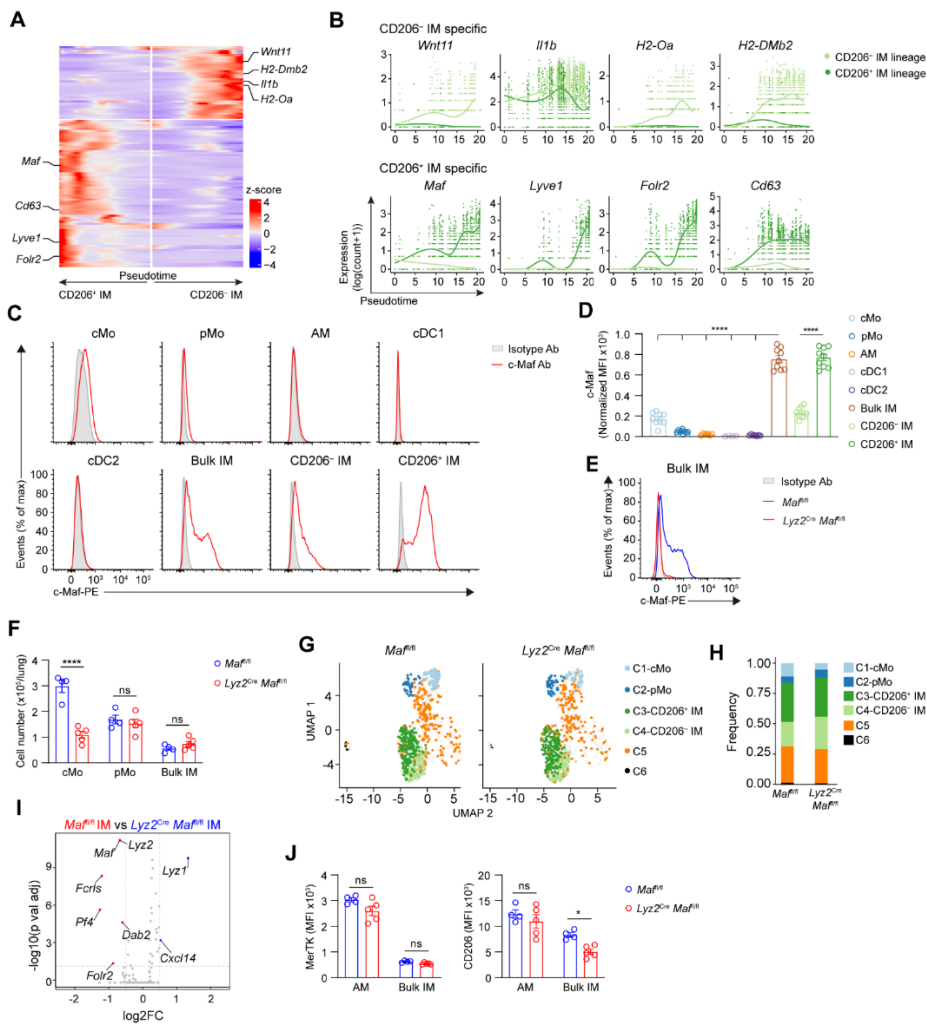


Supplementary figure 2.6. Tr-Mo are BM-derived cells in transition between cMo and IMs and whose proliferation is inhibited by Csf1r antagonists. (A) Expression of the indicated markers in lung cMo, EdU⁺CD64⁺ and EdU⁻CD64⁺ cells from EdU-pulsed IM^{DTR} mice at day 2 post-DT. Values obtained from individual mice are connected with a dashed line. (B) Bar graph showing the % of EdU⁺ cells in CD45.1 donor and CD45.2 host cells from lung cMo and CD64⁺ cells from lethally irradiated, thorax-protected CD45.2

IM^{DTR} mice reconstituted with CD45.1 BM wild-type cells, injected i.p. with DT and evaluated 2 days post-DT and 4 hours after EdU i.p. treatment by flow cytometry. (C) Representative pictures of CD11b⁻CD206^{hi}MHC-II⁻Ki67⁺ AMs, CD11b⁺CD206^{lo}MHC-II^{hi} IMs (CD206⁻ IM), CD11b⁺CD206^{hi}MHC-II^{lo/int} IMs (CD206⁻ IM) and CD11b⁺CD206⁻MHC-II^{lo}Ki67^{hi} cells, identified by confocal microscopy on lung sections from untreated and DT-treated IM^{DTR} mice, at day 2 post-DT. (D) Representative histograms of EdU levels in lung extravascular CD64⁺ cells from DT-treated IM^{DTR} mice that were treated with DT i.p. 3 days before, with the Csf1r antagonist PLX-3397 or with vehicle i.p. 1 and 2 days before, and with EdU i.p. 8 h before. (E) Bar graph showing the % of EdU⁺ cells in lung extravascular CD64⁺ cells, as in D. Data are pooled from 2-3 independent experiments and show individual values (A) ($n = 8$ mice), or mean \pm SEM (B, E) (b,e: $n = 10, 5-8$ mice per group). P values were calculated using a two-way ANOVA with Tukey's post hoc tests (B) or a two-tailed Student's t test (E). Raw data and P values are provided as a source data file. **, $P < 0.01$; ***, $P < 0.0001$; ns, not significant. Scale bar: 10 μ m.



Supplementary figure 2.7. Lung CD64⁺ cells from *Lyz2^{Cre}Mafb^{fl/fl}* mice exhibit a higher proliferative potential as compared to those from littermate controls. (A) Representative histograms of Ki67 stainings within lung CD64⁺ cells from *Lyz2^{Cre}Mafb^{fl/fl}* and littermate controls. Insets indicate the % of Ki67⁺ cells within CD64⁺ cells. (B) Bar graph showing the % of Ki67⁺ cells within lung CD64⁺ cells. Data show mean ± SEM and are pooled from 2 independent experiments (B) ($n = 7$ mice per group). P values were calculated using an unpaired two-tailed Mann-Whitney test. Raw data and P values are provided as a source data file. *, $P < 0.001$.**



Supplementary figure 2.8. c-Maf specifically controls the identity of the CD206⁺ IM subset. (A) Heatmap plot depicting the DEG along pseudotime evaluated by tradeSeq in the subset-specific trajectories starting from cMo (middle) and ending in CD206⁻ IM and CD206⁺ IM subsets. (B) Gene expression of the indicated genes along pseudotime evaluated by tradeSeq in both trajectories leading either to CD206⁻ IM or CD206⁺ IM subsets. (C) Representative histograms of c-Maf protein expression in the indicated lung myeloid cell populations from wild-type mice. (D) Bar graphs showing normalized MFI of c-Maf expression, as in C. *P* values compare bulk IMs vs. every other population, or CD206⁺ IMs vs. CD206⁻ IMs. (E) Efficiency of *Maf* depletion within lung IMs from *Lyz2^{Cre}Mafl/fl* mice evaluated by c-Maf protein intracellular staining. Data are representative of 5 mice, each of them giving similar results. (F) Absolute numbers of lung cMo, pMo and IMs quantified by flow cytometry in *Lyz2^{Cre}Mafl/fl* and *Mafl/fl* mice. (G) UMAP plots showing the distribution of myeloid cells in *Mafl/fl* (left) and *Lyz2^{Cre}Mafl/fl* (right) mice. (H) Stacked bar graph showing the frequency of myeloid cell populations in *Mafl/fl* (left) and *Lyz2^{Cre}Mafl/fl* (right) mice. (I) Volcano plot showing differentially expressed genes (DEGs) in *Mafl/fl* IMs vs. *Lyz2^{Cre}Mafl/fl* IMs. (J) Bar graphs showing the MFI of MerTK and CD206 in AM and Bulk IM populations in *Mafl/fl* (left) and *Lyz2^{Cre}Mafl/fl* (right) mice.

(G) UMAP plot depicting the transcriptional identity of lung CD45⁺SSC^{lo} CD11b⁺F4/80⁺ CD64⁻ monocytes and CD64⁺ cells from *Lyz2^{Cre}Ma^f^{f/f}* mice and littermate controls (n = 5 pooled mice per group). (H) Histogram showing frequency of each cluster in *Lyz2^{Cre}Ma^f^{f/f}* and *Ma^f^{f/f}* mice. (I) Volcano plot depicting the DEG between lung IMs (C3) from *Lyz2^{Cre}Ma^f^{f/f}* and *Ma^f^{f/f}* mice. Transcripts significantly upregulated in IMs from *Ma^f^{f/f}* and *Lyz2^{Cre}Ma^f^{f/f}* mice are colored in red and blue, respectively (\log_2 fold-change \pm 0.5 and adjusted *P* value < 0.05). (J) Surface expression of MerTK and CD206 in lung AMs and IMs, quantified by flow cytometry in *Lyz2^{Cre}Ma^f^{f/f}* and *Ma^f^{f/f}* mice. (D, F, J) Data show mean \pm SEM and are pooled from 3 independent experiments (n = 9 mice per group) (D) or 2 independent experiments (n = 4-5 mice per group) (F, J). *P* values were calculated using a one-way ANOVA with Tukey's post-hoc test (for bulk IMs) or a two-tailed Mann-Whitney test (for IM subsets), or a two-way ANOVA with Tukey's post-hoc test (F, J). Raw data and *P* values are provided as a source data file. *, *P* < 0.05; ****, *P* < 0.0001; ns, not significant. Ab, antibody.

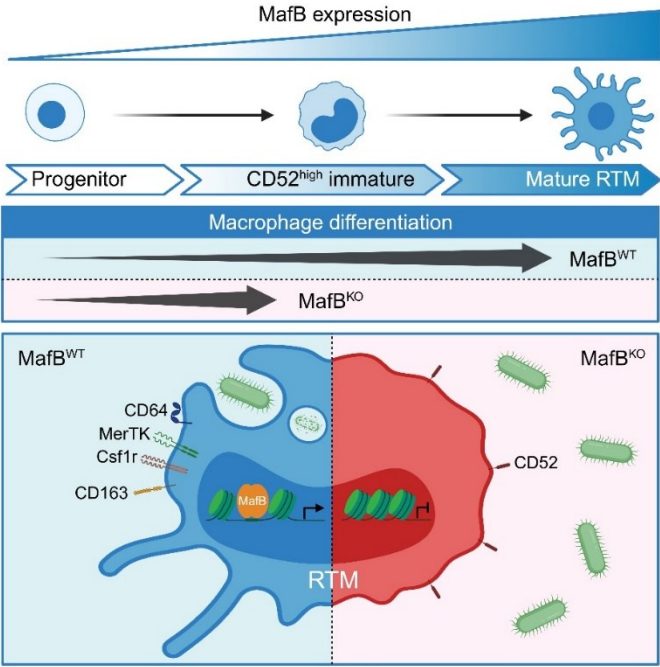
Part II: MafB is a conserved transcriptional regulator of macrophage development and functional identity across tissues and species

After: Domien Vanneste, Wen Peng, Zhuangzhuang Liu, Malik Hamaidia, Raphaël La Rocca, Joan Abinet, Alexis Balthazar, Fabienne Perin, Alexandre Hego, Didier Cataldo, Fabrice Bureau, Philippe Compère, Bénédicte Machiels, Charlotte L. Scott, Coraline Radermecker & Thomas Marichal (2026). MafB is a conserved transcriptional regulator of macrophage development and functional identity across tissues and species *Immunity*, S1074-7613(26)00033-6. Advance online publication. <https://doi.org/10.1016/j.immuni.2026.01.012>

Author contributions: T.M. and D.V. conceived the project and designed the experiments. D.V. did most of the experiments, compiled the data and prepared the figures. W.P. helped with in vivo-related experiments. Z.L. and C.L.S. performed confocal microscopy experiments and analyzed KC specific Maf/Mafb-deficient mice. M.H. prepared MDM. R.L.R. analyzed KC morphology. J.A. and DV performed all the bioinformatic analyses. A.B. and B.M. helped with isolation and analysis of CM. F.P. and D.C. performed the invasive measurements of lung function. A.H. analyzed BMDM morphology. P.C. performed electron microscopy experiments. F.B. generated myeloid-restricted Mafb-deficient mice and F.B. and C.R. helped with the initial characterization of those mice. T.M. and D.V. wrote the manuscript. All authors provided feedback on the manuscript. T.M. supervised and secured funding for the project.

Abstract

Homeostatic resident tissue macrophages (RTMs) exhibit diversity across tissues but also share common features that are driven by conserved transcriptional programs. While the transcription factor MafB is highly expressed in macrophages, its role in establishing RTM identity and functions remains unclear. Here we show that MafB was required for the development of bone-marrow-derived macrophages (BMDMs) and most RTMs *in vivo*. MafB deficiency retained RTM in a CD52^{high} immature stage and disrupted global and tissue-specific identities and functions, impairing phagocytosis, splenic iron recycling, and lung, kidney and gut physiology. Epigenetic profiling revealed that MafB directly regulated key RTM genes in mouse and humans, including *Csf1r*, *Mertk*, *Fcgr1*, *Cd163* and *Zeb2*. In silico analyses further demonstrated strong evolutionary conservation of MafB binding sites across vertebrates. Together, these findings establish MafB as a crucial regulator of RTM development and functional identity, linking MafB-dependent transcriptional programs with defining features of RTMs and tissue homeostasis.



Graphical abstract 3. Resident macrophage maturation and tissue-specific identity depend on transcriptional programming, yet how conserved regulators universally drive these programs remains unresolved across tissues. Vanneste et al. identify MafB as a key transcriptional regulator that directly orchestrates conserved gene network from mouse to human, thereby sustaining macrophage function and multi-organ tissue homeostasis. Graphical abstract was created in BioRender.

Introduction

Macrophages (Macs) are integral parts of most mammalian tissues and exhibit a remarkable functional diversity^{72,298,300,309}. Homeostatic tissue macrophage populations present at steady-state, called resident tissue macrophages (RTMs) hereafter, act as professional phagocytes and are gatekeepers of homeostasis by deploying important functions, including clearance of cells and foreign bodies and defense against pathogens, as well as context-specific duties inherent of their tissue of residence^{63,103,222}. While most RTM populations seed tissues before the establishment of definitive hematopoiesis and are long-lived^{24,67,306,307}, bone marrow(BM)-derived monocytes can also contribute to RTM maintenance throughout adult life^{29,282,297,300}.

RTM developmental and functional heterogeneity has been a subject of intense investigations, which has led to the discovery of tissue-specific niche-instructive signals and transcriptional programs dictating such diversity^{140,172,222,224,297,298,300,301}. However, Macs represent above all, a distinct cell lineage that is defined by common characteristics, including expression of receptors, such as the Csf1 receptor (Csf1r)^{302,303} and the high affinity receptor for the immunoglobulin gamma Fc region 1 (Fcgr1)^{42,304}, and Mac-defining transcription factors (TF), such as the Ets family TF PU.1^{226,305} and Zinc finger E box binding homeobox 2 (Zeb2)²³⁶. Additional conserved factors arguably contribute to RTM identity and regulate shared and tissue-specific transcriptional programs across RTM populations.

First discovered in 1994²³⁷, Maf basic leucine zipper transcription factor B (MafB) has been found to be highly expressed in myelomonocytic cells, including Macs, and contributes to monocytic differentiation^{238–241}. Of note, MafB overexpression can induce Mac differentiation from chick myeloblasts²³⁹,

suggesting a link between MafB and Mac development. Subsequent genome-wide and lineage-tracing studies support elevated MafB expression in RTMs, distinguishing them from dendritic cells (DCs) and monocytes^{42,72,242}.

Initial studies investigating MafB contributions to Mac development *in vivo* have used a *Mafb*^{-/-} mice²⁴¹ or mice reconstituted with MafB-deficient hematopoietic cells^{244,246} and have found no marked defects in Mac numbers^{241,244,246}. *In vitro*, MafB-deficient Macs retain phagocytic and nitric oxide-producing capacities, but display enhanced actin remodeling and membrane protrusions upon macrophage Csf1 stimulation²⁴⁴. When both MafB and c-Maf are deleted, differentiated Macs remain phenotypically and functionally intact yet acquire an unusual capacity for self-renewal, driven by Klf4- and c-Myc-dependent pathways²⁴⁶. Additional analyses of MafB-deficient mice reveal context-specific roles of MafB in the regulation of F4/80²⁴¹ and complement components C1q²⁴⁵, the suppression of antiviral responses in microglia (MG)²⁷², the regulation of brown adipose tissue thermogenesis³³⁵ or the restriction of lung monocyte proliferation prior to interstitial mac (IM) differentiation¹¹⁰. Nevertheless, the potentially conserved role of MafB in governing RTM development and identities across tissues and species remains elusive.

Here, we addressed this question using *in vivo* conditional *Mafb* targeting¹¹⁰, *ex vivo* Mac cultures and *in silico* analyses combined with flow cytometry, microscopy, RNA-sequencing (RNA-seq), functional assays as well as epigenetic profiling of MafB binding sites. We found that MafB was highly expressed and active in all tested RTM populations, at the exception of alveolar Macs (AMs). Myeloid-restricted MafB deficiency profoundly impaired the full development and the identities of mature RTM across mouse tissues, with important consequences for RTM functions and tissue homeostasis. Among more than

conserved 4,000 MafB binding sites identified, we found that MafB directly regulated key differentiation and identity genes, including *Csf1r* and *Fcgr1*, both in mice and humans. Finally, we provided evidence that MafB-dependent regulation of Mac identity was highly conserved across species, thereby revealing MafB as a critical and evolutionarily conserved regulator of RTM development and identity.

Materials and Methods

Reagents and antibodies

A complete list of the reagents, antibodies and commercial assays used in this paper can be found in **Supplementary Table 3.1**.

Mice

The following mice on the C57BL/6 background were used: CD45.2 WT C57BL/6J (The Jackson Laboratory), CD45.1 WT C57BL/6J (The Jackson Laboratory, 002014), *Maf^{fl/fl}* (ref.³¹⁴), *Mafb^{fl/fl}* (ref.¹¹⁰), *Lyz2^{Cre}* (The Jackson Laboratory, 004781)³¹⁵, *Clec4f^{Cre}* (ref.²³⁶), and *Tmem119^{CreERT2}* (The Jackson Laboratory, 031820)³³⁶. Myeloid-restricted *Mafb* depletion was achieved by crossing *Mafb^{fl/fl}* mice with *Lyz2^{Cre}* mice. The corresponding littermate control mice were *Mafb^{fl/fl}* mice. KC-specific Maf/MafB-deficient mice were generated by crossing *Maf^{fl/fl}Mafb^{fl/fl}* mice with *Clec4f^{Cre}* mice, with *Maf^{fl/fl}Mafb^{fl/fl}* littermates serving as controls. MG-specific MafB-deficient mice were obtained by crossing *Tmem119^{CreERT2}* mice with *Mafb^{fl/fl}* mice, with recombination induced by oral gavage of tamoxifen (5 mg/day for 5 consecutive days); corn oil-treated littermates were used as controls. CD45.1.2 mice were generated by crossing CD45.1 with CD45.2 mice.

No differences between sexes were observed in pilot experiments. Each experiment included both male and female mice aged 6 to 10 weeks, except for chimera experiments, which used mice aged 11 to 15 weeks. The mice were bred and housed under specific-pathogen-free conditions at the GIGA Institute (Liège University, Belgium), maintained on a 12-hour light-dark cycle, with access to standard chow and water *ad libitum*. Mice were identified by genotype, and all

experiments were conducted using age- and sex-matched littermates. Investigators were not blinded during data collection and analysis.

All animals and experimental procedures, except experiments involving *Clec4f^{Cre} Maf^{fl/fl} Mafb^{fl/fl}* mice, were reviewed and approved by the Institutional Animal Care and Use Committee of the University of Liège (ethical approval no. 1956 & 2462). *Clec4f^{Cre} Maf^{fl/fl} Mafb^{fl/fl}* mice were bred and maintained at the VIB (Belgium) in accordance with the ethical committee of the Faculty of Science, UGent and VIB (ethical approval no. LN1691). The study adhered to the “Guide for the Care and Use of Laboratory Animals” from the Institute of Laboratory Animal Resources, National Research Council, published by the National Academy Press, as well as relevant European and local legislation. Temperature and relative humidity were maintained at 21°C and 45–60%, respectively.

Isolation of blood, bone marrow and tissue leukocytes

Blood was collected through retro-orbital plexus bleeding from terminally anesthetized mice. Red blood cells were lysed in ACK lysis buffer (155 mM NH₄Cl [VWR, 21235.297], 10 mM KHCO₃ [Sigma-Aldrich, 60338], 0.1 mM EDTA [Merck Millipore, 1084181000]). Mice were then sacrificed by cervical dislocation. Peritoneal lavage was obtained by injecting 10 ml PBS (Thermo Fisher Scientific, 14190094) containing 10 mM EDTA into the peritoneal cavity and collecting the washout. Mice were then perfused with 20 ml PBS through the left ventricle, and liver, kidney, lung, small intestine, colon and brain were dissected.

For BM cell preparation, femurs and tibias were dissected and cleaned of muscle tissue. Bones were opened at the knee joint with a razor blade, and BM was spun out by centrifugation. Cell pellets were resuspended in ice-cold PBS

containing 10 mM EDTA and cell suspensions were filtered using a cell strainer (70 μ m, Corning, 352350) to obtain a single-cell suspension.

Spleen leukocytes were isolated by crushing the spleen through a 70 μ m cell strainer with a syringe plunger. Red blood cells were lysed in ACK lysis buffer.

Liver, kidney, lung and brain were diced into small pieces with razor blades, and digested for 1 h at 37 °C in RPMI (Thermo Fisher Scientific, 21875034) containing 10% vol/vol FBS (Thermo Fisher Scientific, A3160802), 1 mg/ml collagenase IV (Thermo Fisher Scientific, 17104019) and 0.05 mg/ml DNase I (Sigma-Aldrich, 11284932001). After 45 min of digestion, the suspension was homogenized using an 18-gauge needle. Ice-cold PBS containing 10 mM EDTA was added to stop the digestion process and cell suspensions were filtered using a 70 μ m cell strainer. Red blood cells were lysed in ACK lysis buffer. Lung mononuclear leukocytes were enriched by Percoll (GE Healthcare) density gradient centrifugation and collecting cells from the 1.080:1.038 g/ml interface. Brain leukocytes were enriched by Percoll density centrifugation and harvesting cells at the 80%:40% interface.

For gut leukocyte collection, small intestine and colon were washed in ice-cold PBS and remaining fat tissue and Peyer's patches were removed. The intestines were opened longitudinally, cut into segments of 3–4 mm and washed in ice-cold HBSS (Thermo Fisher Scientific, 14025-050) with 2% FBS. To remove mucus and epithelial cells, intestines were incubated with HBSS containing 2 mM EDTA and 1 mM 1,4-Dithiothreitol (DTT) (Sigma-Aldrich, 10708984001) at 37°C with agitation for 20 min followed by an incubation in HBSS supplemented with 2 mM EDTA at 37°C with agitation for 40 min. The remaining tissue was washed in ice-cold PBS and digested for 1 h at 37 °C with agitation in RPMI containing 5% FBS, 1 mg/ml collagenase VIII (Sigma-Aldrich, C2139) and 0.05 mg/ml DNase I. Ice-

cold PBS containing 2 mM EDTA was added to stop the digestion process and cell suspensions were filtered using a 70 μ m cell strainer.

For skin preparation, ears were dissected, separated in dorsal and ventral sections, and digested for 90 min at 37 °C in HBSS supplemented with 5 U/ml Dispase (Sigma-Aldrich, D4693). Dorsal and ventral sections were cut into small pieces using scissors, and further digested for 1 h at 37°C in RPMI containing 10% FBS, 1 mg/ml collagenase IV and 0.05 mg/ml DNase I. After 45 min of digestion, the suspension was homogenized using an 18-gauge needle. Ice-cold PBS containing 10 mM EDTA was added to stop the digestion process and cell suspensions were filtered using a 70 μ m cell strainer.

Flow cytometry and cell sorting

Cells ($0.5\text{--}5 \times 10^6$) were pre-incubated for 10 min at 4 °C with Mouse BD Fc Block (BD Biosciences, 553142) to block unspecific binding to Fc receptors. Cells were then stained with fluorophore-conjugated antibodies for 30 min at 4°C. Lineage markers used RTM analysis included CD3e, CD19, CD49b, Ly6G and SiglecF. For MafB staining, extracellular-stained cells were permeabilized using FoxP3 Transcription Factor Staining Kit (eBioscience™, 00-5523-00), stained with anti-MafB antibody (Bethyl, A700-046) and secondary AF488 Goat anti-Rabbit IgG (H+L) (Thermo Fisher Scientific, A11008) or AF647 Donkey anti-rabbit IgG (Biolegend, 406414). Stained cell suspensions were maintained at 4 °C and analyzed with an LSR Fortessa (BD Biosciences). For scRNA-seq, RTM were sorted using a MA900 (Sony). Dead cells were excluded using by LIVE/DEAD Fixable Near-IR (775) stain (Thermo Fisher Scientific, L34976). The full list of antibodies used for flow cytometry can be found in the **Supplementary table 3.1**. Flow cytometry data were analyzed using FlowJo software (TreeStar).

Wanderlust pseudotime

On flow cytometry data, CD45⁺Lin⁻F4/80⁺CD64⁺ colon cells and CD45⁺Lin⁻CD11b⁺CD115⁺ peritoneal cells were gated, down sampled (1 x 10⁴ cells/ sample) and concatenated using FlowJo. Wanderlust pseudotime³³⁷ was calculated on concatenated flow cytometry data based on Ly6C and MHC-II expression or Ly6C and F4/80 expression for colon and peritoneal cells, respectively.

Bone marrow-derived macrophage differentiation

BMMos were isolated from BM using Monocyte Isolation Kit (BM) (Miltenyi Biotec, 130100629) and were seeded in tissue culture-treated plates and cultured for 4 days in RPMI supplemented with 10% FBS, 1 mM Sodium Pyruvate (Thermo Fisher Scientific, 11360070), 1X Minimum Essential Medium Non-Essential Amino Acids (MEM NEAA; Thermo Fisher Scientific, 11140050), 50 μM β-mercaptoethanol (Thermo Fisher Scientific, 31350010) and 40 ng/ml Csf-1 (Peprotech, 31502) to differentiate them into BMDMs.

Scanning electron microscopy

Fifty thousand BMMos from *Mafb*^{fl/fl} or *Lyz2*^{Cre}*Mafb*^{fl/fl} mice were isolated, seeded on discoid coverslips in tissue culture-treated 24-well plates (Greiner, 662160) and differentiated into BMDMs, as described above. After 4 days, the cells were washed with PBS and fixed for 2 hours in 2.5% glutaraldehyde prepared in 0.1 M sodium cacodylate buffer (pH 7.2). Following fixation, the cells were rinsed in 0.2 M cacodylate buffer and MilliQ water, then post-fixed for 1 hour in aqueous 1% osmium tetroxide. The cells were washed three times with MilliQ water and subsequently dehydrated through a graded ethanol series (30%, 50%, 70%, 90%, and 100%). After three rinses in absolute ethanol, the glass

coverslips containing the cells were dried with CO₂ using a critical point dryer (Leica EM CPD300). The dried coverslips were fixed to glass slides using double-sided carbon tape and coated with a 20 nm layer of gold using a Balzers SCD 004 sputter coater (Balzers). Imaging was performed using a Tescan Clara FEG-SEM (Tescan) equipped with an Everhart-Thornley secondary electron detector under an accelerating voltage of 15 kV.

Cell morphology

Fifty thousand BMMos from *Mafb^{fl/fl}* or *Lyz2^{Cre}Mafb^{fl/fl}* mice were isolated, seeded in a CELLview™ Advanced TC™ petri dish (Greiner, 627975) and differentiated into BMDMs, as described above. After 4 days, differential interference contrast (DIC) images of BMDM cells were acquired using a Zeiss Axio Observer microscope equipped with a 25×/0.8 DIC oil immersion objective and an AxioCam 506 monochromatic camera. For cell segmentation in DIC images, the pre-trained LC2 model of Cellpose 2.0 was retrained with a set of annotated images to enhance its performance and better capture the morphological characteristics of the cells. Predictions were automated using FIJI (1.54) with an ImageJ macro and the BIOP plugin. Morphological characteristics of the segmented cells, including area, perimeter, circularity, roundness, solidity and Feret diameter, were extracted from the masks generated by Cellpose 2.0. One hundred cells were analyzed per biological replicate and three biological replicates were analyzed per group.

Bulk RNA sequencing library preparation

Two hundred fifty thousand BMMos from *Mafb^{fl/fl}* or *Lyz2^{Cre}Mafb^{fl/fl}* mice were isolated, seeded in tissue culture-treated 6-well plates (Greiner, 657160) and differentiated into BMDMs, as described above. After 4 days, non-adherent cells

were washed off with ice-cold PBS and total RNA was isolated with the standard TRIzol (Thermo Fisher Scientific, 15596018) RNA extraction protocol. Total RNA was further purified and concentrated using a RNA Clean & Concentrator Kit (Zymo Research, R1013) according to manufacturer's instructions. RNA quality and quantity were evaluated using a 5200 Fragment Analyzer (Agilent). Samples with a RIN > 9.9 were selected for sequencing. One hundred nanograms of RNA was used to generate the libraries using the TruSeq Stranded mRNA kit (Illumina, 20020594). These libraries were sequenced on an NovaSeq 6000 (Illumina) sequencer on an S4 flow cell.

Bulk RNA sequencing analysis

Preprocessing, alignment to the mouse genome (GRCm38/mm10), sequence counting, and quality control of the bulk RNA-Seq data were carried out with the *nf-core/rnaseq* pipeline. RNA-Seq data were further analyzed using R Bioconductor (4.2.3) and the DESeq2 package (1.38.3)³¹⁶. DEGs were calculated using the DESeq function. Gene Ontology (GO) enrichment analyses on DEGs was performed using the *dag_enrich_on_genes* function from the *simona* package³³⁸.

Gene Set Enrichment Analysis

For bulk RNA-Seq, GSEA was performed using GSEA software (4.1.0). In brief, genes from gene sets were ranked according to their expression levels in *Mafb*^{fl/fl} BMDM and *Lyz2*^{Cre}*Mafb*^{fl/fl} BMDMs using the *Signal2Noise* method. The Normalized Enrichment Score (NES), False Discovery Rate (FDR), and nominal *P*-values were determined through 1000 sample permutations across different phenotypes.

Monocyte signature genes and mac signature genes were retrieved by comparing gene expression levels between monocytes and macs in the ImmGen database using the ImmGen Population Comparison data browser.

Bone marrow chimeras

For mixed bone marrow competitive chimeras, CD45.1.2 mice received two doses of 5.5 Gy lethal irradiation, 15 minutes apart, and were reconstituted by intravenous injection of 10^7 bone marrow cells, consisting of a 1:1 mix of cells from CD45.1 WT and CD45.2 *Lyz2^{Cre}Mafb^{fl/fl}* mice. Starting from the day of irradiation, mice were treated with enrofloxacin (0.05 mg/ml; Baytril, Bayer) in their drinking water for 4 weeks. Four weeks after irradiation, blood chimerism was evaluated by flow cytometry.

Single-cell RNA sequencing library preparation

Two independent scRNA-seq experiments were performed. In the first experiment, peritoneal macrophages and liver macrophages were isolated. In the second experiment, colonic and brain macrophages were isolated. For each experiment, cells were FACS-sorted from *Lyz2^{Cre}Mafb^{fl/fl}* mice and *Mafb^{fl/fl}* littermate controls.

Specifically, in the first experiment we sorted 5×10^4 CD45⁺Lin⁻Ly6C⁻CD11b⁺CD115⁺ live cells from the peritoneal lavage and 5×10^4 CD45⁺Lin⁻Ly6C⁻CD11b^{int/+}F4/80⁺CD64⁺ live cells from the liver. In the second experiment we sorted 5×10^4 CD45⁺Lin⁻CD11b⁺F4/80⁺CD64⁺ live cells from the colon and 5×10^4 CD45⁺Lin⁻Ly6C⁻CD11b⁺F4/80⁺CD64⁺ live cells from the brain. Sorting was performed in PBS with 5% FBS. Sorted cells were barcoded with TotalSeq™-B anti-mouse Hashtag antibodies (Biolegend). Hashtag barcoded cells were washed, pooled per genotype, spun down and resuspended in PBS with

0.04% UltraPure™ BSA (Thermo Fisher Scientific, AM2616) at an estimated final concentration of 1000 cells/ μ l. Cell suspensions were loaded into the Chromium iX (10x Genomics) at a target recovery of 2×10^3 cell per sorted population and scRNA-seq libraries were prepared using Chromium Single Cell 3' GEM, Library & Gel Bead Kit v3.1 (10x Genomics, 1000128) according to demonstrated 10x Genomics protocol "Next GEM Single Cell 3' Reagent Kits v3.1 with Feature Barcoding technology for Cell Surface Protein" (CG000206 Rev D). In brief, single-cell Gene Expression Matrices (GEMs) were generated by combining barcoded Single Cell 3' v3.1 Gel Beads, a Master Mix, and hashtag-labeled cells with Partitioning Oil on a Chromium Chip G (10x Genomics). Reverse transcription was performed using a Veriti Thermocycler (Thermo Fisher Scientific) at 53°C for 45 minutes, 85°C for 5 minutes, and holding at 4°C. Next, GEMs were disrupted, and pooled fractions were purified using DynaBeads MyOne Silane Beads (10x Genomics, No. 2000048). Full-length cell-barcoded cDNA and hashtag were amplified via PCR with a 12-cycle reaction module at 98°C for 3 minutes, 11 cycles at 98°C for 15 seconds, 63°C for 20 seconds, and 72°C for 1 minute, followed by a final extension at 72°C for 1 minute. Feature cDNA Primer 2 (PN2000097, 10x Genomics) was used to amplify both cDNA and hashtag. The cDNA reaction was purified and size-selected for library preparation using SPRI Beads (Beckman Coulter). The supernatant, containing Cell barcoded hashtag amplicons, was separated and purified again for hashtag library preparation. For 3' Gene Expression library construction, amplified cDNA was fragmented and size-selected. Adaptors (read 2 sequences) were added through End Repair, A-tailing, and partial Adaptor Ligation. Libraries were then amplified by PCR (indexing PCR) using different dual index primers per sample (PN-3000431 Dual Index Plate TT Set A). Purified hashtag amplicons were processed in an indexing PCR using Feature SI Primers 2 (PN2000099, 10x Genomics) with single index primers (PN-2000240 Single Index Plate T Set A, 10x Genomics). Both the 3' Gene Expression

and hashtag libraries were quality-checked on QIAxel and quantified by qPCR using Kapa SyberFast (Roche). Libraries were sequenced on an NovaSeq 6000 (Illumina) using an S4 flow cell for paired-end 150 cycles, but demultiplexed with read 1: 28 cycles; read 2: 91 cycles; index i7: 10 cycles; index i5:10 cycles, with a sequencing depth of 20,000 reads per cell for cDNA and 5,000 reads per cell for hashtag libraries.

Single-cell RNA sequencing analysis

Demultiplexing, alignment to the mouse genome (GRCm38/mm10), filtering, unique molecular identifier counting and construction of gene-barcode matrices of the scRNA-seq data were performed using Cell Ranger (7.1.0). ScRNA-seq data were further analyzed using R Bioconductor (4.2.3) and the Seurat package (4.3.0). Filtered matrices containing cell IDs and feature names for each sample were used to construct a Seurat object. Datasets from both experiments were merged and integrated with previously published scRNA-seq data containing CD45⁺SSC^{lo}CD11b⁺F4/80⁺CD64⁺ lung IM cells of *Lyz2^{Cre}Mafb^{fl/fl}* mice and *Mafb^{fl/fl}* littermate controls (GSE193891). Quality control was performed by excluding cells with fewer than 200 detected genes, genes detected in fewer than three cells, and cells with more than 10% mitochondrial gene content. Gene counts for each sample were normalized using the default *LogNormalize* method, with a scale factor of 10,000 followed by log transformation. The top 2,000 highly variable features were identified using the *vst* method. Contaminating and actively proliferating cells were removed based on the expression of specific genes. Cells were clustered using the *FindClusters* function and the macrophage subsets were identified based on the expression of Hashtag barcodes and known macrophage subset specific genes. DEGs between macrophages subsets from *Mafb^{fl/fl}* and *Lyz2^{Cre}Mafb^{fl/fl}* mice were determined using the *FindMarkers* method.

Signature scoring

For scRNA-seq, gene set signature scores were calculated using the *AddModuleScore* function (Seurat). The scores were saved within a Seurat object and visualized using the Seurat package. Differences in gene set signature scores between macrophages subsets from *Mafb^{fl/fl}* and *Lyz2^{Cre}Mafb^{fl/fl}* mice were determined using a Wilcoxon rank sum test.

Mac subset-specific signature scores were calculated using the scRNA-seq data of RTMs from *Mafb^{fl/fl}* mice by comparing each RTM subset to all other subsets in the dataset using the *FindAllMarker* function (Seurat).

EMP, preMac and Mac signature genes have been previously described⁶⁵.

Confocal microscopy

Confocal microscopy was performed as described previously⁵⁸. Immediately after euthanizing mice with CO₂, the inferior vena cava was cannulated, and the liver was perfused with Antigenfix (Diapath, P0014) at 5 ml/min for 5 min at room temperature. Liver slices (2–3 mm) were then fixed by immersion in Antigenfix for 1 h at 4 °C, washed in PBS, cryoprotected overnight in 34% sucrose, and embedded in Tissue-Tek OCT compound (Sakura Finetek). Cryosections (20 μm) were cut using a Microm HM 560 cryostat (Thermo Fisher Scientific), rehydrated in PBS for 5 min, permeabilized with 0.5% saponin (Sigma-Aldrich, 4521), and blocked for 30 min with 2% bovine serum albumin, 1% fetal calf serum, and 1% donkey serum (Abcam, ab7475). Sections were incubated overnight at 4 °C with primary antibodies, followed by incubation with DAPI (Thermo Fisher Scientific, D3571) and secondary antibodies for 1 h at room temperature. Slides were mounted with ProLong Diamond (Thermo Fisher Scientific, P36970), imaged on a Zeiss LSM980 confocal microscope equipped with a spectral detector using

spectral unmixing. For image analysis, Z-stacks were converted to single-plane, per-channel images by mean projection along the Z axis. The projected 2D images were imported into QuPath (0.5.1), where a pixel classifier was first trained and then applied to all images and class-specific binary masks were exported. Each mask was cleaned in scikit-image (0.20.0) using binary opening (disk radius = 2 px), filling of small holes (< 64 px), and removal of very small objects (< 100 px). Masks were resized with nearest-neighbor interpolation to match the measurement-image resolution and converted to labeled objects via connected components (skimage.measure.label; connectivity = 2). A final size filter retained objects with area $\geq 1,500$ px for analysis. For each labeled object (cell), solidity and Tim4 expression were quantified using scikit-image (skimage.measure; regionprops/regionprops_table): solidity was defined as the ratio of the object area to the area of its convex hull, and Tim4 expression was measured as the mean intensity of the Tim4 channel within the object mask.

***In vivo* phagocytosis assay**

pHrodo™ Red *S. aureus* Bioparticles (Thermo Fisher Scientific, A10010) were prepared in PBS according to the manufacturer's instructions. *Mafb^{fl/fl}* or *Lyz2^{Cre}Mafb^{fl/fl}* mice received 50 μ g Bioparticles either intraperitoneally (i.p.) to assess uptake by LPMs or intravenously (i.v.) to assess uptake by KCs. Mice were sacrificed 20 min (i.p.) or 30 min (i.v.) post-injection, followed by collection of peritoneal lavage or dissection of the liver, respectively. As a negative control, one mouse was sacrificed immediately after injection. Bioparticle uptake by LPMs and KCs was analyzed by FACS.

***In vivo* erythrophagocytosis assay**

C57BL/6J wild-type mice were terminally anesthetized and perfused via the left ventricle with 20 ml PBS containing 10 mM EDTA. Perfusate was collected via a small incision in the right atrium using fine scissors, and cells were pelleted by centrifugation at $800 \times g$ for 10 min. CD45⁺ immune cells were depleted using MACS with CD45 MicroBeads (Miltenyi Biotec, 130052301), the flowthrough containing red blood cells (RBCs) was recovered and centrifuged at $800 \times g$ for 10 min.

Senescent RBCs (sRBCs) were generated by mild heat treatment for 20 min at 48 °C under continuous agitation. For labeling, a total of 1×10^{10} sRBCs were resuspended in 1 ml Diluent C and incubated with an equal volume of Diluent C containing 4 μ M PKH26 (Sigma-Aldrich, MIDI26) for 5 min at room temperature in the dark. The reaction was quenched with 10 ml PBS supplemented with 0.5% BSA and 2% FCS, followed by two washes with PBS. PKH26-labeled sRBCs were resuspended in PBS at a final concentration of 1×10^{10} cells/ml.

For the erythrophagocytosis assay, *Mafb^{fl/fl}* or *Lyz2^{Cre}Mafb^{fl/fl}* mice were injected i.v. with 1×10^9 PKH26-labeled sRBCs. After 30 min, mice were sacrificed, spleens were harvested, and RPM uptake of PKH26-sRBCs was analyzed by flow cytometry.

Iron stain

Spleens from *Mafb^{fl/fl}* or *Lyz2^{Cre}Mafb^{fl/fl}* mice were dissected, weighed, fixed overnight in 4% formaldehyde (Fisher, BP531500) in PBS, paraffin-embedded, cut into 5- μ m sections, stained with Perl's Prussian blue solution and counterstained with Nuclear Fast Red. Images were acquired on a Axioscan 7 (Zeiss) and analyzed by QuPath (0.5.1).

Lung function measurements

Mice were anesthetized via i.p. administration of 50 mg/kg sodium pentobarbital (Nembutal). Following a midline incision in the neck, the trachea was exposed and intubated with an 18-gauge blunt metal cannula with a resistance of 0.18 cmH₂O·s/ml. The cannula was secured in place using nylon suture and connected to a computer-controlled small animal ventilator (flexiVent, SCIREQ) through FX adaptor Y-tubing. Ventilator settings were adjusted to standard murine parameters: tidal volume of 10 ml/kg, respiratory rate of 150 breaths/min, positive end-expiratory pressure (PEEP) of 3 cmH₂O, and a fraction of inspired oxygen (FiO₂) of 0.21 (room air). Respiratory system mechanics were then quantified using the forced oscillation technique (FOT) with flexiWare software (8.1.3).

Whole gut transit time assay

Whole-gut transit time was measured using carmine red gavage. After an overnight fast, *Mafb^{fl/fl}* or *Lyz2^{Cre}Mafb^{fl/fl}* mice were orally gavaged with a 6% (w/v) solution of carmine red (Sigma-Aldrich, C1022) prepared in sterile 0.5% methyl cellulose (Sigma-Aldrich, 423181) and subsequently single-housed. Animals were observed at 15-minute intervals, and the time from gavage to the appearance of the first red-colored fecal pellet was recorded as the total whole-gut transit time.

Kidney stone model

Mafb^{fl/fl} or *Lyz2^{Cre}Mafb^{fl/fl}* mice were injected i.p. with sodium oxalate (NaOx, Sigma-Aldrich, 223433) at 40 mg/kg daily for 7 days. Twenty-four hours after the final injection, mice were sacrificed and perfused with cold PBS followed by 4% formaldehyde in PBS. Kidneys were dissected fixed overnight in 4%

formaldehyde, paraffin-embedded, sectioned at 5 μm , and stained with 0.2% Alizarin Red S (pH 6.8) for 10 min at 37 °C. Images were acquired on a Axioscan 7 (Zeiss) and analyzed by QuPath (0.5.1).

Human monocyte-derived macrophages differentiation

Buffy coats from healthy volunteers were obtained through the Belgian Red Cross. Peripheral blood mononuclear cells were isolated by density gradient centrifugation on Lymphoprep (1.077 g/ml; StemCell Technologies). Classical monocytes were negatively selected using the Classical Monocyte Isolation Kit (Miltenyi Biotec, 130117337) according to the manufacturer's instructions. Monocytes were seeded in Petri dishes (10×10^6 cells/dish) in RPMI supplemented with 10% FBS, 1 \times MEM NEAA (Thermo Fisher Scientific, 11140050), 50 μM β -mercaptoethanol, and 50 ng/ml recombinant human CSF-1 (Immunotools, 11343115). Fresh differentiation medium was added on day 3. On day 7, monocyte-derived macrophages (MDMs) were detached using cold PBS containing 0.25 mM EDTA.

CUT&RUN library preparation

CUT&RUN was performed using the CUTANA ChIC/CUT&RUN Kit (EpiCypher, 141048) according to the manufacturer's instructions, with minor modifications. BMDMs or LPMs from *Mafb^{fl/fl}* or *Lyz2^{Cre}Mafb^{fl/fl}* mice, as well as human MDMs from healthy donors, were washed with ice-cold PBS and fixed with 0.1% formaldehyde in PBS for 2 min at room temperature. Fixation was quenched with 0.125 M glycine (Merck, 104691000). For each CUT&RUN sample, 0.5×10^6 fixed cells were incubated with 0.5 μg antibody. The following antibodies were used: anti-MafB (Cell Signaling Technology, 41019), anti-H3K27ac (Thermo Fisher Scientific, MA5-23516), and IgG negative control (EpiCypher, 13-0042).

CUT&RUN libraries were prepared using the CUTANA CUT&RUN Library Prep Kit (EpiCypher, 141001) following the manufacturer's instructions and sequenced on a NovaSeq 6000 (Illumina) with an S4 flow cell at a depth of 10 million reads per sample.

CUT&RUN analysis

Raw reads were processed using the *nf-core/cutandrun* pipeline for adapter trimming, alignment to the mouse reference genome (GRCm38/mm10), and quality control. For MafB CUT&RUN, peaks were called using SEACR (Sparse Enrichment Analysis for CUT&RUN) in stringent mode³³⁹. Normalized tag counts were calculated with the *annotatePeaks.pl* function from HOMER. MafB binding sites were defined as peaks with higher normalized tag counts in wild-type compared with *Mafb*-deficient cells. MafB binding sites were assigned to target genes based on proximity to transcription start sites (± 2 kb) using HOMER. CUT&RUN signal tracks were visualized with the Integrative Genomics Viewer (IGV).

Evolutionary conservation scoring

Multiple alignments of 60 vertebrate species to the mouse genome (mm10) and measurements of evolutionary conservation based on the alignment (*phastCons* and *phyloP*) were retrieved from the UCSC Genome Browser. A phylogenetic tree from the multiple genome alignment was constructed using ETE Toolkit (3.1.3). Evolutionary conservation at MafB and PU.1 binding sites was quantified by calculating the mean *phastCons* and *phyloP* score around -500 to $+500$ bp from peak center. Global evolutionary conservation was quantified by subdividing the mouse genome in fragments of 1 kbp and calculating the mean *phastCons* and *phyloP* score of each fragment.

Analysis of published scRNA-seq data

To create a single-cell transcriptomic myeloid cell atlas, we selected myeloid cell clusters from the Tabula Muris Senis atlas³⁴⁰, based on the combined expression of *Ptprc* (CD45) and *Lyz2*. Cells were reclustered using the *FindClusters* function from the Seurat package (4.3.0). Clusters of contaminating and actively proliferating cells were removed and myeloid cell clusters were identified based on the expression of specific genes. To infer TF activity, we ran a Univariate Linear Model using the decoupleR package (2.10.0)³⁴¹. Briefly, for each TF, a linear model is fitted, which predicts the observed gene expression based on TF-target gene interaction weights. The t-value of the slope from the fitted linear model is extracted as TF enrichment score. A TF with a positive score is interpreted as active, while a TF with a negative score is considered inactive.

To generate a single-cell transcriptomic map of macrophage differentiation, we selected clusters of mac and mac progenitors from recently published scRNA-seq data of FACS-sorted CD11b^{low/+} fetal liver cells at embryonic day of development E14.5¹⁸², based on the expression of EMP, preMac and Mac signature genes⁶⁵. Cells were reclustered using the *FindClusters* function from the Seurat package (4.3.0). To evaluate trajectory-based pseudotime analysis, we used the Slingshot package (2.14.0) with EPM as starting cluster and mac as ending cluster.

To quantify the correlation between *Mafb* expression and the expression of mac signature genes or MafB target genes in single-cell atlases across different species, genes were converted into species-specific orthologs using g:Profiler. Mac signature genes or MafB target genes scores were calculated using the *AddModuleScore* function from the Seurat package. Correlation between *Mafb* expression and the expression of mac signature genes or MafB target genes was calculated using Pearson correlation.

Quantification and statistical analysis

Data was visualized with Prism 9 (GraphPad) and R Bioconductor (4.2.3) using packages *ggplot2* and *ComplexHeatmap*. Data are presented as mean \pm SEM unless stated otherwise. Sample sizes were not pre-determined by statistical methods but are consistent with those used in previous publications^{60,97,104,110,186,326}. Data were assumed to follow a normal distribution for parametric tests, though this was not formally tested. Results from independent experiments were combined for analysis in each panel, unless otherwise specified, and no data were excluded. Investigators were not blinded during data collection and analysis. Statistical analyses were carried out using Prism 9 (GraphPad), and R Bioconductor (4.2.3) with DESeq2 (1.38.3) for bulk RNA-seq and Seurat (4.3.0) for scRNA-seq data. Detailed statistical methods for each experiment are provided in the figure legends. A *P*-value of less than 0.05 was considered statistically significant (*, *P* < 0.05; **, *P* < 0.01; ***, *P* < 0.001; ****, *P* < 0.0001; ns, not significant).

Data and code availability

Bulk RNA-seq, scRNA-seq and CUT&RUN data have been deposited at GEO and are publicly available under accession GSE287347.

All codes for analysis of sequencing data have been deposited at GitHub and are publicly available at: https://github.com/dovneste/MafB_Mac.

Results

Elevated MafB expression and activity are conserved in mouse RTMs

To identify transcriptional regulators of Mac identity, we analyzed ImmGen microarray data from monocyte, DC, and RTMs³⁴². Core Mac genes, such as *Csf1r*, *C1q* and *Mertk*, as well as the gene encoding *Mafb* TF, ranked among the top genes upregulated in RTMs *versus* DCs and monocytes (**Figure 3.1A**). *Mafb* expression was low in AMs, consistent with previous findings^{110,243}. Using the Tabula Muris Senis scRNA-seq dataset³⁴⁰, we found high MafB expression and predicted TF activity based on the co-expression of target genes³⁴¹ in brain MG, liver Kupffer cells (KCs), lung IM and other tissue Macs, but not in AMs (**Figures 3.1B–F**). Intracellular flow cytometry confirmed higher MafB protein levels in RTM populations from C57BL/6 wild-type (WT) mice, except in AM, compared with blood monocytes and DCs from the same tissues (**Figures 3.1G, 3.1H, and Supplementary figure 3.1**). In the colon, where colonic Macs (CMs) are continuously renewed through the “monocyte waterfall”¹⁰¹, MafB expression gradually increased along this trajectory (**Figures 3.1I and 3.1J**). A similar pattern was observed in the peritoneal cavity, where Ly6C⁺ monocytes progressively differentiate into F4/80⁺ large peritoneal Macs (LPMs) via F4/80^o small peritoneal Macs (SPMs)³⁴³ (**Figures 3.1K and 3.1L**). Hence, MafB is highly and exclusively expressed in RTM populations across tissues and its expression is upregulated during Mac differentiation from monocytes.

MafB deficiency impedes the full differentiation of macs *in vitro*

To examine the role of MafB in Mac differentiation *ex vivo*, BM monocytes (BMMos) from myeloid-intrinsic *Mafb*-deficient (i.e., *Lyz2^{Cre}Mafb^{fl/fl}*)¹¹⁰ or control (*Mafb^{fl/fl}*) mice were cultured with *Csf1* to generate BM-derived macs (BMDMs)

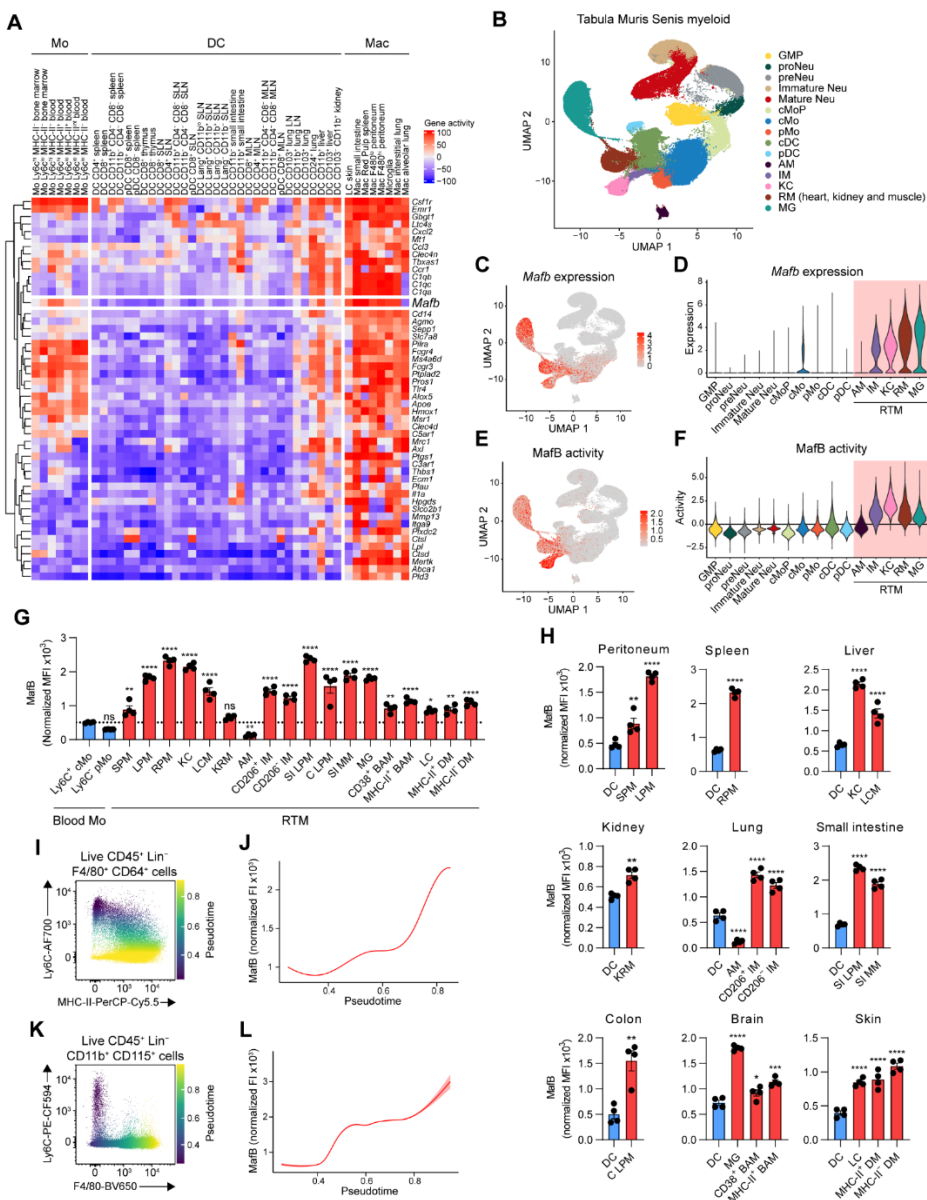


Figure 3.1. Elevated *MafB* expression and activity define mature RTMs in mice. (A) Heatmap showing the top 50 genes upregulated in Macs compared with monocytes (Mo) and DCs, inferred from microarray data on the Gene Expression Commons platform. (B) UMAP of myeloid cell transcriptional identity from the Tabula Muris Senis (TMS) dataset. (C) Feature plot of *MafB* expression, as in B. (D) Violin plot of *MafB*

expression across myeloid cell clusters, as in C (height, expression; width, cell abundance). (E) Feature plot of MafB activity inferred with decoupleR, as in B. (F) Violin plot of MafB activity across myeloid cell clusters, as in E. (G) Bar graphs of MafB expression in blood Mo (blue) and RTM (red) populations, measured by flow cytometry (n = 4). (H) Bar graphs of MafB expression in DC and RTM populations from indicated organs, measured by flow cytometry (n = 4). (I) Scatter plot of Ly6C and MHC-II expression in colon CD45⁺Lin⁻F4/80⁺CD64⁺ cells colored by Wanderlust pseudotime (merged from 4 mice). (J) MafB expression along pseudotime, as in I. (K) Scatter plot of Ly6C and F4/80 expression in CD45⁺Lin⁻CD11b⁺CD115⁺ peritoneal cells colored by Wanderlust pseudotime (merged from 4 mice). (L) MafB expression along pseudotime, as in K. Data are mean ± SEM (G and H). P values were calculated using one-way ANOVA with Tukey's post hoc test (G), two-tailed Student's t test (H, spleen, kidney, and colon), or one-way ANOVA with Dunnett's post hoc test (H and other organs). *, P < 0.05; **, P < 0.01; ***, P < 0.001; ****, P < 0.0001. cDC, conventional DC; C LPM, colonic lamina propria Macs; cMoP, common Mo progenitors; DM, dermal Macs; GMP, granulocyte–monocyte progenitors; LC, Langerhans cells; LCM, liver capsular Macs; LN, lymph node; MFI, mean fluorescence intensity; MLN, mesenteric lymph nodes; Neu, neutrophils; pDC, plasmacytoid DC; pMo, patrolling Mo; RM, resident Mac; SI LPM, small intestinal lamina propria Macs; SI MM, small intestinal muscularis Macs; SLN, skin-draining lymph nodes. See also **Supplementary figure 3.1**.

(Figure 3.2A). Although BMMos from *Lyz2^{Cre}Mafb^{fl/fl}* and control mice both produced CD11b^{hi}F4/80^{hi} cells (**Supplementary figure 3.2A**), *Mafb*-deficient BMDMs did not adopt a typical amoeboid spindle-like cell shape with distinct lamellipodia and remained smaller, spherical and with few filopodia (**Figures 3.2B, 3.2C, and Supplementary figure 3.2B; Supplementary video 1 and 2**), suggesting impaired differentiation. Bulk RNA-seq analyses identified 808 differentially expressed genes (DEGs) (\log_2 fold change > 1 or < -1, adjusted P value < 5×10^{-2}) between control and MafB-deficient BMDM (**Figures 3.2D and 3.2E; Supplementary table 3.2**), with reduced *Mafb* and prototypical Mac genes, such as *Mertk* and C1q complement genes (*C1qa*, *C1qb* and *C1qc*), and increased monocyte genes (*Ly6c*, *Ccr2*) in MafB-deficient BMDMs compared to control BMDMs (Figure 2D). We generated monocyte and Mac signature scores by

comparing monocytes and RTMs in the ImmGen database (**Supplementary table 3.3**) and found, using Gene Set Enrichment Analysis (GSEA), that the monocyte signature was significantly enriched in MafB-deficient BMDMs, while the Mac signature was enriched in control BMDMs (**Figure 3.2F**). In addition, BMDMs from *Lyz2^{Cre}Mafb^{fl/fl}* mice exhibited significantly higher protein expression of the classical monocyte markers Ly6C, CD62L and CD11a and lower protein expression of the Mac markers MerTK, C1qA and FR- β compared to those from control mice (**Figures 3.2G** and **Supplementary figure 3.2C**). Gene ontology (GO) analyses revealed an enrichment of developmental processes (e.g., cell-cell differentiation, development) in control BMDMs, and of stimulus response (e.g., communication, activation) in MafB-deficient BMDMs (**Supplementary figures 3.2D** and **3.2E**), reminiscent of a plastic monocyte phenotype. These findings indicate that MafB regulates Csf1-dependent Mac differentiation *ex vivo*.

MafB controls RTM development and transcriptional identity *in vivo*

Next, to assess whether MafB could also mediate monocyte-to-RTM development *in vivo*, we generated BM competitive chimeras in which CD45.1.2 mice were irradiated and reconstituted with a 1:1 BM cell mix from congenic CD45.1 WT and CD45.2 *Lyz2^{Cre}Mafb^{fl/fl}* mice (**Figure 3.3A**). At week 5 after transfer, the ratio of WT donor chimerism over total donor chimerism of blood neutrophils and monocytes, as well as of SPMs, was between 20 and 45%, while in all other RTMs, such ratio was between 80 and 100% (**Figures 3.3B** and **3.3C**), demonstrating that, in this competitive setting, myeloid-restricted MafB deficiency impaired the ability of monocytes to differentiate in RTMs, at the exception of SPMs.

Next, we asked whether MafB deficiency altered the transcriptional identity of RTMs. Live peritoneal lavage CD45⁺Lin⁻Ly6C⁻CD11b⁺CD115⁺ cells, liver CD45⁺Lin⁻

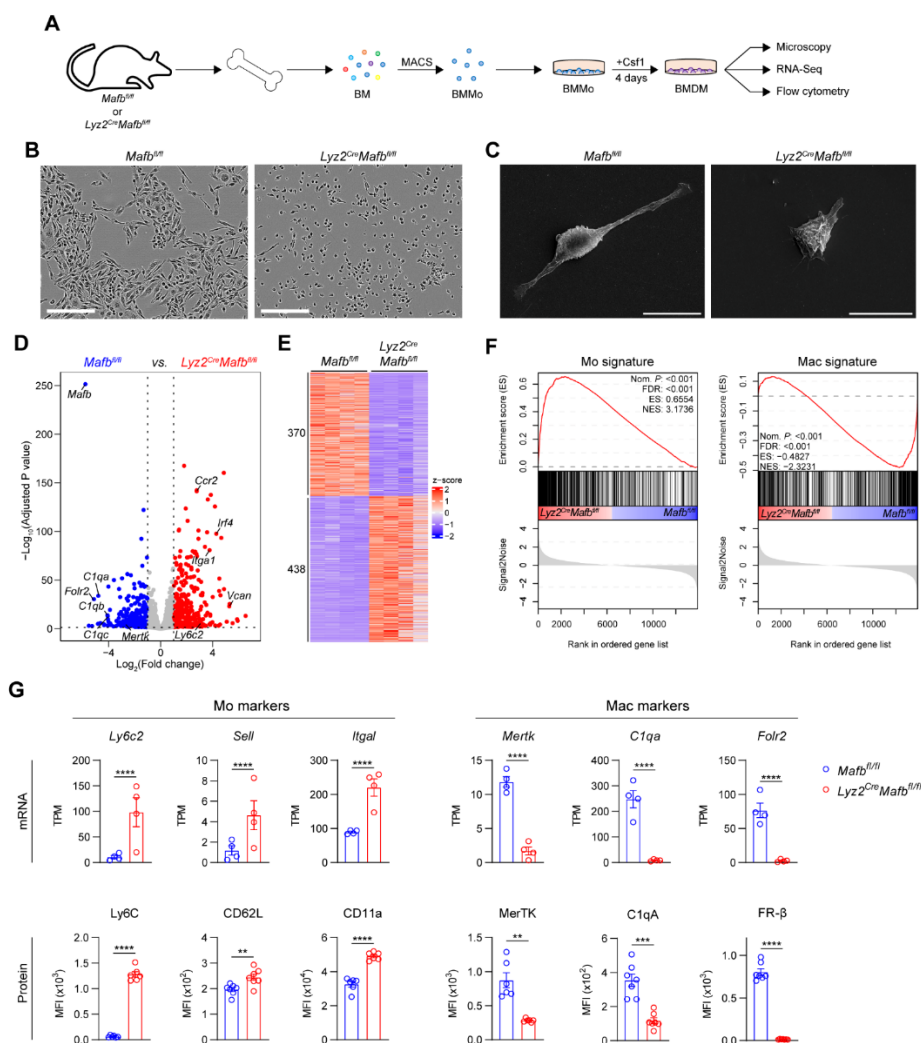


Figure 3.2. MafB deficiency impedes monocyte-to-mac development and mac functional identity *ex vivo*. (A) Experimental outline. (B) Representative phase-contrast images of BMDM (n = 3). Scale bar, 100 μ m. (C) Representative scanning electron microscopy images of BMDM, as in B (n = 3). Scale bar, 20 μ m. (D) Volcano plot of DEGs between BMDM from *Mafb^{fl/fl}* and *Lyz2^{Cre}Mafb^{fl/fl}* mice (n = 4 mice/group). Transcripts enriched in *Mafb^{fl/fl}* and *Lyz2^{Cre}Mafb^{fl/fl}* BMDM are shown in blue and red, respectively (log₂ fold change > 1 or < -1; adjusted P < 0.05). (E) Heatmap of DEGs, as in D. (F) GSEA of Mo and Mac signature genes in DEGs, as in D. (G) Bar graphs of mRNA and protein expression of Mo and Mac markers (n = 4–7). Data are mean \pm SEM, pooled from two independent experiments (G). P values were calculated using a Wald test with Benjamini–Hochberg correction (D and G [mRNA]) or a two-tailed Student’s t test (G

[protein]]. **, $P < 0.01$; ***, $P < 0.001$; ****, $P < 0.0001$. FDR, false discovery rate; NES, normalized enrichment score; TPM, transcripts per kilobase million. See also **Supplementary figure 3.2** and **Supplementary tables 3.2** and **3.3**.

Ly6C⁻CD11b^{int/+}F4/80⁺CD64⁺ cells, colon CD45⁺Lin⁻CD11b⁺F4/80⁺CD64⁺ cells and brain CD45⁺Lin⁻Ly6C⁻CD11b⁺F4/80⁺CD64⁺ cells were FACS-sorted from *Ly2^{Cre}Mafb^{fl/fl}* and *Mafb^{fl/fl}* littermate controls, were hashtag-barcoded and subjected to single cell (sc)RNA-seq (**Figure 3.3D**). Curated data were integrated with previously published scRNA-seq data containing CD45⁺SSC^{lo}CD11b⁺F4/80⁺CD64⁺ lung IMs from *Ly2^{Cre}Mafb^{fl/fl}* mice and *Mafb^{fl/fl}* littermate controls¹¹⁰ and were projected in UMAP plots (**Figure 3.3E** and **Supplementary figure 3.3A**). Based on the expression of hashtag barcodes and known RTM-specific genes, we identified Mac populations corresponding to SPMs (*Cd226*, *Retnla*) and LPMs (*Gata6*, *Icam2*) in the peritoneal lavage; KCs (*Clec4f*, *Cdh5*) in the liver; IMs (*Mgl2*, *Ccl2*) in the lung; and MG (*Tmem119*, *Sall1*) in the brain (**Figure 3.3F**). In the colon, we identified two clusters of CMs characterized by high expression of *Plac8* and *Ly6c2* or of *Cd4* and *H2-M2*, respectively (**Figure 3.3F**). Signature scoring based on DEGs between Ly6C⁺ cells and MHC-II⁺ cells from the monocyte waterfall (**Supplementary table 3.4**)¹³³ showed that these clusters corresponded to Ly6C⁺ CMs and MHC-II⁺ CMs, respectively (**Supplementary figure 3.3B**).

Mafb mRNA was not detected in SPMs, LPMs, KCs, IMs and CMs from *Ly2^{Cre}Mafb^{fl/fl}* mice, while *Mafb* depletion was only partial in MG from *Ly2^{Cre}Mafb^{fl/fl}* mice (**Supplementary figure 3.3C**). Next, we conducted differential gene expression analysis between RTMs from *Ly2^{Cre}Mafb^{fl/fl}* mice and *Mafb^{fl/fl}* littermate controls and identified 92 DEGs in SPMs, 535 DEGs in LPMs, 262 DEGs in KCs, 287 DEGs in IMs, 723 DEGs in Ly6C⁺ CMs, 150 DEGs in MHC-II⁺ CMs and 299 DEGs in MG (**Supplementary figures 3.3D–J**; **Supplementary table 3.5**). Of note, RTM-specific identity genes such as *Retnla*

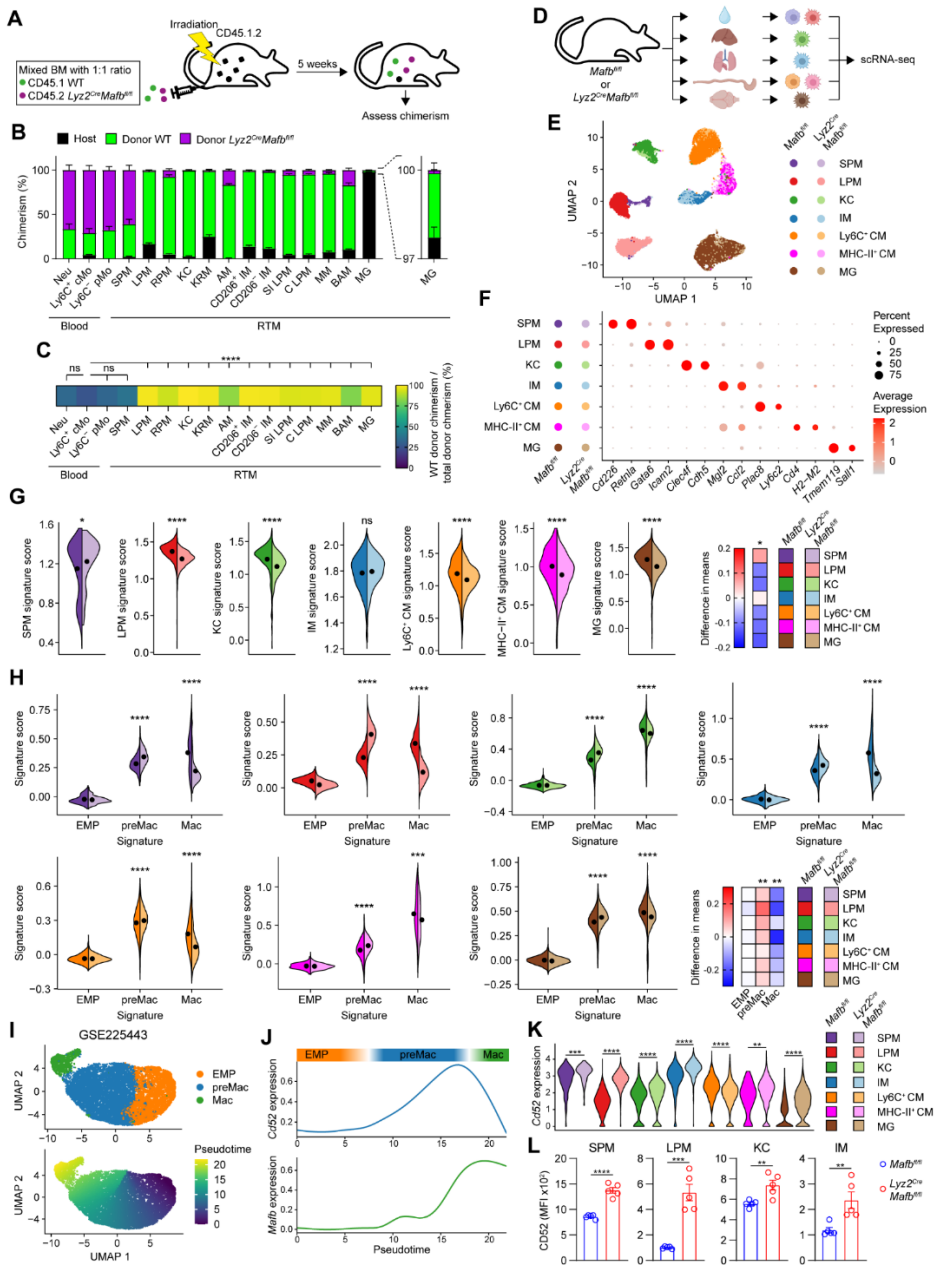


Figure 3.3. Global and subset-specific RTM signatures are disrupted upon myeloid-intrinsic *MafB* depletion *in vivo*. (A) Experimental outline. (B) Bar graphs of donor WT, donor *Lyz2^{Cre}MafB^{fl/fl}*, and host chimerism in blood Neu, Mo, and RTM populations, as in A (n = 5–8). (C) Heatmap of the percentage of WT donor cells relative to total donor

chimerism, as in B. (D) Experimental outline. (E) UMAP plot of RTM transcriptional identity from *Mafb^{fl/fl}* and *Lyz2^{Cre}Mafb^{fl/fl}* mice. (F) Dot plot of average expression and percentage of cells expressing the indicated genes within RTM populations, as in E. (G) Violin plots of RTM subset-specific signature scores in *Mafb^{fl/fl}* and *Lyz2^{Cre}Mafb^{fl/fl}* RTMs (height, score; width, abundance). (H) Violin plots of EMP, pre-Mac, and Mac signature scores in RTM populations from *Mafb^{fl/fl}* and *Lyz2^{Cre}Mafb^{fl/fl}* mice. (I) UMAP of transcriptional identity (top) and pseudotime trajectory (bottom) of fetal liver EMP, pre-Mac, and Mac at embryonic day E14.5. (J) Gene expression of *Cd52* (top) and *Mafb* (bottom) along pseudotime, as in I. (K) Violin plot of *Cd52* expression across RTM populations of *Mafb^{fl/fl}* and *Lyz2^{Cre}Mafb^{fl/fl}* mice (height, expression; width, abundance). (L) Bar graphs of CD52 expression in SPM, LPM, KC, and IM, assessed by flow cytometry in *Mafb^{fl/fl}* and *Lyz2^{Cre}Mafb^{fl/fl}* mice (n = 5). Data are mean ± SEM and are pooled from two independent experiments (B and L). *P* values were calculated using a one-way ANOVA with Sidak's post hoc test (C), a Wilcoxon rank-sum test (G, H, and K) or a two-tailed Student's *t* test (L). *, *P* < 0.05; **, *P* < 0.01; ***, *P* < 0.001; ****, *P* < 0.0001. See also **Supplementary figure 3.3** and **Supplementary tables 3.3–3.7**.

for SPMs, *Vsig4* for LPMs, *Cd163* for KCs, and *Fcrls* for MG were significantly lower expressed in MafB-deficient cells. Next, we created RTM subset-specific scores based on the DEGs of each control RTM subset compared to other RTMs in our scRNA-seq data and found that each RTM subsets from *Lyz2^{Cre}Mafb^{fl/fl}* mice, except for IMs, exhibited a significantly lower score for RTM-subset specific signatures as compared to their respective controls (**Figure 3.3G**; **Supplementary table 3.6**). To examine whether MafB deficiency also affected global Mac differentiation, we mapped previously identified signatures of erythro-myeloid progenitors (EMP), pre-Mac and Mac comprising different stages of Mac differentiation (**Supplementary table 3.7**)⁶⁵. EMP signatures were low in all subsets between MafB-deficient and control RTMs (**Figure 3.3H**). Interestingly, all MafB-deficient RTMs exhibited a significantly higher pre-Mac score as compared to control RTMs (**Figure 3.3H**). Moreover, global Mac signature scores were all significantly lower in MafB-deficient RTMs as compared to their WT counterparts (**Figure 3.3H**). To explore this further, we built a macrophage differentiation atlas from published scRNA-seq data containing CD11b^{low/+} fetal

liver cells at embryonic developmental day E14.5 (**Figure 3.3I** and **Supplementary figure 3.3K**)¹⁸². Using Slingshot pseudotime, we identified *Cd52* as highly expressed in pre-Mac but downregulated at the pre-Mac to Mac transition, coinciding with increased *Mafb* expression (**Figure 3.3J** and **Supplementary figure 3.3L**). Interestingly, *Cd52* was higher expressed in most MafB-deficient RTMs as compared to their WT counterparts, with the exception of Ly6C⁺ CMs (**Figure 3.3K**), and surface expression of CD52 was elevated in SPMs, LPMs, IMs and KCs from *Lyz2^{Cre}Mafb^{f/f}* mice as compared to controls (**Figure 3.3L**). Together, these findings show that MafB mediates RTM differentiation and identity across embryonically-derived and monocyte-derived RTMs, and its absence leads to incomplete differentiation with a persistent CD52^{high} immature signature and loss of subset-specific programs.

Loss of MafB profoundly alters RTM phenotype across tissues

Next, we assessed how MafB deficiency affected RTM abundance and phenotype. MafB deficiency did not alter blood monocyte numbers or proportions, CD62L expression on classical monocytes (cMos), nor the proportion of GMP- or MDP-derived cMos (**Supplementary figures 3.4A–D**)³⁴⁴. In peritoneal lavages, *Lyz2^{Cre}Mafb^{f/f}* mice displayed higher proportion and numbers of LPMs (**Figures 3.4A** and **3.4B**). MafB-deficient SPMs expressed lower MHC-II and Relm α , while LPMs had reduced F4/80,

MerTK and Vsig4 expression (**Figures 3.4C** and **3.4D**). In livers of *Lyz2^{Cre}Mafb^{f/f}* mice, KC proportions decreased while F4/80^{lo}CD11b^{hi} monocyte-macrophage intermediate cells (Mo-Macs) increased (**Figures 3.4E** and **3.4F**). In addition, KC markers FR- β , Tim4, Vsig4, CD163 were reduced in KCs from *Lyz2^{Cre}Mafb^{f/f}* mice as compared to controls (**Figure 3.4G**). Similar decreases in Tim4, Vsig4, CD163

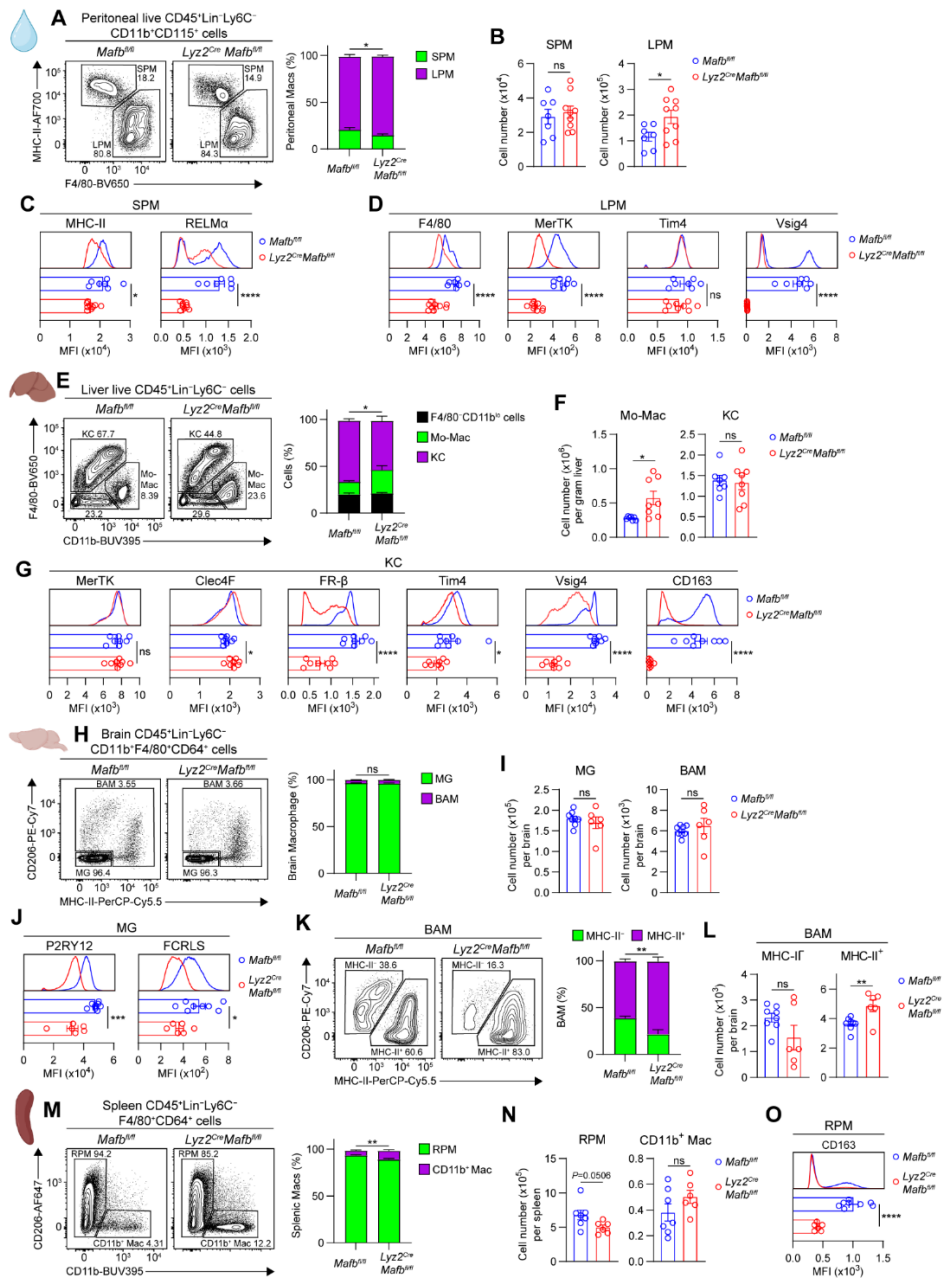


Figure 3.4. Myeloid-specific *Mafb*-deficient mice exhibit drastic changes in the proportion and phenotype of tissue RTMs. (A) Representative contour plots of MHC-II and F4/80 expression in peritoneal CD45⁺Lin⁻Ly6C⁻CD11b⁺CD115⁺ cells from *Mafb*^{fl/fl} and *Lyz2^{Cre}Mafb*^{fl/fl} mice (left) and percentages of SPM and LPM, as gated on the contour.

plots (right) (n = 7–9). All subsequent panels compare *Mafb^{fl/fl}* and *Lyz2^{Cre}Mafb^{fl/fl}* mice. (B) Absolute numbers of SPM and LPM, as in A. (C) Histograms (top) and bar graphs (bottom) of MHC-II and RELM α expression in SPM, as in A. (D) Histograms (top) and bar graphs (bottom) of F4/80, MerTK, Tim4, and Vsig4 expression in LPM, as in A. (E) Representative contour plots of F4/80 and CD11b expression in liver CD45⁺Lin⁻Ly6C⁻ cells (left) and percentages of F4/80⁻CD11b^{lo} cells, CD11b^{hi} Mo-Macs, and KCs, as gated on the contour plots (right) (n = 8). (F) Absolute numbers of CD11b^{hi} Mo-Macs and KCs, as in E. (G) Histograms (top) and bar graphs (bottom) of MerTK, Clec4F, Tim4, Vsig4, FR- β , and CD163 expression in KCs, as in E. (H) Representative contour plots of CD206 and MHC-II expression in brain CD45⁺Lin⁻Ly6C⁻F4/80⁺CD64⁺ cells (left) and percentages of MG and BAM, as gated on the contour plots (right) (n = 6–8). (I) Absolute numbers of MG and BAM, as in H. (J) Histograms (top) and bar graphs (bottom) of P2RY12 and FCRL5 expression in MG, as in H. (K) Representative contour plots of CD206 and MHC-II expression in BAM (left) and percentages of MHC-II⁻ and MHC-II⁺ BAM, as gated on the contour plot (right) (n = 6–8). (L) Absolute numbers of MHC-II⁻ and MHC-II⁺ BAM, as in K. (M) Representative contour plots of CD206 and CD11b expression in spleen CD45⁺Lin⁻Ly6C⁻F4/80⁺CD64⁺ cells (left) and percentages of RPM and CD11b⁺ mac, as gated on the contour plots (right) (n = 6–7). (N) Absolute numbers of RPM and CD11b⁺ macs, as in M. (O) Histograms (top) and bar graphs (bottom) of CD163 expression in RPM, as in M. Data are mean \pm SEM and are pooled from two independent experiments. *P* values were calculated using a two-tailed Student's *t* test. *, *P* < 0.05; **, *P* < 0.01; ***, *P* < 0.001; ****, *P* < 0.0001. ns, not significant. See also **Supplementary figure 3.4** and **3.5**

expression were seen in KCs from *Clec4f^{Cre}Mafb^{fl/fl}Mafb^{fl/fl}* mice as compared to controls (**Supplementary figure 3.5A**). Of note, confocal microscopy analyses revealed that KCs from *Lyz2^{Cre}Mafb^{fl/fl}* and from *Clec4f^{Cre}Mafb^{fl/fl}Mafb^{fl/fl}* mice displayed a less stellate morphology and lower Tim4 expression compared to control KCs (**Supplementary figures 3.5B–E**). In lungs, as reported¹¹⁰, *Lyz2^{Cre}Mafb^{fl/fl}* mice showed an imbalance between CD64⁺ monocytes and IMs with fewer IMs (**Supplementary figures 3.4E** and **3.4F**). MafB-deficient IMs expressed more CD11b but less F4/80, MHC-II and CD206, while IM subset proportions were unchanged (**Supplementary figures 3.4G–I**). In the colons of *Lyz2^{Cre}Mafb^{fl/fl}* mice, Ly6C⁺ CMs increased while Ly6C⁺MHC-II⁺ CMs decreased (**Supplementary figures 3.4J** and **3.4K**). MHC-II⁺ CM numbers were unchanged,

but MafB-deficient MHC-II⁺ CMs expressed more CD11b and less CD163 (**Supplementary figure 3.4L**). CD163 expression in MHC-II⁺ CMs has been proposed to distinguish CD163⁻ colonic lamina propria Macs (C LPMs) and CD163⁺ muscularis Macs (MMs)³⁴⁵. Nevertheless, the proportions and counts of C-LPMs and MMs were unaffected in *Lyz2^{Cre}Mafb^{fl/fl}* mice (**Supplementary figures 3.4M and 3.4N**). In *Lyz2^{Cre}Mafb^{fl/fl}* brains, MG and border-associated Mac (BAM) numbers were unchanged (**Figures 3.4H and 3.4I**), but MG showed reduced P2ry12 and Fcrls expression (**Figure 3.4J**). Lower MG-intrinsic P2ry12 expression was also observed in tamoxifen-treated *Tmem119^{CreERT2}Mafb^{fl/fl}* mice compared to controls (**Supplementary figure 3.5F**). Higher percentage and numbers of MHC-II⁺ BAMs were also found in the brains of *Lyz2^{Cre}Mafb^{fl/fl}* mice (**Figures 3.4K and 3.4L**). In *Lyz2^{Cre}Mafb^{fl/fl}* spleen, red pulp Macs (RPMs) tended to decrease while CD11b⁺ Mac increased, and RPMs showed decreased CD163 expression, similar to KCs (**Figures 3.4O–Q**). In kidneys of *Lyz2^{Cre}Mafb^{fl/fl}* mice, kidney resident Mac (KRM) proportions decreased among CD11b⁺ cells, with reduced F4/80 and increased Ly6C expression (**Supplementary figures 3.4N–P**). These results support that MafB deficiency profoundly disrupts RTM abundance and phenotype across tissues.

MafB mediates key RTM phagocytic and homeostatic functions

Next, we examined the functional consequences of MafB loss on RTMs. First, we focused on the core function of macs, phagocytosis. Upon intraperitoneal injection of *S. aureus* pHrodo-Red particles, both the proportion of positive LPMs and the particle load per cell were significantly reduced in *Lyz2^{Cre}Mafb^{fl/fl}* mice compared to controls (**Figures 3.5A and 3.5B**). KC phagocytosis was even more impaired after intravenous (i.v.) injection (**Figures 3.5C and 3.5D**). Given the key role of splenic RPMs in erythrocyte recycling and iron homeostasis¹⁶⁶, we injected PKH26-labeled senescent red blood cells (sRBCs) i.v. and found that

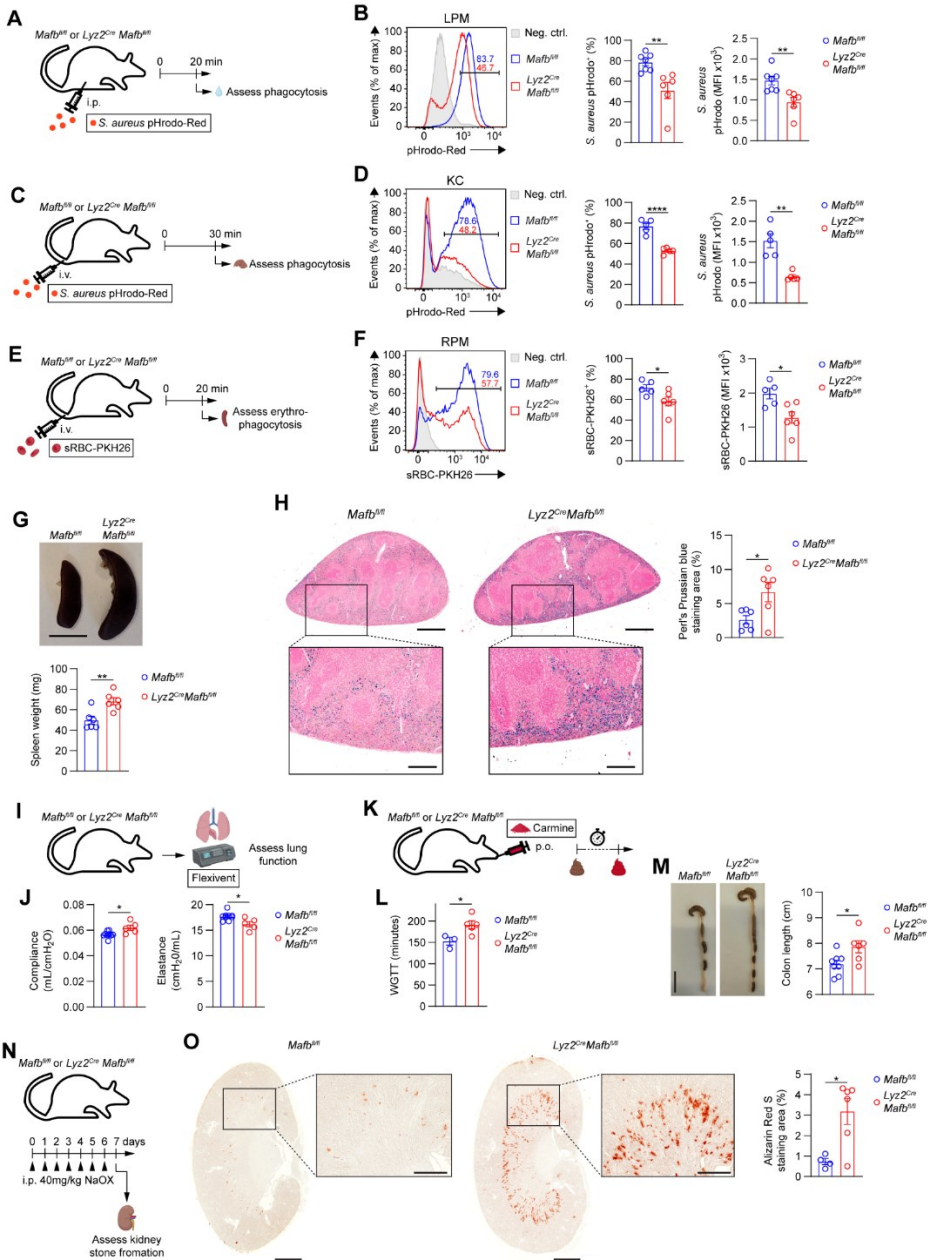


Figure 3.5. MafB deficiency impacts essential core and tissue-specific RTM functions. (A) Experimental outline. (B) Representative histograms (left) and bar graphs (middle, right) of *S. aureus* pHrodo-Red Bioparticle uptake in LPMs from *Mafb^{fl/fl}* and *Lyz2^{Cre}Mafb^{fl/fl}* mice, depicting the percentage of pHrodo⁺ cells (middle) and MFI (right),

as in A (n = 6–7). (C) Experimental outline. (D) Representative histograms (left) and bar graphs (middle, right) of *S. aureus* pHrodo-Red Bioparticle uptake in KCs from *Mafb^{fl/fl}* and *Lyz2^{Cre}Mafb^{fl/fl}* mice, depicting the percentage of pHrodo+ cells (middle) and MFI (right), as in C (n = 5). (E) Experimental outline. (F) Representative histograms (left) and bar graphs (middle, right) of sRBC-PKH26 uptake in RPMs from *Mafb^{fl/fl}* and *Lyz2^{Cre}Mafb^{fl/fl}* mice, depicting the percentage of PKH26+ cells (middle) and MFI (right), as in E (n = 5–6). (G) Representative images (top) and bar graphs of spleen weight (bottom) from *Mafb^{fl/fl}* and *Lyz2^{Cre}Mafb^{fl/fl}* mice (n = 6). Scale bar, 0.5 cm. (H) Representative images of spleens from *Mafb^{fl/fl}* and *Lyz2^{Cre}Mafb^{fl/fl}* mice stained with Perl's Prussian blue to examine iron deposition (left; overview, scale bars 1 mm; bottom, magnified views, scale bars 200 μ m) and bar graphs of Prussian blue+ area (right) (n = 6). (I) Experimental outline. (J) Bar graphs of lung compliance (left) and elastance (right) from *Mafb^{fl/fl}* and *Lyz2^{Cre}Mafb^{fl/fl}* mice measured by FlexiVent assay, as in I (n = 5–9). (K) Experimental outline. (L) Bar graphs of WGTT, as in K (n = 3–4). (M) Representative images (left) and bar graphs of colon length (right) from *Mafb^{fl/fl}* and *Lyz2^{Cre}Mafb^{fl/fl}* mice (n = 6–8). Scale bar, 2 cm. (N) Experimental outline. (O) Representative images of kidneys from *Mafb^{fl/fl}* and *Lyz2^{Cre}Mafb^{fl/fl}* mice stained with Alizarin Red S to examine CaOx crystal deposition (left; overview, scale bars 1 mm; inset, magnified views, scale bars 500 μ m) and bar graphs of Alizarin Red S+ area (right), as in N (n = 4–6). Data are mean \pm SEM and are pooled from two independent experiments. P values were calculated using a two-tailed Student's t test. *, P < 0.05; **, P < 0.01; ****, P < 0.0001.

MafB-deficient RPMs showed reduced erythrophagocytosis (**Figures 3.5E** and **3.5F**). These observations were also reflected at the tissue level without sRBC injection, with *Lyz2^{Cre}Mafb^{fl/fl}* mice suffering from splenomegaly and abnormal iron accumulation in the spleen red pulp, as revealed by Perl's Prussian blue staining (**Figures 3.5G** and **3.5H**). Since IMs and CMs have been shown to support lung mechanics⁶⁰ and gut motility³⁴⁶, respectively, we measured these functions in *Lyz2^{Cre}Mafb^{fl/fl}* mice. We observed increased lung compliance and decreased elastance (**Figures 3.5I** and **3.5J**), along with delayed whole gut transit time (WGTT) and increased colon length (**Figures 3.5K** and **3.5L**), consistent with impaired mucosal RTM functions. Finally, given the role of KRM in preventing kidney stone formation²⁰⁶, we tested this function using sodium oxalate injections and found abnormal oxalate crystal accumulation within the renal medulla of *Lyz2^{Cre}Mafb^{fl/fl}* mice, as revealed by Alizarin Red S stain (**Figures 3.5N**

and **3.50**). Altogether, our data support that MafB deficiency disrupts RTM phenotypes across multiple tissues and leads to impaired phagocytosis, defective tissue clearance functions, and compromised RTM-mediated homeostatic functions.

MafB directly regulates mac differentiation and identity through *cis*-regulatory elements

Although our data so far position MafB as a key regulator of mac functional identity, its direct targets and the underlying mechanisms remain unclear. To address this, we performed cleavage under targets and release using nuclease (CUT&RUN) for MafB on BMDMs from *Mafb^{fl/fl}* and *Lyz2^{Cre}Mafb^{fl/fl}* mice. We identified 7,242 reproducible MafB binding sites in WT BMDMs, whereas MafB-deficient BMDMs yielded only 14 sites (**Figures 3.6A, 3.6B, and Supplementary figures 3.6A–C; Supplementary table 3.8**). These sites were distributed across introns (33%), promoters or transcription start sites (TSS) (31%), intergenic regions (26%), exons (6%), and transcription termination sites (TTS) (2%) (**Figure 3.6C**). To connect MafB binding with transcriptional activity, we also performed CUT&RUN for histone H3 lysine 27 acetylation (H3K27ac), a histone mark of active enhancers and promoters. MafB-deficient BMDMs showed reduced H3K27ac tag counts at MafB binding sites compared with controls, supporting that MafB promotes transcriptional activation from these regions (**Figures 3.6D and 3.6E**).

By linking MafB binding sites to genes within ± 2 kbp of TSSs, we identified 3,511 MafB targets in BMDMs, including 303 core mac signature genes (**Supplementary table 3**). These included known targets (*C1qa*, *C1qb*, *C1qc*) and key mac markers (*Csf1r*, *Fcgr1*, *Mertk*) (**Figures 3.6F and 3.6G**). MafB also bound regulatory regions for TFs central to mac differentiation and identity, such as

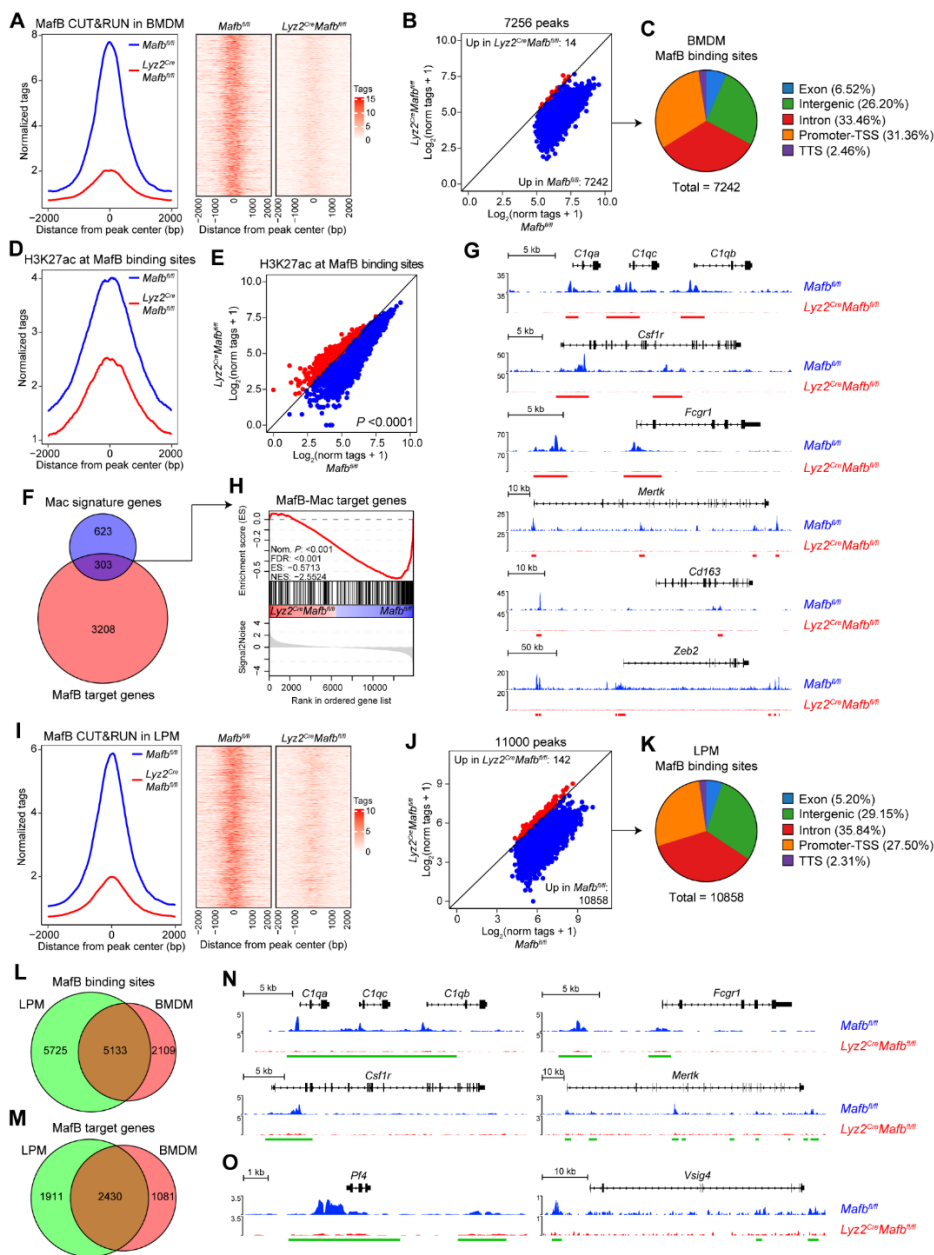


Figure 3.6. MafB binds to *cis*-regulatory elements to promote transcription of key mac differentiation and identity genes. (A and B) Histograms (left) and heatmaps (right) (A) and scatterplot (B) of normalized tag counts at MafB peaks in BMDMs from *Mafb^{fl/fl}* and *Lyz2^{Cre}Mafb^{fl/fl}* mice, as quantified by CUT&RUN. (C) Pie chart showing the genomic distribution of MafB binding sites in BMDMs. (D and E) Histograms (D) and scatterplot

(E) of normalized H3K27ac tag counts at MafB binding sites in BMDMs from *Mafb^{fl/fl}* and *Lyz2^{Cre}Mafb^{fl/fl}* mice, as quantified by CUT&RUN. (F) Venn diagram showing the overlap between mac signature genes and MafB target genes in BMDMs. (G) CUT&RUN tracks depicting MafB binding around representative mac signature genes in BMDMs from *Mafb^{fl/fl}* and *Lyz2^{Cre}Mafb^{fl/fl}* mice, visualized with the integrative genome viewer (IGV). Horizontal red bars, MafB binding sites in BMDMs. (H) GSEA of mac-specific MafB target genes using bulk RNA-seq data from BMDMs of *Mafb^{fl/fl}* and *Lyz2^{Cre}Mafb^{fl/fl}* mice. (I and J) Histograms (left) and heatmaps (right) (I) and scatterplot (J) of normalized tag counts at MafB peaks in LPMs from *Mafb^{fl/fl}* and *Lyz2^{Cre}Mafb^{fl/fl}* mice, as quantified by CUT&RUN. (K) Pie chart showing the genomic distribution of MafB binding sites in LPMs. (L and M) Venn diagrams showing the overlap between MafB binding sites (L) and target genes (M) in LPMs and BMDMs. (N and O) CUT&RUN tracks depicting MafB binding around indicated mac (N) and LPMs (O) signature genes in LPMs, visualized with IGV. Horizontal green bars, MafB binding sites in LPMs. *P* values were calculated using a Wilcoxon signed rank test (E) or a permutation test (H). See also **Supplementary figure 3.6** and **Supplementary table 3.8**.

Zeb2, *Mafb* itself, *Maf*, *Spi1* (PU.1), and *Cebpb*^{236,347,348} (**Figure 3.6G** and **Supplementary figure 3.6D**), as well as *Cd163*, consistent with its reduced expression in KCs, RPMs and MHC-II⁺ CMs. To test whether MafB regulated mac signature genes, we performed GSEA and found significant enrichment of MafB target genes in control BMDMs compared to MafB-deficient BMDMs (**Figure 3.6H**). Consistently, RTMs from *Lyz2^{Cre}Mafb^{fl/fl}* mice showed reduced MafB target scores (**Supplementary figure 6E**).

Next, to assess whether MafB also regulates mac identity in primary RTMs, we performed CUT&RUN for MafB on LPMs from *Mafb^{fl/fl}* or *Lyz2^{Cre}Mafb^{fl/fl}* mice. We identified 10,858 reproducible binding sites in WT LPMs, whereas *Mafb*-deficient LPMs yielded fewer than 150 sites (**Figures 3.6I, 3.6J**, and **Supplementary figures 3.6F–H; Supplementary table 3.8**). MafB sites were largely intronic, intergenic, or at promoters (**Figure 3.6K**), and ~70% sites and target genes overlapped between BMDMs and LPMs, including core mac identity genes, supporting a conserved MafB program (**Figure 3.6N**). In addition, MafB bound LPM-specific

genes such as *Pf4* and *Vsig4*, suggesting that MafB also contributes to tissue-specific Mac specialization (**Figure 3.6O**).

Given the importance of *Csf1r* signaling to RTM biology^{143,144,349}, we assessed its regulation and found *Csf1r* and surface CD115 reduced in multiple RTMs, but not blood monocytes, from *Lyz2^{Cre}Mafb^{fl/fl}* mice as compared to controls (**Supplementary figures 3.6I and 3.6J**). Altogether, these data suggest that MafB directly imprints Mac differentiation and identity through regulation of enhancer and promoter programs.

MafB-driven mac programs are conserved from mouse to human and across vertebrates

We first examined the evolutionarily conserved FIRE enhancer in the second intron of *Csf1r*, which regulates mac-specific *Csf1r* transcription^{55,117,350}. MafB bound FIRE (**Figure 3.7A**), consistent with predictions of conserved MafB occupancy³⁵¹ and with studies showing that FIRE deletion impairs *Csf1r* expression and RTM development³⁴⁹. Genome-wide, 91% of MafB binding sites overlapped with *cis*-regulatory elements (cREs) that together represent only 3% of the mouse genome (**Figures 3.7B and 3.7C**). Conservation analysis across 60 vertebrates revealed elevated phastCons and phyloP scores at FIRE (**Figure 3.7A and Supplementary figure 3.7A**) and broadly at MafB sites (**Figures 3.7D and 3.7E**), which were more conserved than those of PU.1 (**Figures 3.7D and 3.7E**).

To extend these findings to humans, we performed CUT&RUN for MafB on monocyte-derived Macs (MDMs). We identified 24,577 reproducible binding sites, which, similar to mouse BMDMs and LPMs, were predominantly located in introns, intergenic regions, and promoters/TSS (**Figures 3.7F–3.7H and Supplementary figures 3.7B–3.7D; Supplementary table 3.8**). Importantly,

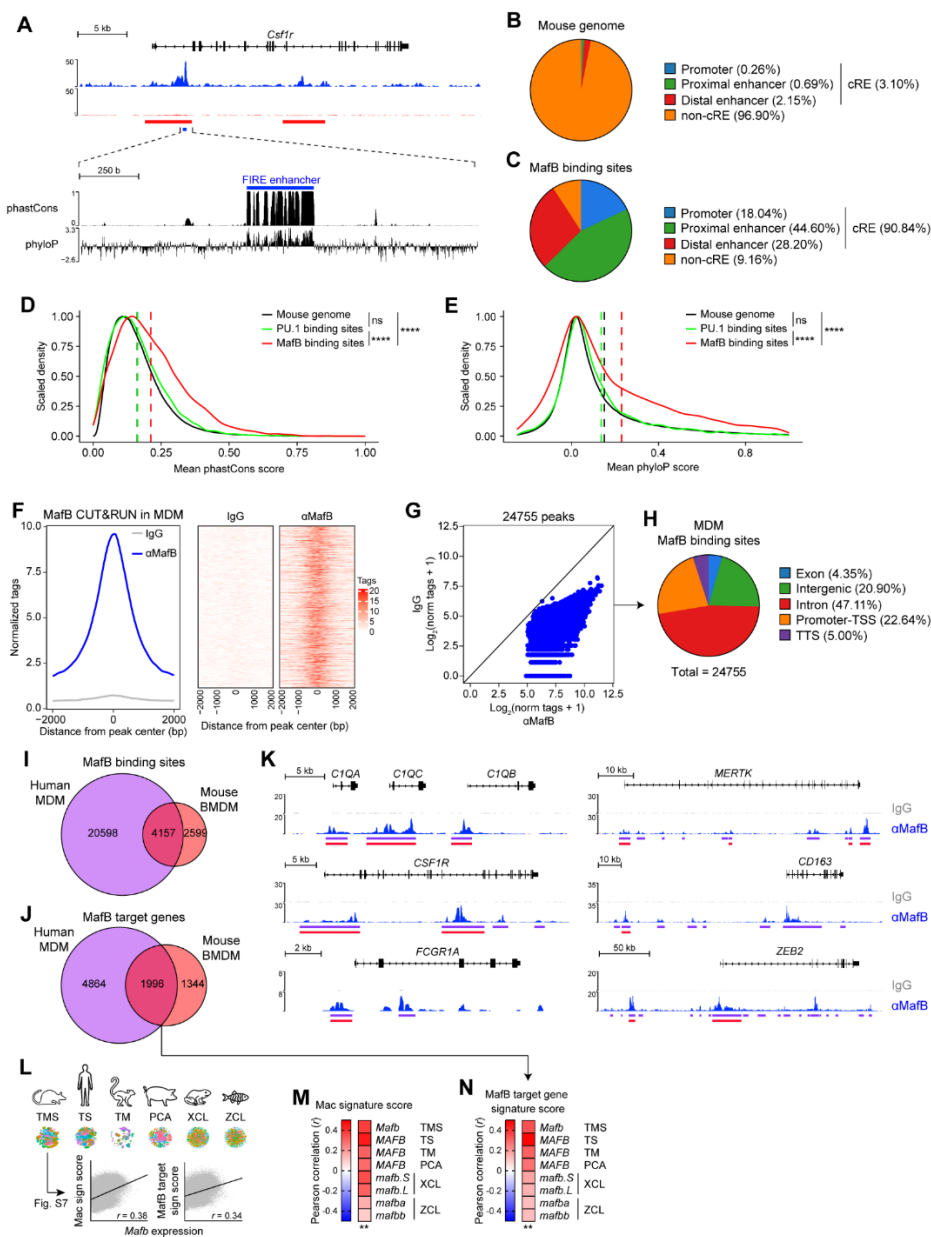


Figure 2.7. MafB binding sites and MafB-dependent regulation of mac identity are highly conserved across species. (A) CUT&RUN tracks depicting MafB binding at the FIRE enhancer within the second intron of the *Csfr1* gene in BMDMs from *Mafb^{f/f}* and *Lyz2^{Cre}Mafb^{f/f}* mice (top), and phastCons and phyloP conservation scoring tracks around the FIRE enhancer (bottom), visualized with IGV. Horizontal red bars, MafB

binding sites in BMDMs; horizontal blue bar, FIRE enhancer. (B) Genomic distribution of cREs in mice. (C) Overlap between MafB binding sites in BMDMs and cREs. (D and E) Distribution of mean phastCons (D) and phyloP (E) scores around PU.1 and MafB binding sites (–500 to +500 bp from peak center). (F and G) Histograms (left) and heatmaps (right) (F) and scatterplot (G) of normalized tag counts at MafB peaks in MDMs, as quantified by CUT&RUN. (H) Pie chart showing the genomic distribution of MafB binding sites in MDMs. (I and J) Venn diagrams showing the overlap between MafB binding sites (I) and target genes (J) in human MDMs and mouse BMDMs. (K) CUT&RUN tracks depicting MafB binding around representative mac signature genes in MDMs, visualized with IGV. Horizontal purple bars, MafB binding sites in MDMs; horizontal red bars, conserved MafB binding sites in human MDMs and mouse BMDMs, as in I. (L) Overview of cross-species single-cell RNA-seq datasets from mouse (TMS), human (TS), mouse lemur (TM), pig (PCA), clawed frog (XCL), and zebrafish (ZCL), used to calculate correlations of MafB expression with mac and conserved MafB target gene signature scores, as in **Supplementary figure 3.7E–3.7J**. (M and N) Heatmaps of Pearson correlations between MafB expression and either mac (M) or conserved MafB target gene (N) signature scores across species, as in L. *P* values were calculated using a pairwise Wilcoxon signed-rank test with Benjamini–Hochberg correction (D and E) or a Wilcoxon signed rank exact test (M and N). **, $P < 0.01$; **** $P < 0.0001$. See also **Supplementary figure 3.7** and **Supplementary table 3.8**.

MafB binding sites and target genes in human MDMs overlapped with 55% of those identified in mouse BMDMs, including at core mac identity genes such as *C1Qs*, *CSF1R*, *FCGR1*, *MERTK*, *CD163*, and *ZEB2*, indicating a conserved MafB-driven regulatory program between mouse and human (**Figures 3.7I–3.7K**).

Finally, across diverse vertebrate single-cell atlases, *MafB* expression positively correlated with both Mac signature genes and conserved MafB target genes (**Figures 3.7L–3.7N** and **Supplementary figures 3.7E–3.7J**), supporting a deeply conserved role for MafB in Mac development and the establishment of a core mac identity program.

Supplementary Information

Supplementary tables

Supplementary table 3.1. Key resources table. (Appendix 1)

Supplementary table 3.2. Differentially expressed genes between BMDM from *Lyz2^{Cre}Mafb^{fl/fl}* mice and *Mafb^{fl/fl}* littermate controls, related to Figure 2.

<https://1drv.ms/x/c/0583cd016ca78380/ETXeA6pCz79ImIVn8cOthxMBNQhXHmAscYy48U-TSI9kuA?e=KeaydS>

Supplementary table 3.3. Monocyte and macrophage signature genes, related to Figure 2.

<https://1drv.ms/x/c/0583cd016ca78380/Eb1mDvDBtLZPp9JcJfPqcccBFMvJsEGZDG0Bz3UeSHuOSA?e=uGcfrl>

Supplementary table 3.4. Ly6C⁺ CM and MHC-II⁺ CM signature genes, related to Figure 3.

<https://1drv.ms/x/c/0583cd016ca78380/EZVgRUjeaLRKjnnGw1XVbE0B3xi7XMGekMtnWQXW-GseMg?e=o69zWr>

Supplementary table 3.5. Differentially expressed genes between RTMs from *Lyz2^{Cre}Mafb^{fl/fl}* mice and *Mafb^{fl/fl}* littermate controls, related to Figure 3.

https://1drv.ms/x/c/0583cd016ca78380/EQgbRPQQNM5LnK54fMXq3soBm3zo47OXgGoqWaD_MaxRhQ?e=9o3uIC

Supplementary table 3.6. RTM subset specific signature genes, related to Figure 3.

https://1drv.ms/x/c/0583cd016ca78380/EQZ_GipIEu9Lpy0D8gVFL4AB18oINk7ZGI6L1PIDjFqA9g?e=TmtEyG

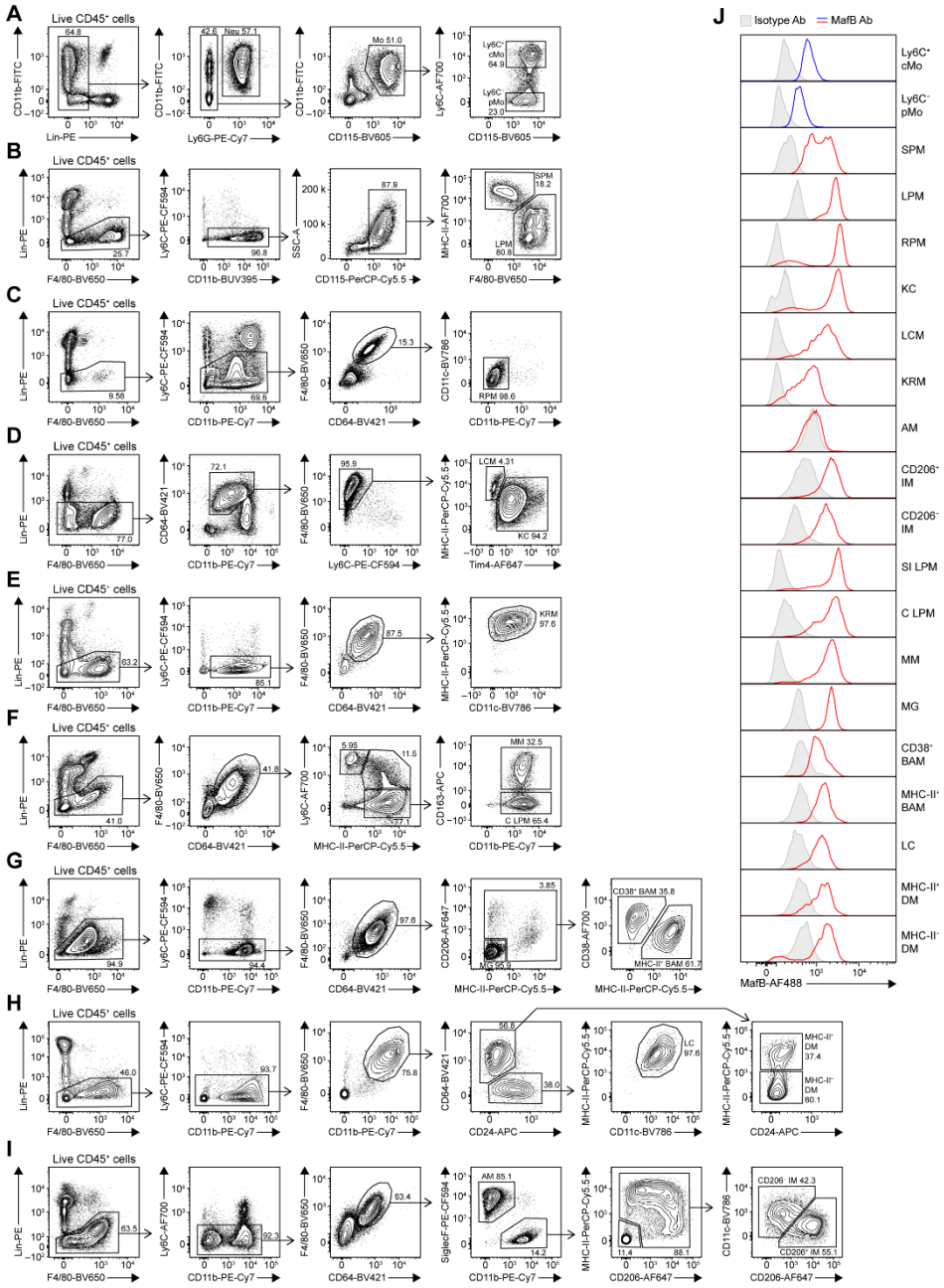
Supplementary table 3.7. EMP, preMac and Mac signature genes, related to Figure 3.

<https://1drv.ms/x/c/0583cd016ca78380/EavPt0sjxcRItgHt4112stkBqyDW1jqCZJyOePjceuxaTQ?e=BxGRGq>

Supplementary table 3.8. MafB binding sites in BMDM, LPM and MDM, related to Figure 6 and 7.

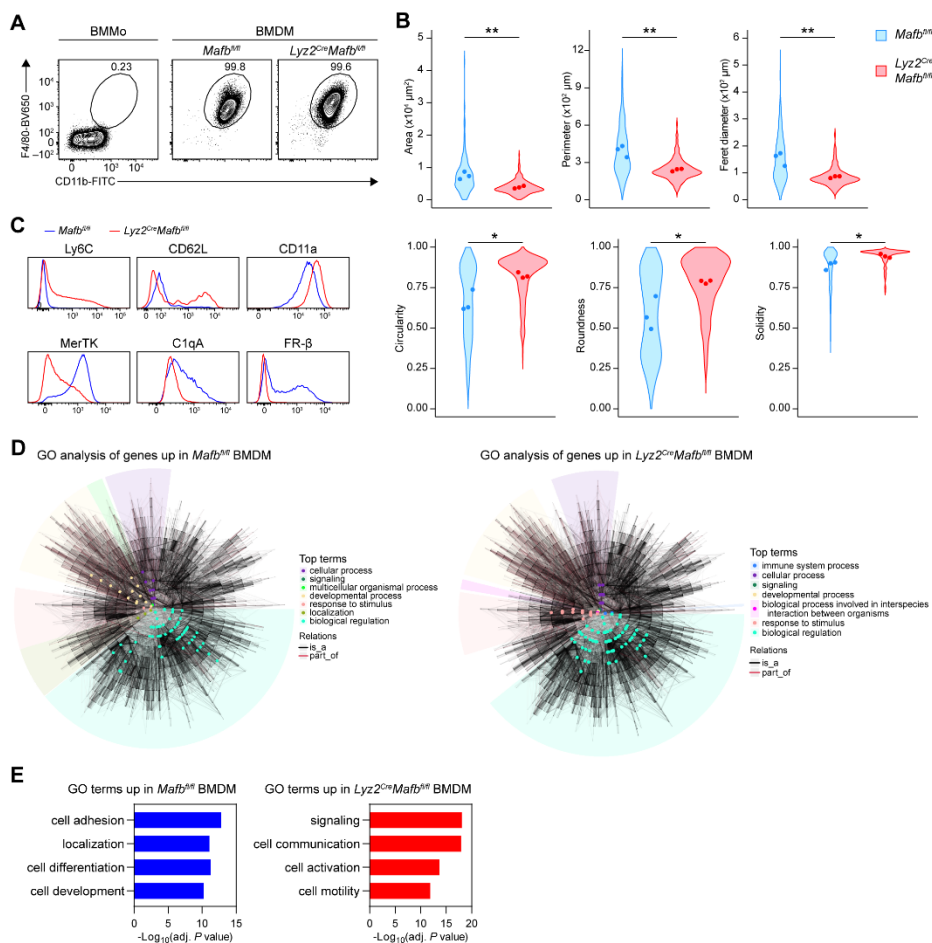
<https://1drv.ms/x/c/0583cd016ca78380/Ec9Zg2EembpCshlqV2JkZe0B0x5aqEjmkfc6yNT5yRSSYg?e=RZCm8f>

Supplementary figures



Supplementary figure 3.1. Flow cytometry gating strategies to delineate RTM and blood monocytes, related to Figure 3.1. (A–I) Flow cytometry gating strategy used to

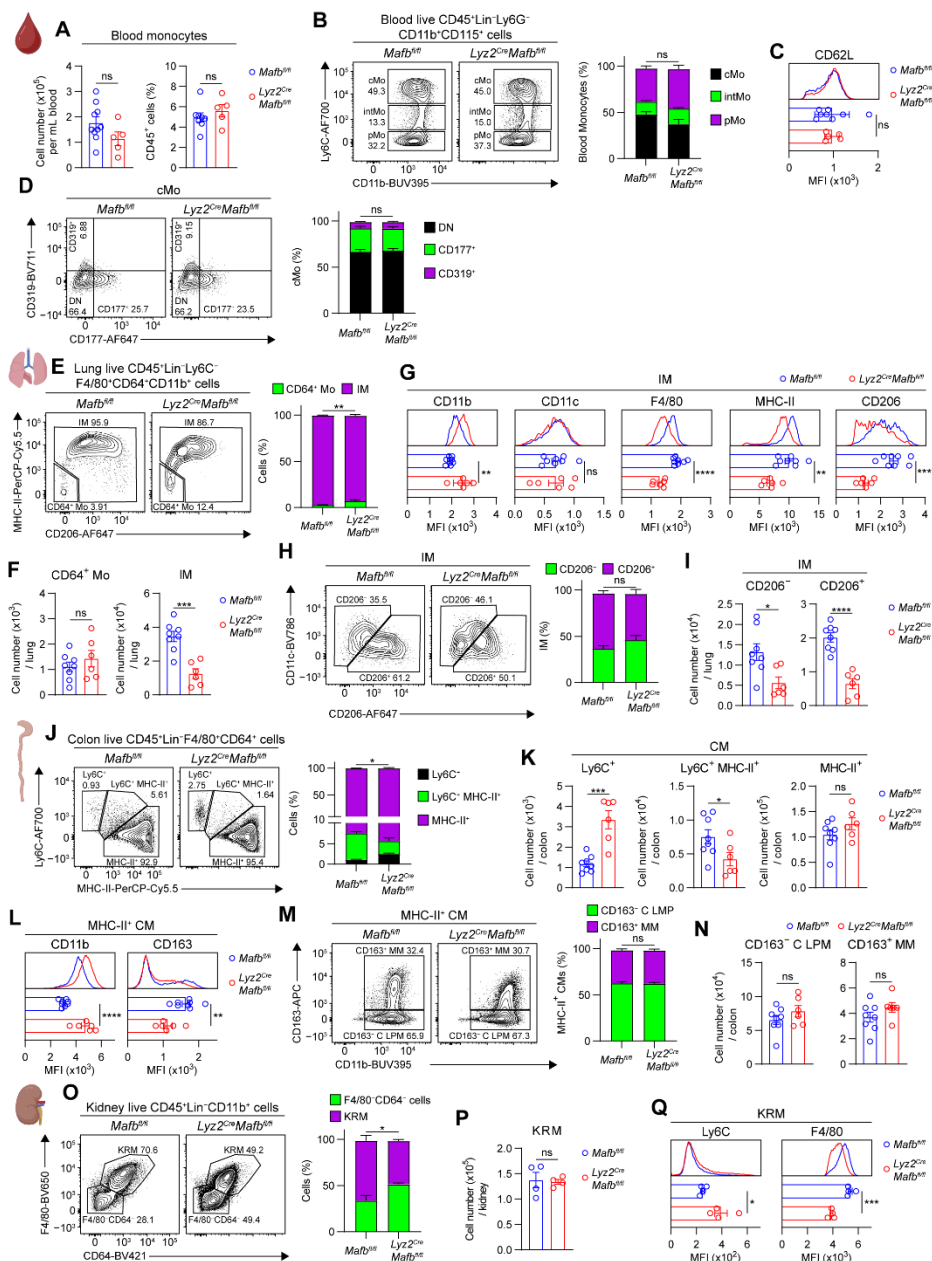
delineate blood CD45⁺Lin⁻Ly6G⁻CD11b⁺CD115⁺Ly6C⁺ classical monocytes (Ly6C⁺ cMo) or Ly6C⁻ patrolling monocytes (Ly6C⁻ pMo) (A), CD45⁺Lin⁻Ly6C⁻CD11b⁺CD115⁺MHC-II⁺F4/80⁻ small peritoneal macs (SPM) and CD45⁺Lin⁻Ly6C⁻CD11b⁺CD115⁺MHC-II⁻F4/80⁺ large peritoneal macs (LPM) (B), spleen CD45⁺Lin⁻Ly6C⁻F4/80⁺CD64⁺CD11c⁻CD11b⁻ red pulp macs (RPM) (C), liver CD45⁺Lin⁻CD64⁺CD11b^{int}F4/80⁺Ly6C⁻MHC-II^{lo}Tim4⁺ Kupffer cells (KC) and CD45⁺Lin⁻CD64⁺CD11b^{int}F4/80⁺Ly6C⁻MHC-II^{hi}Tim4⁻ liver capsular macs (LCM) (D), CD45⁺Lin⁻Ly6C⁻CD11b⁺F4/80⁺CD64⁺MHC-II⁺CD11c^{int} kidney resident macs (KRM) (E), CD45⁺Lin⁻F4/80⁺CD64⁺Ly6C⁻MHC-II⁺CD163⁻ colonic lamina propria macs (C LMP) or CD163⁺ muscularis macs (MM) (F), brain CD45⁺Lin⁻Ly6C⁻F4/80⁺CD64⁺CD206⁻MHC-II⁻ microglia (MG), CD45⁺Lin⁻Ly6C⁻F4/80⁺CD64⁺MHC-II⁻CD38⁺ border associated macs (CD38⁺ BAM) and CD45⁺Lin⁻Ly6C⁻F4/80⁺CD64⁺MHC-II⁺CD38⁻ border associated macs (MHC-II⁺ BAM) (G), skin CD45⁺Lin⁻Ly6C⁻F4/80⁺CD64⁻CD24⁺MHC-II⁺CD11c⁺ Langerhans cells (LC), CD45⁺Lin⁻Ly6C⁻F4/80⁺CD64⁺MHC-II⁺ dermal macs (MHC-II⁺ DM) or MHC-II⁻ DM (H), lung CD45⁺Lin⁻Ly6C⁻F4/80⁺CD64⁺SiglecF⁺CD11b⁻ alveolar macs (AM), CD45⁺Lin⁻Ly6C⁻F4/80⁺CD64⁺SiglecF⁻CD11b⁺CD206⁺ interstitial macs (CD206⁺ IM) or CD206⁻ IM (I). (J) Representative histograms of intracellular MafB expression in the indicated blood monocyte (Mo) and resident tissue mac (RTM) populations from wild-type (WT) mice, as in A-I (n = 4).



Supplementary figure 3.2. Differential morphology and Gene Ontology enrichment in BMDMs from myeloid-restricted MafB-deficient mice, related to Figure 3.2. (A) Representative contour plots of F4/80 and CD11b expression in bone marrow monocytes (BMMo) from WT mice and bone marrow-derived macrophages (BMDM) from *Mafb^{fl/fl}* and *Lyz2^{Cre}Mafb^{fl/fl}* mice (n = 6). (B) Violin plots of BMDM morphology quantified by differential interference contrast microscopy (n = 3). Height indicates morphological parameter; width indicates abundance of cells. One hundred cells were analyzed per biological replicate; dots represent mean values from each replicate. (C) Representative histograms of Mo (top) and Mac (bottom) marker protein expression in BMDM from *Mafb^{fl/fl}* and *Lyz2^{Cre}Mafb^{fl/fl}* mice (n = 6–7). (D) Circular directed acyclic graphs (DAG) of biological process (BP) gene ontology (GO) terms connected by hierarchical relations. Significant BP GO terms from a GO enrichment analysis of differentially expressed genes (DEGs) upregulated in BMDMs from *Mafb^{fl/fl}* (left) and

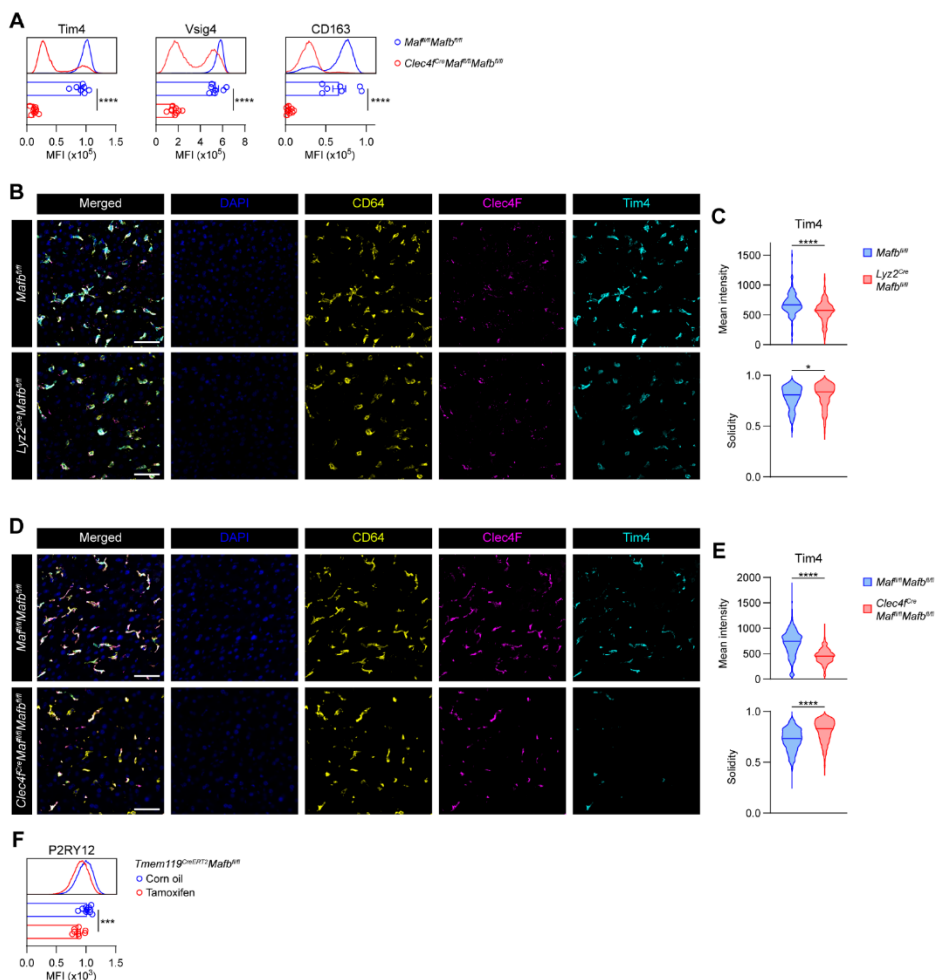
Lyz2^{Cre}Mafb^{fl/fl} (right) mice are highlighted as colored nodes. (E) Bar graphs of the top enriched GO terms on DEGs upregulated in BMDMs from *Mafb^{fl/fl}* (left) and *Lyz2^{Cre}Mafb^{fl/fl}* (right) mice, as in D. *P* values were calculated using a two-tailed Student's *t* test (B). **P* < 0.05; ***P* < 0.01.

subset from *Mafb*^{fl/fl} and *Lyz2*^{Cre}*Mafb*^{fl/fl} mice. (C) Violin plots of *Mafb* expression within RTM populations from *Mafb*^{fl/fl} and *Lyz2*^{Cre}*Mafb*^{fl/fl} mice, as in A (height: expression; width: abundance of cells). (D–J) Volcano plots and heatmaps of DEGs between *Mafb*^{fl/fl} and *Lyz2*^{Cre}*Mafb*^{fl/fl} RTMs, shown for SPM (D), LPM (E), KC (F), IM (G), Ly6C⁺ CM (H), MHC-II⁺ CM (I), and MG (J). Transcripts significantly upregulated in RTM *Mafb*^{fl/fl} and *Lyz2*^{Cre}*Mafb*^{fl/fl} mice are shown in bold and light colors, respectively (\log_2 fold change > 0.25 or < -0.25 ; adjusted $P < 0.05$). (K) Feature plots of EMP (left), preMac (middle) and Mac (right) signature scores, as in **Figure 3.31**. (L) EMP, preMac and Mac signature scores along pseudotime, as in **Figure 3.31**. P values were calculated using a Wilcoxon rank-sum test (C and D–J).



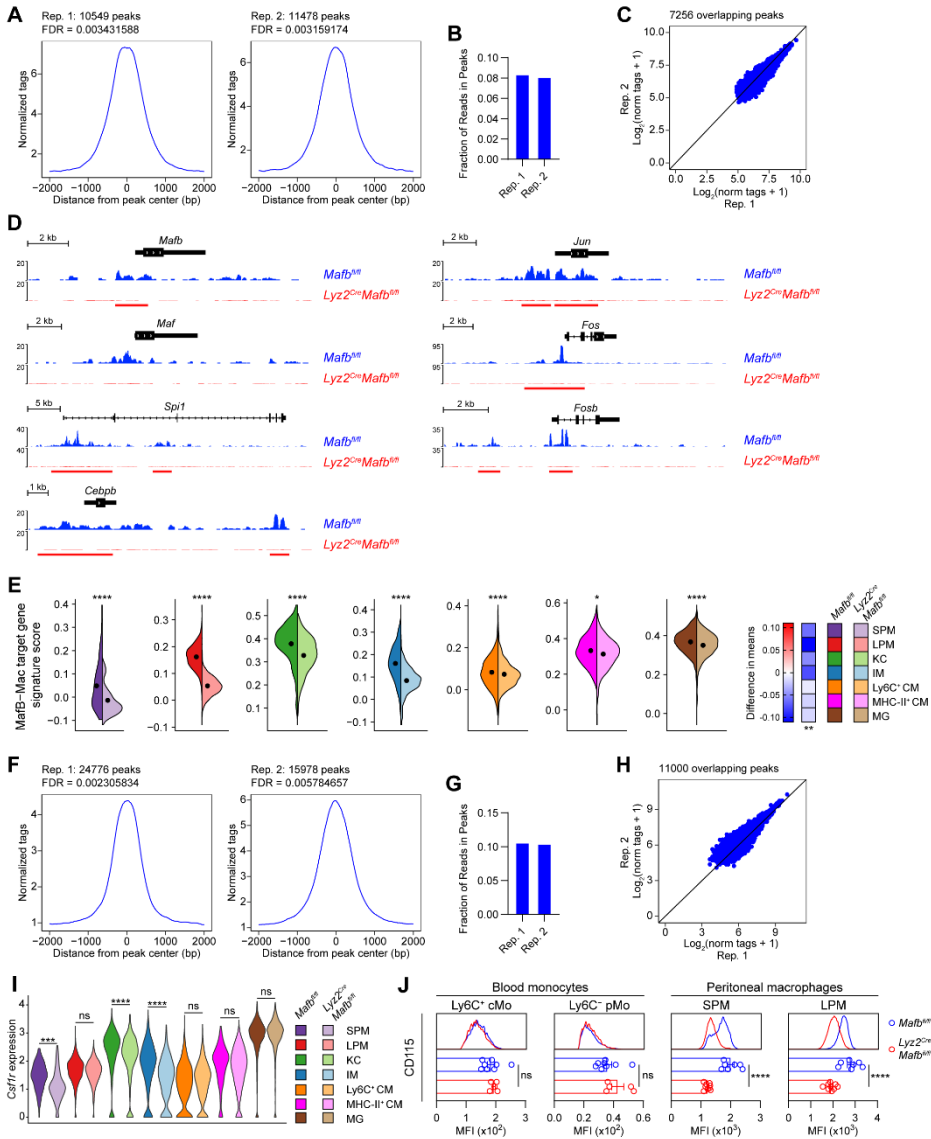
Supplementary figure 3.4. Impact of MafB deficiency on blood monocytes and lung, colon and kidney RTM subsets, related to Figure 3.4. (A) Bar graphs of blood Mo shown as absolute number per mL of blood (left) and percentage of live CD45⁺ cells (right) from *MafB*^{fl/fl} and *Lyz2^{Cre}MafB*^{fl/fl} mice (n = 5–10). All subsequent panels compare *MafB*^{fl/fl} and *Lyz2^{Cre}MafB*^{fl/fl} mice. (B) Representative contour plots of Ly6C

and CD11b expression within blood live CD45⁺Lin⁻Ly6G⁻CD115⁺CD11b⁺ cells (left) and bar graphs of the percentage of cMo, intermediate Mo (intMo), and pMo, as gated on the contour plots (right) (n = 5–8). (C) Histograms (top) and bar graphs (bottom) of CD62L expression in cMo, as in B. (D) Representative contour plots of CD319 and CD177 expression within cMo (left) and bar graphs of the percentage of double negative (DN), CD177⁺, and CD319⁺ cMo, as gated on the contour plots (right) (n = 5–8). (E) Representative contour plots of MHC-II and CD206 expression within lung live CD45⁺Lin⁻Ly6C⁻F4/80⁺CD64⁺CD11b⁺ cells (left) and bar graphs of the percentage of CD64⁺ Mo and IM, as gated on the contour plots (right) (n = 6–8). (F) Bar graphs of absolute numbers of CD64⁺ Mo and IM, as in E. (G) Histograms (top) and bar graphs (bottom) of CD11b, CD11c, F4/80, MHC-II, and CD206 expression in IM, as in E. (H) Representative contour plots of CD11c and CD206 expression within IM (left) and bar graphs of the percentage of CD206⁻ and CD206⁺ IM, as gated on the contour plots (right) (n = 6–8). (I) Bar graphs of absolute numbers of CD206⁻ and CD206⁺ IM, as in H. (J) Representative contour plots of Ly6C and MHC-II expression within colon live CD45⁺Lin⁻F4/80⁺CD64⁺ cells (left) and bar graphs of the percentage of Ly6C⁺, Ly6C⁺MHC-II⁺, and MHC-II⁺ CM, as gated on the contour plots (right) (n = 6–8). (K) Bar graphs of absolute numbers of Ly6C⁺, Ly6C⁺MHC-II⁺, and MHC-II⁺ CM, as in J. (L) Histograms (top) and bar graphs (bottom) of CD11b and CD163 expression in MHC-II⁺ CM, as in J. (M) Representative contour plots of CD163 and CD11b expression within MHC-II⁺ CM (left) and bar graphs of the percentage of CD163⁻ C LPM and CD163⁺ MM, as gated on the contour plots (right) (n = 6–8). (N) Bar graphs of absolute numbers of CD163⁻ C LPM and CD163⁺ MM, as in M. (O) Representative contour plots of F4/80 and CD64 expression within kidney live CD45⁺Lin⁻CD11b⁺ cells (left) and bar graphs of the percentage of F4/80⁻CD64⁻ cells and KRM, as gated on the contour plots (right) (n = 4). (P) Bar graphs of absolute numbers of KRM, as in O. (Q) Histograms (top) and bar graphs (bottom) of F4/80 and Ly6C expression in KRM, as in O. Data are mean ± SEM and are pooled from two independent experiments. *P* values were calculated using a two-tailed Student's *t* test. *, *P* < 0.05; **, *P* < 0.01; ***, *P* < 0.001; ****, *P* < 0.0001. MFI, mean fluorescence intensity; ns, not significant.



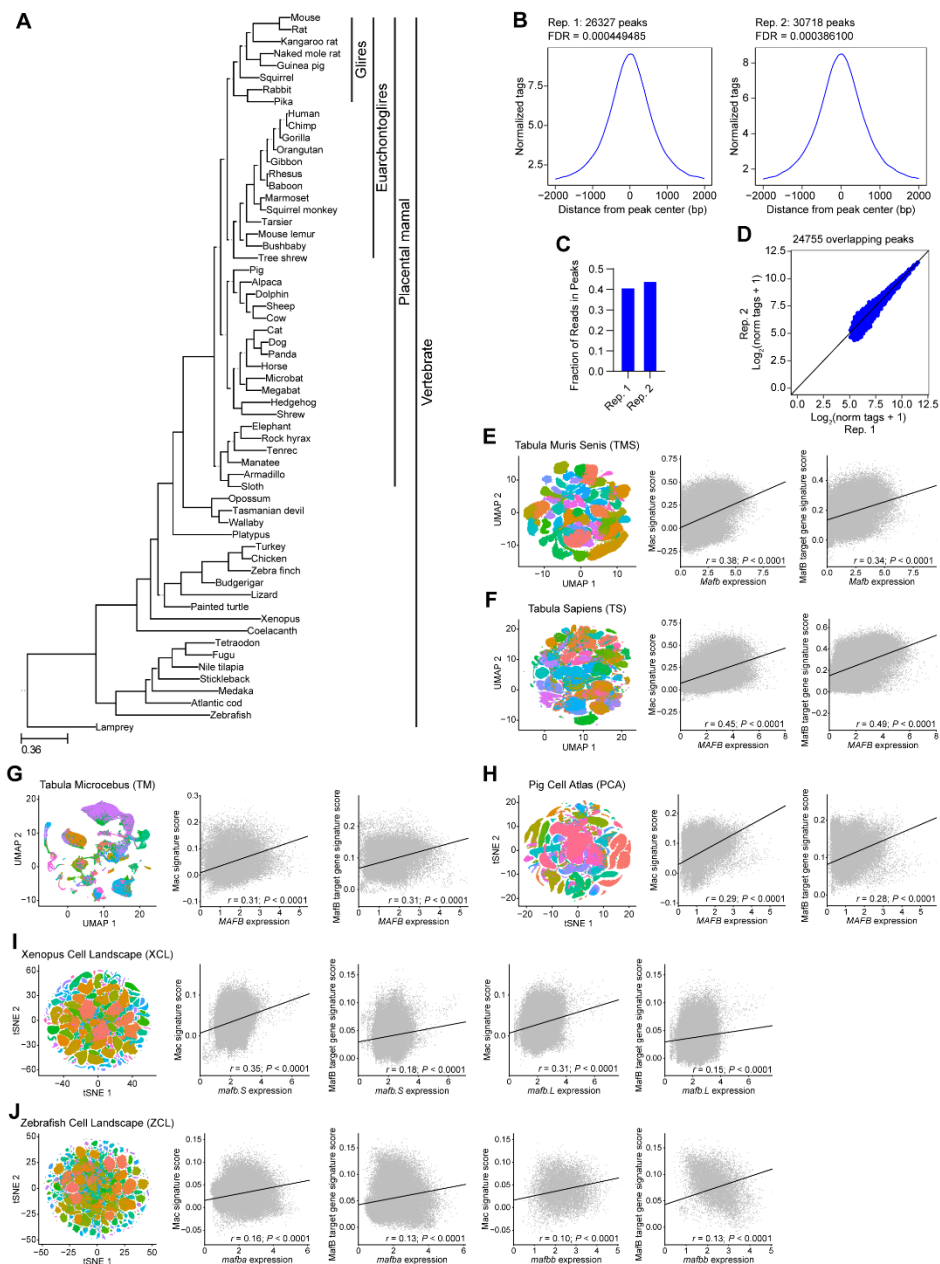
Supplementary figure 3.5. Impact of RTM-specific MafB deficiency on Kupffer cell and microglia phenotypes, related to Figure 3.4. (A) Histograms (top) and bar graphs (bottom) of Tim4, Vsig4, and CD163 expression in KCs from $Maf^{fl/fl}Mafb^{fl/fl}$ and $Clec4f^{Cre}Maf^{fl/fl}Mafb^{fl/fl}$ mice ($n = 7-9$). (B) Representative confocal images of KCs from $Mafb^{fl/fl}$ and $Lyz2^{Cre}Mafb^{fl/fl}$ mice ($n = 3$). Scale bar, 50 μm . (C) Violin plots of Tim4 expression (top) and solidity (bottom) in $CD64^+$ KCs from $Mafb^{fl/fl}$ and $Lyz2^{Cre}Mafb^{fl/fl}$ mice, as in B. (D) Representative confocal images of KCs from $Maf^{fl/fl}Mafb^{fl/fl}$ and $Clec4f^{Cre}Maf^{fl/fl}Mafb^{fl/fl}$ mice ($n = 3$). Scale bar, 50 μm . (E) Violin plots of Tim4 expression (top) and solidity (bottom) in $CD64^+$ KCs from $Maf^{fl/fl}Mafb^{fl/fl}$ and $Clec4f^{Cre}Maf^{fl/fl}Mafb^{fl/fl}$ mice, as in D. (F) Histograms (top) and bar graphs (bottom) of P2RY12 expression in MG from $Tmem119^{CreERT2}Mafb^{fl/fl}$ mice orally gavaged with 5 mg tamoxifen or corn oil (control) for 5 days and analyzed 2 months after the last dose ($n = 9-10$). Data are mean \pm SEM and are pooled from two independent experiments (A

and F). *P* values were calculated using a two-tailed Student's *t* test (A, C[Tim4 expression] and E[Tim4 expression], F) or a two-tailed Mann–Whitney test (C[Solidity] and E[Solidity]). *, *P* < 0.05; ***, *P* < 0.001; ****, *P* < 0.0001.



Supplementary figure 3.6. MafB binds to *cis*-regulatory elements to promote transcription of key mac differentiation and identity genes, related to Figure 3.6. (A–C) Quality control of MafB CUT&RUN peak calling in BMDMs. (A) Histograms of normalized tag counts at MafB peaks for two replicates, with corresponding numbers of called peaks and false discovery rates (FDRs) indicated. (B) Bar graphs of the fraction of reads in peaks (FRiP) for each replicate. (C) Scatterplot of normalized tag counts at overlapping MafB peaks in both replicates. (D) CUT&RUN tracks depicting MafB binding around representative transcriptional regulators of mac differentiation in

BMDMs from *Mafb^{fl/fl}* and *Lyz2^{Cre}Mafb^{fl/fl}* mice, visualized with the Integrative Genomics Viewer (IGV). Horizontal red bars, MafB binding sites in BMDMs. (E) Violin plots of mac-specific MafB target gene signature scores in RTMs from *Mafb^{fl/fl}* and *Lyz2^{Cre}Mafb^{fl/fl}* mice, as in **Figure 3.3** (height, score; width, abundance). (F–H) Quality control of MafB CUT&RUN peak calling in LPMs. (F) Histograms of normalized tag counts at MafB peaks for two replicates, with corresponding numbers of called peaks and FDRs indicated. (G) Bar graphs of FRiP for each replicate. (H) Scatterplot of normalized tag counts at overlapping MafB peaks in both replicates. (I) Violin plots of *Csf1r* expression within RTM populations from *Mafb^{fl/fl}* and *Lyz2^{Cre}Mafb^{fl/fl}* mice, as in Figure 3 (height, expression; width, abundance of cells). (J) Histograms (top) and bar graphs (bottom) of CD115 expression in blood Mo (left) and peritoneal macs (right) from *Mafb^{fl/fl}* and *Lyz2^{Cre}Mafb^{fl/fl}* mice (n = 5–9). Data are mean ± SEM and are pooled from two independent experiments (J). *P* values were calculated using a Wilcoxon rank-sum test (E and I) or a two-tailed Student's *t* test (J). **P* < 0.05; ****P* < 0.001; *****P* < 0.0001.



Supplementary figure 3.7. MafB binding site conservation across species, related to Figure 3.7. (A) Phylogenetic tree derived from the multiple sequence alignment of 60 vertebrate genomes with mouse as the reference genome. (B–D) Quality control of MafB CUT&RUN peak calling in human monocyte-derived macrophages (MDMs). (B)

Histograms of normalized tag counts at MafB peaks for two replicates, with corresponding numbers of called peaks and FDRs indicated. (C) Bar graphs of FRiP for each replicate. (D) Scatterplot of normalized tag counts at overlapping MafB peaks in both replicates. (E–J) Correlations between *Mafb* expression and either mac or conserved MafB target gene signature scores across species, as in Figure 7J, using the Tabula Muris Senis (E), Tabula Sapiens (F), Tabula Microcebus (G), Pig Cell Atlas (H), Xenopus Cell Landscape (I), and Zebrafish Cell Landscape (J) datasets. *P* values were calculated using a Pearson correlation test.

DISCUSSION

Part I: Dynamic regulation of monocyte-to-macrophage differentiation *in vivo*

A key unresolved question in macrophage biology is how circulating monocytes differentiate into resident tissue macrophages (RTMs) and how transitions between successive states are regulated *in vivo*. This issue remains difficult to address due to the slow turnover of RTMs and the rarity of observable differentiation events under steady-state conditions. To answer this question in the first part, we used lung interstitial macrophages (IMs), a long-lived RTM population gradually replenished by Ly6C⁺ monocytes^{103,104,186,352}, as a model to define the stages of monocyte-to-RTM differentiation and the transcriptional programs that govern these transitions. We aimed to generate a transgenic mouse model enabling diphtheria toxin (DT)-inducible depletion of the IM niche, thereby creating a vacant environment that accelerates and synchronizes IM repopulation. DT-based depletion strategies are widely used in mice to achieve rapid and cell type-specific ablation by expressing the human diphtheria toxin receptor (DTR) under a cell specific promoters, enabling precise temporal control over niche clearance^{311,353,354}. This approach provides a powerful means to transiently remove defined cell populations *in vivo* and to study their subsequent replacement and differentiation within a controlled and synchronized setting. However, despite their high temporal control and potential specificity, DTR-based systems also have important practical and conceptual limitations. They require the generation and validation of dedicated transgenic mouse lines, which is time-consuming and costly, particularly when intersectional strategies are needed to achieve sufficient selectivity. Moreover, the specificity of depletion is not intrinsically guaranteed by the genetic design and must be empirically assessed in each model and tissue context, as low-level or transient expression

of the driver genes in unintended cell types can result in off-target ablation. Other complementary approaches have been developed to deplete macrophages *in vivo*. For instance, whole-body irradiation followed by bone marrow transplantation has historically been used to ablate resident macrophage populations and to study their replacement by donor-derived monocytes, thereby providing important insights into macrophage ontogeny and turnover. However, irradiation induces broad tissue damage, inflammation and niche perturbation, and often fails to completely eliminate radio-resistant embryonically derived macrophages such as microglia (MG)^{73,307} or Langerhans cells (LCs)³⁵⁵, complicating the interpretation of differentiation dynamics. Another widely used method is the administration of clodronate-loaded liposomes (CLL), which are phagocytosed by macrophages and induce apoptosis³⁵⁶. This approach enables rapid depletion of phagocytic macrophages in multiple tissues but lacks specificity, as it also targets monocytes, neutrophils and some dendritic cells, and its efficiency depends on liposome uptake and tissue accessibility^{357,358}. In addition, repeated injections are often required, and off-target effects or inflammatory responses may occur due to the sudden release of intracellular contents from dying cells. Another strategy relies on genetic targeting of macrophage survival pathways, most notably through blockade or deletion of the Csf1/Csf1r axis, which is essential for macrophage maintenance³⁵⁹. Pharmacological Csf1r inhibitors or anti-Csf1r antibodies can efficiently reduce macrophage numbers systemically, but they typically affect multiple mononuclear phagocyte populations simultaneously and may also impact progenitors, thereby complicating the interpretation of niche-specific effects³⁶⁰. In principle, CLL or anti-Csf1r-mediated depletion can be delivered locally to restrict macrophage ablation to a given organ or tissue compartment. For example, intratracheal administration of CLL is commonly used to deplete alveolar macrophages (AMs)⁷¹, and local injection of anti-Csf1r (AFS98) into the

muscularis externa, particularly when combined with systemic anti-Ccr2 (MC21) to prevent rapid monocyte replacement, has been used to deplete resident macrophages in that niche³⁶¹. However, translating such local approaches to lung IMs is less straightforward. IMs reside within the lung parenchyma, positioned between the alveolar epithelium and the vascular endothelium, which makes them far less accessible and complicates attempts to achieve efficient and selective depletion by local administration. Hence, these anatomical constraints provided a strong rationale for adopting a DT-mediated depletion strategy to selectively and acutely ablate IMs *in vivo*. It should be noted that all currently used depletion strategies, including DT administration, irradiation, CLL or Csf1r blockade, ultimately eliminate resident macrophages through cell death. This inevitably perturbs the tissue niche, induces local remodeling signals and may even exert systemic effects, which need to be considered when interpreting the dynamics of niche refilling and macrophage differentiation.

RTMs exhibit distinct tissue-specific gene expression profiles⁴², which has opened up the possibility of detecting unique markers for the respective macrophage populations. For example, Clec4f was identified as a unique marker for Kupffer cells (KCs) and an inducible KC-specific DTR mouse model (*Clec4f^{DTR}* or *KC^{DTR}*) was generated to specifically deplete these cells⁴⁴. Nevertheless, in the majority of cases, genes or markers that are exclusively expressed in one macrophage population are exceedingly rare. In this regard, intersectional strategies in which a specific RTM population is defined by the combined expression of two different genes offer very interesting opportunities for the specific targeting of such population *in vivo*. The strategy we envisioned was to generate a mutant mouse encoding a DTR preceded by a loxP-flanked transcriptional Stop element under the control of a promoter that is uniquely expressed by mononuclear phagocytes, but not in other cell types of the body

(e.g., *Csf1r*, *Cx3cr1*). The presence of the Stop cassette will prevent expression of DTR, except in cells that express the Cre recombinase, in which Cre-mediated excision of the Stop cassette will trigger DTR and fluorescence expression. Thus, to specifically target IMs, such transgenic mouse should be crossed with mice expressing the Cre under the control of a gene promoter that is uniquely expressed within the IM compartment, but not in other cells of the mononuclear phagocytes.

Transcriptomic comparisons between IMs and other mononuclear phagocytes indicated that IMs can be defined by the combined expression of *Cx3cr1* and *Tmem119*. *Cx3cr1* (C-X3-C motif chemokine receptor 1) is a G protein-coupled receptor expressed predominantly by monocytes, macrophages, and dendritic cells, and serves as the receptor for the chemokine Cx3cl1 (fractalkine). Through this interaction, *Cx3cr1* regulates cell adhesion, migration, and survival during development, immune responses, and tissue homeostasis^{362–364}. Notably, during embryogenesis, yolk sac-derived pre-macrophages (pre-Macs) already express *Cx3cr1*, and their colonization of embryonic tissues has been shown to depend on *Cx3cr1* signaling⁶⁵. *Cx3cr1* expression is largely absent from AMs, the dominant lung RTM population, a pattern we and others confirmed using *Cx3cr1*^{GFP} reporter mice^{102,104,110}. In addition, *Cx3cr1*^{LSL-DTR} mice have been previously generated and in combination with a specific Cre line allow efficient depletion of *Cx3cr1*-expressing macrophages^{264,311,365,366}. *Tmem119* (Transmembrane protein 119) is primarily known as a homeostatic marker of MG^{57,367}, but our data indicate that it is also specifically expressed in lung IMs. Although the precise function of *Tmem119* remains unclear, several studies have reported that IMs, or a subset thereof, can localize in close association with nerves^{103,104,264}, reminiscent of the neuro-immune positioning observed for MG. Based on this expression pattern, we generated *Tmem119*^{Cre} mice to be crossed

with *Cx3cr1*^{LSL-DTR} mice in order to selectively target lung IMs. We first assessed Cre activity in these mice and confirmed that Cre expression was restricted to IMs and MG, with no detectable activity in macrophage progenitors, circulating monocytes, or other RTM populations. To further characterize the specificity and developmental history of *Tmem119*-driven recombination, we analyzed *Tmem119*^{Cre}*Rosa26*^{LSL-YFP} reporter mice. In this system, irreversible YFP expression marks cells that currently express, or have previously expressed, *Tmem119*. Our results revealed limited YFP labeling in bone marrow progenitors, indicating that *Tmem119* expression is largely absent at early hematopoietic stages, although a small fraction of progenitors already displayed recombination. In peripheral blood, the near absence of YFP in lymphoid and granulocytic populations contrasted with the partial labeling observed in classical and patrolling monocytes, suggesting that transient *Tmem119* expression may occur in a subset of monocyte precursors or during early differentiation. In the lung, IMs showed the highest proportion of YFP⁺ cells, consistent with active Cre expression and sustained *Tmem119* transcription in this population. In contrast, the intermediate YFP labeling observed in monocytes, dendritic cells, alveolar macrophages and other RTMs likely reflects past, rather than ongoing, *Tmem119* expression, resulting in permanent reporter activation in their progeny. However, this pattern could also be partially explained by germline recombination, as Cre expression was detected in both testes and ovaries (data not shown). Additionally, we also generated *Tmem119*^{CreERT2}*Rosa26*^{LSL-tdTomato} reporter mice and confirmed that inducible *Tmem119*-driven labeling efficiently marks IMs *in vivo* (data not shown), further supporting the specificity of this strategy for tracking and targeting this population.

To minimize this potential confounding effect like germline deletion, when generating *Tmem119*^{Cre}*Cx3cr1*^{LSL-DTR} mice we systematically crossed *Tmem119*^{Cre}

animals with *Cx3cr1*^{LSL-DTR} mice, rather than using *Tmem119*^{Cre}*Cx3cr1*^{LSL-DTR} double-transgenic mice as active breeders. By crossing *Tmem119*^{Cre} with *Cx3cr1*^{LSL-DTR} mice, we generated IM^{DTR} animals in which cells co-expressing *Cx3cr1* and *Tmem119* (i.e. IMs) become selectively susceptible to DT-induced ablation. Administration of DT resulted in an efficient and rapid depletion of both CD206⁺ and CD206⁻ IM subsets, while sparing AMs, lung monocytes and lung dendritic cells, demonstrating the high specificity of this intersectional targeting strategy. Dose response analysis further indicated that moderate DT doses (50 ng) achieve robust IM ablation with minimal off-target effects, whereas higher doses led to partial depletion of lung monocytes and, at later time points, MG, consistent with their shared expression of *Tmem119* and *Cx3cr1*. This might be due to lower access of DT to the brain, due to the blood-brain barrier, or a lower sensitivity of microglia to DT-induced cell death, or both. The lack of major effects on bone marrow progenitors, blood monocytes and most RTM populations in other tissues supports the notion that this model enables relatively selective manipulation of the lung IM niche. The transient increase in KC numbers may reflect compensatory systemic responses to macrophage depletion. Indeed, we detected a rapid upregulation of *Tnf* expression in IMs as early as 12 h after DT treatment, suggesting that dying IMs actively contribute to the local cytokine milieu (**Figure 2.4E**). Similar observations have been reported in models of specific KC depletion (KC^{DTR}) and in specific alveolar macrophage (SPAM) deleter mice, in which dying macrophages upregulate TNF expression^{58,105,368}. In the liver, Bonnardel *et al.* showed that TNF released from dying KCs activates hepatic stellate cells and endothelial cells, which in turn promote monocyte recruitment and adhesion to restore the macrophage niche⁵⁸. But, a transient systemic increase in TNF following IM ablation could also exert distal effects, potentially stimulating proliferation or expansion of KCs³⁶⁹. This mechanism may therefore explain the modest increase in KC numbers

observed after DT-mediated IM depletion, reflecting a broader systemic response. However, it is important to note that IM depletion at the selected dose of 50 ng did not elicit overt inflammatory responses, as evidenced by the absence of neutrophil or eosinophil recruitment, suggesting that DT-mediated cell death was largely immunologically silent. Notably, a similar lack of inflammatory cell recruitment has been reported in KC^{DTR} mice, supporting the idea that targeted RTM ablation can occur without triggering acute inflammatory responses⁴⁴. This lack of inflammation may be explained by both the sterile nature of DT-induced cell death and the transient character of IM depletion in this model. Indeed, DT-mediated ablation represents a form of sterile cell death that does not inherently trigger inflammatory responses. In addition, the IM compartment is rapidly repopulated following DT administration, thereby limiting the duration of IM absence and preventing a sustained disruption of local immune homeostasis. Consequently, the temporary loss of IM-derived anti-inflammatory signals, including IL-10, is unlikely to be sufficient to induce spontaneous inflammation under steady-state conditions. Overall, these results validate the IM^{DTR} model as a powerful tool to specifically and acutely clear the IM compartment, thereby providing a synchronized framework to investigate monocyte engraftment and differentiation into IMs *in vivo*. It is important to mention that devising a strategy that efficiently and specifically targets lung IMs was far from being 'quick and easy'. No fewer than eight different strains of mice were generated and tested in total, by crossing $Psd3^{cre}$, $Cxcl13^{cre}$, $Tgfb3^{cre}$, $Tmem119^{cre}$ or $Lyz2^{cre}$ mice with $Cx3cr1^{LSL-DTR}$ or $Csf1r^{LSL-DTR}$ mice, and only one of them, the $Tmem119^{cre}Cx3cr1^{LSL-DTR}$ line, turned out to be successful (data not shown).

We employed time-course analyses following DT-mediated niche clearance in IM^{DTR} mice to demonstrate that IM depletion was rapidly followed by a transient accumulation of classical monocytes (cMo) in the lung, preceding the gradual

restoration of both CD206⁺ and CD206⁻ IM subsets, which returned to baseline levels within approximately 1–2 weeks after depletion. Very similar repopulation kinetics have been reported in KC^{DTR} and SPAM deleter mice^{44,58,105,368}, suggesting that the timing of niche refilling after targeted macrophage ablation is largely conserved across distinct RTM compartments. Just before cMo recruitment we observed a rapid increase in Ccl2 levels in the lung very shortly after IM depletion, which also became detectable in the circulation, strongly suggesting that niche vacancy triggers a chemokine-driven recruitment of Ccr2-dependent Ly6C⁺ monocytes. This mechanism is consistent with previous reports describing Ccl2/Ccr2-mediated monocyte mobilization following tissue macrophage depletion^{44,58}. In the liver, Bonnardel et al. showed that hepatic stellate cells are the main source of Ccl2 and that its production is rapidly and transiently induced following KC depletion. Of note, we also performed time-course scRNA-seq analyses of niche cells, including endothelial cells, epithelial cells and fibroblasts (**Figures 4.1A** and **4.1B**), and found that *Ccl2* expression was rapidly induced in fibroblasts shortly after IM depletion (**Figures 4.1C** and **4.1D**), highlighting these cells as the main local source of Ccl2. Interestingly, this coincided with an increased production of *Cx3cl1* by endothelial cells (**Figures 4.1C** and **4.1E**), suggesting a coordinated chemokine response in which fibroblast-derived Ccl2 promotes cMo recruitment, while endothelial Cx3cl1 may facilitate their adhesion, retention and extravasation within the lung IM niche. However, this hypothesis remains to be formally validated. One approach would be to generate mixed bone marrow chimeras using Cx3cr1-deficient (e.g. *Cx3cr1*^{GFP/GFP}) and wild-type donor cells in thorax-protected IM^{DTR} recipients and assess their relative contribution to IM niche refilling following depletion. Such experiments would directly test whether Cx3cl1–Cx3cr1 interactions provide a selective advantage for monocyte recruitment and engraftment within the refilling IM niche.

Contradictory, Nr4a1-dependent CD16.2⁺ monocytes have been suggested to be putative precursors of CD206⁻ IMs, but this was uniquely based on scRNA-seq trajectory analyses¹⁰⁴. While a contribution of CD16.2⁺ monocytes to CD206⁻ IMs cannot be ruled out, no definitive proof exists so far, and their contribution would arguably be minimal as compared to the one of Ccr2-dependent cMo. Importantly, repopulated IMs acquired a transcriptomic profile nearly identical to that of resident IMs, in line with previous findings showing that tissue niches imprint macrophage identity and drive convergence of precursors toward resident RTM programs^{43,44,73}. Hence, this model provides a powerful and tractable system to study the dynamics and regulatory mechanisms of monocyte-to-IM differentiation *in vivo*.

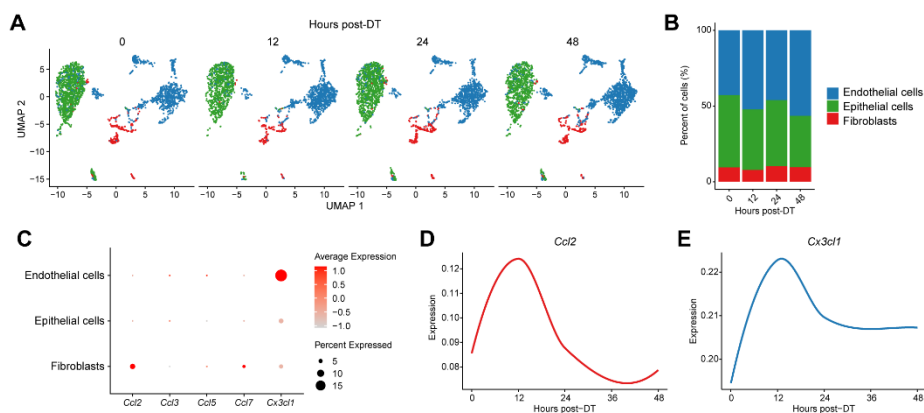


Figure 4.1. Time-resolved scRNA-seq of lung niche cells reveals coordinated induction of Ccl2 in fibroblasts and Cx3cl1 in endothelial cells following IM depletion. (A) UMAP plot depicting the transcriptional identity of sorted lung CD45⁻CD31⁺EpCAM⁻ endothelial cells, CD45⁻CD31⁻EpCAM⁺ epithelial cells, and CD45⁻CD31⁻EpCAM⁻ fibroblasts from IM^{DTR} mice injected with DT i.p. at 0, 12, 24, 48 and 96 h before the analysis (n = 3–4 pooled mice per time point). (B) Histogram showing the percentage of each cell type at each time point after DT. (C) Dot plots showing average expression of the indicated genes and the percentage of cells expressing the genes within each cell type. (D) Ccl2 expression in fibroblasts along different time points post-DT. (E) Cx3cl1 expression in endothelial cells along different time points post-DT.

By sampling lung myeloid cells at multiple time points after DT-mediated depletion and subjecting them to scRNA-seq and trajectory analyses, we were able to reconstruct the continuum of IM differentiation states emerging during repopulation. We identified a transient population of “transitioning monocytes” (Tr-Mo) that arise from classical monocytes and give rise to both CD206⁺ and CD206⁻ IM subsets. Notably, the transcriptional profile of Tr-Mo suggested a proliferative state, characterized by the upregulation of cell cycle-associated genes. This was experimentally validated by increased EdU incorporation in CD64⁺ cells two days after IM depletion. Furthermore, in bone marrow chimeric mice, the highest EdU incorporation was observed in monocyte-derived donor cells compared to residual host cells, indicating that recently recruited monocytes locally proliferate during the repopulation phase. Tr-Mo proliferation occurred before the branching toward CD206⁻ IMs or CD206⁺ IMs and the phenotype of EdU⁺CD64⁺ cells was intermediate between those of cMo and IMs. We found that the majority of EdU⁺CD64⁺ cells did not express the IM markers MHC-II or CD206 and were transient tissue monocytes (Tr-Mo). The high variability observed in the expression levels of IM markers in EdU⁺CD64⁺ Tr-Mo further suggested that this cell state was highly dynamic. The current view was that, in the myeloid compartment, the ability to proliferate is limited to progenitor cells and mature RTMs³⁷⁰. RTM maintenance is thus thought to be achieved through either the self-renewal of differentiated RTM, or the recruitment of monocytes that differentiate into RTMs in a tissue-specific manner^{24,298,300,305,307,309}. Our results showed that monocytes can also proliferate in vacant tissue niches to contribute to RTM development *in vivo*. By blocking Csf1/Csf1r signaling we demonstrate that Tr-Mo proliferate transiently in the tissue through Csf1r-dependent mechanisms. Our data are thus consistent with the idea that a limited number of cMo can give rise to a larger number of RTMs in tissues through a sequence of events involving first a proliferation in response

to local Csf1r ligands, followed by the activation of common and subset-specific transcriptional programs that drive RTM differentiation. This can be explained by a model proposing two thresholds of Csf1 activity: a lower “survival threshold” required to maintain macrophage longevity and a higher “proliferation threshold” that triggers macrophage division²⁹⁸. Following macrophage depletion, Csf1 is no longer consumed, leading to a transient local increase in available Csf1. This surplus growth factor may allow newly recruited or neighboring macrophages to surpass the proliferation threshold, thereby promoting their expansion and accelerating niche repopulation. While the relative contribution of the Csf1r ligands Csf1 and IL-34 to monocyte proliferation remains to be determined, reports indicating that IM maintenance requires Csf1 rather than IL-34 would be consistent with a preferential contribution of the Csf1/Csf1r axis to this process^{145,146,264}. However, through a recent collaboration with the group of Willinger, we show that fibroblasts in the empty IM niche actively attract monocytes in a Gpr183-dependent manner and subsequently provide local Csf1, thereby coordinating both the recruitment, proliferation and differentiation of incoming monocytes during IM niche refilling³⁶⁸.

Mafb expression slightly increased in CD206⁻ IM and CD206⁺ IM trajectories after the upregulation of cycling genes, and MafB expression was decreased in proliferating monocytes and increased in IMs compared to cMo. MafB restricts Csf1-dependent proliferation in myeloid progenitor cells^{239,333}, as well as the self-renewal ability of differentiated macrophages²⁴⁶, linking MafB activity with Csf1 responsiveness and the balance between proliferation and differentiation. Our data are consistent with the hypothesis that low MafB expression is required for monocyte proliferation, while subsequent increased MafB expression would restrict proliferation and drive their differentiation into IMs. Supporting this claim, *Mafb*-deficient CD64⁺ cells exhibited an increased proliferation potential

compared to wild-type IMs and seemed to be held in a transitioning state. Our results emphasized a differential requirement for MafB and c-Maf in lung IM development, as c-Maf deficiency was uniquely associated with changes that were restricted to CD206⁺ IMs, which have been shown to be preferentially associated with the vasculature¹⁰³. Of note, c-Maf was reported to regulate perivascular RTM phenotypes across different tissues³⁴⁷.

In conclusion, here we found that tissue cMo that transitioned toward IMs had the ability to proliferate locally in a vacant niche, in a MafB-restricted fashion, before undergoing differentiation into distinct IM subsets. We used a model of lung IM niche depletion and refilling that allowed us to characterize the transient, Csf1r-dependent, proliferation of monocytes, which would be difficult to capture in a steady-state setting. These observations shed new light on the complex regulation of monocyte proliferation versus RTM differentiation.

Despite these advances, several important questions remain. For example, the precise signals that instruct the bifurcation of transitioning monocytes into CD206⁺ versus CD206⁻ IM subsets remain to be fully defined. While our data suggest that local niche-derived cues and differential transcription factor activity, including MafB and c-Maf, contribute to this process, the upstream environmental factors and spatial cues that drive subset-specific specialization are still unclear. In a follow-up study we found that Tgfβ1 derived from lung endothelial cells plays a key role in IM development⁶⁰. More specifically, Tgfβ1 may act synergistically with Csf1 to induce expression of *Mafb* and IM signature genes (i.e., *Cx3cr1*, *Tmem119*, and *C1q*), and disruption of Tgfβ1/TgfβRII-signaling resulted abrogated differentiation of both CD206⁻ IMs and CD206⁺ IMs. On the other hand, a recent study using adoptive transfer of GMP- or MDP-derived monocytes reported that, although most IMs are replaced by MDP-derived cells, GMP-derived IMs preferentially adopt a transcriptomic profile

closer to CD206⁺ IMs, whereas MDP-derived IMs more closely resemble CD206⁻ IMs³⁴⁴. These findings suggest that, in addition to local niche signals, the ontogeny of incoming monocytes may also imprint biases in their differentiation potential and thereby contribute to shaping tissue macrophage subset identity.

One key question is whether the transient proliferative phase we observed represents a lung IM-specific feature of monocyte-to-macrophage differentiation or whether similar proliferative intermediates also occur in other tissue macrophage niches during repopulation. Addressing this will be important to determine whether local monocyte expansion constitutes a general principle of RTM development or a context-dependent adaptation of the lung environment. In this regard, the groups of Guilliams and Glass independently demonstrated that monocyte-derived differentiating KCs also undergo a proliferative phase, as evidenced by increased expression of cell cycle-associated genes (e.g. *Mki67*) (**Figure 4.2**) and elevated EdU incorporation peaking 2–3 days after KC depletion, suggesting that proliferation of monocyte-derived precursors may be a shared feature of niche refilling across tissues^{58,59}. Moreover, the group of Guilliams further showed that this proliferation of monocyte-derived KCs

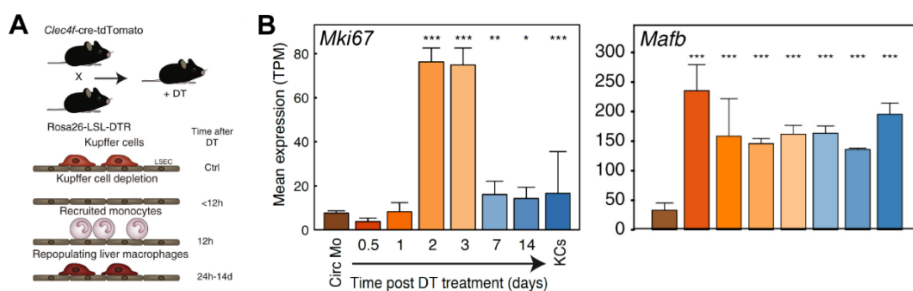


Figure 4.2. Transient proliferation during monocyte-to-Kupffer cell differentiation after niche depletion. (A) Experimental outline. (B) *Mki67* and *Mafb* expression in sorted circulating monocytes (Circ Mo), KCs and differentiating repopulating liver macrophages at different indicated time points post-DT, as quantified by bulk RNA-seq. After Sakai *et al.* Liver-Derived Signals Sequentially Reprogram Myeloid Enhancers to Initiate and Maintain Kupffer Cell Identity. *Immunity*, 51(4), 655–670.e8.⁵⁹

occurs in a *Csf1r*-dependent manner, reinforcing the idea that local growth factor-driven expansion of recruited monocytes may represent a conserved mechanism during RTM niche regeneration⁵⁸. However, it remains unclear whether this proliferative phase is similarly regulated by *MafB*, as newly recruited monocytes already begin to express high levels of *Mafb* soon after entering the niche (**Figure 4.2**)⁵⁹.

In addition, the precise nature of monocyte proliferation within the niche remains to be clarified. It is currently unclear whether recruited monocytes divide symmetrically, generating two equivalent monocyte-like progeny that subsequently differentiate, or asymmetrically, directly producing one differentiated IM and one monocyte precursor. Resolving this question will be essential to understand how proliferative intermediates quantitatively and qualitatively contribute to niche refilling. One way to address this could be using clonal lineage tracing (e.g., lentiviral barcoding combined with time-resolved scRNA-seq) to quantify clonal expansion and differentiation output in situ.

Finally, it will be important to determine how these differentiation dynamics operate under non-homeostatic conditions. RTM depletion is commonly observed in various inflammatory contexts, and this creates vacant niches that need to be refilled²²². Indeed, transient mo-macs and/or macrophage proliferation have been described in different homeostatic and non-homeostatic contexts^{23,25,99,371–374}. However, inflammatory cues, tissue injury or chronic remodeling may profoundly alter chemokine production, growth factor availability and transcriptional programming, thereby reshaping monocyte recruitment, proliferation and specialization. Further understanding the molecular mechanisms underlying *Csf1r*-dependent monocyte proliferation in peripheral organs, both at homeostasis and during inflammation, will be crucial

to enable the rational manipulation of these pathways for preventive or therapeutic purposes.

Part II: MafB as a central regulator of macrophage maturation, identity and function

Resident macrophage maturation and tissue-specific identity depend on transcriptional programming, yet how conserved regulators universally drive these programs remains unresolved across tissues. In the first part of the thesis, we focused on the transcriptional regulation, as well as the cellular and environmental dynamics, governing monocyte-to-RTM differentiation, using a model of inducible IM depletion to synchronize niche refilling and capture intermediate developmental states *in vivo*. Using this model, we identified MafB as a key transcriptional regulator dynamically modulated along the monocyte-to-IM differentiation trajectory and potentially involved in controlling the balance between proliferation and terminal macrophage differentiation. These observations prompted us to investigate whether MafB acts more broadly as a central regulator of RTM development and identity across tissues.

Consistent with this hypothesis, MafB is known to be highly expressed in myelomonocytic cells, including macrophages, and to play a key role in monocytic differentiation^{238–240}. Genome-wide expression analyses revealed that *Mafb* is among the most strongly upregulated transcription factors in RTMs compared to monocytes and DCs, and is broadly expressed across multiple tissue macrophage populations, with the notable exception of AMs, consistent with previous reports^{42,72}. Querying the Tabula Muris Senis dataset, a comprehensive single-cell transcriptomic atlas of adult mouse tissues, showed that indeed in adult mice *Mafb* is highest expressed in RTMs. However, other cell types showing notable *Mafb* expression include keratinocytes and kidney podocytes, in which MafB has also been implicated in their differentiation^{375,376}. During development and in adulthood, MafB is also expressed in specific neuronal populations^{377–380},

particularly in hindbrain and brainstem neurons involved in respiratory control³⁸¹, as well as in pancreatic islets where it contributes to β -cell formation³⁸². Consistent with these roles, MafB-deficient mice are embryonically lethal and die at birth due to severe defects in respiratory rhythm generation³⁸¹. The preferential expression of MafB in macrophages was confirmed at the protein level and was further shown to progressively increase along monocyte-to-macrophage differentiation trajectories, such as the “monocyte waterfall” in the gut. By generating *Mafb*^{Cre} reporter mice, Wu et al. demonstrated that *Mafb* expression distinguishes macrophages from classical DCs, neutrophils, and B cells across multiple organs²⁴². Moreover, they observed progressively increasing *Mafb* expression along the “monocyte waterfall” in the gut, suggesting that cells acquiring macrophage identity accumulate MafB until reaching a steady-state concentration at late stages of differentiation.

Having established that MafB is highly and preferentially expressed in RTMs and upregulated during monocyte-to-macrophage differentiation, we next sought to directly assess its functional role in macrophage development. Since germline MafB deficiency is embryonically lethal and MafB is also expressed in other cell types, albeit at lower levels, we used the *Lyz2*^{Cre}*Mafb*^{fl/fl} mice described in the first part to achieve conditional myeloid-specific MafB depletion. *Lyz2* is predominantly expressed in myelomonocytic cells, including monocytes, macrophages and granulocytes in mice, and *Lyz2*-driven Cre is therefore widely used to conditionally delete genes in the macrophage lineage^{383,384}. In most RTM populations, *Lyz2*^{Cre}-mediated recombination reaches high efficiency (>90%), although some subsets, such as MG and certain splenic macrophages, display lower recombination rates of around 40%^{385,386}. Of note, *Mafb* is a relatively small single-exon gene (~3.4 kb), and in the first part we were able to efficiently delete *Mafb* using *Ms4a3*^{Cre} mice, a line notoriously known for its relatively low

recombination efficiency of floxed alleles (unpublished observations from multiple labs), further supporting the feasibility of achieving robust *Mafb* deletion in the myeloid compartment. Based on gene expression analyses and western blotting (data not shown), we confirmed efficient *Mafb* deletion in *ex vivo*-derived macrophages as well as in multiple RTM populations of *Lyz2^{Cre}Mafb^{fl/fl}* mice. Alternatively, other monocyte/macrophage-lineage-specific Cre lines, such as *Csf1r^{Cre}*, could have been used, as shown to efficiently delete *Mafb* in MG²⁷². Subset-specific Cre drivers, for example *Clec4f^{Cre}* for KCs, might also allow targeted deletion in individual RTM populations, however, such genes are typically expressed at later stages of differentiation. As our aim was to assess the role of MafB during macrophage differentiation process, we first opted for an early myeloid-targeting strategy to delete *Mafb* prior to terminal macrophage specialization.

Having established an efficient myeloid-specific MafB deletion model, we next examined the consequences of MafB loss on macrophage differentiation *ex vivo*. MafB-deficient BMDMs exhibited impaired differentiation, as reflected by altered morphology together with an immature transcriptomic profile and phenotype. A previous study reports that MafB-deficient macrophages display increased membrane protrusions²⁴⁴, a phenotype opposite to our observations. This discrepancy may arise from differences in experimental models, as that study used *in vitro*-derived macrophages from fetal liver cells of globally MafB-deficient mice, whereas we analyzed BMDMs from conditionally targeted mice. Of note, in our study, MafB-deficient KCs *in vivo* also showed reduced pseudopods, validating the phenotype observed in BMDMs. Although BMMo were not directly analyzed, comparison of lung classical monocytes between WT and MafB-deficient mice revealed very few differentially expressed genes (data not shown), suggesting that MafB loss has minimal impact at the monocyte

stage. This supports the notion that the observed defects primarily arise during macrophage differentiation rather than in precursor cells.

In competitive bone marrow chimeras, MafB-deficient monocytes showed a markedly reduced capacity to contribute to most RTM compartments, demonstrating that MafB intrinsically promotes monocyte-to-RTM differentiation across tissues. Notably, this competitive disadvantage was not observed in SPMs. One possible explanation is that SPMs are considered an intermediate stage in the differentiation of LPMs and express only intermediate levels of MafB, suggesting that their development may be less dependent on MafB than that of fully mature RTMs. In addition, Wu et al. using *Mafb^{Cre}Rosa26^{LSL-YFP}Zbtb46^{GFP}* mice reported that the conventional flow cytometric gating strategy used to define SPMs can be contaminated by YFP⁻GFP⁺ dendritic cells, which do not express MafB²⁴². Consistent with this, our scRNA-seq analyses of similarly sorted SPM populations also revealed the presence of contaminating DCs, which could further mask a potential competitive defect of MafB-deficient cells within the bona fide SPM compartment. In contrast, AMs displayed an unexpected phenotype. Although mature AMs do not express detectable MafB, MafB-deficient monocytes exhibited a clear competitive disadvantage in contributing to the AM compartment, indicating that MafB is nevertheless required during their postnatal differentiation from monocytes in this genotoxic model. This suggests that MafB may be transiently expressed and functionally important in monocyte-derived precursors in some contexts. Alternatively, MafB might act during earlier developmental stages of AM ontogeny and subsequently be silenced in fully differentiated cells to permit their self-renewal capacity, as proposed by Soucie et al²⁴³. Supporting this interpretation, lineage tracing in *Mafb^{Cre}Rosa26^{LSL-tdTomato}* mice revealed that a substantial fraction of AMs are tdTomato⁺, indicating a history of MafB

expression despite the absence of MafB in the mature steady-state population³⁸⁷.

Single-cell transcriptomic profiling further revealed that MafB-deficient RTMs exhibited diminished expression of subset-specific identity genes and lower global macrophage signature scores, accompanied by increased preMac signatures. Of note, in IMs we did not observe a decrease in IM-specific identity genes, which appears in contradiction with the findings from the first part of this work. However, this discrepancy likely reflects differences in how the identity signatures were defined. In the present analysis, the IM-specific signature was based on DEGs distinguishing IMs from all other RTM populations, thereby emphasizing genes uniquely enriched in IMs. In contrast, the IM signature used in the first part was derived from comparisons with lung monocytes and alveolar macrophages, and therefore included a broader set of genes related to general macrophage differentiation and activation. These data indicate that MafB not only supports terminal macrophage differentiation but also reinforces the transcriptional identity and maturation state of RTMs *in vivo*, acting as a central regulator of macrophage specification across multiple tissue environments. Interestingly, similar observations have been reported in RTM-specific Zeb2-deficient mice²³⁶. Loss of Zeb2 primarily affected tissue-specific identity programs, however, the broader macrophage differentiation program remained largely intact.

Notably, CD52 emerged as a consistent marker of the immature state associated with MafB deficiency. *Cd52* is highly expressed in preMac stages and is normally downregulated during the transition to fully differentiated RTMs. The sustained elevation of CD52 in MafB-deficient RTMs therefore supports the notion that these cells are arrested at an intermediate developmental stage rather than fully acquiring a mature tissue-resident phenotype. CD52 is a small

glycosylphosphatidylinositol (GPI)-anchored glycoprotein that is highly expressed on the surface of circulating immune cells, including lymphocytes, monocytes and dendritic cells, as well as on mature sperm cells. Although its precise biological function remains incompletely understood, its highly negatively charged characteristic has led to the hypothesis that CD52 may exert anti-adhesive properties, helping to maintain cells in a migratory and non-adherent state until they reach their appropriate target tissues³⁸⁸. In this context, the sustained high expression of CD52 observed in MafB-deficient RTMs may reflect their immature differentiation state, suggesting that these cells have not fully acquired stable niche residency and may still retain a migratory, pre-niche-seeking phenotype rather than being fully anchored within their tissue microenvironment.

The single-cell transcriptomic data are further supported by multiparameter flow cytometry analyses of RTMs from multiple organs. Taken together, these data are consistent with the idea that, in the absence of MafB, RTMs fail to fully mature and persist in an immature state, irrespective of embryonic or postnatal origin. First, both embryonic RTMs (i.e., MG) and postnatal monocyte-derived RTMs (i.e., CMs) were affected by MafB targeting. Second, immaturity was supported by reduced expression of maturity markers, including Tim4, Vsig4 and CD163 in KCs, Vsig4 in LPMs, P2ry12 and Fcrls in MG, or CD163 in RPMs and in MHC-II⁺ CMs while the preMac marker CD52 remained elevated. Third, downregulation of RTM maturity markers in MG and KCs upon MafB deletion with cell type-specific Cre drivers (*Tmem119* for MG, *Clec4f* for KCs) supported MafB's dual role in both RTM development and maintenance of identity *in vivo*. Finally, our findings are also consistent with the idea that MafB-deficient RTMs fail to adapt to their niches or occupy alternative spatial niches, subsequently leading to phenotypical and functional deficits. Advanced imaging techniques

and spatial proteogenomic approaches will be instrumental in clarifying how RTMs interact with their microenvironment in specific tissues and to what extent such interactions are modulated by MafB.

Having established that MafB controls RTM maturation and identity, we examined the functional consequences of MafB loss on RTM activity *in vivo*. Collectively, our findings indicate that MafB deficiency profoundly compromises RTM functions *in vivo*, including phagocytosis, tissue clearance and several homeostatic processes across organs. While the list of functions tested is not exhaustive, the extent of defects observed supports MafB's essential role in sustaining RTM activity and tissue homeostasis. These impairments are likely to have even greater consequences with aging or under environmental, inflammatory, or metabolic stressors, raising the possibility that MafB deficiency predisposes RTMs to dysfunction under challenge. Notably, whereas previous studies report normal macrophage functionality in the absence of MafB *ex vivo*^{244,246}, our *in vivo* analyses challenge this notion and reveal clear defects in RTM phagocytosis and clearance functions, highlighting the importance of assessing macrophage biology in tissue contexts. How MafB integrates stress responses and environmental cues to safeguard RTM functions over the lifespan represents exciting perspectives for future research.

To gain mechanistic insight into how MafB controls macrophage maturation and identity, we investigated its direct genomic targets using CUT&RUN in BMDMs. MafB binding sites were widely distributed across promoters, introns and distal regulatory regions, and were associated with reduced H3K27ac levels upon MafB deletion, indicating that MafB promotes transcriptional activation at these cis-regulatory elements. These observations raise the possibility that MafB may function, at least in part, as a pioneer transcription factor that facilitates chromatin accessibility and the recruitment of additional lineage-defining

regulators. In support of this notion, MafB has been shown in podocytes to act as a pioneering factor that opens chromatin and enables the recruitment of WT1 to promoters of podocyte-specific genes³⁷⁶, suggesting that a similar mechanism could operate in macrophages to establish and stabilize the macrophage-specific transcriptional landscape.

Integration of binding and transcriptional data revealed that MafB directly targets a large set of core macrophage genes, including *Csf1r*, *Mertk* and *C1q* family members, as well as transcription factors central to macrophage identity such as *Zeb2*, *Sp1* (encoding for PU.1) and *Cebpb*. These findings support a model in which MafB operates as a central node in the transcriptional network governing macrophage differentiation, reinforcing both lineage-defining genes and secondary regulators that stabilize macrophage identity.

Interestingly, MafB binds the evolutionarily conserved FIRE enhancer within the *Csf1r* locus^{55,117,350}, and *Csf1r* expression together with CD115 surface levels were reduced in multiple MafB-deficient RTMs, suggesting a link between MafB activity and the *Csf1r*/*Csf1* signaling pathway required for RTM maintenance and survival. Computational predictions based on cross-species open chromatin profiles in MG have also proposed an evolutionarily conserved MafB binding site within the FIRE enhancer³⁵¹. Moreover, mice lacking the FIRE enhancer display reduced CD115 expression on RTMs and certain RTM subsets fail to develop, such as MG³⁴⁹, although the phenotypes observed upon MafB deletion are less pronounced. This difference likely reflects the fact that the FIRE enhancer is a hotspot for multiple transcription factor binding sites could sustain *Csf1r* expression^{55,351}. In addition, *Csf1r* expression in some RTM populations could to be partially independent of FIRE and may be controlled by other cis-regulatory elements, such as the *Csf1r* upstream regulatory element A (CUREA), which can drive *Csf1r* expression in trophoblasts^{124,125,389}.

A substantial proportion of MafB binding sites and target genes overlapped between BMDMs and primary LPMs, indicating that MafB controls a conserved core macrophage program while also binding tissue-specific loci, such as *Pf4* and *Vsig4*, suggesting an additional role in tissue specialization. Together, these data indicate that MafB directly imprints macrophage differentiation and identity through coordinated regulation of enhancer and promoter landscapes.

Interestingly, many of the genes identified as direct MafB targets converge on the core macrophage function of phagocytosis. These targets span multiple steps of the phagocytic cascade, including target/pattern recognition (e.g., *Cd36*, *Cd14*, *Mrc1*, *Mertk*, *C3ar1*, *C5ar1*)⁵⁴, cytoskeletal remodeling and engulfment (*Arhgef7*, *Arhgap*, *Rhob*, *Myo1e*)^{390–392}, and phagosome formation and trafficking (*Eea1*, *Dab2*, *Washc5*)^{393–395}. In addition, MafB directly regulates genes required for phagolysosomal maturation and degradation, such as v-ATPase components (*Atp6v0a1*, *Atp6v1a*)³⁹⁶, lysosomal proteases (*Ctsb*, *Ctsl*, *Lgmn*)^{397,398}, and metal/ion transporters (*Slc11a1*)³⁹⁹, supporting efficient acidification and cargo processing. Complement genes (*C1qa*, *C1qb*, *C1qc*)²⁴⁵ and lipid-handling factors (*Apoe*, *Abca1*) further indicate that MafB reinforces opsonin-mediated uptake and post-engulfment metabolic adaptation. Notably, several of these targets also align with pathways implicated in erythrophagocytosis, including receptors and complement components involved in recognition of senescent erythrocytes, scavenger and hemoglobin–haptoglobin receptors such as *Cd163*⁴⁰⁰, and lysosomal/iron-handling genes (e.g., *Slc11a1*, *Steap3*) required for safe processing of erythrocyte-derived cargo, consistent with a broader role of MafB in specialized clearance functions.

Strikingly, MafB's binding sites exhibit greater evolutionary conservation across vertebrates than those of PU.1, revealing an unappreciated central role in macrophage biology and suggesting that MafB integrates tissue-specific cues and

translates them into core transcriptional programs define RTM identity across diverse tissues and species. Moreover, CUT&RUN analyses in human monocyte-derived macrophages revealed substantial overlap with mouse MafB binding sites and target genes, including core macrophage identity genes such as *CSF1R*, *MERTK* and *CD163*. These cross-species analyses highlight that MafB-driven transcriptional programs are deeply conserved, supporting the notion that MafB functions as an evolutionarily conserved master regulator of macrophage differentiation and identity.

In conclusion, this study identifies MafB as a pivotal and evolutionarily conserved transcriptional regulator of RTM development, identity and function across diverse tissues. Using conditional gene targeting combined with epigenetic, transcriptomic, phenotypic and functional analyses, we have shown that MafB deficiency disrupted RTM-specific transcriptional programs, altered RTM phenotypes and functions, and impaired tissue homeostasis in mice. Mechanistically, we have shown that MafB directly controlled pivotal macrophage differentiation and identity genes through *cis*-regulatory elements, establishing a core macrophage regulatory network preserved across vertebrates.

Despite identifying MafB as a central and evolutionarily conserved regulator of RTM differentiation, identity and function, several important questions remain to be addressed. First, although our data support a model in which MafB promotes terminal macrophage maturation and stabilizes tissue-resident identity, the precise upstream signals that dynamically regulate MafB expression during monocyte-to-RTM differentiation remain unclear. We observed that MafB expression increases along the differentiation trajectory within a refilling niche, suggesting that environmental cues, such as Csf1/IL-34 availability, niche-derived cytokines or metabolic signals, may directly control MafB induction.

Defining the extracellular signals and intracellular pathways that regulate MafB expression will therefore be essential to understand how tissue niches instruct macrophage maturation in a context-dependent manner. This could be addressed by combining candidate-based approaches, in which key niche-derived signals or their corresponding receptors are perturbed *in vitro* and *in vivo* to assess their impact on MafB expression, with unbiased strategies such as single-cell transcriptomics, chromatin accessibility profiling and regulon inference to identify upstream transcriptional regulators and signaling pathways. In addition, assessing MafB activity through analysis of downstream target gene expression and chromatin occupancy would help distinguish between regulation of MafB expression versus functional activation.

Another key unresolved issue concerns the exact chromatin-related mechanisms through which MafB controls macrophage identity. Our CUT&RUN data suggest that MafB promotes transcriptional activation at enhancer and promoter regions and may function as a pioneer transcription factor. However, whether MafB directly remodels chromatin accessibility or instead cooperates with other lineage-defining factors such as PU.1, C/EBP β or Zeb2 to establish stable macrophage enhancer landscapes remains to be determined. Future studies combining ATAC-seq, CUT&RUN profiling and perturbation of cooperating transcription factors will help clarify whether MafB initiates or merely stabilizes macrophage-specific regulatory circuits.

A role for MafB in restraining macrophage proliferation has been proposed by the group of Sieweke, who showed that MafB represses self-renewal-associated genes such as *Klf2/4* and *Myc*, and that MafB- and c-Maf-deficient macrophages display increased colony-forming capacity and enhanced proliferation *ex vivo*. They further observed that proliferating macrophages *in vivo* express lower levels of MafB, suggesting an inverse relationship between MafB expression and

cell-cycle activity. Our data in the first part are consistent with this model. During IM niche refilling, monocytes pass through a proliferative transitioning state characterized by low *Mafb* expression, which subsequently increases as cells differentiate into mature IMs. Accordingly, MafB-deficient IMs displayed higher Ki67 expression and a less differentiated phenotype, supporting the idea that MafB acts as a molecular switch that terminates proliferation and promotes terminal macrophage differentiation. Interestingly, such an increase in proliferation signatures was not evident in other MafB-deficient RTM populations, indicating that the link between MafB and proliferation may be particularly prominent in niches undergoing active refilling. Notably, transplanted MafB/c-Maf-deficient macrophages do not undergo uncontrolled expansion *in vivo* but instead integrate into host tissues, suggesting that extrinsic niche constraints, such as limited availability of Csf1 or IL-34, normally restrict their proliferative potential. In this context, IMs may represent a unique case, as they were among the most numerically reduced RTM populations upon MafB deletion, potentially resulting in increased local Csf1 availability that could further drive proliferation of the remaining or newly recruited cells.

An additional question concerns the role of MafB in regulating RTM survival and the balance between self-maintenance and monocyte replacement. In RTM-specific Zeb2-deficient mice, Scott et al. demonstrated that loss of Zeb2 impaired macrophage survival, resulting in increased cell turnover and enhanced replacement by circulating monocytes²³⁶. Interestingly, our data suggest a similar phenomenon in the absence of MafB. RTMs that lack MafB expressed higher levels of monocyte signature genes, and KCs did not express CD163 (**Figure 4.3A** and **4.3B**), a marker of embryonically-derived KCs^{44,401} but rather expressed higher levels of the monocyte-derived KC marker Ly6A/E⁴⁰¹ (**Figure 4.3C** and **4.3D**). We therefore hypothesized that MafB-deficient RTMs were being

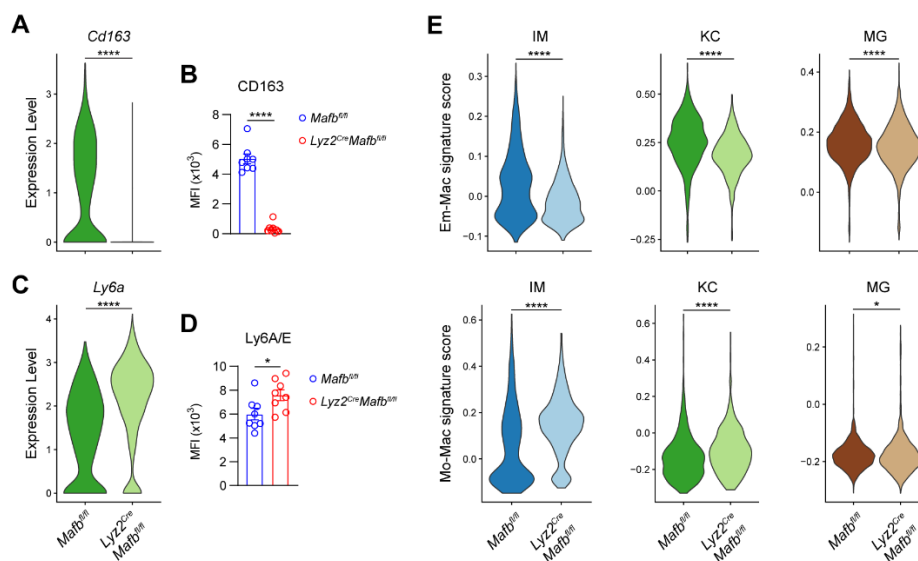


Figure 4.3. *MafB* deficiency may promote monocyte-driven replacement of RTMs. (A) Violin plot of *Cd163* expression in KC of *Mafb*^{fl/fl} and *Lyz2^{Cre}Mafb*^{fl/fl} mice (height: expression; width: abundance of cells). (B) Bar graphs of *CD163* expression in KC, assessed by flow cytometry in *Mafb*^{fl/fl} and *Lyz2^{Cre}Mafb*^{fl/fl} mice (n = 8/group). (C) Violin plot of *Ly6a* expression in KC of *Mafb*^{fl/fl} and *Lyz2^{Cre}Mafb*^{fl/fl} mice (height: expression; width: abundance of cells). (D) Bar graphs of *Ly6A/E* expression in KC, assessed by flow cytometry in *Mafb*^{fl/fl} and *Lyz2^{Cre}Mafb*^{fl/fl} mice (n = 8/group). (E) Violin plots of Em-Mac (top) and Mo-Mac (bottom) signature scores within IM, KC and MG of *Mafb*^{fl/fl} and *Lyz2^{Cre}Mafb*^{fl/fl} mice (height: score; width: abundance of cells). Data are mean ± SEM, pooled from two independent experiments (B and D). *P* values were calculated using a Wilcoxon rank-sum test (A, C and E) or two-tailed Student's *t* test (B and D). **P*<0.05; ***P*<0.01; ****P*<0.001; *****P*<0.0001.

replenished by monocytes at a higher rate as compared to WT RTMs. We created embryonically-derived and monocyte-derived signature scores of IMs¹¹⁰, KCs⁴⁴ and MG⁷³ and found that IMs, KCs and MG from *Lyz2^{Cre}Mafb*^{fl/fl} mice expressed lower levels of embryonically-derived scores and higher levels monocyte-derived scores as compared to controls (**Figure 4.3E**), suggesting a higher rate of replacement by monocytes. Bone marrow chimera experiments further supported an increased albeit minor contribution of donor-derived monocytes to *MafB*-deficient RTM compartments (data not shown). However, these

approaches do not formally distinguish whether MafB deficiency primarily affects macrophage survival, niche retention, or differentiation dynamics. Addressing this question will require more direct fate-mapping strategies, such as parabiosis experiments to quantify monocyte contribution under steady-state conditions, or crossing MafB-deficient mice with *Ms4a3^{FlpO}Rosa26^{FSF-TdTomato}* reporter mice to specifically trace monocyte-derived macrophages over time. Such studies will be essential to determine whether MafB safeguards long-term RTM maintenance.

Another important limitation of the present study is that it was largely conducted under homeostatic conditions. Given the pronounced defects in phagocytosis, clearance and tissue homeostasis observed in MafB-deficient RTMs, it will be essential to determine how these cells respond to inflammatory, infectious or metabolic challenges, as well as during aging, to assess whether MafB acts as a resilience factor that preserves RTM function under stress. In support of this idea, in a mouse model of influenza A virus infection we recently identified a distinct population of Ly6G⁺ monocyte-derived macrophages emerging during the early recovery phase after viral lung injury⁹⁷. Notably, both cMaf and MafB were highly expressed and predicted to be transcriptionally active in these Ly6G⁺ macrophages, and this population was absent in myeloid-specific MafB/cMaf-deficient mice, which exhibited worsened disease outcomes. Additional evidence supporting a context-dependent role of MafB in macrophage adaptation comes from allergic inflammation models. In a recent study, the group of Lambrecht reported that, in type 2 allergic asthma, IL-33-activated ILC2s produced IL-13, which reprogrammed tissue-resident AMs (trAMs) toward enhanced chemokine production and multinucleated giant cell formation¹⁰⁵. Of note, although AMs express little to no MafB at steady state, IL-33-treated trAMs exhibited increased expression of *Mafb*, as well as several

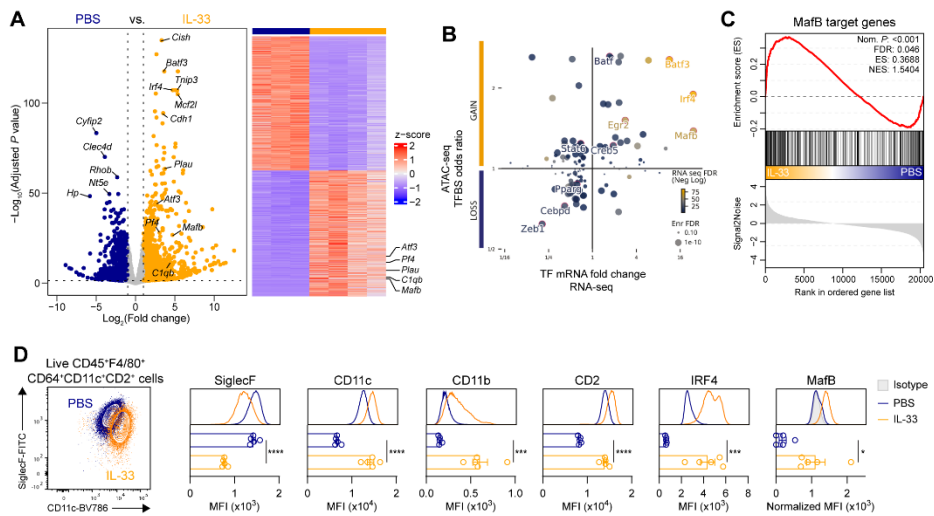


Figure 4.4. IL-33–induced reprogramming of trAMs is associated with MafB induction and enrichment of MafB-dependent transcriptional programs. (A) Volcano plot (left) and heatmap (right) of DEGs between trAMs from PBS- and IL-33-treated mice (ArrayExpress: E-MTAB-15952). (B) Integration of TF expression and motif enrichment analysis in PBS- versus IL-33-treated trAMs. (C) GSEA showing enrichment of MafB target genes in IL-33-treated trAMs compared to control trAMs. MafB target genes were defined as genes harboring a MafB CUT&RUN peak within ± 2 kb of the transcription start site and enriched in WT compared to MafB-deficient BMDMs. (D) Flow cytometric analysis of trAMs isolated from PBS- and IL-33-treated mice. Representative contour plots (left) show gating of trAMs. Histograms depict expression levels of indicated surface markers and TFs ($n=5/\text{group}$). Data are mean \pm SEM, pooled from two independent experiments (D). P values were calculated using a Wald test with Benjamini-Hochberg correction (A), a permutation test (C) or two-tailed Student's t test (D). * $P < 0.05$; ** $P < 0.01$; *** $P < 0.001$; **** $P < 0.0001$.

MafB target genes (including *Atf3*, *Pf4*, *Plau* and *C1q*) (Figure 4.4A). While IRF4 was identified as a key molecular switch in this process, the authors also reported enrichment of MafB binding motifs in IL-33-treated trAMs (Figure 4.4B). We further found, using GSEA, that IL-33 trAMs displayed an enrichment in MafB target genes, as identified here, as compared to PBS-treated controls (Figure 4.4C). Consistent with these transcriptional changes, we found that trAMs from IL-33-treated mice displayed expected phenotypic changes¹⁰⁵ as well as

upregulation of MafB protein expression (**Figure 4.4D**). These findings suggest that MafB-dependent transcriptional programs are dynamically engaged during inflammatory reprogramming and may contribute to the functional adaptation of RTMs in pro-allergic settings. To further address these questions, we have initiated collaborative efforts to examine the role of MafB under non-homeostatic conditions and during macrophage ontogeny. In collaboration with Bart Lambrecht and Bénédicte Machiels, we will investigate how MafB regulates trAM adaptation to environmental stress and inflammation in models of allergy and viral infection, contexts in which we and others have observed increased *Mafb* expression despite the low *Mafb* levels in steady-state AMs. In parallel, together with Philipp Henneke, we aim to study the role of MafB in AM development, as *Mafb* reporter mice label a substantial fraction of AMs, suggesting a history of *Mafb* expression, and to assess its contribution to macrophage responses during murine cytomegalovirus infection.

Furthermore, although our data suggest that MafB-deficient RTMs may fail to properly adapt to or occupy their appropriate tissue niches, direct evidence for altered spatial positioning or niche engagement is still lacking. Advanced intravital imaging, spatial transcriptomics and spatial proteogenomic approaches will be instrumental to determine how MafB shapes RTM–niche interactions and whether defective niche anchoring contributes to the immature and dysfunctional phenotypes observed in MafB-deficient cells.

Finally, the strong evolutionary conservation of MafB binding sites and target genes across mouse and human macrophages raises the important question of how MafB dysregulation may contribute to human disease. Given the central role of RTMs in tissue homeostasis, inflammation and repair, altered MafB activity could potentially impact a wide range of pathologies, including chronic inflammatory diseases, fibrosis, neurodegeneration or metabolic disorders.

Understanding how MafB integrates environmental signals to maintain RTM identity and function over the lifespan therefore represents an important avenue for future research and may open new therapeutic strategies aimed at restoring macrophage homeostasis in disease contexts. In this regard, recent work performed in collaboration with us, using humanized *in vivo* models has identified MAFB as a key transcriptional regulator of tumor-associated macrophage (TAM) identity and plasticity, supporting the notion that MafB-dependent programs may also operate in TAMs⁴⁰². These findings suggest that MafB could represent a potential therapeutic target to modulate tumor-promoting macrophage functions. However, such an approach should be considered with caution, as MafB also plays a broader role in the differentiation and functional stability of tissue-resident macrophages across organs. Systemic targeting of MafB may therefore lead to unintended side effects, including impaired tissue repair, defective immune regulation and disruption of macrophage-dependent homeostatic functions. In this context, targeting upstream regulators that control MafB in a context-dependent manner may represent a more selective and therapeutically relevant strategy.

Conclusion

The work presented in this thesis advances our understanding of how macrophage identity and functional specialization are established through transcriptional regulation. In particular, our results identify the transcription factor MafB as a central regulator orchestrating key stages of macrophage maturation.

The identification of proliferative transitioning monocytes during lung IM differentiation provides new insight into the dynamic nature of macrophage development *in vivo*. Rather than representing a simple linear progression, monocyte-to-macrophage differentiation appears to involve distinct intermediate states that integrate proliferative expansion with the progressive acquisition of macrophage identity. In this context, MafB expression increases as cells transition toward a mature macrophage state, suggesting a role for this transcription factor in coordinating the shift from proliferation to terminal differentiation. Together, these observations indicate that the timing and coordination of transcriptional programs, including MafB, are closely linked to the establishment of RTM populations.

More broadly, our findings demonstrate that MafB plays a crucial role in stabilizing macrophage identity by regulating core macrophage gene programs while permitting tissue-specific specialization. The evolutionary conservation of MafB-dependent regulatory networks across vertebrates further underscores the fundamental nature of this transcriptional pathway in macrophage biology. Together, these results place MafB at a key regulatory node linking differentiation cues, transcriptional identity, and macrophage function across tissues.

Beyond their conceptual implications, these findings may also have translational relevance. Macrophages contribute to the pathogenesis of numerous diseases, including chronic inflammatory disorders, fibrosis, infection, and cancer. Understanding the transcriptional mechanisms that govern macrophage differentiation and functional programming could therefore open new avenues for therapeutic intervention. Targeting regulators such as MafB or the pathways that control its activity may provide opportunities to modulate macrophage identity and function in pathological contexts. Future work aimed at dissecting how MafB integrates environmental signals and interacts with other transcriptional regulators will be essential to determine whether this regulatory axis can be harnessed to selectively reprogram macrophage responses in disease.

REFERENCES

REFERENCES

1. Élie Metchnikoff. *Leçons Sur La Pathologie Comparée de l'inflammation : Faites à l'Institut Pasteur En Avril et Mai 1891*. (Libraire de l'académie de médecine, Paris, 1892).
2. Metchnikoff, E. Untersuchungen über die mesodermalen Phagozyten einiger Wirbeltiere. *Biol Zentralbl* **3**, 560–565 (1883).
3. Kölliker, A. *Handbuch Der Gewebelehre Des Menschen*. (W. Engelmann, Leipzig, 1847).
4. Preyer, W. Ueber amöboide Blutkörperchen. *Virchows Archiv* **30**, 417–441 (1867).
5. Kupffer, C. Ueber Sternzellen der Leber. *Archiv für mikroskopische Anatomie* **12**, 353–358 (1876).
6. Browicz. Ueber intravasculäre Zellen in den Blutcapillaren der Leberacini. *Archiv für mikroskopische Anatomie* **55**, 420–426 (1899).
7. Metschnikoff, E. Ueber den Kampf der Zellen gegen Erysipel-kokken. *Archiv für pathologische Anatomie und Physiologie und für klinische Medicin* **107**, 209–249 (1887).
8. de Duve, C., Pressman, B. C., Gianetto, R., Wattiaux, R. & Appelmans, F. Tissue fractionation studies. 6. Intracellular distribution patterns of enzymes in rat-liver tissue*. *Biochemical Journal* **60**, 604–617 (1955).
9. Novikoff, A. B. & Essner, E. The liver cell: Some new approaches to its study. *The American Journal of Medicine* **29**, 102–131 (1960).
10. Carr, Ian. *The Macrophage; a Review of Ultrastructure and Function [by] Ian Carr*. (Academic Press, 1973).
11. Cohn, Z. A. The Structure and Function of Monocytes and Macrophages. in *Advances in Immunology* (eds Dixon, F. J. & Kunkel, H. G.) vol. 9 163–214 (Academic Press, 1968).
12. van Furth, R. ORIGIN AND KINETICS OF MONONUCLEAR PHAGOCYTES. *Annals of the New York Academy of Sciences* **278**, 161–175 (1976).
13. Aschoff, L. Das reticulo-endotheliale System. in *Ergebnisse der Inneren Medizin und Kinderheilkunde: Sechszwanzigster Band* (eds Kraus, F. et al.) 1–118 (Springer Berlin Heidelberg, Berlin, Heidelberg, 1924). doi:10.1007/978-3-642-90639-8_1.
14. van Furth, R. *et al.* The mononuclear phagocyte system: a new classification of macrophages, monocytes, and their precursor cells. *Bulletin of the World Health Organization* **46**, 845–52 (1972).
15. van Furth, R. & Cohn, Z. A. THE ORIGIN AND KINETICS OF MONONUCLEAR PHAGOCYTES. *Journal of Experimental Medicine* **128**, 415–435 (1968).
16. Volkman, A., Chang, N. C., Strausbauch, P. H. & Morahan, P. S. Differential effects of chronic monocyte depletion on macrophage populations. *Laboratory investigation; a journal of technical methods and pathology* **49**, 291–8 (1983).

REFERENCES

17. Sawyer, R. T., Strausbauch, P. H. & Volkman, A. Resident macrophage proliferation in mice depleted of blood monocytes by strontium-89. *Laboratory investigation; a journal of technical methods and pathology* **46**, 165–70 (1982).
18. Bittmann, I. *et al.* Cellular Chimerism of the Lung After Transplantation: An Interphase Cytogenetic Study. *American Journal of Clinical Pathology* **115**, 525–533 (2001).
19. Bittmann, I., Hentrich, M., Bise, K., Kolb, H. J. & Löhrs, U. Endothelial Cells but Not Epithelial Cells or Cardiomyocytes Are Partially Replaced by Donor Cells after Allogeneic Bone Marrow and Stem Cell Transplantation. *Journal of Hematotherapy & Stem Cell Research* **12**, 359–366 (2003).
20. Bajpai, G. *et al.* The human heart contains distinct macrophage subsets with divergent origins and functions. *Nature Medicine* **24**, 1234–1245 (2018).
21. Nayak, D. K. *et al.* Long-Term Persistence of Donor Alveolar Macrophages in Human Lung Transplant Recipients That Influences Donor-Specific Immune Responses. *American Journal of Transplantation* **16**, 2300–2311 (2016).
22. Byrne, A. J. *et al.* Dynamics of human monocytes and airway macrophages during healthy aging and after transplant. *Journal of Experimental Medicine* **217**, e20191236 (2020).
23. Tamoutounour, S. *et al.* Origins and Functional Specialization of Macrophages and of Conventional and Monocyte-Derived Dendritic Cells in Mouse Skin. *Immunity* **39**, 925–938 (2013).
24. Yona, S. *et al.* Fate Mapping Reveals Origins and Dynamics of Monocytes and Tissue Macrophages under Homeostasis. *Immunity* **38**, 79–91 (2013).
25. Bain, C. C. *et al.* Constant replenishment from circulating monocytes maintains the macrophage pool in the intestine of adult mice. *Nature Immunology* **15**, 929–937 (2014).
26. Molawi, K. *et al.* Progressive replacement of embryo-derived cardiac macrophages with age. *Journal of Experimental Medicine* **211**, 2151–2158 (2014).
27. Epelman, S. *et al.* Embryonic and Adult-Derived Resident Cardiac Macrophages Are Maintained through Distinct Mechanisms at Steady State and during Inflammation. *Immunity* **40**, 91–104 (2014).
28. Calderon, B. *et al.* The pancreas anatomy conditions the origin and properties of resident macrophages. *Journal of Experimental Medicine* **212**, 1497–1512 (2015).
29. Liu, Z. *et al.* Fate Mapping via Ms4a3-Expression History Traces Monocyte-Derived Cells. *Cell* **178**, 1509–1525.e19 (2019).
30. Mackaness, G. B. THE INFLUENCE OF IMMUNOLOGICALLY COMMITTED LYMPHOID CELLS ON MACROPHAGE ACTIVITY IN VIVO. *Journal of Experimental Medicine* **129**, 973–992 (1969).
31. Mackaness, G. B. CELLULAR RESISTANCE TO INFECTION. *Journal of Experimental Medicine* **116**, 381–406 (1962).

REFERENCES

32. Mackaness, G. B. THE IMMUNOLOGICAL BASIS OF ACQUIRED CELLULAR RESISTANCE. *Journal of Experimental Medicine* **120**, 105–120 (1964).
33. Tripathy, S. P. & Mackaness, G. B. THE EFFECT OF CYTOTOXIC AGENTS ON THE PASSIVE TRANSFER OF CELL-MEDIATED IMMUNITY. *Journal of Experimental Medicine* **130**, 17–30 (1969).
34. Nathan, C. F., Murray, H. W., Wiebe, M. E. & Rubin, B. Y. Identification of interferon-gamma as the lymphokine that activates human macrophage oxidative metabolism and antimicrobial activity. *Journal of Experimental Medicine* **158**, 670–689 (1983).
35. Adams, D. O. & Hamilton, T. A. The Cell Biology of Macrophage Activation. *Annual Review of Immunology* **2**, 283–318 (1984).
36. Mills, C. D., Kincaid, K., Alt, J. M., Heilman, M. J. & Hill, A. M. M-1/M-2 Macrophages and the Th1/Th2 Paradigm1. *The Journal of Immunology* **164**, 6166–6173 (2000).
37. Stein, M., Keshav, S., Harris, N. & Gordon, S. Interleukin 4 potently enhances murine macrophage mannose receptor activity: a marker of alternative immunologic macrophage activation. *Journal of Experimental Medicine* **176**, 287–292 (1992).
38. Rosenthal, A. S. & Shevach, E. M. FUNCTION OF MACROPHAGES IN ANTIGEN RECOGNITION BY GUINEA PIG T LYMPHOCYTES : I. REQUIREMENT FOR HISTOCOMPATIBLE MACROPHAGES AND LYMPHOCYTES. *Journal of Experimental Medicine* **138**, 1194–1212 (1973).
39. ZINKERNAGEL, R. M. & DOHERTY, P. C. Restriction of in vitro T cell-mediated cytotoxicity in lymphocytic choriomeningitis within a syngeneic or semiallogeneic system. *Nature* **248**, 701–702 (1974).
40. Unanue, E. R. Antigen-Presenting Function of the Macrophage. *Annual Review of Immunology* **2**, 395–428 (1984).
41. Nathan, C. F. Secretory products of macrophages. *Journal of Clinical Investigation* **79**, 319–326 (1987).
42. Gautier, E. L. *et al.* Gene-expression profiles and transcriptional regulatory pathways that underlie the identity and diversity of mouse tissue macrophages. *Nature Immunology* **13**, 1118–1128 (2012).
43. van de Laar, L. *et al.* Yolk Sac Macrophages, Fetal Liver, and Adult Monocytes Can Colonize an Empty Niche and Develop into Functional Tissue-Resident Macrophages. *Immunity* **44**, 755–768 (2016).
44. Scott, C. L. *et al.* Bone marrow-derived monocytes give rise to self-renewing and fully differentiated Kupffer cells. *Nature Communications* **7**, 10321 (2016).
45. Guilliams, M. & Scott, C. L. Does niche competition determine the origin of tissue-resident macrophages? *Nature Reviews Immunology* **17**, 451–460 (2017).
46. Li, K. & Underhill, D. M. Phagocytosis: a process that shapes immune responses to engulfed meals. *Nature Reviews Immunology* <https://doi.org/10.1038/s41577-025-01231-9> (2025) doi:10.1038/s41577-025-01231-9.

REFERENCES

47. Cosson, P. & Soldati, T. Eat, kill or die: when amoeba meets bacteria. *Current Opinion in Microbiology* **11**, 271–276 (2008).
48. May, R. C. & Machesky, L. M. Phagocytosis and the actin cytoskeleton. *Journal of Cell Science* **114**, 1061–1077 (2001).
49. Dzik, J. M. The ancestry and cumulative evolution of immune reactions. *Acta Biochimica Polonica* **57**, (2010).
50. Lu, Y. *et al.* Pattern recognition receptors in Drosophila immune responses. *Developmental & Comparative Immunology* **102**, 103468 (2020).
51. Hillyer, J. F. Insect immunology and hematopoiesis. *Developmental & Comparative Immunology* **58**, 102–118 (2016).
52. Nonaka, M. & Kimura, A. Genomic view of the evolution of the complement system. *Immunogenetics* **58**, 701–713 (2006).
53. Nonaka, M. Evolution of the Complement System. in 31–43 (2014). doi:10.1007/978-94-017-8881-6_3.
54. Mass, E., Nimmerjahn, F., Kierdorf, K. & Schlitzer, A. Tissue-specific macrophages: how they develop and choreograph tissue biology. *Nature Reviews Immunology* **23**, 563–579 (2023).
55. Hume, D. A., Wollscheid-Lengeling, E., Rojo, R. & Pridans, C. The evolution of the macrophage-specific enhancer (Fms intronic regulatory element) within the CSF1R locus of vertebrates. *Scientific Reports* **7**, 17115 (2017).
56. Hume, D. A. *et al.* Functional evolution of the colony-stimulating factor 1 receptor (CSF1R) and its ligands in birds. *Journal of Leukocyte Biology* **107**, 237–250 (2020).
57. Butovsky, O. *et al.* Identification of a unique TGF- β -dependent molecular and functional signature in microglia. *Nature Neuroscience* **17**, 131–143 (2014).
58. Bonnardel, J. *et al.* Stellate Cells, Hepatocytes, and Endothelial Cells Imprint the Kupffer Cell Identity on Monocytes Colonizing the Liver Macrophage Niche. *Immunity* **51**, 638-654.e9 (2019).
59. Sakai, M. *et al.* Liver-Derived Signals Sequentially Reprogram Myeloid Enhancers to Initiate and Maintain Kupffer Cell Identity. *Immunity* **51**, 655-670.e8 (2019).
60. Peng, W. *et al.* Endothelial-driven TGF β signaling supports lung interstitial macrophage development from monocytes. *Science Immunology* **10**, eadr4977 (2025).
61. Guilliams, M. *et al.* Spatial proteogenomics reveals distinct and evolutionarily conserved hepatic macrophage niches. *Cell* **185**, 379-396.e38 (2022).
62. Viola, M. F., Franco Taveras, E. & Mass, E. Developmental programming of tissue-resident macrophages. *Frontiers in Immunology* **15**, (2024).
63. Ginhoux, F. & Guilliams, M. Tissue-Resident Macrophage Ontogeny and Homeostasis. *Immunity* **44**, 439–449 (2016).

REFERENCES

64. Palis, J., Robertson, S., Kennedy, M., Wall, C. & Keller, G. Development of erythroid and myeloid progenitors in the yolk sac and embryo proper of the mouse. *Development* **126**, 5073–5084 (1999).
65. Mass, E. *et al.* Specification of tissue-resident macrophages during organogenesis. *Science* **353**, aaf4238 (2016).
66. Stremmel, C. *et al.* Yolk sac macrophage progenitors traffic to the embryo during defined stages of development. *Nat Commun* **9**, 75 (2018).
67. Gomez Perdiguero, E. *et al.* Tissue-resident macrophages originate from yolk-sac-derived erythro-myeloid progenitors. *Nature* **518**, 547–551 (2015).
68. Kissa, K. & Herbomel, P. Blood stem cells emerge from aortic endothelium by a novel type of cell transition. *Nature* **464**, 112–115 (2010).
69. Boisset, J.-C. *et al.* In vivo imaging of haematopoietic cells emerging from the mouse aortic endothelium. *Nature* **464**, 116–120 (2010).
70. Bertrand, J. Y. *et al.* Haematopoietic stem cells derive directly from aortic endothelium during development. *Nature* **464**, 108–111 (2010).
71. Gibbings, S. L. *et al.* Transcriptome analysis highlights the conserved difference between embryonic and postnatal-derived alveolar macrophages. *Blood* **126**, 1357–1366 (2015).
72. Lavin, Y. *et al.* Tissue-Resident Macrophage Enhancer Landscapes Are Shaped by the Local Microenvironment. *Cell* **159**, 1312–1326 (2014).
73. Shemer, A. *et al.* Engrafted parenchymal brain macrophages differ from microglia in transcriptome, chromatin landscape and response to challenge. *Nature Communications* **9**, 5206 (2018).
74. Buttgereit, A. *et al.* Sall1 is a transcriptional regulator defining microglia identity and function. *Nature Immunology* **17**, 1397–1406 (2016).
75. Bastos, J. *et al.* Monocytes can efficiently replace all brain macrophages and fetal liver monocytes can generate bona fide SALL1⁺ microglia. *Immunity* **58**, 1269–1288.e12 (2025).
76. Gosselin, D. *et al.* Environment Drives Selection and Function of Enhancers Controlling Tissue-Specific Macrophage Identities. *Cell* **159**, 1327–1340 (2014).
77. Ahlback, A. & Gentek, R. Fate-Mapping Macrophages: From Ontogeny to Functions. *Methods Mol Biol* **2713**, 11–43 (2024).
78. Barth, M. W., Hendrzak, J. A., Melnicoff, M. J. & Morahan, P. S. Review of the macrophage disappearance reaction. *J Leukoc Biol* **57**, 361–367 (1995).
79. Ait Ahmed, Y. *et al.* Kupffer cell restoration after partial hepatectomy is mainly driven by local cell proliferation in IL-6-dependent autocrine and paracrine manners. *Cell Mol Immunol* **18**, 2165–2176 (2021).
80. Blériot, C. *et al.* Liver-resident macrophage necroptosis orchestrates type 1 microbicidal inflammation and type-2-mediated tissue repair during bacterial infection. *Immunity* **42**, 145–158 (2015).

REFERENCES

81. Misharin, A. V. *et al.* Monocyte-derived alveolar macrophages drive lung fibrosis and persist in the lung over the life span. *J Exp Med* **214**, 2387–2404 (2017).
82. Aegerter, H. *et al.* Influenza-induced monocyte-derived alveolar macrophages confer prolonged antibacterial protection. *Nat Immunol* **21**, 145–157 (2020).
83. Netea, M. G. *et al.* Defining trained immunity and its role in health and disease. *Nat Rev Immunol* **20**, 375–388 (2020).
84. Xu, G. *et al.* Macrophage-augmented intestinal organoids model virus-host interactions in enteric viral diseases and facilitate therapeutic development. *Nat Commun* **16**, 4475 (2025).
85. Park, D. S. *et al.* iPS-cell-derived microglia promote brain organoid maturation via cholesterol transfer. *Nature* **623**, 397–405 (2023).
86. Bidan, N. *et al.* Multicellular tumor spheroid model to study the multifaceted role of tumor-associated macrophages in PDAC. *Drug Deliv Transl Res* **14**, 2085–2099 (2024).
87. Han, J. *et al.* Human serous cavity macrophages and dendritic cells possess counterparts in the mouse with a distinct distribution between species. *Nature Immunology* **25**, 155–165 (2024).
88. Ito, M. *et al.* NOD/SCID/gamma(c)(null) mouse: an excellent recipient mouse model for engraftment of human cells. *Blood* **100**, 3175–3182 (2002).
89. Rongvaux, A. *et al.* Development and function of human innate immune cells in a humanized mouse model. *Nat Biotechnol* **32**, 364–372 (2014).
90. Voss, L., Reitinger, C. & Lux, A. Phenotyping of Macrophages in Human Immune System Mice. *Methods Mol Biol* **2713**, 117–128 (2024).
91. Evren, E. *et al.* Distinct developmental pathways from blood monocytes generate human lung macrophage diversity. *Immunity* **54**, 259-275.e7 (2021).
92. Shimoyama, M. *et al.* Exploring human disease using the Rat Genome Database. *Dis Model Mech* **9**, 1089–1095 (2016).
93. Lunney, J. K. *et al.* Importance of the pig as a human biomedical model. *Sci Transl Med* **13**, eabd5758 (2021).
94. Link, B. A. & Megason, S. G. Zebrafish as a Model for Development. in *Sourcebook of Models for Biomedical Research* (ed. Conn, P. M.) 103–112 (Humana Press, Totowa, NJ, 2008). doi:10.1007/978-1-59745-285-4_13.
95. Gore, A. V., Pillay, L. M., Venero Galanternik, M. & Weinstein, B. M. The zebrafish: A fantastic model for hematopoietic development and disease. *WIREs Developmental Biology* **7**, e312 (2018).
96. Shaw, T. N. *et al.* Tissue-resident macrophages in the intestine are long lived and defined by Tim-4 and CD4 expression. *J Exp Med* **215**, 1507–1518 (2018).
97. Ruscitti, C. *et al.* Recruited atypical Ly6G+ macrophages license alveolar regeneration after lung injury. *Science Immunology* **9**, eado1227 (2025).

REFERENCES

98. Guilliams, M. *et al.* Unsupervised High-Dimensional Analysis Aligns Dendritic Cells across Tissues and Species. *Immunity* **45**, 669–684 (2016).
99. Dick, S. A. *et al.* Three tissue resident macrophage subsets coexist across organs with conserved origins and life cycles. *Sci Immunol* **7**, eabf7777 (2022).
100. Dunsmore, G. *et al.* Timing and location dictate monocyte fate and their transition to tumor-associated macrophages. *Science Immunology* **9**, eadk3981 (2025).
101. Tamoutounour, S. *et al.* CD64 distinguishes macrophages from dendritic cells in the gut and reveals the Th1-inducing role of mesenteric lymph node macrophages during colitis. *European Journal of Immunology* **42**, 3150–3166 (2012).
102. Gibbings, S. L. *et al.* Three Unique Interstitial Macrophages in the Murine Lung at Steady State. *American Journal of Respiratory Cell and Molecular Biology* **57**, 66–76 (2017).
103. Chakarov, S. *et al.* Two distinct interstitial macrophage populations coexist across tissues in specific subtissular niches. *Science* **363**, eaau0964 (2019).
104. Schyns, J. *et al.* Non-classical tissue monocytes and two functionally distinct populations of interstitial macrophages populate the mouse lung. *Nature Communications* **10**, 3964 (2019).
105. Verwaerde, S. *et al.* Innate type 2 lymphocytes trigger an inflammatory switch in alveolar macrophages. *Immunity* **59**, 60-78.e9 (2026).
106. Kim, K.-W. *et al.* MHC II+ resident peritoneal and pleural macrophages rely on IRF4 for development from circulating monocytes. *Journal of Experimental Medicine* **213**, 1951–1959 (2016).
107. Gautier, E. L. *et al.* Gata6 regulates aspartoacylase expression in resident peritoneal macrophages and controls their survival. *Journal of Experimental Medicine* **211**, 1525–1531 (2014).
108. Valladeau, J. *et al.* Langerin, a novel C-type lectin specific to Langerhans cells, is an endocytic receptor that induces the formation of Birbeck granules. *Immunity* **12**, 71–81 (2000).
109. Jung, S. *et al.* Analysis of Fractalkine Receptor CX3CR1 Function by Targeted Deletion and Green Fluorescent Protein Reporter Gene Insertion. *Molecular and Cellular Biology* **20**, 4106–4114 (2000).
110. Vanneste, D. *et al.* MafB-restricted local monocyte proliferation precedes lung interstitial macrophage differentiation. *Nature Immunology* **24**, 827–840 (2023).
111. Satpathy, A. T. *et al.* Notch2-dependent classical dendritic cells orchestrate intestinal immunity to attaching-and-effacing bacterial pathogens. *Nat Immunol* **14**, 937–948 (2013).
112. De Ponti, F. F. *et al.* Spatially restricted and ontogenically distinct hepatic macrophages are required for tissue repair. *Immunity* **58**, 362-380.e10 (2025).

REFERENCES

113. Huang, H. *et al.* Kupffer cell programming by maternal obesity triggers fatty liver disease. *Nature* **644**, 790–798 (2025).
114. Karl, R. *et al.* Renal tissue-resident macrophages promote cystogenesis in early polycystic kidney disease. *J Cell Sci* **138**, jcs263992 (2025).
115. Makdissi, N. *et al.* Kupffer cells control neonatal hepatic metabolism via Igf1 signaling. *Development* **153**, dev204962 (2026).
116. Summers, K. M., Bush, S. J. & Hume, D. A. Network analysis of transcriptomic diversity amongst resident tissue macrophages and dendritic cells in the mouse mononuclear phagocyte system. *PLoS Biol* **18**, e3000859 (2020).
117. Sasmono, R. T. *et al.* A macrophage colony-stimulating factor receptor–green fluorescent protein transgene is expressed throughout the mononuclear phagocyte system of the mouse. *Blood* **101**, 1155–1163 (2003).
118. Sasmono, R. T. *et al.* Mouse neutrophilic granulocytes express mRNA encoding the macrophage colony-stimulating factor receptor (CSF-1R) as well as many other macrophage-specific transcripts and can transdifferentiate into macrophages in vitro in response to CSF-1. *J Leukoc Biol* **82**, 111–123 (2007).
119. Grabert, K. *et al.* A Transgenic Line That Reports CSF1R Protein Expression Provides a Definitive Marker for the Mouse Mononuclear Phagocyte System. *J Immunol* **205**, 3154–3166 (2020).
120. Liu, Z., Gu, Y., Shin, A., Zhang, S. & Ginhoux, F. Analysis of Myeloid Cells in Mouse Tissues with Flow Cytometry. *STAR Protoc* **1**, 100029 (2020).
121. Kapanadze, T. *et al.* Validation of CSF-1 receptor (CD115) staining for analysis of murine monocytes by flow cytometry. *J Leukoc Biol* **115**, 573–582 (2024).
122. Stanley, E. R. & Chitu, V. CSF-1 receptor signaling in myeloid cells. *Cold Spring Harb Perspect Biol* **6**, a021857 (2014).
123. Hawley, C. A. *et al.* Csf1r-mApple Transgene Expression and Ligand Binding In Vivo Reveal Dynamics of CSF1R Expression within the Mononuclear Phagocyte System. *J Immunol* **200**, 2209–2223 (2018).
124. Ovchinnikov, D. A. *et al.* Expression of Gal4-dependent transgenes in cells of the mononuclear phagocyte system labeled with enhanced cyan fluorescent protein using Csf1r-Gal4VP16/UAS-ECFP double-transgenic mice. *J Leukoc Biol* **83**, 430–433 (2008).
125. Ovchinnikov, D. A., DeBats, C. E. E., Sester, D. P., Sweet, M. J. & Hume, D. A. A conserved distal segment of the mouse CSF-1 receptor promoter is required for maximal expression of a reporter gene in macrophages and osteoclasts of transgenic mice. *J Leukoc Biol* **87**, 815–822 (2010).
126. Petit, M. *et al.* Visualizing the spatial organization of monocytes, interstitial macrophages, and tissue-specific macrophages in situ. *Cell Rep* **43**, 114847 (2024).

REFERENCES

127. Garcia-Morales, C. *et al.* Production and characterisation of a monoclonal antibody that recognises the chicken CSF1 receptor and confirms that expression is restricted to macrophage-lineage cells. *Dev Comp Immunol* **42**, 278–285 (2014).
128. Waddell, L. A. *et al.* ADGRE1 (EMR1, F4/80) Is a Rapidly-Evolving Gene Expressed in Mammalian Monocyte-Macrophages. *Front Immunol* **9**, 2246 (2018).
129. Keshvari, S. *et al.* CSF1R-dependent macrophages control postnatal somatic growth and organ maturation. *PLoS Genet* **17**, e1009605 (2021).
130. Huang, S. *et al.* Genetic and Immunohistochemistry Tools to Visualize Rat Macrophages In Situ. *Methods Mol Biol* **2713**, 99–115 (2024).
131. Rovira, M., Pozo, J., Miserocchi, M. & Wittamer, V. Isolation of Tissue Macrophages in Adult Zebrafish. *Methods Mol Biol* **2713**, 81–98 (2024).
132. Heng, T. S. P., Painter, M. W., & Immunological Genome Project Consortium. The Immunological Genome Project: networks of gene expression in immune cells. *Nat Immunol* **9**, 1091–1094 (2008).
133. Schridde, A. *et al.* Tissue-specific differentiation of colonic macrophages requires TGF β 2; receptor-mediated signaling. *Mucosal Immunology* **10**, 1387–1399 (2017).
134. Blériot, C. *et al.* A subset of Kupffer cells regulates metabolism through the expression of CD36. *Immunity* **54**, 2101-2116.e6 (2021).
135. Mulder, K. *et al.* Cross-tissue single-cell landscape of human monocytes and macrophages in health and disease. *Immunity* **54**, 1883-1900.e5 (2021).
136. Coulis, G. *et al.* Single-cell and spatial transcriptomics identify a macrophage population associated with skeletal muscle fibrosis. *Sci Adv* **9**, eadd9984 (2023).
137. Garrido-Trigo, A. *et al.* Macrophage and neutrophil heterogeneity at single-cell spatial resolution in human inflammatory bowel disease. *Nat Commun* **14**, 4506 (2023).
138. Gessain, G. *et al.* TREM2-Expressing Multinucleated Giant Macrophages Are a Biomarker of Good Prognosis in Head and Neck Squamous Cell Carcinoma. *Cancer Discov* **14**, 2352–2366 (2024).
139. Mulder, K. *et al.* DC subsets and states unraveled across human juxtatumoral and malignant tissues. *Nat Immunol* **27**, 135–149 (2026).
140. Vanneste, D. & Marichal, T. Transcriptional Regulation of Macrophage Specification and Function. *Eur J Immunol* **55**, e70097 (2025).
141. Sender, R. *et al.* The total mass, number, and distribution of immune cells in the human body. *Proc Natl Acad Sci U S A* **120**, e2308511120 (2023).
142. Tay, T. L. *et al.* A new fate mapping system reveals context-dependent random or clonal expansion of microglia. *Nat Neurosci* **20**, 793–803 (2017).
143. Dai, X.-M. *et al.* Targeted disruption of the mouse colony-stimulating factor 1 receptor gene results in osteopetrosis, mononuclear phagocyte deficiency,

REFERENCES

- increased primitive progenitor cell frequencies, and reproductive defects. *Blood* **99**, 111–120 (2002).
144. Pridans, C. *et al.* Pleiotropic Impacts of Macrophage and Microglial Deficiency on Development in Rats with Targeted Mutation of the *Csf1r* Locus. *The Journal of Immunology* **201**, 2683–2699 (2018).
145. Greter, M. *et al.* Stroma-Derived Interleukin-34 Controls the Development and Maintenance of Langerhans Cells and the Maintenance of Microglia. *Immunity* **37**, 1050–1060 (2012).
146. Wang, Y. *et al.* IL-34 is a tissue-restricted ligand of CSF1R required for the development of Langerhans cells and microglia. *Nature Immunology* **13**, 753–760 (2012).
147. Hwang, S.-J. *et al.* Interleukin-34 produced by human fibroblast-like synovial cells in rheumatoid arthritis supports osteoclastogenesis. *Arthritis Res Ther* **14**, R14 (2012).
148. Tian, Y., Shen, H., Xia, L. & Lu, J. Elevated serum and synovial fluid levels of interleukin-34 in rheumatoid arthritis: possible association with disease progression via interleukin-17 production. *J Interferon Cytokine Res* **33**, 398–401 (2013).
149. Van Hove, H. *et al.* Interleukin-34-dependent perivascular macrophages promote vascular function in the brain. *Immunity* **58**, 1289-1305.e8 (2025).
150. Chitu, V. & Stanley, E. R. Colony-stimulating factor-1 in immunity and inflammation. *Curr Opin Immunol* **18**, 39–48 (2006).
151. Nandi, S., Akhter, M. P., Seifert, M. F., Dai, X.-M. & Stanley, E. R. Developmental and functional significance of the CSF-1 proteoglycan chondroitin sulfate chain. *Blood* **107**, 786–795 (2006).
152. Yao, G.-Q., Troiano, N., Simpson, C. A. & Insogna, K. L. Selective deletion of the soluble Colony-Stimulating Factor 1 isoform in vivo prevents estrogen-deficiency bone loss in mice. *Bone Res* **5**, 17022 (2017).
153. Dai, X.-M., Zong, X.-H., Sylvestre, V. & Stanley, E. R. Incomplete restoration of colony-stimulating factor 1 (CSF-1) function in CSF-1-deficient *Csf1op/Csf1op* mice by transgenic expression of cell surface CSF-1. *Blood* **103**, 1114–1123 (2004).
154. Bellomo, A. *et al.* Reticular Fibroblasts Expressing the Transcription Factor WT1 Define a Stromal Niche that Maintains and Replenishes Splenic Red Pulp Macrophages. *Immunity* **53**, 127-142.e7 (2020).
155. Vollmers, A. C. *et al.* Reciprocal regulation of fibroblast-macrophage equilibrium governs skin integrity. *Nat Immunol* <https://doi.org/10.1038/s41590-026-02434-5> (2026) doi:10.1038/s41590-026-02434-5.
156. Hume, D. A. *et al.* Phenotypic impacts of CSF1R deficiencies in humans and model organisms. *J Leukoc Biol* **107**, 205–219 (2020).
157. Wei, S. *et al.* Modulation of CSF-1-regulated post-natal development with anti-CSF-1 antibody. *Immunobiology* **210**, 109–119 (2005).

REFERENCES

158. Monies, D. *et al.* Autozygosity reveals recessive mutations and novel mechanisms in dominant genes: implications in variant interpretation. *Genet Med* **19**, 1144–1150 (2017).
159. Oosterhof, N. *et al.* Homozygous Mutations in CSF1R Cause a Pediatric-Onset Leukoencephalopathy and Can Result in Congenital Absence of Microglia. *Am J Hum Genet* **104**, 936–947 (2019).
160. Guo, L. *et al.* Bi-allelic CSF1R Mutations Cause Skeletal Dysplasia of Dysosteosclerosis-Pyle Disease Spectrum and Degenerative Encephalopathy with Brain Malformation. *Am J Hum Genet* **104**, 925–935 (2019).
161. Rademakers, R. *et al.* Mutations in the colony stimulating factor 1 receptor (CSF1R) gene cause hereditary diffuse leukoencephalopathy with spheroids. *Nat Genet* **44**, 200–205 (2011).
162. Konno, T., Kasanuki, K., Ikeuchi, T., Dickson, D. W. & Wszolek, Z. K. CSF1R-related leukoencephalopathy: A major player in primary microgliopathies. *Neurology* **91**, 1092–1104 (2018).
163. Bissinger, S. *et al.* Macrophage depletion induces edema through release of matrix-degrading proteases and proteoglycan deposition. *Sci Transl Med* **13**, eabd4550 (2021).
164. Suzuki, T. *et al.* Pulmonary macrophage transplantation therapy. *Nature* **514**, 450–454 (2014).
165. Guilliams, M. *et al.* Alveolar macrophages develop from fetal monocytes that differentiate into long-lived cells in the first week of life via GM-CSF. *Journal of Experimental Medicine* **210**, 1977–1992 (2013).
166. Kohyama, M. *et al.* Role for Spi-C in the development of red pulp macrophages and splenic iron homeostasis. *Nature* **457**, 318–321 (2009).
167. Munro, D. A. D. *et al.* Microglia protect against age-associated brain pathologies. *Neuron* **112**, 2732–2748.e8 (2024).
168. Zhao, D. *et al.* ALK1 signaling is required for the homeostasis of Kupffer cells and prevention of bacterial infection. *J Clin Invest* **132**, e150489 (2022).
169. Bain, C. C. & Jenkins, S. J. The biology of serous cavity macrophages. *Cell Immunol* **330**, 126–135 (2018).
170. Wang, J. & Kubes, P. A Reservoir of Mature Cavity Macrophages that Can Rapidly Invade Visceral Organs to Affect Tissue Repair. *Cell* **165**, 668–678 (2016).
171. Zindel, J. *et al.* Primordial GATA6 macrophages function as extravascular platelets in sterile injury. *Science* **371**, eabe0595 (2021).
172. Guilliams, M. & Scott, C. L. Liver macrophages in health and disease. *Immunity* **55**, 1515–1529 (2022).
173. Slusarczyk, P. & Mleczko-Sanecka, K. The Multiple Facets of Iron Recycling. *Genes (Basel)* **12**, 1364 (2021).

REFERENCES

174. Tran, S. *et al.* Impaired Kupffer Cell Self-Renewal Alters the Liver Response to Lipid Overload during Non-alcoholic Steatohepatitis. *Immunity* **53**, 627-640.e5 (2020).
175. Remmerie, A. *et al.* Osteopontin Expression Identifies a Subset of Recruited Macrophages Distinct from Kupffer Cells in the Fatty Liver. *Immunity* **53**, 641-657.e14 (2020).
176. Bilzer, M., Roggel, F. & Gerbes, A. L. Role of Kupffer cells in host defense and liver disease. *Liver Int* **26**, 1175–1186 (2006).
177. Wong, C. H. Y., Jenne, C. N., Petri, B., Chrobok, N. L. & Kubes, P. Nucleation of platelets with blood-borne pathogens on Kupffer cells precedes other innate immunity and contributes to bacterial clearance. *Nat Immunol* **14**, 785–792 (2013).
178. Jenne, C. N. & Kubes, P. Platelets in inflammation and infection. *Platelets* **26**, 286–292 (2015).
179. Yang, W. *et al.* Neutrophils promote the development of reparative macrophages mediated by ROS to orchestrate liver repair. *Nat Commun* **10**, 1076 (2019).
180. Araujo David, B. *et al.* Kupffer cell reverse migration into the liver sinusoids mitigates neonatal sepsis and meningitis. *Sci Immunol* **9**, eadq9704 (2024).
181. Palis, J. Primitive and definitive erythropoiesis in mammals. *Front Physiol* **5**, 3 (2014).
182. Kayvanjoo, A. H. *et al.* Fetal liver macrophages contribute to the hematopoietic stem cell niche by controlling granulopoiesis. *eLife* **13**, e86493 (2024).
183. MacLean, J. A. *et al.* Sequestration of inhaled particulate antigens by lung phagocytes. A mechanism for the effective inhibition of pulmonary cell-mediated immunity. *Am J Pathol* **148**, 657–666 (1996).
184. Westphalen, K. *et al.* Sessile alveolar macrophages communicate with alveolar epithelium to modulate immunity. *Nature* **506**, 503–506 (2014).
185. Bedoret, D. *et al.* Lung interstitial macrophages alter dendritic cell functions to prevent airway allergy in mice. *The Journal of Clinical Investigation* **119**, 3723–3738 (2009).
186. Sabatel, C. *et al.* Exposure to Bacterial CpG DNA Protects from Airway Allergic Inflammation by Expanding Regulatory Lung Interstitial Macrophages. *Immunity* **46**, 457–473 (2017).
187. Legrand, C. *et al.* Lung Interstitial Macrophages Can Present Soluble Antigens and Induce Foxp3+ Regulatory T Cells. *American Journal of Respiratory Cell and Molecular Biology* **70**, 446–456 (2024).
188. Cunningham, C. L., Martínez-Cerdeño, V. & Noctor, S. C. Microglia regulate the number of neural precursor cells in the developing cerebral cortex. *J Neurosci* **33**, 4216–4233 (2013).

REFERENCES

189. Checchin, D., Sennlaub, F., Levavasseur, E., Leduc, M. & Chemtob, S. Potential role of microglia in retinal blood vessel formation. *Invest Ophthalmol Vis Sci* **47**, 3595–3602 (2006).
190. Ueno, M. *et al.* Layer V cortical neurons require microglial support for survival during postnatal development. *Nat Neurosci* **16**, 543–551 (2013).
191. Stevens, B. *et al.* The classical complement cascade mediates CNS synapse elimination. *Cell* **131**, 1164–1178 (2007).
192. Schafer, D. P. *et al.* Microglia sculpt postnatal neural circuits in an activity and complement-dependent manner. *Neuron* **74**, 691–705 (2012).
193. Hoshiko, M., Arnoux, I., Avignone, E., Yamamoto, N. & Audinat, E. Deficiency of the microglial receptor CX3CR1 impairs postnatal functional development of thalamocortical synapses in the barrel cortex. *J Neurosci* **32**, 15106–15111 (2012).
194. Li, Y., Du, X.-F., Liu, C.-S., Wen, Z.-L. & Du, J.-L. Reciprocal regulation between resting microglial dynamics and neuronal activity in vivo. *Dev Cell* **23**, 1189–1202 (2012).
195. Safaiyan, S. *et al.* Age-related myelin degradation burdens the clearance function of microglia during aging. *Nat Neurosci* **19**, 995–998 (2016).
196. Ho, M. S. Microglia in Parkinson's Disease. *Adv Exp Med Biol* **1175**, 335–353 (2019).
197. Hansen, D. V., Hanson, J. E. & Sheng, M. Microglia in Alzheimer's disease. *J Cell Biol* **217**, 459–472 (2018).
198. Sekar, A. *et al.* Schizophrenia risk from complex variation of complement component 4. *Nature* **530**, 177–183 (2016).
199. Clarke, B. E. & Patani, R. The microglial component of amyotrophic lateral sclerosis. *Brain* **143**, 3526–3539 (2020).
200. Kurotaki, D., Uede, T. & Tamura, T. Functions and development of red pulp macrophages. *Microbiol Immunol* **59**, 55–62 (2015).
201. Kang, Y.-S. *et al.* SIGN-R1, a novel C-type lectin expressed by marginal zone macrophages in spleen, mediates uptake of the polysaccharide dextran. *Int Immunol* **15**, 177–186 (2003).
202. Aichele, P. *et al.* Macrophages of the splenic marginal zone are essential for trapping of blood-borne particulate antigen but dispensable for induction of specific T cell responses. *J Immunol* **171**, 1148–1155 (2003).
203. You, Y. *et al.* Marginal zone B cells regulate antigen capture by marginal zone macrophages. *J Immunol* **186**, 2172–2181 (2011).
204. den Haan, J. M. M. & Kraal, G. Innate immune functions of macrophage subpopulations in the spleen. *J Innate Immun* **4**, 437–445 (2012).
205. McGaha, T. L., Chen, Y., Ravishankar, B., van Rooijen, N. & Karlsson, M. C. I. Marginal zone macrophages suppress innate and adaptive immunity to apoptotic cells in the spleen. *Blood* **117**, 5403–5412 (2011).

REFERENCES

206. He, J. *et al.* Renal macrophages monitor and remove particles from urine to prevent tubule obstruction. *Immunity* **57**, 106-123.e7 (2024).
207. Kanda, H. *et al.* MCP-1 contributes to macrophage infiltration into adipose tissue, insulin resistance, and hepatic steatosis in obesity. *J Clin Invest* **116**, 1494–1505 (2006).
208. Weisberg, S. P. *et al.* CCR2 modulates inflammatory and metabolic effects of high-fat feeding. *J Clin Invest* **116**, 115–124 (2006).
209. Cox, N. *et al.* Diet-regulated production of PDGF α by macrophages controls energy storage. *Science* **373**, eabe9383 (2021).
210. Yu, X. *et al.* Septal LYVE1+ macrophages control adipocyte stem cell adipogenic potential. *Science* **389**, eadg1128 (2025).
211. Cho, S. W. *et al.* Osteal macrophages support physiologic skeletal remodeling and anabolic actions of parathyroid hormone in bone. *Proc Natl Acad Sci U S A* **111**, 1545–1550 (2014).
212. Sinder, B. P., Pettit, A. R. & McCauley, L. K. Macrophages: Their Emerging Roles in Bone. *J Bone Miner Res* **30**, 2140–2149 (2015).
213. Zsigmond, E. *et al.* Macrophage-restricted interleukin-10 receptor deficiency, but not IL-10 deficiency, causes severe spontaneous colitis. *Immunity* **40**, 720–733 (2014).
214. Gabanyi, I. *et al.* Neuro-immune Interactions Drive Tissue Programming in Intestinal Macrophages. *Cell* **164**, 378–391 (2016).
215. Bain, C. C. & Schridde, A. Origin, Differentiation, and Function of Intestinal Macrophages. *Front Immunol* **9**, 2733 (2018).
216. Heinz, S. & Glass, C. K. Roles of lineage-determining transcription factors in establishing open chromatin: lessons from high-throughput studies. *Curr Top Microbiol Immunol* **356**, 1–15 (2012).
217. Zaret, K. S. Pioneer Transcription Factors Initiating Gene Network Changes. *Annu Rev Genet* **54**, 367–385 (2020).
218. Heinz, S. *et al.* Simple Combinations of Lineage-Determining Transcription Factors Prime *cis*-Regulatory Elements Required for Macrophage and B Cell Identities. *Molecular Cell* **38**, 576–589 (2010).
219. Näär, A. M., Lemon, B. D. & Tjian, R. Transcriptional coactivator complexes. *Annu Rev Biochem* **70**, 475–501 (2001).
220. Renkawitz, R. Transcription Factors and Regulation of Gene Expression. in *Encyclopedic Reference of Genomics and Proteomics in Molecular Medicine* 1886–1890 (Springer Berlin Heidelberg, Berlin, Heidelberg, 2005). doi:10.1007/3-540-29623-9_2520.
221. Gaston, K. & Jayaraman, P. S. Transcriptional repression in eukaryotes: repressors and repression mechanisms. *Cell Mol Life Sci* **60**, 721–741 (2003).

REFERENCES

222. Park, M. D., Silvin, A., Ginhoux, F. & Merad, M. Macrophages in health and disease. *Cell* **185**, 4259–4279 (2022).
223. Epelman, S., Lavine, K. J. & Randolph, G. J. Origin and Functions of Tissue Macrophages. *Immunity* **41**, 21–35 (2014).
224. Aegerter, H., Lambrecht, B. N. & Jakubzick, C. V. Biology of lung macrophages in health and disease. *Immunity* **55**, 1564–1580 (2022).
225. Blériot, C., Dunsmore, G., Alonso-Curbelo, D. & Ginhoux, F. A temporal perspective for tumor-associated macrophage identities and functions. *Cancer Cell* **42**, 747–758 (2024).
226. Scott, E. W., Simon, M. C., Anastasi, J. & Singh, H. Requirement of Transcription Factor PU.1 in the Development of Multiple Hematopoietic Lineages. *Science* **265**, 1573–1577 (1994).
227. DeKoter, R. P. & Singh, H. Regulation of B Lymphocyte and Macrophage Development by Graded Expression of PU.1. *Science* **288**, 1439–1441 (2000).
228. Hoeffel, G. *et al.* C-Myb+ Erythro-Myeloid Progenitor-Derived Fetal Monocytes Give Rise to Adult Tissue-Resident Macrophages. *Immunity* **42**, 665–678 (2015).
229. Schulz, C. *et al.* A Lineage of Myeloid Cells Independent of Myb and Hematopoietic Stem Cells. *Science* **336**, 86–90 (2012).
230. Buchrieser, J., James, W. & Moore, M. D. Human Induced Pluripotent Stem Cell-Derived Macrophages Share Ontogeny with MYB-Independent Tissue-Resident Macrophages. *Stem Cell Reports* **8**, 334–345 (2017).
231. Goossens, S. *et al.* The EMT regulator Zeb2/Sip1 is essential for murine embryonic hematopoietic stem/progenitor cell differentiation and mobilization. *Blood* **117**, 5620–5630 (2011).
232. Scott, C. L. *et al.* The transcription factor Zeb2 regulates development of conventional and plasmacytoid DCs by repressing Id2. *Journal of Experimental Medicine* **213**, 897–911 (2016).
233. Wu, X. *et al.* Transcription factor Zeb2 regulates commitment to plasmacytoid dendritic cell and monocyte fate. *Proceedings of the National Academy of Sciences* **113**, 14775–14780 (2016).
234. Li, J. *et al.* The EMT transcription factor Zeb2 controls adult murine hematopoietic differentiation by regulating cytokine signaling. *Blood* **129**, 460–472 (2017).
235. Huang, X. *et al.* Differential usage of transcriptional repressor Zeb2 enhancers distinguishes adult and embryonic hematopoiesis. *Immunity* **54**, 1417–1432.e7 (2021).
236. Scott, C. L. *et al.* The Transcription Factor ZEB2 Is Required to Maintain the Tissue-Specific Identities of Macrophages. *Immunity* **49**, 312–325.e5 (2018).

REFERENCES

237. Kataoka, K., Fujiwara, K. T., Noda, M. & Nishizawa, M. MafB, a New Maf Family Transcription Activator That Can Associate with Maf and Fos but Not with Jun. *Molecular and Cellular Biology* **14**, 7581–7591 (1994).
238. Sieweke, M. H., Tekotte, H., Frampton, J. & Graf, T. MafB Is an Interaction Partner and Repressor of Ets-1 That Inhibits Erythroid Differentiation. *Cell* **85**, 49–60 (1996).
239. Kelly, L. M., Englmeier, U., Lafon, I., Sieweke, M. H. & Graf, T. MafB is an inducer of monocytic differentiation. *The EMBO Journal* **19**, 1987–1997–1997 (2000).
240. Hamada, M. *et al.* The Mouse mafB 5'-Upstream Fragment Directs Gene Expression in Myelomonocytic Cells, Differentiated Macrophages and the Ventral Spinal Cord in Transgenic Mice. *The Journal of Biochemistry* **134**, 203–210 (2003).
241. Moriguchi, T. *et al.* MafB Is Essential for Renal Development and F4/80 Expression in Macrophages. *Molecular and cellular biology* **26**, 5715–5727 (2006).
242. Wu, X. *et al.* MafB lineage tracing to distinguish macrophages from other immune lineages reveals dual identity of Langerhans cells. *Journal of Experimental Medicine* **213**, 2553–2565 (2016).
243. Soucie, E. L. *et al.* Lineage-specific enhancers activate self-renewal genes in macrophages and embryonic stem cells. *Science* **351**, aad5510 (2016).
244. Aziz, A. *et al.* Development of Macrophages with Altered Actin Organization in the Absence of MafB. *Molecular and Cellular Biology* **26**, 6808–6818 (2006).
245. Tran, M. T. N. *et al.* MafB is a critical regulator of complement component C1q. *Nature Communications* **8**, 1700 (2017).
246. Aziz, A., Soucie, E., Sarrazin, S. & Sieweke, M. H. MafB/c-Maf Deficiency Enables Self-Renewal of Differentiated Functional Macrophages. *Science* **326**, 867–871 (2009).
247. Goudot, C. *et al.* Aryl Hydrocarbon Receptor Controls Monocyte Differentiation into Dendritic Cells versus Macrophages. *Immunity* **47**, 582–596.e6 (2017).
248. T'Jonck, W., Guilliams, M. & Bonnardel, J. Niche signals and transcription factors involved in tissue-resident macrophage development. *Cellular Immunology* **330**, 43–53 (2018).
249. Ghosn, E. E. B. *et al.* Two physically, functionally, and developmentally distinct peritoneal macrophage subsets. *Proceedings of the National Academy of Sciences* **107**, 2568–2573 (2010).
250. Cain, D. W. *et al.* Identification of a Tissue-Specific, C/EBP β -Dependent Pathway of Differentiation for Murine Peritoneal Macrophages. *The Journal of Immunology* **191**, 4665–4675 (2013).
251. Okabe, Y. & Medzhitov, R. Tissue-Specific Signals Control Reversible Program of Localization and Functional Polarization of Macrophages. *Cell* **157**, 832–844 (2014).

REFERENCES

252. Rosas, M. *et al.* The Transcription Factor Gata6 Links Tissue Macrophage Phenotype and Proliferative Renewal. *Science* **344**, 645–648 (2014).
253. Pestal, K., Slayden, L. C. & Barton, G. M. KLF family members control expression of genes required for tissue macrophage identities. *Journal of Experimental Medicine* **222**, e20240379 (2025).
254. Wang, Z. *et al.* An immune cell atlas reveals the dynamics of human macrophage specification during prenatal development. *Cell* **186**, 4454–4471.e19 (2023).
255. Gautier, E. L. *et al.* Systemic Analysis of PPAR γ in Mouse Macrophage Populations Reveals Marked Diversity in Expression with Critical Roles in Resolution of Inflammation and Airway Immunity. *The Journal of Immunology* **189**, 2614–2624 (2012).
256. Bonfield, T. L. *et al.* Peroxisome Proliferator-Activated Receptor- γ Regulates the Expression of Alveolar Macrophage Macrophage Colony-Stimulating Factor. *The Journal of Immunology* **181**, 235–242 (2008).
257. Schneider, C. *et al.* Induction of the nuclear receptor PPAR- γ by the cytokine GM-CSF is critical for the differentiation of fetal monocytes into alveolar macrophages. *Nature Immunology* **15**, 1026–1037 (2014).
258. Yu, X. *et al.* The Cytokine TGF- β 2; Promotes the Development and Homeostasis of Alveolar Macrophages. *Immunity* **47**, 903–912.e4 (2017).
259. Nakamura, A. *et al.* Transcription repressor Bach2 is required for pulmonary surfactant homeostasis and alveolar macrophage function. *Journal of Experimental Medicine* **210**, 2191–2204 (2013).
260. McCowan, J. *et al.* The transcription factor EGR2 is indispensable for tissue-specific imprinting of alveolar macrophages in health and tissue repair. *Science Immunology* **6**, eabj2132 (2025).
261. Janssen, P. *et al.* Comparison of Droplet- and Microwell-based Methods to Analyze Cryopreserved Human BAL Cells by Single-Cell RNA Sequencing. *American Journal of Respiratory Cell and Molecular Biology* **73**, 16–25 (2025).
262. Bosteels, C. *et al.* Loss of GM-CSF-dependent instruction of alveolar macrophages in COVID-19 provides a rationale for inhaled GM-CSF treatment. *Cell Reports Medicine* **3**, 100833 (2022).
263. Li, X. *et al.* Coordinated chemokine expression defines macrophage subsets across tissues. *Nature Immunology* **25**, 1110–1122 (2024).
264. Ural, B. B. *et al.* Identification of a nerve-associated, lung-resident interstitial macrophage subset with distinct localization and immunoregulatory properties. *Science Immunology* **5**, eaax8756 (2020).
265. Tang, X.-Z., Kreuk, L. S. M., Cho, C., Metzger, R. J. & Allen, C. D. C. Bronchus-associated macrophages efficiently capture and present soluble inhaled antigens and are capable of local Th2 cell activation. *eLife* **11**, e63296 (2022).

REFERENCES

266. Prinz, M. & Priller, J. Microglia and brain macrophages in the molecular age: from origin to neuropsychiatric disease. *Nature Reviews Neuroscience* **15**, 300–312 (2014).
267. Fixsen, B. R. *et al.* SALL1 enforces microglia-specific DNA binding and function of SMADs to establish microglia identity. *Nature Immunology* **24**, 1188–1199 (2023).
268. Kierdorf, K. *et al.* Microglia emerge from erythromyeloid precursors via Pu.1- and Irf8-dependent pathways. *Nature Neuroscience* **16**, 273–280 (2013).
269. Hagemeyer, N. *et al.* Transcriptome-based profiling of yolk sac-derived macrophages reveals a role for Irf8 in macrophage maturation. *The EMBO Journal* **35**, 1730-1744–1744 (2016).
270. Masuda, T. *et al.* IRF8 Is a Critical Transcription Factor for Transforming Microglia into a Reactive Phenotype. *Cell Reports* **1**, 334–340 (2012).
271. Yamasaki, A. *et al.* IRF8 and MAFB drive distinct transcriptional machineries in different resident macrophages of the central nervous system. *Communications Biology* **7**, 896 (2024).
272. Matcovitch-Natan, O. *et al.* Microglia development follows a stepwise program to regulate brain homeostasis. *Science* **353**, aad8670 (2016).
273. Borges da Silva, H. *et al.* Splenic Macrophage Subsets and Their Function during Blood-Borne Infections. *Frontiers in Immunology* **6**, (2015).
274. Haldar, M. *et al.* Heme-Mediated SPI-C Induction Promotes Monocyte Differentiation into Iron-Recycling Macrophages. *Cell* **156**, 1223–1234 (2014).
275. Zenke-Kawasaki, Y. *et al.* Heme induces ubiquitination and degradation of the transcription factor Bach1. *Mol Cell Biol* **27**, 6962–6971 (2007).
276. Lu, Y. *et al.* Interleukin-33 Signaling Controls the Development of Iron-Recycling Macrophages. *Immunity* **52**, 782-793.e5 (2020).
277. A-Gonzalez, N. *et al.* The nuclear receptor LXR α controls the functional specialization of splenic macrophages. *Nature Immunology* **14**, 831–839 (2013).
278. Kolter, J. *et al.* A Subset of Skin Macrophages Contributes to the Surveillance and Regeneration of Local Nerves. *Immunity* **50**, 1482-1497.e7 (2019).
279. Kolter, J. *et al.* Sensory neurons shape local macrophage identity via TGF- β signaling. *Immunity* <https://doi.org/10.1016/j.immuni.2025.08.004> (2025) doi:10.1016/j.immuni.2025.08.004.
280. Fainaru, O. *et al.* Runx3 regulates mouse TGF- β -mediated dendritic cell function and its absence results in airway inflammation. *The EMBO Journal* **23**, 969-979–979 (2004).
281. Borkowski, T. A., Letterio, J. J., Farr, A. G. & Udey, M. C. A Role for Endogenous Transforming Growth Factor β 1 in Langerhans Cell Biology: The Skin of Transforming Growth Factor β 1 Null Mice Is Devoid of Epidermal Langerhans Cells. *Journal of Experimental Medicine* **184**, 2417–2422 (1996).

REFERENCES

282. Williams, M. & Svedberg, F. R. Does tissue imprinting restrict macrophage plasticity? *Nature Immunology* **22**, 118–127 (2021).
283. Amorim, A. *et al.* IFN γ and GM-CSF control complementary differentiation programs in the monocyte-to-phagocyte transition during neuroinflammation. *Nature Immunology* **23**, 217–228 (2022).
284. De Vlamincq, K. *et al.* Differential plasticity and fate of brain-resident and recruited macrophages during the onset and resolution of neuroinflammation. *Immunity* **55**, 2085-2102.e9 (2022).
285. Mirchandani, A. S. *et al.* Hypoxia shapes the immune landscape in lung injury and promotes the persistence of inflammation. *Nature Immunology* **23**, 927–939 (2022).
286. Xuan, W., Lesniak, M. S., James, C. D., Heimberger, A. B. & Chen, P. Context-Dependent Glioblastoma-Macrophage/Microglia Symbiosis and Associated Mechanisms. *Trends in Immunology* **42**, 280–292 (2021).
287. Khan, F. *et al.* Macrophages and microglia in glioblastoma: heterogeneity, plasticity, and therapy. *The Journal of Clinical Investigation* **133**, (2023).
288. Dumas, A. A. *et al.* Microglia promote glioblastoma via mTOR-mediated immunosuppression of the tumour microenvironment. *The EMBO Journal* **39**, e103790 (2020).
289. Maas, S. L. N. *et al.* Glioblastoma hijacks microglial gene expression to support tumor growth. *Journal of Neuroinflammation* **17**, 120 (2020).
290. Sa, J. K. *et al.* Transcriptional regulatory networks of tumor-associated macrophages that drive malignancy in mesenchymal glioblastoma. *Genome Biology* **21**, 216 (2020).
291. Rodriguez-Baena, F. J. *et al.* Microglial reprogramming enhances antitumor immunity and immunotherapy response in melanoma brain metastases. *Cancer Cell* **43**, 413-427.e9 (2025).
292. Deng, Z. *et al.* The nuclear factor ID3 endows macrophages with a potent anti-tumour activity. *Nature* **626**, 864–873 (2024).
293. Liu, W. *et al.* In situ expansion and reprogramming of Kupffer cells elicit potent tumoricidal immunity against liver metastasis. *The Journal of Clinical Investigation* **133**, (2023).
294. Liu, M. *et al.* Transcription factor c-Maf is a checkpoint that programs macrophages in lung cancer. *The Journal of Clinical Investigation* **130**, 2081–2096 (2020).
295. Shikanai, S. *et al.* Prognostic Impact of Tumor-Associated Macrophage-Related Markers in Patients with Adenocarcinoma of the Lung. *Annals of Surgical Oncology* **30**, 7527–7537 (2023).
296. Nixon, B. G. *et al.* Tumor-associated macrophages expressing the transcription factor IRF8 promote T cell exhaustion in cancer. *Immunity* **55**, 2044-2058.e5 (2022).

REFERENCES

297. Hume, D. A., Irvine, K. M. & Pridans, C. The Mononuclear Phagocyte System: The Relationship between Monocytes and Macrophages. *Trends in Immunology* **40**, 98–112 (2019).
298. Guilliams, M., Thierry, G. R., Bonnardel, J. & Bajenoff, M. Establishment and Maintenance of the Macrophage Niche. *Immunity* **52**, 434–451 (2020).
299. Schyns, J., Bureau, F. & Marichal, T. Lung Interstitial Macrophages: Past, Present, and Future. *Journal of Immunology Research* **2018**, 5160794 (2018).
300. Blériot, C., Chakarov, S. & Ginhoux, F. Determinants of Resident Tissue Macrophage Identity and Function. *Immunity* **52**, 957–970 (2020).
301. Ginhoux, F., Schultze, J. L., Murray, P. J., Ochando, J. & Biswas, S. K. New insights into the multidimensional concept of macrophage ontogeny, activation and function. *Nature Immunology* **17**, 34–40 (2016).
302. Hume, D. A., Pavli, P., Donahue, R. E. & Fidler, I. J. The effect of human recombinant macrophage colony-stimulating factor (CSF-1) on the murine mononuclear phagocyte system in vivo. *The Journal of Immunology* **141**, 3405–3409 (1988).
303. Tagliani, E. *et al.* Coordinate regulation of tissue macrophage and dendritic cell population dynamics by CSF-1. *Journal of Experimental Medicine* **208**, 1901–1916 (2011).
304. Allen, J. M. & Seed, B. Isolation and Expression of Functional High-Affinity Fc Receptor Complementary DNAs. *Science* **243**, 378–381 (1989).
305. Molawi, K. & Sieweke, M. H. Chapter Ten - Transcriptional Control of Macrophage Identity, Self-Renewal, and Function. in *Advances in Immunology* (eds Murphy, K. M. & Merad, M.) vol. 120 269–300 (Academic Press, 2013).
306. Ginhoux, F. *et al.* Fate Mapping Analysis Reveals That Adult Microglia Derive from Primitive Macrophages. *Science* **330**, 841–845 (2010).
307. Hashimoto, D. *et al.* Tissue-Resident Macrophages Self-Maintain Locally throughout Adult Life with Minimal Contribution from Circulating Monocytes. *Immunity* **38**, 792–804 (2013).
308. Mould, K. J. *et al.* Airspace Macrophages and Monocytes Exist in Transcriptionally Distinct Subsets in Healthy Adults. *American Journal of Respiratory and Critical Care Medicine* **203**, 946–956 (2020).
309. Lavin, Y., Mortha, A., Rahman, A. & Merad, M. Regulation of macrophage development and function in peripheral tissues. *Nature Reviews Immunology* **15**, 731–744 (2015).
310. Srinivas, S. *et al.* Cre reporter strains produced by targeted insertion of EYFP and ECFP into the ROSA26 locus. *BMC Developmental Biology* **1**, 4 (2001).
311. Diehl, G. E. *et al.* Microbiota restricts trafficking of bacteria to mesenteric lymph nodes by CX3CR1hi cells. *Nature* **494**, 116–120 (2013).

REFERENCES

312. Boring, L. *et al.* Impaired monocyte migration and reduced type 1 (Th1) cytokine responses in C-C chemokine receptor 2 knockout mice. *Journal of Clinical Investigation* **100**, 2552–2561 (1997).
313. Lee, S. L. *et al.* Unimpaired Thymic and Peripheral T Cell Death in Mice Lacking the Nuclear Receptor NGFI-B (Nur77). *Science* **269**, 532–535 (1995).
314. Wende, H. *et al.* The Transcription Factor c-Maf Controls Touch Receptor Development and Function. *Science* **335**, 1373–1376 (2012).
315. Clausen, B. E., Burkhardt, C., Reith, W., Renkawitz, R. & Förster, I. Conditional gene targeting in macrophages and granulocytes using LysMcre mice. *Transgenic Research* **8**, 265–277 (1999).
316. Love, M. I., Huber, W. & Anders, S. Moderated estimation of fold change and dispersion for RNA-seq data with DESeq2. *Genome Biology* **15**, 550 (2014).
317. Stuart, T. *et al.* Comprehensive Integration of Single-Cell Data. *Cell* **177**, 1888–1902.e21 (2019).
318. La Manno, G. *et al.* RNA velocity of single cells. *Nature* **560**, 494–498 (2018).
319. Bergen, V., Lange, M., Peidli, S., Wolf, F. A. & Theis, F. J. Generalizing RNA velocity to transient cell states through dynamical modeling. *Nature Biotechnology* **38**, 1408–1414 (2020).
320. Wu, T. *et al.* clusterProfiler 4.0: A universal enrichment tool for interpreting omics data. *The Innovation* **2**, 100141 (2021).
321. Aibar, S. *et al.* SCENIC: single-cell regulatory network inference and clustering. *Nature Methods* **14**, 1083–1086 (2017).
322. Trapnell, C. *et al.* The dynamics and regulators of cell fate decisions are revealed by pseudotemporal ordering of single cells. *Nature Biotechnology* **32**, 381–386 (2014).
323. Van den Berge, K. *et al.* Trajectory-based differential expression analysis for single-cell sequencing data. *Nature Communications* **11**, 1201 (2020).
324. Gu, Z., Eils, R. & Schlesner, M. Complex heatmaps reveal patterns and correlations in multidimensional genomic data. *Bioinformatics* **32**, 2847–2849 (2016).
325. DeTomaso, D. *et al.* Functional interpretation of single cell similarity maps. *Nature Communications* **10**, 4376 (2019).
326. Radermecker, C. *et al.* Locally instructed CXCR4hi neutrophils trigger environment-driven allergic asthma through the release of neutrophil extracellular traps. *Nature Immunology* **20**, 1444–1455 (2019).
327. Huber, W. *et al.* Orchestrating high-throughput genomic analysis with Bioconductor. *Nature Methods* **12**, 115–121 (2015).
328. Seita, J. *et al.* Gene Expression Commons: An Open Platform for Absolute Gene Expression Profiling. *PLoS ONE* **7**, e40321 (2012).

REFERENCES

329. Serbina, N. V. & Pamer, E. G. Monocyte emigration from bone marrow during bacterial infection requires signals mediated by chemokine receptor CCR2. *Nature Immunology* **7**, 311–317 (2006).
330. Zheng, G. X. Y. *et al.* Massively parallel digital transcriptional profiling of single cells. *Nature Communications* **8**, 14049 (2017).
331. Tushinski, R. J. *et al.* Survival of mononuclear phagocytes depends on a lineage-specific growth factor that the differentiated cells selectively destroy. *Cell* **28**, 71–81 (1982).
332. Jenkins, S. J. & Hume, D. A. Homeostasis in the mononuclear phagocyte system. *Trends in Immunology* **35**, 358–367 (2014).
333. Sarrazin, S. *et al.* MafB Restricts M-CSF-Dependent Myeloid Commitment Divisions of Hematopoietic Stem Cells. *Cell* **138**, 300–313 (2009).
334. Hamada, M., Tsunakawa, Y., Jeon, H., Yadav, M. K. & Takahashi, S. Role of MafB in macrophages. *Experimental Animals* **69**, 1–10 (2020).
335. Yadav, M. K. *et al.* MAFB in macrophages regulates cold-induced neuronal density in brown adipose tissue. *Cell Reports* **43**, 113978 (2024).
336. Kaiser, T. & Feng, G. Tmem119-EGFP and Tmem119-CreERT2 Transgenic Mice for Labeling and Manipulating Microglia. *eneuro* **6**, ENEURO.0448-18.2019 (2019).
337. Bendall, S. C. *et al.* Single-Cell Trajectory Detection Uncovers Progression and Regulatory Coordination in Human B Cell Development. *Cell* **157**, 714–725 (2014).
338. Gu, Z. simona: a comprehensive R package for semantic similarity analysis on bio-ontologies. *BMC Genomics* **25**, 869 (2024).
339. Meers, M. P., Tenenbaum, D. & Henikoff, S. Peak calling by Sparse Enrichment Analysis for CUT&RUN chromatin profiling. *Epigenetics & Chromatin* **12**, 42 (2019).
340. Almanzar, N. *et al.* A single-cell transcriptomic atlas characterizes ageing tissues in the mouse. *Nature* **583**, 590–595 (2020).
341. Badia-i-Mompel, P. *et al.* decoupleR: ensemble of computational methods to infer biological activities from omics data. *Bioinformatics Advances* **2**, vbac016 (2022).
342. Heng, T. S. P. *et al.* The Immunological Genome Project: networks of gene expression in immune cells. *Nature Immunology* **9**, 1091–1094 (2008).
343. Bain, C. C. *et al.* Long-lived self-renewing bone marrow-derived macrophages displace embryo-derived cells to inhabit adult serous cavities. *Nature Communications* **7**, ncomms11852 (2016).
344. Trzebanski, S. *et al.* Classical monocyte ontogeny dictates their functions and fates as tissue macrophages. *Immunity* **57**, 1225-1242.e6 (2024).
345. Prise, I. E. *et al.* CD163 and Tim-4 identify resident intestinal macrophages across sub-tissular regions that are spatially regulated by TGF- β . *bioRxiv* 2023.08.21.553672 (2023) doi:10.1101/2023.08.21.553672.

REFERENCES

346. Viola, M. F. *et al.* Dedicated macrophages organize and maintain the enteric nervous system. *Nature* **618**, 818–826 (2023).
347. Moura Silva, H. *et al.* c-MAF–dependent perivascular macrophages regulate diet-induced metabolic syndrome. *Science Immunology* **6**, eabg7506 (2021).
348. Nakamura, M. *et al.* c-Maf is essential for the F4/80 expression in macrophages in vivo. *Gene* **445**, 66–72 (2009).
349. Rojo, R. *et al.* Deletion of a Csf1r enhancer selectively impacts CSF1R expression and development of tissue macrophage populations. *Nature Communications* **10**, 3215 (2019).
350. Pridans, C., Lillico, S., Whitelaw, B. & Hume, D. A. Lentiviral vectors containing mouse Csf1r control elements direct macrophage-restricted expression in multiple species of birds and mammals. *Molecular Therapy Methods & Clinical Development* **1**, (2014).
351. Hecker, N. *et al.* Enhancer-driven cell type comparison reveals similarities between the mammalian and bird pallium. *Science* **387**, eadp3957 (2025).
352. Tan, S. Y. S. & Krasnow, M. A. Developmental origin of lung macrophage diversity. *Development* **143**, 1318–1327 (2016).
353. Saito, M. *et al.* Diphtheria toxin receptor-mediated conditional and targeted cell ablation in transgenic mice. *Nat Biotechnol* **19**, 746–750 (2001).
354. Jung, S. *et al.* In vivo depletion of CD11c+ dendritic cells abrogates priming of CD8+ T cells by exogenous cell-associated antigens. *Immunity* **17**, 211–220 (2002).
355. Merad, M. *et al.* Langerhans cells renew in the skin throughout life under steady-state conditions. *Nat Immunol* **3**, 1135–1141 (2002).
356. van Rooijen, N., Sanders, A. & van den Berg, T. K. Apoptosis of macrophages induced by liposome-mediated intracellular delivery of clodronate and propamidine. *J Immunol Methods* **193**, 93–99 (1996).
357. Culemann, S. *et al.* Stunning of neutrophils accounts for the anti-inflammatory effects of clodronate liposomes. *J Exp Med* **220**, e20220525 (2023).
358. Mass, E. The stunning clodronate. *J Exp Med* **220**, e20230339 (2023).
359. Hume, D. A. & MacDonald, K. P. A. Therapeutic applications of macrophage colony-stimulating factor-1 (CSF-1) and antagonists of CSF-1 receptor (CSF-1R) signaling. *Blood* **119**, 1810–1820 (2012).
360. Claeys, W. *et al.* Limitations of PLX3397 as a microglial investigational tool: peripheral and off-target effects dictate the response to inflammation. *Front Immunol* **14**, 1283711 (2023).
361. De Schepper, S. *et al.* Intestinal macrophages modulate synucleinopathy along the gut-brain axis. *Nature* <https://doi.org/10.1038/s41586-025-09984-y> (2026) doi:10.1038/s41586-025-09984-y.
362. Prinz, M. & Priller, J. Tickets to the brain: role of CCR2 and CX3CR1 in myeloid cell entry in the CNS. *J Neuroimmunol* **224**, 80–84 (2010).

REFERENCES

363. Carlin, L. M. *et al.* Nr4a1-dependent Ly6C(low) monocytes monitor endothelial cells and orchestrate their disposal. *Cell* **153**, 362–375 (2013).
364. Stolla, M. *et al.* Fractalkine is expressed in early and advanced atherosclerotic lesions and supports monocyte recruitment via CX3CR1. *PLoS One* **7**, e43572 (2012).
365. Schreiber, H. A. *et al.* Intestinal monocytes and macrophages are required for T cell polarization in response to *Citrobacter rodentium*. *J Exp Med* **210**, 2025–2039 (2013).
366. McKendrick, J. G. *et al.* CSF1R-dependent macrophages in the salivary gland are essential for epithelial regeneration after radiation-induced injury. *Sci Immunol* **8**, eadd4374 (2023).
367. Bennett, M. L. *et al.* New tools for studying microglia in the mouse and human CNS. *Proceedings of the National Academy of Sciences* **113**, E1738–E1746 (2016).
368. Bub, L. *et al.* Sensing of Metabolic Signals via GPR183 Promotes Occupation of Lung Macrophage Niches by Monocytes. *Journal of Experimental Medicine* <https://doi.org/10.1084/jem.20252667> doi:<https://doi.org/10.1084/jem.20252667>.
369. Feingold, K. R., Barker, M. E., Jones, A. L. & Grunfeld, C. Localization of tumor necrosis factor-stimulated DNA synthesis in the liver. *Hepatology* **13**, 773–779 (1991).
370. Swirski, F. K., Hilgendorf, I. & Robbins, C. S. From proliferation to proliferation: monocyte lineage comes full circle. *Semin Immunopathol* **36**, 137–148 (2014).
371. Bartneck, M. *et al.* The CCR2+ Macrophage Subset Promotes Pathogenic Angiogenesis for Tumor Vascularization in Fibrotic Livers. *Cell Mol Gastroenterol Hepatol* **7**, 371–390 (2019).
372. Wen, J., Guan, Y., Niu, H., Dang, Y. & Guan, J. Targeting cardiac resident CCR2+ macrophage-secreted MCP-1 to attenuate inflammation after myocardial infarction. *Acta Biomater* S1742-7061(24)00469-0 (2024) doi:10.1016/j.actbio.2024.08.025.
373. Daniel, B. *et al.* Macrophage inflammatory and regenerative response periodicity is programmed by cell cycle and chromatin state. *Mol Cell* **83**, 121-138.e7 (2023).
374. Little, M. C., Hurst, R. J. M. & Else, K. J. Dynamic changes in macrophage activation and proliferation during the development and resolution of intestinal inflammation. *J Immunol* **193**, 4684–4695 (2014).
375. Miyai, M. *et al.* Transcription Factor MafB Coordinates Epidermal Keratinocyte Differentiation. *J Invest Dermatol* **136**, 1848–1857 (2016).
376. Massa, F. M. *et al.* MAFB drives differentiation by permitting WT1 binding to podocyte specific promoters. Preprint at <https://doi.org/10.7554/eLife.93138.1> (2023).
377. Sturgeon, K. *et al.* Cdx1 refines positional identity of the vertebrate hindbrain by directly repressing Mafb expression. *Development* **138**, 65–74 (2011).

REFERENCES

378. Del Barrio, M. G. *et al.* A transcription factor code defines nine sensory interneuron subtypes in the mechanosensory area of the spinal cord. *PLoS One* **8**, e77928 (2013).
379. Pai, E. L.-L. *et al.* Mafb and c-Maf Have Prenatal Compensatory and Postnatal Antagonistic Roles in Cortical Interneuron Fate and Function. *Cell Rep* **26**, 1157-1173.e5 (2019).
380. Bastille, I. *et al.* Combinatorial transcriptional regulation establishes subtype-appropriate synaptic properties in auditory neurons. *Cell Rep* **44**, 115796 (2025).
381. Blanchi, B. *et al.* MafB deficiency causes defective respiratory rhythmogenesis and fatal central apnea at birth. *Nat Neurosci* **6**, 1091–1100 (2003).
382. Artner, I. *et al.* MafB is required for islet beta cell maturation. *Proc Natl Acad Sci U S A* **104**, 3853–3858 (2007).
383. Cross, M. & Renkawitz, R. Repetitive sequence involvement in the duplication and divergence of mouse lysozyme genes. *EMBO J* **9**, 1283–1288 (1990).
384. Shi, J., Hua, L., Harmer, D., Li, P. & Ren, G. Cre Driver Mice Targeting Macrophages. *Methods Mol Biol* **1784**, 263–275 (2018).
385. Goldmann, T. *et al.* A new type of microglia gene targeting shows TAK1 to be pivotal in CNS autoimmune inflammation. *Nat Neurosci* **16**, 1618–1626 (2013).
386. Abram, C. L., Roberge, G. L., Hu, Y. & Lowell, C. A. Comparative analysis of the efficiency and specificity of myeloid-Cre deleting strains using ROSA-EYFP reporter mice. *J Immunol Methods* **408**, 89–100 (2014).
387. Vo, T. & Saini, Y. Case report: Mafb promoter activity may define the alveolar macrophage dichotomy. *Front Immunol* **13**, 1050494 (2022).
388. Waldmann, H. & Hale, G. CAMPATH: from concept to clinic. *Philos Trans R Soc Lond B Biol Sci* **360**, 1707–1711 (2005).
389. Maxwell, E. *et al.* A conserved upstream element in the mouse *Csf1r* locus contributes to transcription in hematopoietic and trophoblast cells. *Journal of Leukocyte Biology* **118**, qiag004 (2026).
390. Zhang, J. *et al.* Cdc42 and RhoB activation are required for mannose receptor-mediated phagocytosis by human alveolar macrophages. *Mol Biol Cell* **16**, 824–834 (2005).
391. Mao, Y. & Finnemann, S. C. Regulation of phagocytosis by Rho GTPases. *Small GTPases* **6**, 89–99 (2015).
392. Barger, S. R. *et al.* Membrane-cytoskeletal crosstalk mediated by myosin-I regulates adhesion turnover during phagocytosis. *Nat Commun* **10**, 1249 (2019).
393. Overton, N. L. D., Brakhage, A. A., Thywißen, A., Denning, D. W. & Bowyer, P. Mutations in EEA1 are associated with allergic bronchopulmonary aspergillosis and affect phagocytosis of *Aspergillus fumigatus* by human macrophages. *PLoS One* **13**, e0185706 (2018).

REFERENCES

394. Depierre, M., Pompili, C. & Niedergang, F. Phagocytosis at a glance. *J Cell Sci* **138**, jcs263833 (2025).
395. Figliuolo da Paz, V. *et al.* Rapid Downregulation of DAB2 by Toll-Like Receptor Activation Contributes to a Pro-Inflammatory Switch in Activated Dendritic Cells. *Front Immunol* **10**, 304 (2019).
396. Chen, Q. *et al.* The different roles of V-ATPase a subunits in phagocytosis/endocytosis and autophagy. *Autophagy* **20**, 2297–2313 (2024).
397. Turk, B., Turk, D. & Turk, V. Lysosomal cysteine proteases: more than scavengers. *Biochim Biophys Acta* **1477**, 98–111 (2000).
398. Patel, S., Homaei, A., El-Seedi, H. R. & Akhtar, N. Cathepsins: Proteases that are vital for survival but can also be fatal. *Biomed Pharmacother* **105**, 526–532 (2018).
399. Soe-Lin, S. *et al.* Nramp1 promotes efficient macrophage recycling of iron following erythrophagocytosis in vivo. *Proc Natl Acad Sci U S A* **106**, 5960–5965 (2009).
400. Schaer, D. J. *et al.* CD163 is the macrophage scavenger receptor for native and chemically modified hemoglobins in the absence of haptoglobin. *Blood* **107**, 373–380 (2006).
401. Musrati, M. A. *et al.* Infection history imprints prolonged changes to the epigenome, transcriptome and function of Kupffer cells. *J Hepatol* **81**, 1023–1039 (2024).
402. Goriely, S. *et al.* Regulatory Networks Shaping Human Tumor-Associated Macrophages In Vivo Identify MAFB as a Key Transcriptional Driver. Preprint at <https://doi.org/10.21203/rs.3.rs-8562817/v1> (2026).
403. Jones, R. C. *et al.* The Tabula Sapiens: A multiple-organ, single-cell transcriptomic atlas of humans. *Science* **376**, eabl4896 (2025).
404. de Morree, A. *et al.* A molecular cell atlas of mouse lemur, an emerging model primate. *Nature* **644**, 173–184 (2025).
405. Wang, F. *et al.* Endothelial cell heterogeneity and microglia regulons revealed by a pig cell landscape at single-cell level. *Nature Communications* **13**, 3620 (2022).
406. Liao, Y. *et al.* Cell landscape of larval and adult *Xenopus laevis* at single-cell resolution. *Nature Communications* **13**, 4306 (2022).
407. Wang, R. *et al.* Construction of a cross-species cell landscape at single-cell level. *Nucleic Acids Research* **51**, 501–516 (2023).
408. Huerta-Cepas, J., Serra, F. & Bork, P. ETE 3: Reconstruction, Analysis, and Visualization of Phylogenomic Data. *Molecular Biology and Evolution* **33**, 1635–1638 (2016).
409. Schindelin, J. *et al.* Fiji: an open-source platform for biological-image analysis. *Nature Methods* **9**, 676–682 (2012).

REFERENCES

410. Subramanian, A. *et al.* Gene set enrichment analysis: A knowledge-based approach for interpreting genome-wide expression profiles. *Proceedings of the National Academy of Sciences* **102**, 15545–15550 (2005).
411. Kolberg, L. *et al.* g:Profiler—interoperable web service for functional enrichment analysis and gene identifier mapping (2023 update). *Nucleic Acids Research* **51**, W207–W212 (2023).
412. Robinson, J. T. *et al.* Integrative genomics viewer. *Nature Biotechnology* **29**, 24–26 (2011).
413. Ewels, P. A. *et al.* The nf-core framework for community-curated bioinformatics pipelines. *Nature Biotechnology* **38**, 276–278 (2020).
414. Bankhead, P. *et al.* QuPath: Open source software for digital pathology image analysis. *Scientific Reports* **7**, 16878 (2017).
415. van der Walt, S. *et al.* scikit-image: image processing in Python. *PeerJ* **2**, e453 (2014).
416. Perez, G. *et al.* The UCSC Genome Browser database: 2025 update. *Nucleic Acids Research* **53**, D1243–D1249 (2025).

APPENDICES

Appendix 1: Supplementary tables

Supplementary table 2.1. List of reagents, antibodies and commercial assays used in this study.

Antibodies	Source	Cat. Number
Anti-Cre Recombinase Monoclonal Antibody (Rabbit, clone D7L7L), unconjugated	Cell Signaling Technology	15036
Anti-mouse C1qA Monoclonal Antibody (Mouse, clone JL-1), biotin conjugated	Bio-techne	NBP1-51140B
Anti-mouse CD3 Monoclonal Antibody (Rat, clone 17A2), eFluor450 conjugated	ThermoFisher	48-0032-82
Anti-mouse CD3e Monoclonal Antibody (Armenian Hamster, clone 145-2C11), PE conjugated	BD Biosciences	553064
Anti-mouse CD11b Monoclonal Antibody (Rat, clone M1/70), APC conjugated	ThermoFisher	17-0112-82
Anti-mouse CD11b Monoclonal Antibody (Rat, clone M1/70), BUV395 conjugated	BD Biosciences	563553
Anti-mouse CD11b Monoclonal Antibody (Rat, clone M1/70), BUV563 conjugated	BD Biosciences	741242
Anti-mouse CD11b Monoclonal Antibody (Rat, clone M1/70), FITC conjugated	BD Biosciences	557396

Anti-mouse CD11b Monoclonal Antibody (Rat, clone M1/70), PE-Cy7 conjugated	BD Biosciences	552850
Anti-mouse CD11c Monoclonal Antibody (Hamster, clone HL3), BV786 conjugated	BD Biosciences	563735
Anti-mouse CD16/32 (Mouse BD Fc Block™) Monoclonal Antibody (Rat, clone 2.4G2), unconjugated	BD Biosciences	553142
Anti-mouse CD16/32 Monoclonal Antibody (Rat, clone 2.4G2), APC-Cy7 conjugated	BD Biosciences	560541
Anti-mouse CD19 Monoclonal Antibody (Rat, clone 1D3), PE conjugated	BD Biosciences	553786
Anti-mouse CD31 Monoclonal Antibody (Rat, clone 390), APC conjugated	ThermoFisher	17-0311-82
Anti-mouse CD34 Monoclonal Antibody (Rat, clone SA376A4), BV421 conjugated	BioLegend	152207
Anti-mouse CD45.1 Monoclonal Antibody (Mouse, clone A20), BUV395 conjugated	BD Biosciences	565212
Anti-mouse CD45.1 Monoclonal Antibody (Mouse, clone A20), BV510 conjugated	BD Biosciences	565278
Anti-mouse CD45.2 Monoclonal Antibody (Mouse, clone 104), BUV395 conjugated	BD Biosciences	564616

Anti-mouse CD45.2 Monoclonal Antibody (Mouse, clone 104), FITC conjugated	BD Biosciences	561874
Anti-mouse CD45.2 Monoclonal Antibody (Mouse, clone 104), PE-Cy7 conjugated	BD Biosciences	560696
Anti-mouse CD45.2 Monoclonal Antibody (Mouse, clone 104), PerCP-Cy5.5 conjugated	BD Biosciences	552950
Anti-mouse CD45.2 Monoclonal Antibody (Mouse, clone 104), V500 conjugated	BD Biosciences	562129
Anti-mouse CD64 Monoclonal Antibody (Mouse, clone X54-5/7.1), BV421 conjugated	BioLegend	139309
Anti-mouse CD115 (CSF1R) Monoclonal Antibody (Rat, clone AFS98), unconjugated	Bio X Cell	BE0213
Anti-mouse CD115 (CSF1R) Monoclonal Antibody (Rat, clone AFS98), APC conjugated	ThermoFisher	17-1152-82
Anti-mouse CD115 (CSF1R) Monoclonal Antibody (Rat, clone AFS98), PerCP-Cy5.5 conjugated	BioLegend	135526
Anti-mouse CD117 (c-Kit) Monoclonal Antibody (Rat, 2B8), BV786 conjugated	BD Biosciences	564012
Anti-mouse CD117 (c-Kit) Monoclonal Antibody (Rat, 2B8), PE conjugated	BioLegend	105807

Anti-mouse CD135 (Flt3) Monoclonal Antibody (Rat, clone A2F10), PE conjugated	ThermoFisher	12-1351-82
Anti-mouse CD170 (SiglecF) Monoclonal Antibody (Rat, clone E50-2440), PE conjugated	BD Biosciences	552126
Anti-mouse CD170 (SiglecF) Monoclonal Antibody (Rat, clone E50-2440), PE-CF594 conjugated	BD Biosciences	562757
Anti-mouse CD172a (SIRPa) Monoclonal Antibody (Rat, clone P84), APC conjugated	BioLegend	144013
Anti-mouse CD206 (MMR) Monoclonal Antibody (Rat, clone C068C2), AF647 conjugated	BioLegend	141712
Anti-mouse CD206 (MMR) Monoclonal Antibody (Rat, clone C068C2), AF647 conjugated	BioLegend	141712
Anti-mouse CD206 (MMR) Monoclonal Antibody (Rat, clone C068C2), PE-Cy7 conjugated	BioLegend	141719
Anti-mouse cMaf Monoclonal Antibody (Mouse, clone sym0F1), PE conjugated	ThermoFisher	12-9855-42
Anti-mouse F4/80 Monoclonal Antibody (Rat, BM8), BV650 conjugated	BioLegend	123149
Anti-mouse F4/80 Monoclonal Antibody (Rat, BM8), FITC conjugated	BioLegend	123108
Anti-mouse F4/80 Monoclonal Antibody (Rat, BM8), PE conjugated	Sony Biotechnology	1215550

Anti-mouse FcεRIα (MAR-1) Monoclonal Antibody (Armenian Hamster, clone MAR- 1), PE-Cy7 conjugated	BioLegend	134317
Anti-mouse I-A/I-E (MHC-II) Monoclonal Antibody (Rat, clone M5/114.15.2), unconjugated	ThermoFisher	56-5321-82
Anti-mouse I-A/I-E (MHC-II) Monoclonal Antibody (Rat, clone M5/114.15.2), AF700 conjugated	ThermoFisher	56-5321-80
Anti-mouse I-A/I-E (MHC-II) Monoclonal Antibody (Rat, clone M5/114.15.2), PerCP- Cy5.5 conjugated	Sony Biotechnology	1138125
Anti-mouse Ki-67 Monoclonal Antibody (Rat, clone SolA15), eFluor570 conjugated	ThermoFisher	41-5698-82
Anti-mouse Ki-67 Monoclonal Antibody (Rat, clone SolA15), PerCP-eFluor710 conjugated	ThermoFisher	46-5698-80
Anti-mouse Ly6A/E Monoclonal Antibody (Rat, clone D7), PE-Cy7 conjugated	BD Biosciences	561021
Anti-mouse Ly6C Monoclonal Antibody (Rat, clone HK1.4), AF700 conjugated	BioLegend	128024
Anti-mouse Ly6C Monoclonal Antibody (Rat, clone AL-21), PE-CF594 conjugated	BD Biosciences	562728
Anti-mouse Ly6G Monoclonal Antibody (Rat, clone 1A8), APC conjugated	BD Biosciences	560599

Anti-mouse Ly6G Monoclonal Antibody (Rat, clone 1A8), FITC conjugated	BD Biosciences	551461
Anti-mouse Ly6G Monoclonal Antibody (Rat, clone 1A8), PE conjugated	BD Biosciences	551461
Anti-mouse Ly6G Monoclonal Antibody (Rat, clone 1A8), PE-Cy7 conjugated	BD Biosciences	560601
Anti-mouse Ly6G Monoclonal Antibody (Rat, clone 1A8), PerCP-Cy5.5 conjugated	BioLegend	127615
Anti-mouse MafB Recombinant Monoclonal Antibody (Rabbit, clone BLR046F), unconjugated	Bethyl Laboratories Inc.	A700-046
Anti-mouse MerTK Monoclonal Antibody (Rat, clone DS5MMER), PE-Cy7 conjugated	ThermoFisher	25-5751-80
Anti-mouse XCR-1 Monoclonal Antibody (Mouse, clone ZET), APC-Cy7 conjugated	BioLegend	148223
Anti-rabbit IgG (H+L) Cross-Adsorbed Secondary Polyclonal Antibody (Goat), AF488 conjugated	ThermoFisher	A-11008
Anti-rabbit IgG (H+L) Cross-Adsorbed Secondary Polyclonal Antibody (Goat), AF647 conjugated	ThermoFisher	A-21244
Anti-rat IgG (H+L) Cross-Adsorbed Secondary Polyclonal Antibody (Donkey), AF594 conjugated	ThermoFisher	A-21209

Anti-trinitrophenol (isotype control) Monoclonal Antibody (Rat, 2A3), unconjugated	Bio X Cell	BE0089
TotalSeq™-A0305 anti-mouse Hashtag 5 Antibody	BioLegend	155809
TotalSeq™-A0306 anti-mouse Hashtag 6 Antibody	BioLegend	155811
TotalSeq™-A0307 anti-mouse Hashtag 7 Antibody	BioLegend	155813
TotalSeq™-A0308 anti-mouse Hashtag 8 Antibody	BioLegend	155815
Chemicals, Peptides and Recombinant Proteins	Source	Cat. Number
1,4 Dithiothreitol (DTT)	Sigma	10197777001
5-Ethynyl-2'-deoxyuridine (EdU)	Santa Cruz Biotechnology	sc-284628
Baytrill (enrofloxacin)	Bayer	616300
Bovine Serum Albumin (BSA)	Sigma	A7906
Brilliant Stain Buffer	BD Bioscience	563794
Collagenase A, from <i>Clostridium histolyticum</i>	Sigma	11088793001
Collagenase IV	ThermoFisher	17104019
cComplete™ Protease Inhibitor Cocktail	Sigma	11697498001
Diphtheria Toxin (DT), from <i>Corynebacterium diphtheriae</i>	List Biological Labs	150
DAPI	Biolegend	422801
DNase I	Sigma	11284932001
dNTP	ThermoFisher	N8080260

Donkey serum	Sigma	D9663
DPBS	ThermoFisher	14190094
EDTA	Merck Millipore	1084181000
Fetal Bovine Serum (FBS)	ThermoFisher	10270098
Glycerol	ThermoFisher	158920025
GoTaq G2 Hot Start Taq Polymerase	Promega	M7401
HBSS with Phenol Red	Lonza	BE10-508F
IsoFlo (Isoflurane)	Zoetis	B506
KAPA Express Extract	Merck	KK7100
Methanol	Merck	67-56-1
Nimatek (Ketamine)	Dechra	804132
Nonidet P 40 Substitute	Sigma	74385
O.C.T. Compound	Tissue-Tek	4583
Paraformaldehyde	ThermoFisher	F/1501/PB15
Percoll	GE Healthcare	17089101
Pexidartinib (PLX-3397)	MedChemExpress	HY-16749
Poly(ethylene glycol), average Mn 400	Sigma	202398
ProLong Antifade Mountant	ThermoFisher	P36961
Quant-iT™ RiboGreen™ RNA Assay Kit	ThermoFisher	R11490
Rompun (Xylazine)	Bayer	0076901
Sucrose	Merck	57-50-1
Streptavidin, PE conjugated	BD Biosciences	554061
SYTOX Blue Nucleic Acid Stain	ThermoFisher	S11348
Tris(hydroxymethyl)aminomethane	Merck Millipore	108382
TRIzol Reagent	ThermoFisher	10296010
Triton X-100	Merck	648466
Truseq Stranded mRNA kit	Illumina	20020594

Tween-20	ThermoFisher	233360010
Tween-80	Sigma	P1754
G418	ThermoFisher	10131027
UltraPure BSA	ThermoFisher	AM2616
Sucrose	Merck	57-50-1
Streptavidin, PE conjugated	BD Biosciences	554061
SYTOX Blue Nucleic Acid Stain	ThermoFisher	S11348
Tris(hydroxymethyl)aminomethane	Merck Millipore	108382
TRIzol Reagent	ThermoFisher	10296010
Triton X-100	Merck	648466
Truseq Stranded mRNA kit	Illumina	20020594
Tween-20	ThermoFisher	233360010
Tween-80	Sigma	P1754
G418	ThermoFisher	10131027
UltraPure BSA	ThermoFisher	AM2616
Commercial Assays	Source	Cat. Number
APC Mouse Lineage Antibody Cocktail, with Isotype Control	BD Bioscience	558074
CD11b MicroBeads, human and mouse	Miltenyi Biotec	130-049-601
Chromium Next GEM Single Cell 3' GEM, Library & Gel Bead Kit v3.1	10X Genomics	1000128
CD11b MicroBeads, human and mouse	Miltenyi Biotec	130-049-601
Chromium Next GEM Single Cell 3' GEM, Library & Gel Bead Kit v3.1	10X Genomics	1000128
Chromium Next GEM Chip G Single Cell Kit	10X Genomics	1000120

Click-iT™ Plus EdU Alexa Fluor™ 488 Flow Cytometry Assay Kit	ThermoFisher	10632
FITC Mouse Anti-Ki-67 Set	BD Bioscience	556026
LIVE/DEAD™ Fixable Near-IR Dead Cell Stain Kit, for 633 or 635 nm excitation	Invitrogen	L34976
MCP-1/CCL2 Mouse Uncoated ELISA Kit	ThermoFisher	88-7391-88
Monocyte Isolation Kit (BM), mouse	Miltenyi Biotec	130-100-629
Pierce™ BCA Protein Assay Kit	ThermoFisher	23225
Single Index Kit T Set A	10X Genomics	1000213
NovaSeq 6000 S1 Reagent Kit v1.5 (100 cycles)	Illumina	20028319

Supplementary table 2.2. List of the deposited data generated and used in this study.

Bulk RNA-seq data	Source	Identifier
Raw and analyzed RNA-seq data	This study	GEO: GSE194021
scRNA-seq data	Source	Identifier
Raw and analyzed scRNA-seq data	This study	GEO: GSE194021
Lung IM and classical monocytes	Schyns et al. ¹⁰⁴	EMBL-EBI: E-MTAB-7678
Microarray data	Source	Identifier
Classical Monocytes MHCII ⁺ in blood	ImmGen	GEO: GSM605868, GSM605870, GSM605871
Classical Monocytes MHCII ⁻ in bone marrow	ImmGen	GEO: GSM854329, GSM854330, GSM854331
Classical Monocytes MHCII ⁻ in blood	ImmGen	GEO: GSM605872, GSM605873, GSM605874
Nonclassical Monocytes, MHCII ⁺	ImmGen	GEO: GSM605878, GSM605879
Nonclassical Monocytes in bone marrow	ImmGen	GEO: GSM854332, GSM854333, GSM854334
Nonclassical Monocytes in blood	ImmGen	GEO: GSM605884, GSM605885
Nonclassical Monocytes, MHCII ^{int}	ImmGen	GEO: GSM605886, GSM605887, GSM605888, GSM605889, GSM605890
Lung CD11b ⁺ CD24 ⁻ macrophages	ImmGen	GEO: GSM854271, GSM854272

Small Intestinal Lamina Propria CD11c ^{hi} CD103 ⁻ CD11b ⁺ macrophages	ImmGen	GEO: GSM854262, GSM854263, GSM854264, GSM854265, GSM854266, GSM854267, GSM854268
Bone marrow macrophages	ImmGen	GEO: GSM854317, GSM854318, GSM854319
Spleen Red Pulp macrophages	ImmGen	GEO: GSM605853, GSM605854, GSM605855
Peritoneal macrophage steady state	ImmGen	GEO: GSM854294, GSM854295, GSM854296
Peritoneal cavity macrophages steady state	ImmGen	GEO: GSM605850, GSM605851, GSM605852
Medullary macrophages from skin draining lymph nodes	ImmGen	GEO: GSM854322, GSM854323
Central nervous system microglia	ImmGen	GEO: GSM854326, GSM854327, GSM854328
CD103 ⁺ migratory DC, Mediastinal LN CD103 ⁺ DC	ImmGen	GEO: GSM854243, GSM854244, GSM854245
CD11b ⁺ migratory DC, Mediastinal LN CD11b ⁺ DC	ImmGen	GEO: GSM854255, GSM854256, GSM854257
Lung CD103 ⁺ dendritic cells	ImmGen	GEO: GSM538231, GSM538232, GSM538233, GSM854241,
Lung MHCII ⁺ CD11c ⁺ CD103 ⁻ CD11b ⁺ CD24 ⁺ dendritic cells	ImmGen	GEO: GSM854269, GSM854270
Lung IM, Ly6C ⁺ cMo and AM	Sabatel et al. ¹⁸⁶	EMBL-EBI: E-MTAB-5012

Supplementary table 3.1. Key resources table.

REAGENT or RESOURCE	SOURCE	IDENTIFIER
Antibodies		
Anti-mouse C1qA Monoclonal Antibody (Mouse, clone JL-1), biotin conjugated	Novus	Cat#NBP1-51140B; RRID: AB_11014205
Anti-mouse CD3e Monoclonal Antibody (Armenian Hamster, clone 145-2C11), PE conjugated	BD Biosciences	Cat#553064; RRID: AB_394597
Anti-mouse CD11b Monoclonal Antibody (Rat, clone M1/70), BVU395 conjugated	BD Biosciences	Cat#563553; RRID: AB_2738276
Anti-mouse CD11b Monoclonal Antibody (Rat, clone M1/70), FITC conjugated	BD Biosciences	Cat#557396; RRID: AB_396679
Anti-mouse CD11b Monoclonal Antibody (Rat, clone M1/70), BV605 conjugated	BD Biosciences	Cat#563015; RRID: AB_2737951
Anti-mouse CD11b Monoclonal Antibody (Rat, clone M1/70), PE-Cy7 conjugated	BD Biosciences	Cat#552850; RRID: AB_394491
Anti-mouse CD11c Monoclonal Antibody (Armenian Hamster, clone N418), eFluor 450 conjugated	Thermo Fisher Scientific	Cat#48-0114-82; RRID: AB_1548654
Anti-mouse CD11c Monoclonal Antibody (Hamster, clone HL3), BV786 conjugated	BD Biosciences	Cat#563735; RRID: AB_2738394
Anti-mouse CD16/32 (Mouse BD Fc Block™) Monoclonal Antibody (Rat, clone 2.4G2), unconjugated	BD Biosciences	Cat#553142; RRID: AB_394657
Anti-mouse CD19 Monoclonal Antibody (Rat, clone 1D3), PE conjugated	BD Biosciences	Cat#553786; RRID: AB_395050
Anti-mouse CD19 Monoclonal Antibody (Rat, clone 1D3), RB780 conjugated	BD Biosciences	Cat#755522; RRID: AB_3676664

Anti-mouse CD24 Monoclonal Antibody (Mouse, clone M1/69), biotin conjugated	BioLegend	Cat#101803; RRID: AB_312836
Anti-mouse CD31 Monoclonal Antibody (Rat, clone 390), BV785 conjugated	BioLegend	Cat#102435; RRID: AB_2810334
Anti-mouse CD43 Monoclonal Antibody (Rat, clone S7), RY586 conjugated	BD Biosciences	Cat#753416
Anti-mouse CD45 Monoclonal Antibody (Rat, clone 30-F11), AF700 conjugated	Thermo Fisher Scientific	Cat# 56-0451-82, RRID: AB_891454
Anti-mouse CD45.1 Monoclonal Antibody (Mouse, clone A20), BUV395 conjugated	BD Biosciences	Cat#565212; RRID: AB_2722493
Anti-mouse CD45.1 Monoclonal Antibody (Mouse, clone A20), APC conjugated	BD Biosciences	Cat#558701; RRID: AB_1645214
Anti-mouse CD45.2 Monoclonal Antibody (Mouse, clone 104), BUV395 conjugated	BD Biosciences	Cat#564616; RRID: AB_2738867
Anti-mouse CD45.2 Monoclonal Antibody (Mouse, clone 104), FITC conjugated	BD Biosciences	Cat#561874; RRID: AB_10894189
Anti-mouse CD45.2 Monoclonal Antibody (Mouse, clone 104), PE-Cy7 conjugated	BD Biosciences	Cat#560696; RRID: AB_1727494
Anti-mouse CD45.2 Monoclonal Antibody (Mouse, clone 104), PerCP-Cy5.5 conjugated	BD Biosciences	Cat#552950; RRID: AB_394528
Anti-mouse CD45.2 Monoclonal Antibody (Mouse, clone 104), V500 conjugated	BD Biosciences	Cat#562129; RRID: AB_10897142
Anti-mouse CD49b Monoclonal Antibody (Rat, clone DX5), PE conjugated	BioLegend	Cat#108907; RRID: AB_313414
Anti-mouse CD62L Monoclonal Antibody (Rat, clone MEL-14), BV421 conjugated	BD Biosciences	Cat#562910; RRID: AB_2737885

Anti-mouse CD64 Monoclonal Antibody (Rabbit, clone 027), unconjugated	Thermo Fisher Scientific	Cat#MA5-29706; RRID: AB_2785530
Anti-mouse CD64 Monoclonal Antibody (Mouse, clone X54-5/7.1), BV421 conjugated	BioLegend	Cat#139309; RRID: AB_2562694
Anti-mouse CD64 Monoclonal Antibody (Mouse, clone X54-5/7.1), PE-Dazzle594 conjugated	BioLegend	Cat#139320; RRID: AB_2566559
Anti-mouse CD115 (CSF1R) Monoclonal Antibody (Rat, clone AFS98), AF488 conjugated	BioLegend	Cat#135511; RRID: AB_11218605
Anti-mouse CD115 (CSF1R) Monoclonal Antibody (Rat, clone AFS98), BV605 conjugated	BioLegend	Cat#135517; RRID: AB_2562760
Anti-mouse CD115 (CSF1R) Monoclonal Antibody (Rat, clone AFS98), APC conjugated	Thermo Fisher Scientific	Cat#17-1152-82; RRID: AB_1210789
Anti-mouse CD115 (CSF1R) Monoclonal Antibody (Rat, clone AFS98), PerCP-Cy5.5 conjugated	BioLegend	Cat#135526; RRID: AB_2566462
Anti-mouse CD163 Monoclonal Antibody (Rat, clone TNKUPJ), APC conjugated	Thermo Fisher Scientific	Cat#17-1631-80; RRID: AB_2784645
Anti-mouse CD163 Monoclonal Antibody (Rat, clone TNKUPJ), PE-eF610 conjugated	Thermo Fisher Scientific	Cat#61-1631-80; RRID: AB_2848497
Anti-mouse CD170 (SiglecF) Monoclonal Antibody (Rat, clone S17007L), FITC conjugated	BioLegend	Cat# 155504; RRID: AB_2750233
Anti-mouse CD170 (SiglecF) Monoclonal Antibody (Rat, clone E50-2440), PE conjugated	BD Biosciences	Cat#552126; RRID: AB_394341
Anti-mouse CD170 (SiglecF) Monoclonal Antibody (Rat, clone E50-2440), PE-CF594 conjugated	BD Biosciences	Cat#562757; RRID: AB_2687994
Anti-mouse CD170 (SiglecF) Monoclonal Antibody (Rat, clone E50-2440), BV750 conjugated	BD Biosciences	Cat#747316; RRID: AB_2872024

Anti-mouse CD177 Monoclonal Antibody (Rat, clone Y127), AF647 conjugated	BD Biosciences	Cat#566599; RRID: AB_2869790
Anti-mouse CD206 (MMR) Monoclonal Antibody (Rat, clone C068C2), AF647 conjugated	BioLegend	Cat#141712; RRID: AB_10900420
Anti-mouse CD206 (MMR) Monoclonal Antibody (Rat, clone C068C2), PE-Cy7 conjugated	BioLegend	Cat#141719; RRID: AB_2562247
Anti-mouse CD319 (CRACC) Monoclonal Antibody (Rat, clone 4G2), BV711 conjugated	BD Biosciences	Cat#747994; RRID: AB_2872455
Anti-mouse Clec-2 Monoclonal Antibody (Rat, clone 17D9), PE conjugated	BioLegend	Cat#146104; RRID: AB_2562383
Anti-mouse Clec4f Polyclonal Antibody (Goat), unconjugated	R&D Systems	Cat# AF2784; RRID: AB_2081339
Anti-mouse F4/80 Monoclonal Antibody (Rat, BM8), FITC conjugated	BioLegend	Cat#123108; RRID: AB_893502
Anti-mouse F4/80 Monoclonal Antibody (Rat, BM8), PE conjugated	Sony Biotechnology	Cat#1215550
Anti-mouse F4/80 Monoclonal Antibody (Rat, BM8), BV650 conjugated	BioLegend	Cat#123149; RRID: AB_2564589
Anti-mouse F4/80 Monoclonal Antibody (Rat, BM8), BV785 conjugated	BioLegend	Cat#123141; RRID: AB_2563667
Anti-mouse F4/80 Monoclonal Antibody (Rat, BM8), APC-eFluor 780 conjugated	Thermo Fisher Scientific	Cat# 47-4801-82; RRID: AB_2735036
Anti-mouse FCRL5 Monoclonal Antibody (Rat, 4G11), AF647 conjugated	Butovsky Lab, validated in ⁵⁷	N/A
Anti-mouse FR- β Monoclonal Antibody (Rat, 10/FR2), APC conjugated	BioLegend	Cat#153305; RRID: AB_2721312

Anti-H3K27ac Monoclonal Antibody (Mouse), unconjugated	Thermo Fisher Scientific	Cat#MA5-23516; RRID: AB_2608307
Anti-mouse I-A/I-E (MHC-II) Monoclonal Antibody (Rat, clone M5/114.15.2), BV421 conjugated	BioLegend	Cat#107632; RRID: AB_10900075
Anti-mouse I-A/I-E (MHC-II) Monoclonal Antibody (Rat, clone M5/114.15.2), PerCP-Cy5.5 conjugated	BioLegend	Cat#107625; RRID: AB_2191072
Anti-mouse I-A/I-E (MHC-II) Monoclonal Antibody (Rat, clone M5/114.15.2), AF700 conjugated	Thermo Fisher Scientific	Cat#56-5321-80; RRID: AB_494010
Anti-goat IgG (H+L) Cross-Adsorbed Secondary Polyclonal Antibody (Donkey), AF555 conjugated	Thermo Fisher Scientific	Cat#A-21432; RRID: AB_2535853
Anti-rat IgG (H+L) Cross-Adsorbed Secondary Polyclonal Antibody (Donkey), AF488 conjugated	Thermo Fisher Scientific	Cat#A-21208; RRID: AB_141709
Anti-rabbit IgG (H+L) Cross-Adsorbed Secondary Polyclonal Antibody (Goat), AF488 conjugated	Thermo Fisher Scientific	Cat#A-11008; RRID: AB_143165
Anti-rabbit IgG (H+L) Cross-Adsorbed Secondary Polyclonal Antibody (Goat), AF647 conjugated	Thermo Fisher Scientific	Cat#A-31573; RRID: AB_2536183
Anti-rabbit IgG (minimal x-reactivity) Secondary Polyclonal Antibody (Donkey), AF647 conjugated	BioLegend	Cat#406414, RRID: AB_2563202
Anti-mouse Ly6C Monoclonal Antibody (Rat, clone AL-21), PE-CF594 conjugated	BD Biosciences	Cat#562728; RRID: AB_2737749
Anti-mouse Ly6C Monoclonal Antibody (Rat, clone HK1.4), BV570 conjugated	BioLegend	Cat#128030; RRID: AB_2562617

Anti-mouse Ly6C Monoclonal Antibody (Rat, clone HK1.4), AF700 conjugated	BioLegend	Cat#128024; RRID: AB_10643270
Anti-mouse Ly6G Monoclonal Antibody (Rat, clone 1A8), PE conjugated	BD Biosciences	Cat#551461; RRID: AB_394208
Anti-mouse Ly6G Monoclonal Antibody (Rat, clone 1A8), BV650 conjugated	BD Biosciences	Cat#740554; RRID: AB_2740255
Anti-mouse Ly6G Monoclonal Antibody (Rat, clone 1A8), PE-Cy7 conjugated	BD Biosciences	Cat#560601; RRID: AB_1727562
Anti-mouse MafB Recombinant Monoclonal Antibody (Rabbit, clone BLR046F), unconjugated	Bethyl	Cat#A700-046; RRID: AB_2891845
Anti-human MAFB Polyclonal Antibody (Rabbit), unconjugated	Cell Signaling Technology	Cat#41019; RRID: AB_2799192
Anti-mouse MerTK Monoclonal Antibody (Rat, clone DS5MMER), PerCP-eF710 conjugated	Thermo Fisher Scientific	Cat#46-5751-82; RRID: AB_2688094
Anti-mouse MerTK Monoclonal Antibody (Rat, clone DS5MMER), PE-Cy7 conjugated	Thermo Fisher Scientific	Cat#25-5751-80; RRID: AB_2573465
Anti-mouse NK1.1 Monoclonal Antibody (Mouse, clone PK136), AF660 conjugated	Thermo Fisher Scientific	Cat#606-5941-82; RRID: AB_2896296
Anti-mouse P2ry12 Monoclonal Antibody (Rat, clone S16007D), AF488 conjugated	BioLegend	Cat#848015; RRID: AB_2936702
Anti-mouse RELM α Monoclonal Antibody (Rat, clone DS8RELM), APC conjugated	Thermo Fisher Scientific	Cat#17-5441-82; RRID: AB_2762696
Anti-mouse Tim4 Monoclonal Antibody (Rat, clone RMT4-54), unconjugated	BioLegend	Cat# 130002; RRID: AB_1227802
Anti-mouse Tim4 Monoclonal Antibody (Rat, clone RMT4-54), AF647 conjugated	BioLegend	Cat#130007; RRID: AB_2201842

Anti-mouse Tim4 Monoclonal Antibody (Rat, clone RMT4-54), PE-Cy7 conjugated	BioLegend	Cat#130009; RRID: AB_2565718
Anti-mouse Vsig4 Monoclonal Antibody (Rat, clone NLA14), APC conjugated	Thermo Fisher Scientific	Cat#17-5752-80; RRID: AB_2637428
Anti-mouse Vsig4 Monoclonal Antibody (Rat, clone NLA14), SB600 conjugated	Thermo Fisher Scientific	Cat#63-5752-82; RRID: AB_2802437
Anti-mouse Vsig4 Monoclonal Antibody (Rat, clone NLA14), PE-Cy7 conjugated	Thermo Fisher Scientific	Cat#25-5752-82; RRID: AB_2637431
Anti-mouse XCR1 Monoclonal Antibody (Mouse, clone ZET), BV510 conjugated	BioLegend	Cat#148218; RRID: AB_2565231
Rabbit IgG Isotype Control Antibody (Rabbit, polyclonal), unconjugated	Thermo Fisher Scientific	Cat#31235; RRID: AB_243593
Rabbit IgG CUT&RUN Negative Control Antibody (Rabbit, polyclonal)	EpiCypher	Cat#13-0042; RRID: AB_2923178
TotalSeq™-B0301 anti-mouse Hashtag 1 Antibody	BioLegend	Cat#155831; RRID: AB_2814067
TotalSeq™-B0302 anti-mouse Hashtag 2 Antibody	BioLegend	Cat#155833; RRID: AB_2814068
TotalSeq™-B0303 anti-mouse Hashtag 3 Antibody	BioLegend	Cat#155835; RRID: AB_2814069
Chemicals, peptides, and recombinant proteins		
1,4-Dithiothreitol (DTT)	Sigma-Aldrich	Cat#10197777001
2-Mercaptoethanol	Thermo Fisher Scientific	Cat#31350010
Antigenfix	Diapath	Cat#P0014
Alizarin Red S	Thermo Fisher Scientific	Cat#400480250
Baytrill (enrofloxacin)	Bayer	Cat#616300
Bovine Serum Albumin (BSA)	Sigma-Aldrich	Cat#A7906
Brilliant Stain Buffer	BD Biosciences	Cat#563794
Collagenase A, from <i>Clostridium histolyticum</i>	Sigma-Aldrich	Cat#11088793001
Collagenase IV, from <i>Clostridium histolyticum</i>	Thermo Fisher Scientific	Cat#17104019

Collagenase VIII, from <i>Clostridium histolyticum</i>	Sigma-Aldrich	Cat#C2139
cComplete™ Protease Inhibitor Cocktail	Sigma-Aldrich	Cat#11697498001
cComplete™ EDTA-free Protease Inhibitor Cocktail	Sigma-Aldrich	Cat#11873580001
DAPI	Thermo Fisher Scientific	Cat#D3571
Dispase II	Sigma-Aldrich	Cat#D4693
Donkey Serum	Abcam	Cat#ab7475
DNase I	Sigma-Aldrich	Cat#11284932001
DPBS	Thermo Fisher Scientific	Cat#14190094
EDTA	Merck Millipore	Cat#1084181000
Fetal Bovine Serum (FBS)	Thermo Fisher Scientific	Cat#10270098
Glycine	Merck	Cat#104691000
Glycerol	Thermo Fisher Scientific	Cat#158920025
GlycoBlue™ Coprecipitant	Thermo Fisher Scientific	Cat#AM9515
HBSS without Phenol Red	Thermo Fisher Scientific	Cat# 14025050
HBSS with Phenol Red	Lonza	Cat#BE10-508F
IsoFlo (Isoflurane)	Zoetis	Cat#B506
MEM Non-Essential Amino Acids Solution	Thermo Fisher Scientific	Cat# 11140050
Mouse M-CSF Recombinant Protein	PeptoTech	Cat#315-02
Nimatek (Ketamine)	Dechra	Cat#804132
Nonidet P 40 Substitute	Sigma-Aldrich	Cat#74385
Formaldehyde	Thermo Fisher Scientific	Cat#BP531-500
Percoll	GE Healthcare	Cat#17089101
PKH26	Sigma-Aldrich	Cat#MIDI26
ProLong™ Diamond Antifade Mountant	Thermo Fisher Scientific	Cat#P36970
Rompun (Xylazine)	Bayer	Cat#0076901
RPMI 1640 Medium	Thermo Fisher Scientific	Cat#21875034
Saponin	Sigma-Aldrich	Cat#4521
Sodium Pyruvate	Thermo Fisher Scientific	Cat#11360070
Streptavidin, PE-CF594 conjugated	BD Biosciences	Cat#562318; RRID: AB_11154218
Streptavidin, APC conjugated	BD Biosciences	Cat#554067; RRID: AB_10050396)
SYTOX™ Blue	Thermo Fisher Scientific	Cat#S11348
Tris(hydroxymethyl)aminomethane	Merck Millipore	Cat#108382
TRIzol Reagent	Thermo Fisher Scientific	Cat#10296010
Triton X-100	Merck	Cat#648466

Tween-20	Thermo Fisher Scientific	Cat#233360010
UltraPure BSA	Thermo Fisher Scientific	Cat#AM2616
Critical commercial assays		
Chromium Next GEM Single Cell 3' GEM, Library & Gel Bead Kit v3.1	10X Genomics	Cat#1000128
Chromium Next GEM Chip G Single Cell Kit	10X Genomics	Cat#1000120
Classical Monocyte Isolation Kit, human	Miltenyi Biotec	Cat#130-117-337
CUTANA™ ChIC/CUT&RUN Kit	EpiCypher	Cat#14-1048
CUTANA™ CUT&RUN Library Prep Kit	EpiCypher	Cat#14-1001
FoxP3 Transcription Factor Staining Kit	Thermo Fisher Scientific	Cat#00-5523-00
LIVE/DEAD™ Fixable Near-IR Dead Cell Stain Kit	Thermo Fisher Scientific	Cat#L34976
Monocyte Isolation Kit (BM), mouse	Miltenyi Biotec	Cat#130-100-629
NovaSeq 6000 S4 Reagent Kit v1.5 (300 cycles)	Illumina	Cat#20028312
pHrodo™ Red S. aureus BioParticles™ Conjugate for Phagocytosis	Thermo Fisher Scientific	Cat#A10010
RNA Clean & Concentrator Kit	Zymo Research	Cat#R1013
TruSeq Stranded mRNA kit	Illumina	Cat#20020594
Deposited data		
Microarray data	ImmGen	https://www.immgen.org/ ; RRID: SCR_021792
Tabula Muris Senis	The Tabula Muris Consortium ³⁴⁰	https://registry.opendata.aws/tabula-muris-senis/ ; GEO: GSE132042
RNA-Seq of BMDM from <i>Mafb^{f/f}</i> and <i>Lyz2^{Cre}Mafb^{f/f}</i> mice	This paper	GEO: GSE286897

scRNA-Seq of RTM from <i>Mafb^{fl/fl}</i> and <i>Lyz2^{Cre}Mafb^{fl/fl}</i> mice	This paper	GEO: GSE287347
scRNA-Seq of lung IM from <i>Mafb^{fl/fl}</i> and <i>Lyz2^{Cre}Mafb^{fl/fl}</i> mice	Vanneste et al. ¹¹⁰	GEO: GSE193891
MafB CUT&RUN of BMDM from <i>Mafb^{fl/fl}</i> and <i>Lyz2^{Cre}Mafb^{fl/fl}</i> mice	This paper	GEO: GSE287346
H3K27ac CUT&RUN of BMDM from <i>Lyz2^{Cre} Mafb^{fl/fl}</i> mice and <i>Mafb^{fl/fl}</i> littermate controls	This paper	GEO: GSE287476
MafB CUT&RUN of LPM from <i>Mafb^{fl/fl}</i> and <i>Lyz2^{Cre}Mafb^{fl/fl}</i> mice	This paper	GEO: GSE287346
MafB CUT&RUN of MDM	This paper	GEO: GSE287346
PU.1 ChIP-Seq data	Soucie et al. ²⁴³ ChIP-Atlas	http://chip-atlas.org/ ; RRID: SCR_015511; GEO: GSM1964736
Tabula Sapiens	The Tabula Sapiens Consortium ⁴⁰³	https://registry.opendata.aws/tabula-sapiens/ ; GEO: GSE201333
Tabula Microcebus	The Tabula Microcebus Consortium ⁴⁰⁴	https://figshare.com/projects/Tabula_Microcebus/112227
Pig Cell Atlas	Wang et al. ⁴⁰⁵	https://dreamapp.biomed.au.dk/pigatlas/ ; GEO: GSE196055, GSE193975
Xenopus Cell Landscape	Liao et al. ⁴⁰⁶	https://doi.org/10.6084/m9.figshare.19152839 ; GEO: GSE195790
Zebrafish Cell Landscape	Wang et al. ⁴⁰⁷	https://figshare.com/s/1ab3c6d7648d12247eb2 ; GEO: GSE198571, GSE178150

Experimental models: Organisms/strains

Mouse: C57BL/6J	The Jackson Laboratory	N/A
Mouse: C57BL/6J CD45.1: B6.SJL- <i>Ptprca</i> ^a <i>Pepcb</i> ^b /BoyJ	The Jackson Laboratory	Cat#002014; RRID: IMSR_JAX:002014
Mouse: <i>Lyz2</i> ^{Cre} : B6.129P2- <i>Lyz2</i> ^{tm1(cre)lfo} /J	Clausen et al. ³¹⁵ The Jackson Laboratory	Cat#004781; RRID: IMSR_JAX:004781
Mouse: <i>Clec4f</i> ^{Cre} : <i>Clec4f</i> ^{tm2.1(cre)Ciphe}	Scott et al. ²³⁶	N/A
Mouse: <i>Tmem119</i> ^{CreERT2} : C57BL/6- <i>Tmem119</i> ^{em1(cre/ERT2)Gfng} /J	Kaiser et al. ³³⁶ The Jackson Laboratory	Cat#031820; RRID: IMSR_JAX:031820
Mouse: <i>Maf</i> ^{fl/fl} : <i>Maf</i> ^{tm2.1Cbm}	Wende et al. ³¹⁴	N/A
Mouse: <i>Mafb</i> ^{fl/fl} : <i>Mafb</i> ^{tm1.1Mari}	Vanneste et al. ¹¹⁰	N/A
Software and algorithms		
BioRender	BioRender	https://www.biorender.com/ ; RRID: SCR_018361
Cell Ranger	10X Genomics	RRID: SCR_023221
Code for analysis sequencing data	This paper	https://github.com/dovnneste/MafB_Mac
ETE Toolkit	Huerta-Cepas et al. ⁴⁰⁸	https://etetoolkit.org/
FIJI (ImageJ)	Schindelin et al. ⁴⁰⁹	https://imagej.net/Fiji ; RRID: SCR_003070
FlowJo	TreeStar	https://www.flowjo.com/ ; RRID: SCR_008520
Gene Set Enrichment Analysis	Subramanian et al. ⁴¹⁰	http://www.broadinstitute.org/gsea/ ; RRID: SCR_003199
g:Profiler	Kolberg et al. ⁴¹¹	http://biit.cs.ut.ee/gprofiler/ ; RRID: SCR_006809

GraphPad Prism	GraphPad Software	https://www.graphpad.com/scientific-software/prism/ ; RRID: SCR_002798
HOMER	Heinz et al. ²¹⁸	http://homer.ucsd.edu/ ; RRID: SCR_010881
Illustrator	Adobe	https://www.adobe.com/ ; RRID: SCR_010279
Integrative Genomic Viewer	Robinson et al. ⁴¹²	https://igv.org/ ; RRID: SCR_011793
nf-core	Ewels et al. ⁴¹³	https://nf-co.re/
QuPath	Bankhead et al. ⁴¹⁴	https://qupath.github.io/ ; RRID: SCR_018257
R Project for Statistical Computing	The R Foundation	http://www.r-project.org/ ; RRID: SCR_001905
SEACR	Meers et al. ³³⁹	https://seacr.fredhutch.org/
scikit-image	van der Walt et al. ⁴¹⁵	https://scikit-image.org/ ; RRID: SCR_021142
UCSC Genome Browser	Perez et al. ⁴¹⁶	http://genome.ucsc.edu/ ; RRID: SCR_005780
Other		
Axioscan 7	Zeiss	N/A
Chromium iX	10X Genomics	N/A
LSM 980	Zeiss	N/A
LSRFortessa™ Cell Analyzer	BD Biosciences	N/A
MA900 Multi-Application Cell Sorter	Sony Biotechnology	N/A
NovaSeq 6000	Illumina	N/A

CURRICULUM VITAE

CURRICULUM VITAE

Personal data

Name Domien Vanneste
Place of birth Ghent, Belgium
Date of birth 9th of October 1995
Nationality Belgian



Contact details

Work address Bât. B34 GIGA Immunobiology – Immunophysiology,
Avenue de l'Hôpital 11, 4000 Liège, Belgium
Phone +32(0)4 366 98 42; +32 (0)493 71 04 92
Email domien.vanneste@uliege.be; domienvanneste@live.be

Education and Positions

2019-Present **Doctoral researcher**
Laboratory of Immunophysiology, GIGA Institute, University of Liège, Belgium
Faculty of Veterinary Medicine, University of Liège, Belgium
Promoter: Dr. Thomas Marichal

2018-2019 **Researcher**
Unit of Molecular Signal Transduction in Inflammation, VIB-UGent Center for Inflammation Research, Belgium
Department of Biomedical Molecular Biology, Ghent University, Belgium

2016-2018 **Master of Science (M.Sc.), Biochemistry and Biotechnology**
Ghent University, Belgium
Grade: *Magna cum laude*

2016 **ERASMUS European Exchange Program**
Uppsala University, Sweden

CURRICULUM VITAE

2013-2016 **Bachelor of Science (B.Sc.), Biochemistry and Biotechnology**
Ghent University, Belgium
Grade: *Magna cum laude*

Awards and Grants

Awards

2025 2nd Best poster award – Belgian Immunological Society
2024 **ECI Bright Sparks Award – European Federation of Immunological Societies**

Grants

2024 Mobility and Congress funding – Fund for Scientific Research – FNRS
2024 Lauréat Bourse de Fonctionnement – Fondation Léon Fredericq
2023 Travel Grant – EDT-Immunology of the Fund for Scientific Research - FNRS
2023 Lauréat Crédits forfaitaires – Fondation Léon Fredericq
2022 Lauréat Crédits forfaitaires – Fondation Léon Fredericq
2022-2024 **Research Fellow Aspirant (Renewal) – Fund for Scientific Research – FNRS**
2022 Mobility and Congress funding – Fund for Scientific Research – FNRS
2022 **Keystone Symposia Scholarship**
2021 Lauréat Crédits forfaitaires – Fondation Léon Fredericq
2020-2022 **Research Fellow Aspirant – Fund for Scientific Research - FNRS**

Scientific Publications

H-index 7 and 246 citations (Google Scholar on 27th of May 2026)

Peer-reviewed scientific articles in A1 journals

Bub, L., Evren, E., Verwaerde, S., Ruscitti, C., **Vanneste, D.**, Ghosh, P., Gao, Y., Sleiers, N., Deng, R., López Montes, M., Howley, K., La Rocca, R., Niehrs, A., Glaros, V., Dahlen, B., Smed-Sørensen, A., Kreslavsky, T., Björkström, N. K., Reboldi, A., Bossios, A., Marichal, T., Lambrecht, B. N., & Willinger, T. (2026). [The Oxysterol Receptor GPR183 Senses Metabolic Niche Signals that Promote Differentiation of Monocytes into Tissue Resident Lung Macrophages.](#) *Journal of Experimental Medicine*, 223(4), e20252667.

CURRICULUM VITAE

<https://doi.org/10.1084/jem.20252667> Co-second author

Vanneste, D., Peng, W., Liu, Z., Hamaïdia, M., La Rocca, R., Abinet, J., Balthazar, A., Perin, F., Hego, A., Cataldo, D., Bureau, F., Compère, P., Machiels, B., Scott, C. L., Radermecker, C., & Marichal, T. (2026). [MafB is a conserved transcriptional regulator of macrophage development and functional identity across tissues and species](#). *Immunity*, S1074-7613(26)00033-6. Advance online publication. <https://doi.org/10.1016/j.immuni.2026.01.012> First and co-corresponding author

Vanneste, D., & Marichal, T. (2025). [Transcriptional Regulation of Macrophage Specification and Function](#). *European journal of immunology*, 55(12), e70097. <https://doi.org/10.1002/eji.70097> First and co-corresponding author

Peng, W., **Vanneste, D.**, Bejarano, D., Abinet, J., Meunier, M., Radermecker, C., Perin, F., Cataldo, D., Bureau, F., Schlitzer, A., Bai, Q., & Marichal, T. (2025). [Endothelial-driven TGFβ signaling supports lung interstitial macrophage development from monocytes](#). *Science immunology*, 10(106), eadr4977. <https://doi.org/10.1126/sciimmunol.adr4977> Second author

Ruscitti, C., Abinet, J., Maréchal, P., Meunier, M., de Meeûs, C., **Vanneste, D.**, Janssen, P., Dourcy, M., Thiry, M., Bureau, F., Schneider, C., Machiels, B., Hidalgo, A., Ginhoux, F., Dewals, B. G., Guiot, J., Schleich, F., Garigliany, M. M., Bellahcène, A., Radermecker, C., & Marichal, T. (2024). [Recruited atypical Ly6G+ macrophages license alveolar regeneration after lung injury](#). *Science immunology*, 9(98), eado1227. <https://doi.org/10.1126/sciimmunol.ado1227>

Highlighted in Focus by Iliakis, C. S., & Wack, A. Iliakis, C. S., & Wack, A. (2024). Never trust a single myeloid marker: Ly6G on repair-promoting lung macrophages. *Science immunology*, 9(98), eadq7306. <https://doi.org/10.1126/sciimmunol.adq7306>

Legrand, C., **Vanneste, D.**, Hego, A., Sabatel, C., Mollers, K., Schyns, J., Maréchal, P., Abinet, J., Tytgat, A., Liégeois, M., Polese, B., Meunier, M., Radermecker, C., Fiévez, L., Bureau, F., & Marichal, T. (2024). [Lung Interstitial Macrophages Can Present Soluble Antigens and Induce Foxp3+ Regulatory T Cells](#). *American journal of respiratory cell and molecular biology*, 70(6), 446–456. <https://doi.org/10.1165/rcmb.2023-0254OC> Second author

Highlighted in Editorial by Schworer, S. A., & Moran, T. P. Schworer, S. A., & Moran, T. P. (2024). Pulmonary Interstitial Macrophages stIMulate Regulatory T-Cell Responses. *American journal of respiratory cell and molecular biology*, 70(6), 429–430. <https://doi.org/10.1165/rcmb.2024-0049ED>.

Vanneste, D., Bai, Q., Hasan, S., Peng, W., Pirottin, D., Schyns, J., Maréchal, P., Ruscitti, C., Meunier, M., Liu, Z., Legrand, C., Fievez, L., Ginhoux, F., Radermecker, C., Bureau,

CURRICULUM VITAE

F., & Marichal, T. (2023). [MafB-restricted local monocyte proliferation precedes lung interstitial macrophage differentiation.](#) *Nature immunology*, 24(5), 827–840. <https://doi.org/10.1038/s41590-023-01468-3> **First author**

Highlighted in News&views by Khan, A. B., & Robbins, C. S. Khan, A. B., & Robbins, C. S. (2023). Macrophage niche availability enables local monocyte proliferation in peripheral tissues. *Nature immunology*, 24(5), 743–745. <https://doi.org/10.1038/s41590-023-01482-5>

Vanneste, D., Staal, J., Haegman, M., Driège, Y., Carels, M., Van Nuffel, E., De Bleser, P., Saeys, Y., Beyaert, R., & Afonina, I. S. (2022). [CARD14 Signalling Ensures Cell Survival and Cancer Associated Gene Expression in Prostate Cancer Cells.](#) *Biomedicines*, 10(8), 2008. <https://doi.org/10.3390/biomedicines10082008> **First author**

Staal, J., Driège, Y., Haegman, M., Kreike, M., Iliaki, S., **Vanneste, D.**, Lork, M., Afonina, I. S., Braun, H., & Beyaert, R. (2021). [Defining the combinatorial space of PKC::CARD-CC signal transduction nodes.](#) *The FEBS journal*, 288(5), 1630–1647. <https://doi.org/10.1111/febs.15522>

Holgado, A., Braun, H., Verstraete, K., **Vanneste, D.**, Callewaert, N., Savvides, S. N., Afonina, I. S., & Beyaert, R. (2020). [Single-Chain Soluble Receptor Fusion Proteins as Versatile Cytokine Inhibitors.](#) *Frontiers in immunology*, 11, 1422. <https://doi.org/10.3389/fimmu.2020.01422>

Under review

Meunier, M., Abinet, J., Ruscitti, C., **Vanneste, D.**, Maréchal, P., Di Cesare, M., La Rocca, R., Hego, A., Bureau, F., Herkenne, S., Nobis, M., Marichal, T., & Radermecker, C. [Lung-margined neutrophils regulate capillary blood flow to safeguard blood oxygenation and endothelial fitness.](#) *Under review.*

Wong, A., Vohra, S., Ellis, K., Hamidzada, H., **Vanneste, D.**, Bellworthy, R., Arlidge, C., Macklin, J., Kantores, C., Dick, S., Clemente-Casares, X., Marichal, T., Langlais, D., Wilson, M., Lupien, M., & Epelman, S. [Distinct Chromatin Landscapes Dictate Resident Cardiac Macrophage Lifecycles and Functions.](#) *Under review.*

Detavernier, A., Donckier de Donceel, E., Patanè, F., Pedron, A., Acolty, V., Nguyen, M., Thomas, S., Martens, V., Vanhulst, T., Van Horenbeke, F., Collin, A., Zindy, E., El Korchi, S., Melchior, M., Venturoli, D., Szymczak, F., **Vanneste, D.**, Marichal, T., Willard-Gallo, K., Rongvaux, A., Bizet, M., Azouz, A., & Stanislas, G. [Regulatory Networks Shaping Human Tumor-Associated Macrophages In Vivo Identify MAFB as a Key Transcriptional Driver.](#) *Under review.*

CURRICULUM VITAE

Kempen, L., **Vanneste, D.**, Javaux, J., Dams, L., Sandor, R., Pathammavong, M., Han, L., Donners, M., Wieland, E., Gijbels, M., Meuwis, M., Louis, E., Reif, M., Balsamo, M., Kasakovski, D., Rohlfing, M., Biessen, E., Marichal, T., Goossens, P., & Machiels, B. [Gammaherpesvirus infection impairs fibrosis resolution through PD-L1⁺ fibroblasts and PD-1⁺ CD8⁺ T cell interaction.](#) *Under review.* Co-first author

Scientific activities

Reviewer for *Science*, *Immunity*, *Nature communications*, *Cell Reports*, *LabAnimal* and *Development*.

Communications

- 2025 Annual Meeting of the Belgian Immunological Society (BIS), Liège, Belgium – Poster presentation
- 2024 7th European Congress of Immunology: Conquering Challenges with Immunology, Dublin, Ireland – Oral presentation**
- 2024 EDT-Immunology PhD Day: From Disease to Therapeutic Solutions, Liège, Belgium – Oral presentation
- 2023 EMDS2023@VIB, Ghent, Belgium – Poster presentation
- 2023 The 2nd ImmunoSensation2-IFReC International School on Advanced Immunology, Maria-Laach, Germany – Oral and poster presentation**
- 2023 Keystone Symposium - Myeloid Cells: Development, Diversity and Distinct Biological Role – Poster presentation
- 2022 FARAH-Day, Liège, Belgium – Poster presentation
- 2022 EDT-Immunology PhD Day: Technological Innovations in Immunology, Liège, Belgium – Oral and poster presentation
- 2022 Keystone Symposium - Myeloid Cells: From Birth to Immunity and Disease, Banff, Canada – Oral and poster presentation**

References

CURRICULUM VITAE

Name Thomas MARICHAL, DMV, PhD
Position Full professor
Affiliation Laboratory of Immunophysiology, GIGA Institute, Liège University, Liège, Belgium
Mailing Address Avenue de l'Hôpital 1, 4000 Liège, Belgium
Phone Office: +32 (0) 4 / 366 95 55; Lab: +32 (0) 4 / 366 36 71
or 98 42
E-mail t.marichal@uliege.be

Name Bénédicte MACHIELS, DMV, PhD
Position Associate professor
Affiliation Laboratory of Immunology-Vaccinology, FARAH Institute, University of Liège, Liège, Belgium.
Mailing Address Avenue de Cureghem 10, 4000 Liège, Belgium
Phone +32 (0) 4 / 366 43 93
E-mail bmachiels@uliege.be



Presses de la Faculté de Médecine vétérinaire de l'Université de Liège

4000 Liège (Belgique)

D/2026/0480/6

ISBN 978-2-87543-250-6



9 782875 432506